Multimessenger studies of point-sources using the IceCube neutrino telescope and the MAGIC gamma-ray telescope

DISSERTATION

zur Erlangung des akademischen Grades

doctor rerum naturalium
(Dr. rer. nat.)
im Fach Physik

eingereicht an der
Mathematisch-Naturwissenschaftlichen
Fakultät I
Humboldt-Universität zu Berlin

von
Frau Magister Konstancja Satalecka
geboren am 03.03.1983 in Olkusz

Präsident der Humboldt-Universität zu Berlin:
Prof. Dr. Dr. h.c. Christoph Markschies

Dekan der Mathematisch-Naturwissenschaftlichen
Fakultät I:
Prof. Dr. Lutz-Helmut Schön

Gutachter:
1. Dr. Elisa Bernardini
2. Prof. Dr. Thomas Lohse
3. Prof. dr hab. Włodzimierz Bednarek

eingereicht am: 04.02.2010
Tag der mündlichen Prüfung: 20.05.2010

Dla moich Rodziców
a także
dla Małego i Dużego Żubra

Abstract

Three messengers can be used to extract information about the sources of cosmic rays: photons, charged particles (cosmic rays) and neutrinos. In this work the connection between the Very High Energy (VHE) gamma-rays and neutrinos is investigated in the context of recent observations and theoretical models.

In order to increase the probability of detecting a neutrino point source two new approaches were developed. First, a correlation study of possible time and directional coincidences of neutrino events, detected by the AMANDA-II telescope at the South Pole, and gamma-ray flares, observed by the Imaging Atmospheric Cherenkov Telescopes (IACTs), in the years 2004-2006, was performed for 7 objects. Second, taking the same AMANDA-II data set, 18 sources were analyzed, using a new algorithm which looks for structures in the time distribution of the neutrino events from pre-defined directions. None of the analysis resulted in a detection of a neutrino point source.

The sparse time and flux state coverage of the TeV gamma-ray data is one of the most serious issues connected with any correlation study involving photons from the high energy range. This problem was addressed in this work by an analysis of historical gamma-ray data from the public archive at DESY and of the recently obtained results from the MAGIC Active Galactic Nuclei (AGN) monitoring program. Based on this data a statistical analysis of different emission states of two extragalactic VHE gamma-ray sources, Mrk 421 and Mrk 501, was performed. Due to still low flux statistics, no final conclusions concerning the probability of finding those sources in a flux state above a certain threshold can be made.

The results of the MAGIC AGN monitoring program from the observational season 2007/2008 are presented here, for two sources: Mrk 501 and 1ES 1959+650. Both sources were found in a similarly low state (around 0.2 Crab) and showed moderate (Mrk 501) or no (1ES 1959+650) variability with no prominent flares. Since a part of the 2008 monitoring data of Mrk 501 was collected during a multi-wavelength campaign a modeling of the broad-band Spectral Energy Distribution of Mrk 501 is also discussed.

Zusammenfassung

Drei Botenteilchen können benutzt werden, um Informationen über Quellen der Kosmischer Strahlung zu erhalten: Photonen, geladene Teilchen (kosmische Strahlung) und Neutrinos. In dieser Arbeit wird anhand von Beobachtungsdaten und theoretischen Modellen der Zusammenhang zwischen extrem hochenergetischer Gammastrahlung und Neutrinos untersucht.

Um die Wahrscheinlichkeit für die Entdeckung einer Neutrino-Punktquelle zu erhöhen, wurden zwei neue Ansätze entwickelt. Zum einen wurde für 7 Objekte eine Suche nach Zeit- und Richtungskorrelationen zwischen Neutrinoereignissen, registriert vom AMANDA-II Teleskop am Südpol, und den von IACT-Teleskopen im Zeitraum 2004-2006 beobachteten Gammastrahlungsausbrüchen durchgeführt. Zum anderen wurden im selben AMANDA-II Datensatz 18 Quellen analysiert, unter Verwendung eines neuen Algorithmus zur Suche nach Strukturen in der zeitlichen Verteilung von Neutrino-Ereignissen aus einer vordefinierten Richtungen. Keine der Analysen führte zur Entdeckung einer Neutrino-Punktquelle.

Die zeitlich lückenhafte Aufzeichnung von TeV Gammastrahlungs Daten, zusammen mit der Tatsache, daß die Aufzeichnung nicht alle Emmisionszustände abdeckt, stellt eine der schwerwiegendsten Einschränkungen bei Korrelationsstudien unter Einbeziehung hochenergetischer Photonen dar. Dieses Problem wurde in der vorliegenden Arbeit durch die Analyse historischer Daten aus den öffentlichen Archiven am DESY und neuer Ergebnisse des MAGIC Active Galactic Nuclei (AGN) Beobachtungsprogramms berücksichtigt. Anhand dieser Daten konnte eine statistische Analyse der verschiedenen Emissionszustände zweier extragalaktischer Gammastrahlungsquellen durchgeführt werden. Aufgrund einer zu geringen Statistik der Messungen konnten jedoch keine endgültigen Schlüsse über die Wahrscheinlichkeit, diese Quellen in einem Emmisionszustand oberhalb eines gewissen Schwellenwertes anzufinden, gezogen werden.

Für die zwei Quellen, Mrk 501 und 1ES 1959+650, werden hier die Ergebnisse des MAGIC AGN Beobachtungsprogramms von 2007 bis 2008 vorgestellt. Beide Quellen wurden in einem ähnlich niedrigen Zustand (ca. 0.2 Crab) vorgefunden und wiesen mäßige (Mrk 501) bzw. keine (1ES 1959+650) Variabilität und keine auffälligen Ausbrüche auf. Da ein Teil der Mrk 501 Daten von 2008 während einer Kampagne zur gleichzeitigen Beobachtung in verschiedenen Wellenlängenbereichen aufgenommen wurden, wird die Modelierung der spektralen Energieverteilung von Mrk 501 ebenfalls diskutiert. (Übersetzung: Jürgen Schiefele)

Contents

1 Introduction 1

2 Instruments 25

1 Introduction

Four hundred years ago Galileo constructed his telescope and pointed it to the Jupiter - the era of modern astronomy has began. Since then our perception of the Universe has changed dramatically. Today we not only posses more sensitive instruments, but also can observe much more than optical light: photons of radio to TeV energies, protons, nuclei up to iron and cosmic neutrinos (not yet detected). We now know, that behind what looks like a peaceful harmony of the celestial spheres, violent processes take place, in which particles are accelerated to ultra high energies and emitted from sources in our Galaxy and beyond. In order to understand those processes, it is crucial to develop analysis methods which will allow us to study correlations between events observed by experiments which, till now, usually concentrated on one messenger only - photon, proton or neutrino. In what follows a brief overview of the recent experimental results and theoretical models concerning the connection between the three messenger particles will be given, concentrating on one class of the extragalactic emitters - the blazars.

1.1 Cosmic Rays (CR)

In 1912 Victor Hess performed several balloon flights in order to measure the ionization of the atmosphere. Contrary to what was expected, if the ionization was only caused by radioactive decays in the Earth's rocks, he discovered that it was increasing with height. As an explanation he proposed that Earth is exposed to a constant flux of charged particles of cosmic origin - the Cosmic Rays (CR) [Hes12].

Since then the spectrum of CR was measured over a wide energy range (Fig. 1.1). Balloons and satellites observed it directly at low energies ($<10^{14}$ eV). For examining it in higher energies, where the flux is lower, large arrays of shower detectors for indirect measurements were build on the Earth surface.

The spectrum of CR (Fig. 1.1) is very well described by a power law:

$$dN/dE \propto E^{-\alpha} \tag{1.1}$$

with two kinks commonly refered to as *knee* (E $\sim 10^{16}$ eV) and *ankle* (E $\sim 10^{18}$ eV). The spectral indices for the different parts of the spectrum are [WSBM98] [B+99]:

$$\alpha = \begin{cases} 2.67 & \text{for } \log(\mathrm{E/eV}) < 15.4 \\ 3.10 & \text{for } 15.4 < \log(\mathrm{E/eV}) < 18.5 \\ 2.75 & \text{for } 18.5 > \log(\mathrm{E/eV}) \end{cases} \tag{1.2}$$

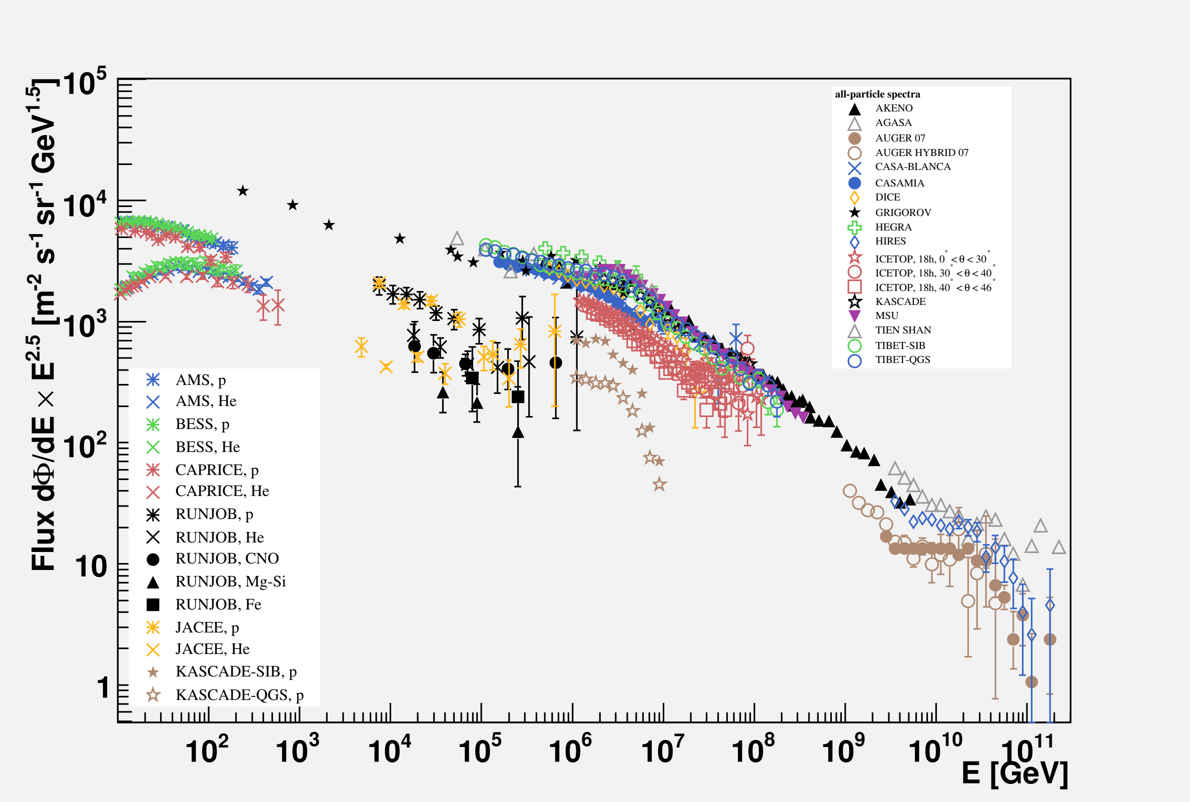

Figure 1.1: Cosmic rays spectrum as measured by various experiments. Data collected by T. K. Gaisser.

At the energies above 5×10^{19} eV the flux should be attenuated and the spectrum altered due to the proton interactions with the Cosmic Microwave Background (CMB):

$$p + \gamma_{CMB} \rightarrow \Delta \rightarrow p + \pi^0 \text{ or } n + \pi^+. \tag{1.3}$$

This effect is known as the Greisen, Zatsepin, Kuzmin (GZK) cutoff [Gre66] [KZ66]. It's main consequence is an exponential attenuation of CR flux. For the objects located at distances grater than 200 Mpc from Earth the CR flux is to faint to be measured.

Observations performed by the HiRes experiment, measuring the fluorescent light emission of CR induced showers, seemed to confirm the existence of the GZK cutoff [A+04a]. This results were contradicted by AGASA, a surface array for measurements of the showers' charged component, which detected several events above the predicted cutoff [Y+95]. Recent results from the AUGER experiment, which combines those two techniques in a hybrid array of 3000 km^2, confirmed the HiRes observations [A+08b] (see Fig. 1.1).

It was shown by Fermi [Fer49] that the general spectral powerlaw like behavior can be explained by stochastic shock acceleration of particles in collision-less plasma. Such acceleration sites could be the Super Novae Remnants (SNR) in our Galaxy. With the typical rate of SN explosions in a galaxy of ∼3/100 yr and a mean ejected mass of $\sim 10\, M_{SUN}$ per SN the SNR shock front is active for about 1000 yr. The luminosity of a single SNR can be converted into the total luminosity of SNRs in the Milky Way, which gives $\sim 3\times10^{42}$ erg/s a power output sufficiently large to explain the CR production at energies above 10^9 eV. This calculation however does not explain the observed kink in the spectrum.

In [Hil84] Hillas calculated that the maximum energy obtained by particles in the Fermi acceleration mechanism depends strongly on the magnetic field and size of the acceleration region (see Fig. 1.2). The maximum energies attainable by diffusive shock acceleration in SNR are limited to $< 10^{15}$ eV due to finite acceleration times, finite volumes as well as synchrotron losses of the accelerated particles. As a consequence objects in our Galaxy can produce the CR spectrum only up to the *ankle*. Particles observed at higher energies have to come from extragalactic sources such as Active Galactic Nuclei (AGN) or Gamma Ray Bursts (GRB). Another argument for the extragalactic origin of the high energy cosmic rays is the fact that at these energies the particles' gyroradius is larger than the size of the Milky Way and most of them would escape from it before we would have a chance of detecting them on Earth.

In [A+08a] a correlation of CR events with energies above 6×10^{19} eV with positions of AGN lying within ∼75 Mpc (or sources of similar spatial distribution) was claimed. In the section 1.4 the properties of AGN as possible CR emitters are discussed in more detail.

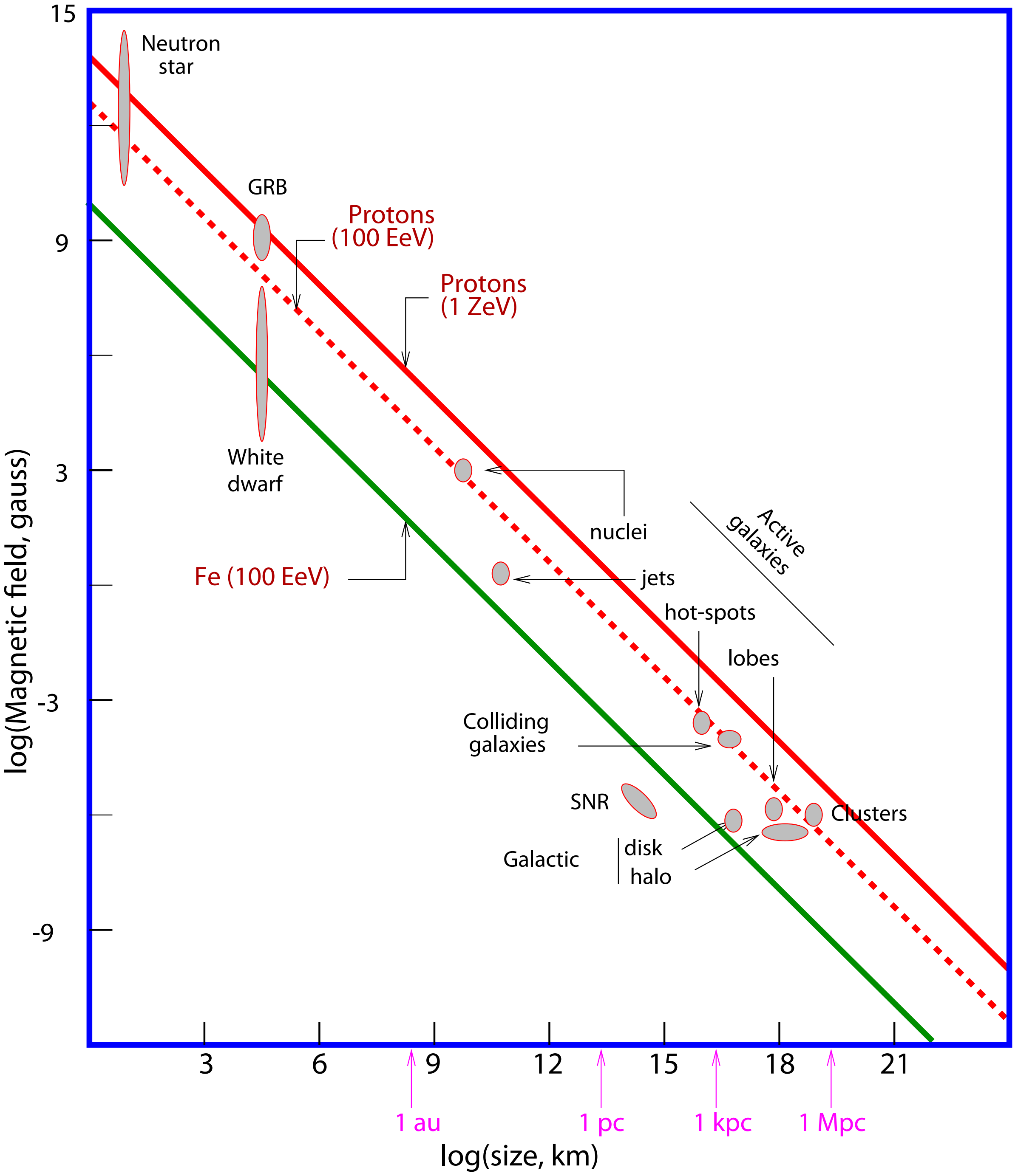

Figure 1.2: The Hillas plot shows up to which energies cosmic objects can in principle confine cosmic rays [Hil84]. The confinement energy is a function of the size of the acceleration region and the strength of the magnetic field.

1.2 Very High Energy (VHE) γ-rays

Unlike the protons and other charged particles photons are not deflected in magnetic fields and point straight to their source. This quality gives us an advantage of an immediate identification of the photon emitter.

Similarly to cosmic rays, gamma rays of cosmic origin are absorbed high in the Earth's atmosphere (Fig. 1.3) and direct detection is possible only with a balloon or space satellite. Explorer-11 was the first satellite to detect cosmic γ-rays [KC62] and since then many successful missions followed, e.g. the Compton Gamma-Ray Observatory (CGRO) (1991-2000), INTEGRAL (2000-present) [B$^+$06], AGILE (2007-present) [T$^+$08b], and the Gamma-ray Large Area Space Telescope (GLAST/Fermi) (launched in June 2008). The EGRET instrument on board CGRO completed the first γ-ray sky survey at energies above 100 MeV, discovering 271 γ-ray sources [H$^+$99a]. Also Fermi, which carries the LAT instrument sensitive from 20 MeV to 300 GeV, recently published its first source catalog. It achieved EGRET sensitivity after a few days long sky survey and so far detected 205 γ-ray sources [A$^+$09c].

At energies above 10 GeV the detection efficiency of satellite based experiments is unfortunately limited by their effective area. Even Fermi, with it's relatively large effective area of 0.8 m^2, achieves low photon statistics for bright sources. The Imaging Atmospheric Cherenkov Technique (IACT), introduced for the first time in the 1980s by the Whipple Collaboration, allows to detect the Cherenkov radiation from large air showers produced in an interaction of γ-rays with air molecules high in Earth's atmosphere. In section 2.5 it is described how air showers can be detected by ground-based IACT telescopes; section 2.7 introduce in more detail the MAGIC telescope.

1.3 Extragalactic Background Light (EBL)

On their way to Earth photons from extragalactic sources interact with the Extragalactic Background Light (EBL), i.e. low energy photons radiated by stars and galaxies along the history of the Universe:

$$\gamma + \gamma_{EBL} \rightarrow e^+ + e^-. \tag{1.4}$$

This effect leads to an attenuation of the intrinsic γ-ray flux Φ_0:

$$\Phi = \Phi_0 \times e^{-\tau(E,z)}. \tag{1.5}$$

The opacity τ increases with the photon energy E and the redshift z of the source. A recent review of the existing measurements of EBL is given in [MR07]. Due to large uncertainties of these measurements different models were developed to calculate the expected EBL density and photon opacity (see e.g. [K$^+$04a] or [F$^+$08]). If one could measure the intrinsic spectrum emitted by the source and then compare it with the observed one the calculation of the optical depth at different energies would be straightforward. Unfortunately this is not possible and the usual procedure is to assume that the standard acceleration processes cannot produce a spectrum with photon index harder

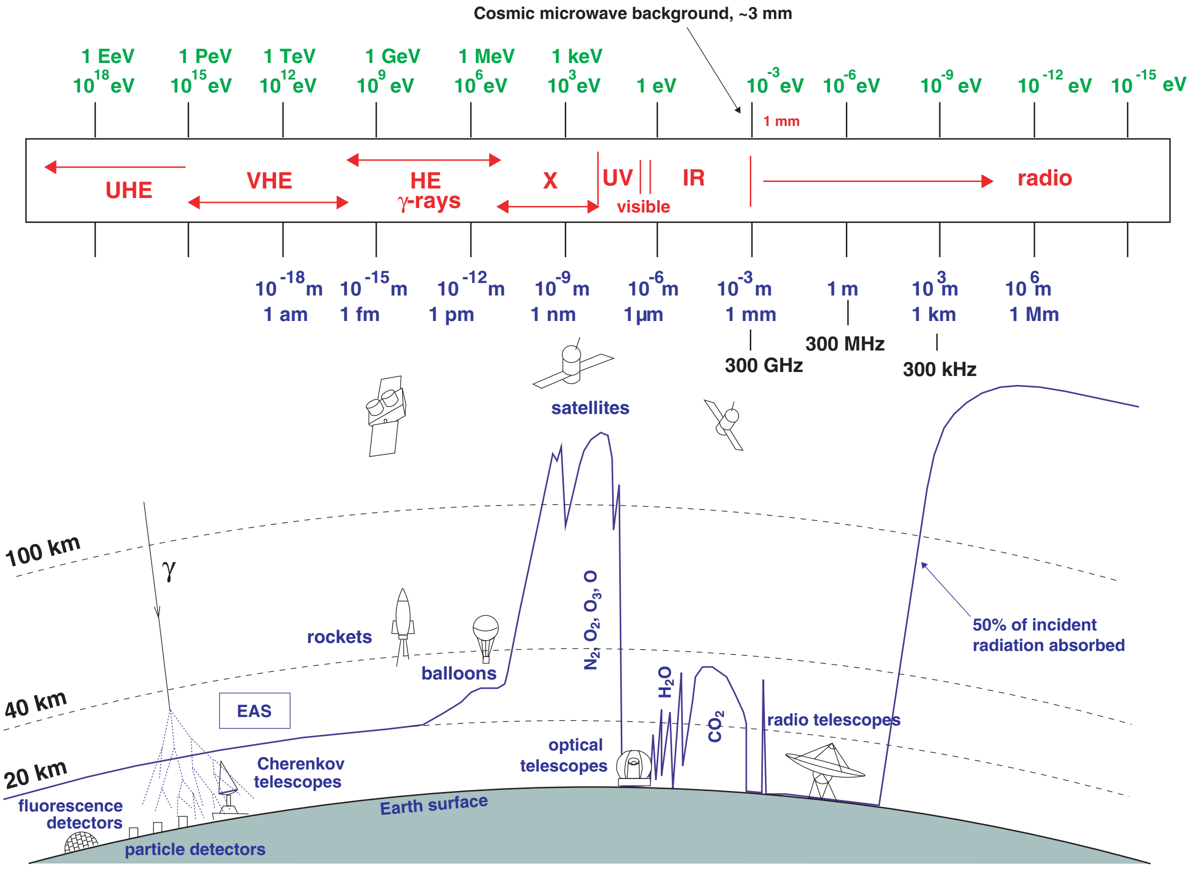

Figure 1.3: Picture of atmosphere transparency for different wavelengths [Lon92]. The continuous line indicates the height at which a detector can receive half of the incoming radiation. Only the photons of optical and radio frequencies can be directly measured on Earth. Other wavelengths are (partially) absorbed in the atmosphere. In the case of γ-rays an indirect measurement with the Imaging Atmospheric Cherenkov Technique is possible.

than -1.5. If, after deabsorption, this condition is not fulfilled, one can rule out the proposed model.

An example of one of the recent models, commonly known as "Kneiske Low" [K+02] is given in Fig. 1.4. The "Low" in the name comes from the fact that the authors chose the infrared star formation rate as low as allowed by observational lower limits (dark red triangles [E+99]), in order to consider the least possible γ-ray attenuation. The infrared part of the low redshift ($z \leq 0.5$) EBL is important for the absorption of γ-rays from low redshift sources. This model is used in section 6.4.4 to correct the spectra of Mrk 501 measured during a MW campaign in 2008.

1.4 Active Galactic Nuclei (AGN)

Active Galactic Nuclei are a small ($\sim$1%) but very interesting fraction of the whole galaxies population [H+05]. The general scheme of an AGN is presented in Fig. 1.5. It is assumed that all galaxies posses a super massive black hole (SMBH) in their cores. The name AGN comes from the fact that the central BH shows a strong activity. Most of the energy output of this type of sources is powered by the release of the gravitational energy of the accreted gas. While falling onto the BH the gas heats up to $\sim 10^4$ K and radiates photons in the UV-X-ray band. This radiation can be reprocessed by gas in the so-called Broad Line Region (BLR) located $\sim$0.1-1 pc away from the center. Further out ($\sim$1-10 pc) a dusty torus is formed, it may obscure the disc and the BLR if the source is observed at a large angle. At larger scales ($\sim$100 pc) a Narrow Line Region can be found composed of slowly moving ionized matter. In some sources two relativistic jets are emitted perpendicular to the disc and propagate for kiloparsecs or even megaparsecs from the core. Their production mechanism is not well understood, the most commonly accepted theory connects it with the spin of the black hole [BR90].

Since not all of the discussed features have been observed in all AGN historically they were classified under several groups depending on different criteria. It was later realized that all AGN can be unified within a simple framework. Fig. 1.6 shows the unification scheme of different AGN classes. The three principal criteria of the classification are:

1. The activity of the source in radio wavelengths which is connected to the presence of the jets. Only $\sim$10% of AGN show strong radio emission. They are usually located at the centers of elliptical galaxies, while the radio quiet sources are hosted mainly by the spiral ones.

2. The luminosity of the source. Radio weak objects are subdivided into optically weak and optically strong according to the features of their emission lines. Narrow emission lines are usually present only in the optically weak sources. The subdivision of the radio loud sources is based on their luminosity at the radio frequency of 178 MHz.

3. The orientation of the AGN towards the observer. In the radio loud branch the highly luminous Flat Spectrum Radio Quasars (FSQRs) and weaker BL Lac objects

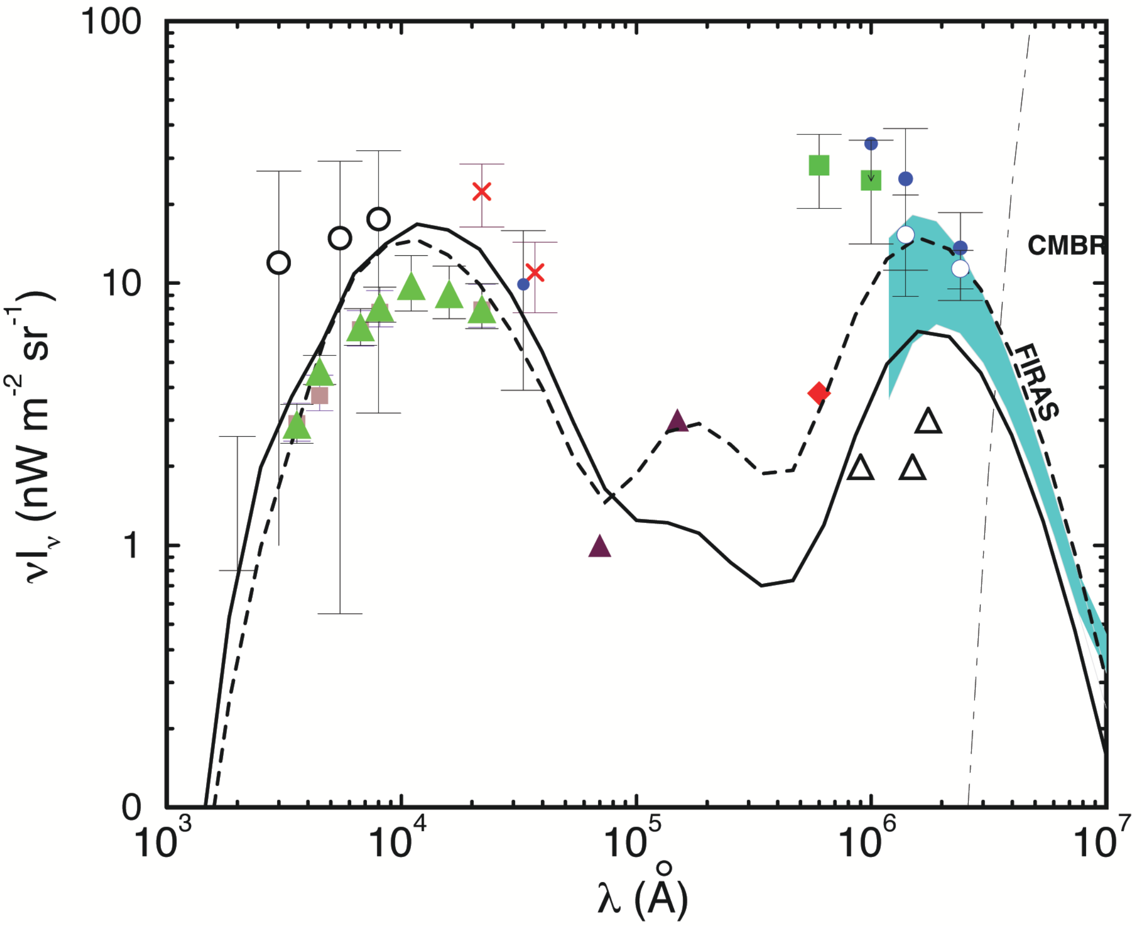

Figure 1.4: The EBL density computed according to the "Knieske Low" model (solid line) [K+02] and experimental data from: green triangles - HIST [P+98], big white circles - [B+02], red crosses - [G+00], dark red triangles - [E+99], red diamond - IRAS [S+87], green squares - DIRBE [F+00], white triangles - ISOPHOT [J+00], blue circles - DIRBE [H+98] [DA98], small white circles - [L+99], blue shade - FIRAS [F+98a]. Figure adapted from [K+02].

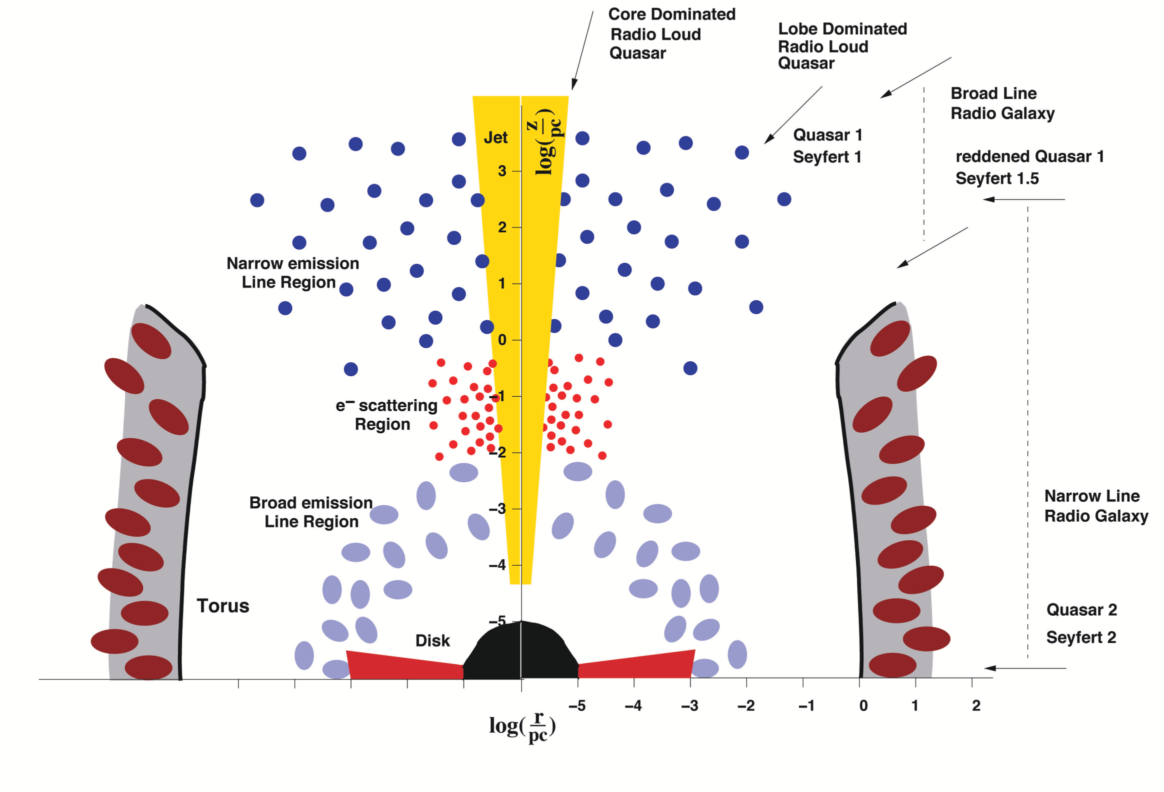

Figure 1.5: A sketch of an AGN from [ZB02].

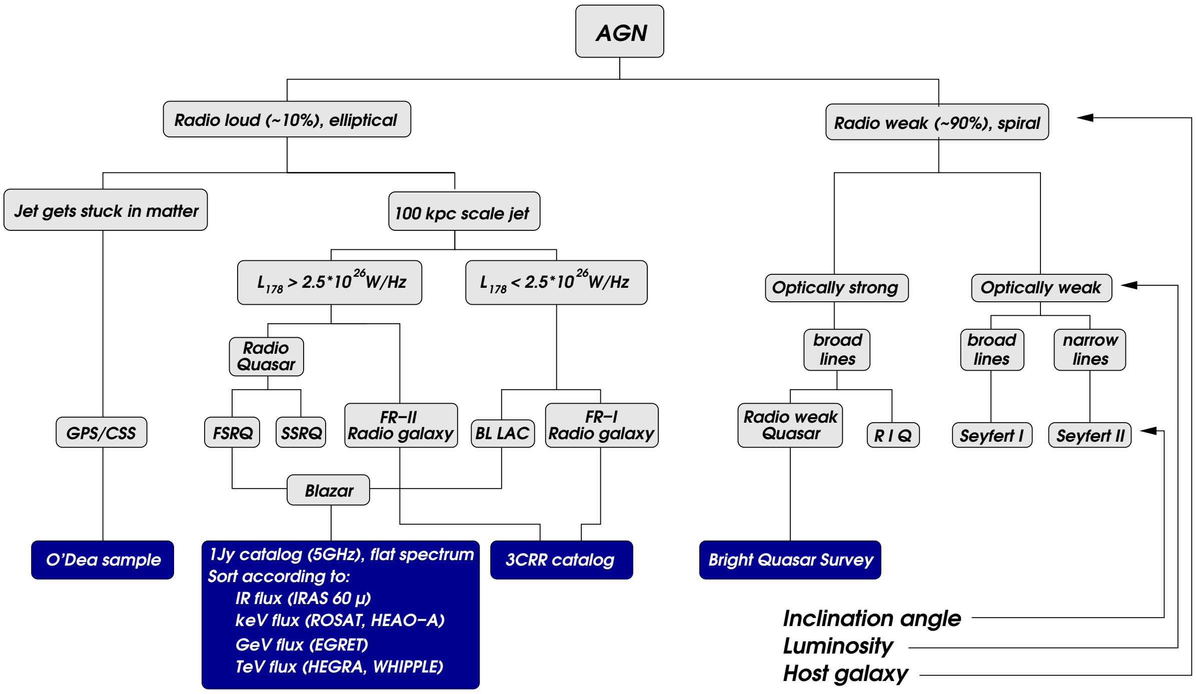

Figure 1.6: Unification scheme of different AGN classes, figure from [Gro06].

are classified together as *blazars* because their jets point directly towards the observer. A radio quiet equivalent of blazar is called Radio Intermediate Quasar (RIQ). Sources looked at intermediate angles (e.g. viewing the gap between the torus and the jet/core) are Steep Spectrum Radio Quasars (SSRQs), Seyfert I type galaxies and Radio Weak Quasars. In Faranoff Riley and Seyfert II galaxies the center is obscured by the torus, because we look at them from the side.

Most of the objects detected in the Very High Energy (VHE) γ-rays belong to the blazar class, for this reason the next section focuses on this type of sources.

1.5 Blazars phenomenology

Blazars are defined as radio loud AGN with the jet axis aligned close to the line of sight. As a consequence the jet radiation is highly relativistically beamed. The characteristic observational features are:

- visibility of the compact radio core with flat or inverted spectrum,
- extreme flux variability in time at all frequencies,
- high optical and radio polarization.

Blazars division into FSQRs and BL Lac objects is based on their power output and the strength of the optical emission lines – FSQRs showing higher luminosity and stronger optical lines. This dichotomy will be discussed in section 1.6.3.

Blazars have been observed in all frequency bands from radio to TeV. Due to their prominent flux variability simultaneous observations performed by instruments sensitive in different energy ranges are the most interesting. Therefore, very often, dedicated observational campaigns called *multiwavelength (MW) campaigns* are organized, in which the participating experiments agree to perform the measurements during an a priori fixed time window. Another way of obtaining contemporaneous data are the Target of Opportunity (ToO) programs where one instrument sends an alert requesting further observations by other instruments when an interesting event (e.g. flare) is detected.

As an example a multifrequency light curve of a nearby (z=0.031) BL Lac object Markarian 421 (Mrk 421), taken during a multiwavelength campaign in June 2008, is shown in Fig. 1.7 [$\mathrm{D}^{+}09$]. An interesting aspect is the possible correlated variability between the optical, X-ray and VHE γ-ray visible in the picture. The collected data was divided into two periods: MJD 54623 (period 1) and MJD 54627-32 (period 2). For each of them a Spectral Energy Distribution (SED) extending over 12 decades of energy was derived (Fig. 1.8) and fitted with a leptonic Synchrotron Self-Compton emission model [$\mathrm{T}^{+}98\mathrm{b}$] (see section 1.6).

Fig. 1.8 is also a good example of a typical blazar SED which extends from radio to TeV energies, is smooth and rather featureless, with a very characteristic double humped structure. According to predictions of several models the low energy (radio - X-ray) hump is produced through synchrotron emission of particles accelerated in magnetic fields. The nature of the high energy (X-rays to VHE γ-rays) hump, which as the recent observations show dominates the power output of most of the blazars, is still debated. Leptonic models (see section 1.6) assume that the high energy photons are produced through Inverse Compton (IC) up-scattering of low energy photons by the same population of electrons which was responsible for the synchrotron emission. In hadronic models (see section 1.7) the source of the emission is a population of high energy protons which can interact with an ambient photon field or nucleonic gas and initiate a pair cascade or, in a presence of extremal magnetic fields (30-100 G), produce high energy photons through synchrotron radiation.

The rapid variability of blazars, their high bolometric luminosity and the apparent superluminal motions suggest strongly that their non-thermal continuum emission is produced in emission regions ("blobs") of typical size of a few light days or less, which propagate relativistically along the jet. Most of the models discussed in more detail below, assume a single, homogeneous "blob" of spherical shape. Interesting alternative solutions, with multiple emission regions or non typical geometry, will be only shortly mentioned. A good overview of leptonic and hadronic models can be found in [Boe04] or [Lev06].

1.6 Leptonic emission models

The high polarization of the observed optical and radio emission of blazars indicates that the first spectral component must be due to a synchrotron emission from relativistic particles in the jet. In leptonic models those particles are electrons (and positrons). The

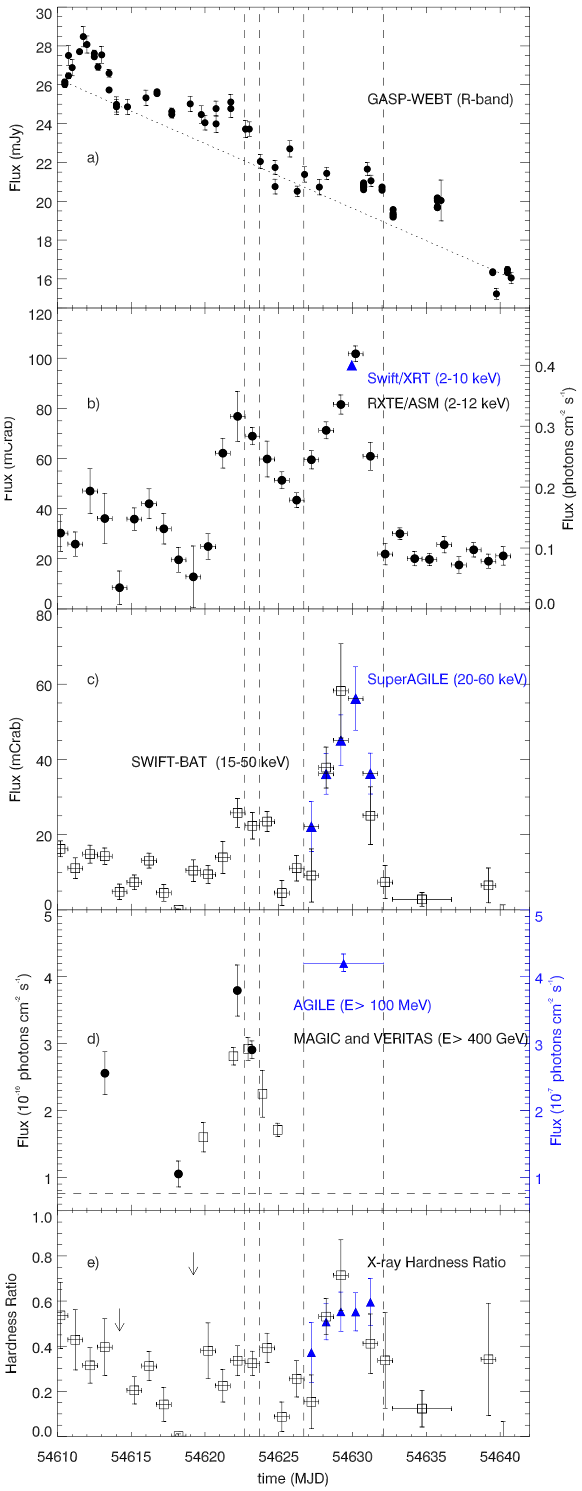

Figure 1.7: Multifrequency light curve of Mrk 421 taken during a multiwavelength campaign in June 2008 [D^{+}09]. The vertical dashed lines define the two periods for which the SEDs were derived: MJD 54623 (period 1) and MJD 54627-32 (period 2) - see Fig. 1.8.

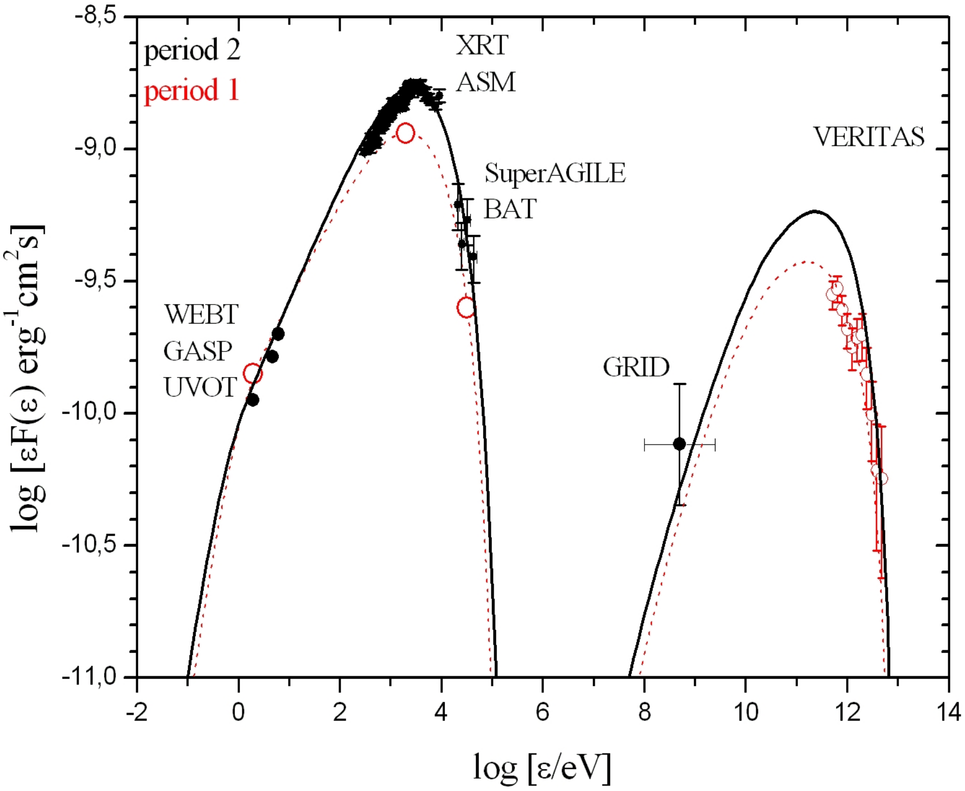

Figure 1.8: Spectral Energy Distribution of Mrk 421 measured during a multiwavelength campaign in June 2008 [D$^+$09] and fitted with a leptonic Synchrotron Self-Compton emission model [T$^+$98b]. The collected data was divided into two periods (see Fig. 1.7) and for each of them a SED was derived. For detailed model description see section 1.6.1. Fit parameters: blob size $R = 4\times10^{16}\,\mathrm{cm}$, relativistic Doppler factor $\delta = 20$, magnetic field $B = 0.1\,\mathrm{G}$, Lorentz factor range $\gamma_{min} = 4\times10^3 < \gamma < \gamma_{max} = 1.3\times10^6$, for period 1: the normalization (density) constant $K = 4\times10^4\,\mathrm{cm}^{-3}$, the break energy $\gamma_{break} = 3.6\times10^5$, the low-energy and high-energy power-law indices: $n_1 = 2.22$, $n_2 = 4.5$ respectively; for period 2: $n_1 = 2.1$, $n_2 = 5$, $\gamma_{break} = 4.2\times10^5$, $K = 6\times10^4\,\mathrm{cm}^{-3}$.

same electron population is assumed to participate in IC scattering of soft photons into higher energies. Different sources of soft photons can be considered (e.g. accretion disc).

1.6.1 Synchrotron Self-Compton

In the Synchrotron Self-Compton (SSC) class of models the target photons are the synchrotron photons radiated by the same relativistic electrons [M$^+$92] [T$^+$98b]. Therefore a strong correlation of the strength and time of the emission of synchrotron and IC photons should be observed (like in the above mentioned MW campaign). The model assumes a spherical emission region of radius R moving with a Lorenz factor γ and observed at an angle θ resulting in a Doppler factor δ; the magnetic field of strength B is tangled and uniform. The injected electron population have a broken power law distribution with a particle density K, spectral indices n_1 and n_2 and break energy γ_{break}:

$$N(\gamma) = \begin{cases} K\gamma^{n1} & \text{for } \gamma_{min} \leq \gamma \leq \gamma_{break} \\ K\gamma_{break}^{n_2-n_1}\gamma^{n_2} & \text{for } \gamma_{break} \leq \gamma \leq \gamma_{min} \end{cases} \tag{1.6}$$

The γ_{min} and γ_{max} are the minimal and maximal electron energy. A discussion on this and alternative model [KSK01] is presented in section 6.4.4 on an example of Mrk 501 Spectral Energy Distribution.

1.6.2 External Compton

In External Compton (EC) models one assumes that the dominant contribution to the soft photon field comes from the regions outside of the jet. In the first model of this type [DS93a] the UV photons from the accretion disc were considered. It was later shown by [S$^+$94] that this radiation is strongly debeamed in the reference frame of the jet and cannot be of major importance. As a solution a reprocessing of the disc radiation by the BLR gas was proposed. These photons would be strongly amplified in the rest frame of the emitting region. In more recent version of the model [B$^+$00] the authors argue that IC scattering of the infrared radiation from the dusty torus could be responsible for the major part of the observed high energy emission, especially in the 10 keV - 100 MeV range. In the so called "Mirror Model" [GM96] the jet synchrotron radiation reflected at the BLR is considered. The energy density of the soft photon field is highly increased by the double reference frame change (jet-BLR-jet), but the time scale of this process is too long to credibly explain the fast variability observed in several objects.

In order to build a complete leptonic blazar emission model one has to take into account a few more processes like the photon-photon absorption, pair production and synchrotron self absorption. Many authors neglect some, or all, of them and as a result very often the spectral fits do not reproduce the radio spectra, while coping very well with the X-ray and γ-ray ones. Another reason for the problems with the radio band could be a different emission region responsible for the low energy radiation. For example in the "blob-in-the-jet" model by [KSK01] the authors assume that the low frequency radiation comes from a slowly changing jet, while the rapid flux variations and flares observed in X-ray and γ-rays are due to a blob of relativistic plasma moving along the jet.

An alternative to the SSC model for the Mrk 421 data presented above was also discussed in [D$^+$09]. Authors propose that the different behavior of the X-ray radiation (two flares) and of the optical emission (variations of the order of 10% on a time scale of few days, superimposed on a long decay during the entire period) may suggest that the optical and X radiation comes from two different jet regions, each one characterized by its own variability. A possible scenario developed by [VR99] [V$^+$04] and assuming a helical shape of the jet is considered.

1.6.3 The blazar sequence

The first systematic investigation of the blazars' SEDs was proposed by [F$^+$98b]. They produced "average" spectra by binning the objects according to their radio luminosity at 5 GHz (L_{5Hz}). The result was the so-called "blazar sequence" shown in Fig. 1.9. Two trends are clearly visible:

1. High luminosity sources (FSQRs) have their peaks located at low energies, typically in the IR and MeV γ-rays regions. With decreasing luminosity the peaks shift towards higher energies (UV - soft X-ray and TeV γ-rays respectively).

2. In low luminosity sources (BL Lac) the high energy component contributes less significantly to the total power output of the object, compared to the high luminosity ones.

In a subsequent theoretical paper [GCC02] it was argued that the observed correlation of the L_{5Hz} and the position of the synchrotron peak (ν_S) can be explained by a correlation of the Lorenz factor of the e$^-$ emitting at the peak (γ_{break}) and the energy density of the magnetic (U_B) and radiation (U_{rad}) fields.

The blazar sequence was later strongly criticized (see e.g. [Pad07][G$^+$07a]). The main point of critics was the source selection bias towards most beamed and powerful objects and the fact that due to strong variability of blazars the sequence could have only an "average" meaning. Recently a revised version of the model and study on a more carefully chosen sample were published [M$^+$08]. The earlier observed correlation of L_{5Hz} and ν_S does not hold anymore. The new model, based on two parameters: the mass of the BH and the disc luminosity (or accretion rate), describes the transition from FSQRs to BL Lac objects as a graduate weakening of the role of the BLR in the emission mechanism (increasing contribution from the SSC processes). It also naturally explains the division of BL Lac type sources into high- or low-frequency peaked (HBL/ LBL) depending on the frequency of their peaks and relative peak fluxes.

1.7 Hadronic emission models

In hadronic models the source of the emission are relativistic protons (and electrons). As in leptonic models the low energy hump of the spectra is explained as due to synchrotron

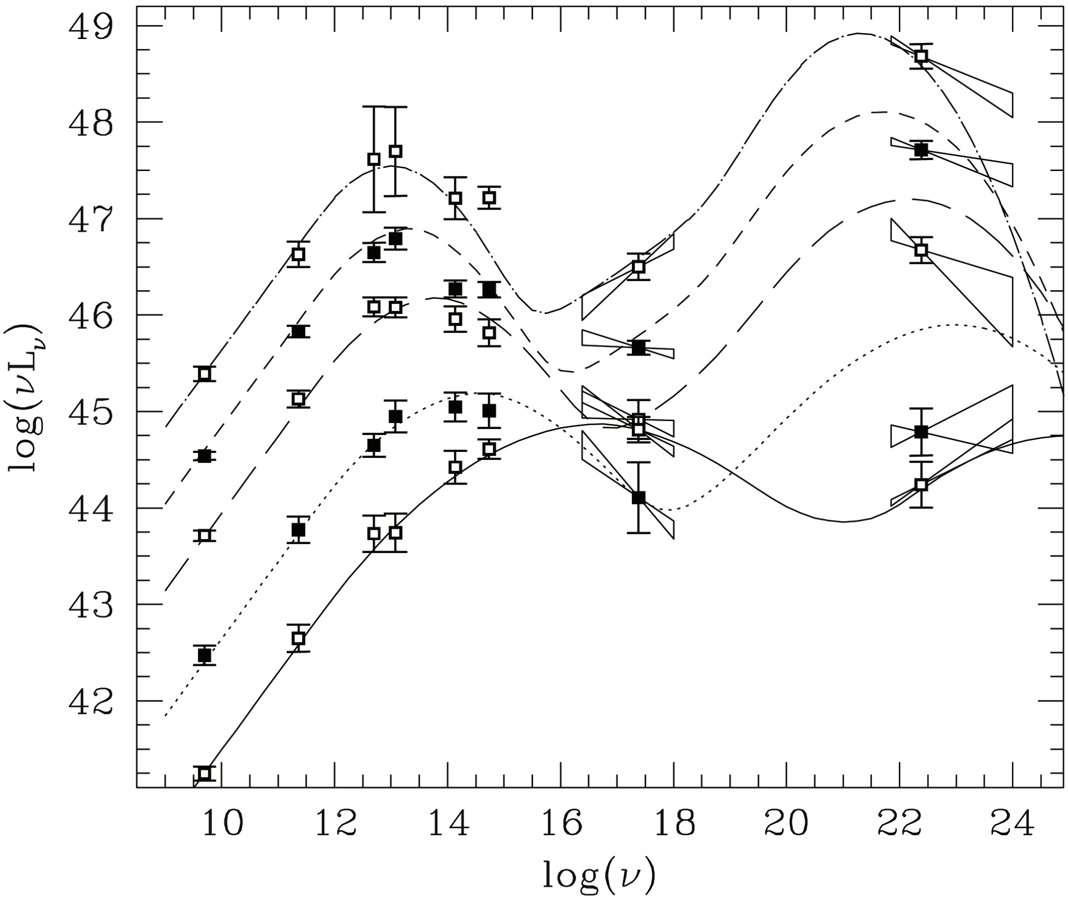

Figure 1.9: The blazar sequence [F$^+$98b]: the transition from highly luminous FSQRs to weaker BL Lac objects. The points depict "average" spectra produced by binning the objects according to their radio luminosity at 5 GHz, the lines fits with a leptonic model. Two trends are clearly visible: with decreasing luminosity the peaks shift towards higher energies, in low luminosity sources the high energy component contributes less significantly to the total power output of the object.

radiation of the accelerated particles, although much higher magnetic fields are required in order to produce relativistic protons. In the most popular scenarios protons interact with a soft photon field (after reaching the threshold for pion production) and initiate pair cascades. As an alternative *pp* interactions can be considered. Below both types of models will be briefly explained.

1.7.1 Proton-photon interactions

The proton initiated cascades (PIC) were first proposed by [Man93]. Later the scheme was refined by [M+03] and developed into a full Synchrotron-Proton Blazar model (SPB). SPB takes into account not only the radiation losses suffered by protons due to proton-photon interactions, synchrotron radiation and adiabatic expansion of the emitting region, but also the synchrotron radiation of secondary mesons and muons (before they decay). If electrons are co-accelerated with the protons, they will radiate synchrotron photons, which are responsible for the low energy peak of the SED and serve as target radiation field for $p\gamma$ interactions (for the reaction chain see section 1.7.3). The subsequently developing pair cascade will redistribute the photons to lower energies, allowing them to eventually escape from the emission region. The cascade can be initiated by photons from π^0 decay, $e^\pm$ from $\pi^\pm$ decay chain, p-synchrotron photons, charged μ, π and K-synchrotron photons or $e^\pm$ from Bethe-Heitler pair production (mostly negligible). In general, direct proton and muon synchrotron radiation is mainly responsible for the high energy peak, while the π-initiated cascades produce rather featureless spectra. The low energy bump, as mentioned before, is dominated by the synchrotron radiation from the primary e^- with a small contribution from the secondary $e^\pm$. Since this model assumes a negligible external photon contribution it is especially suitable for BL Lac objects. In contrast to most of the models which predict equal γ-ray and neutrino fluxes, here the calculated neutrino output (from the $\pi^\pm$ and $K^\pm$ decay chains) depends on the source type and is higher for LBLs than for HBLs, because they possess intrinsically denser target photon fields. More power (by a factor of 10^3 - 10^4) is channeled into the photon component in HBLs, while in LBLs the power output of photons and neutrinos is approximately equal.

A variation on the proton-synchrotron scenario was proposed by [Aha00]. The author argues that the synchrotron radiation from ultra high energy protons ($E > 10^{19}\,\mathrm{eV}$) can be directly responsible for the observed emission of the TeV photons in a presence of magnetic fields $\sim$100 G. One also has to assume that the optical thickness of the source is rather small. The resulting lower limit for the characteristic time for proton-photon interaction is several orders of magnitude larger than the synchrotron cooling time and in contrary to the SPB model described above the photo-meson production is strongly suppressed. Another difference is the origin of the low energy peak of the SED. It cannot be due to the primary e^-, because in such strong magnetic fields they would produce a flat spectrum from optical/UV to MeV/GeV energies, which is in clear contradiction to the observations. The existence of the first hump can only be explained by synchrotron radiation of secondary electrons produced by TeV γ-rays interacting with the ambient low frequency photons. This model, due to the assumption of an optically thin emitting region, implies very low TeV neutrino fluxes.

1.7.2 Proton-proton interactions

One of the first models which considered *pp* interactions instead of $p\gamma$ was proposed in [Bed93]. The author assumed the existence of a geometrically thick accretion disk around the central black hole. The disk should have a dense corona, illuminated by relativistic protons released in blobs and moving along the disk funnel. The VHE γ-rays are produced in inelastic collisions of relativistic protons with the matter in the disc through the π^0 decay and Inverse Compton scattering of the UV thermal photons by the secondary electrons from the $\pi^{\pm}$ decays (for the reaction chain see section 1.7.3). The column density of the matter crossed by the relativistic particles should be less than one interaction length for inelastic *pp* collisions in order to permit a free escape of the γ-rays. The model predicts strong, anisotropic emission of low energy neutrinos. In one case AGN, seen close to face-on, might emit γ-rays and neutrinos during an outburst when the relativistic blobs are formed and their spectra and intensity will be similar. In the second case AGN, observed at large angles, are stronger neutrino emitters, because the density of the disk matter further from the axis of the disk funnel is probably larger than one *pp* interaction length.

Another interesting model was presented in [DL97]. Here the TeV γ-ray emission is a result of collisions of a high energy proton jet with the gas clouds emerging from the BLR and crossing near the line of sight. It is accompanied by a simultaneous emission of TeV neutrinos and of secondary $e^{\pm}$ with similar intensities and energy spectra. According to this model, one should also expect delayed optical, X-ray and low energy γ-ray (MeV-GeV) flares due to cooling of the secondary $e^{\pm}$ by synchrotron radiation and IC scattering. Moreover there should be a correlation between the hardness of the X-ray spectrum and the intensity of the flare. Both features were observed during the flare from Mrk 421 in May 1995.

The theoretical difficulties of "BLR clouds models" [DL97] [BB99] were pointed out in [PS00]: the proton beams are too weak and quickly stopped and the BLR clouds are usually optically thick, therefore the system has a very low efficiency. The authors propose a different solution: a strong electron-proton beam, a blast wave, which sweeps up the ambient matter. This model is similar to the "fireball model" for GRBs, but in case of the AGN the emission is anisotropic - the outflow is channeled along the magnetic flux tubes due to the structure of the medium surrounding the AGN engine. In the inelastic collisions of the ambient and blast wave protons an equal part of the proton energy ($\sim 0.2\ E_p$) is transfered to VHE γ-rays and neutrinos. In the subsequent paper [SPS02] the authors argue that their emission should be correlated and the bulk of the neutrino emission is expected to be in the energy range between 100 GeV and 1 TeV.

1.7.3 Cosmic neutrinos from point-like sources

Neutrinos, like photons, are not deflected in the intergalactic magnetic fields and also point straight to their source. In contrast to the electromagnetic emission which can have either leptonic or hadronic origin, the neutrino emission is the only evidence for a hadronic component in the jet. Astrophysical neutrinos are a product of $p\gamma$ or pp collisions:

$$p + \gamma \rightarrow \Delta \rightarrow \begin{cases} p + \pi^0 & \text{with branching ratio } \sim 2/3 \\ n + \pi^+ & \text{with branching ratio } \sim 1/3 \end{cases} \tag{1.7}$$

$$p + p \rightarrow \begin{cases} p + p + \pi^0 & \text{with branching ratio } \sim 2/3 \\ p + n + \pi^+ & \text{with branching ratio } \sim 1/3. \end{cases} \tag{1.8}$$

and the following decay of charged pions,

$$\pi^+ \rightarrow \mu^+ \nu_\mu \rightarrow e^+ \nu_e \bar{\nu_\mu} \nu_\mu \tag{1.9}$$

The pn interaction is also possible and the same processes take place, but π^- instead of π^+ are produced. Under the assumption that the negative and positive pions are produced with the same efficiency, the flavor ratio of neutrinos at the source is:

$$(\nu_\mu : \nu_e : \nu_\tau) = (\bar{\nu_\mu} : \bar{\nu_e} : \bar{\nu_\tau}) = (2 : 1 : 0). \tag{1.10}$$

Since it is known that the differences of the squares of the neutrino mass eigenvalues are non-zero, one has to take into account that they will oscillate on their way to Earth. After traveling a path of the length comparable to at least the Solar System radius the flavor ratio approaches:

$$(\nu_\mu : \nu_e : \nu_\tau) = (\bar{\nu_\mu} : \bar{\nu_e} : \bar{\nu_\tau}) = (1 : 1 : 1). \tag{1.11}$$

and we expect to observe the same number of electron, muon and tau neutrinos of cosmic origin at Earth.

The neutrino flux should be closely connected to the γ-ray flux due to the interaction channel in which the π^0 are produced and decay to MeV-TeV photons:

$$\pi^0 \rightarrow \gamma + \gamma. \tag{1.12}$$

An example of a calculation of muon neutrino rates in the AMANDA-II detector estimated from the γ-ray “orphan flare” of 1ES1959+650 is presented in [HH05]. The authors argue that the energy densities of the observed fluxes of photons and neutrinos should be proportional:

$$\int_{E_{min}} E_\gamma \frac{dN_\gamma}{dE_\gamma} dE_\gamma = x_{\gamma/\nu} \int_{E_{min}} E_\nu \frac{dN_\nu}{dE_\nu} dE_\nu. \tag{1.13}$$

The proportionality constant $x_{\gamma/\nu}$ depens on the fraction of energy which goes into the pion production. In pp interactions on average each of the pion flavors gets 1/3 of the proton energy. In the pion decay chain two muon neutrinos are produced with energy $E_\pi/4$ for every photon with energy $E_\pi/2$ (on average). Therefore the energy in neutrinos matches the energy in photons and $x_{\gamma/\nu} = 1$. Similar reasoning leads to $x_{\gamma/\nu} = 4$ for the $p\gamma$ case.

This calculation is quite simplified and does not take into account possible corrections for the absorbtion of high energy photons on the infrared background on their way to Earth (see section 1.3) or the internal absorbtion in the source (an optically thin source is assumed). It also favours sources in which the accelerated protons interact with a nucleonic target, their jet Lorentz factor is rather small and the observed γ-ray spectral index is steep.

1.7.4 Diffuse flux of cosmic neutrinos

If the neutrino flux from an individual source is too small to be detected by current instruments and analysis methods, it is still possible that many sources, isotropically distributed throughout the Universe, could combine to make a detectable signal. An excess of events over the expected atmospheric neutrino background would be a clear proof of an extraterrestrial neutrino flux.

There are many theoretical models predicting a diffuse neutrino signal for different classes of objects. These predictions are usually based on the observed diffuse photon or cosmic rays fluxes. For example if the studied objects are optically thin to the photon-neutron interactions (e.g. HBLs) neutrons can escape and decay in the source vicinity producing a flux of charged cosmic rays [AD04] [CH08]. In this case the resulting neutrino flux is assumed to be proportional to the CR flux measured on Earth. For optically thick sources (e.g. LBLs, FSRQs) a similar calculation is made using the diffuse γ-ray flux [M$^+$03].

Figure 1.10 shows the predictions of the most popular models. The first model for the diffuse astrophysical neutrino spectrum was proposed by Stecker, Done, Salamon and Sommers (SDSS) [SS96] and revised by Stecker in 2005 [Ste05]. This model predicts a neutrino flux from cores of AGN, mostly from Seyfert galaxies. In the first version the estimated neutrino flux was normalized to the observed X-ray background assuming that is in 100% due to a non thermal emission. Subsequent observations by the COMPTEL satellite proved this assumption to be wrong and the neutrino limit was scaled down by a factor of 20 (taking into account also the neutrino oscillations discovered after the first paper was published). Mannheim, Protheroe and Rachen (MPR) [MPR01], using the diffuse extragalactic γ-ray background observed by EGRET as an upper limit on the hadronic extragalactic γ-ray flux, calculated the upper bound for high-energy neutrino flux from optically thick sources, less strict then SDSS. They also proposed an upper bound for neutrinos from generic optically thin sources based on the, then available, data from the CR experiments and an upper bound for AGN jets as well. Another popular model has beeen proposed by Waxman and Bahcall (W&B) [WB97] [WB00] where neutrinos are assumed to be produced in the after glow of the Gamma Ray Bursts.

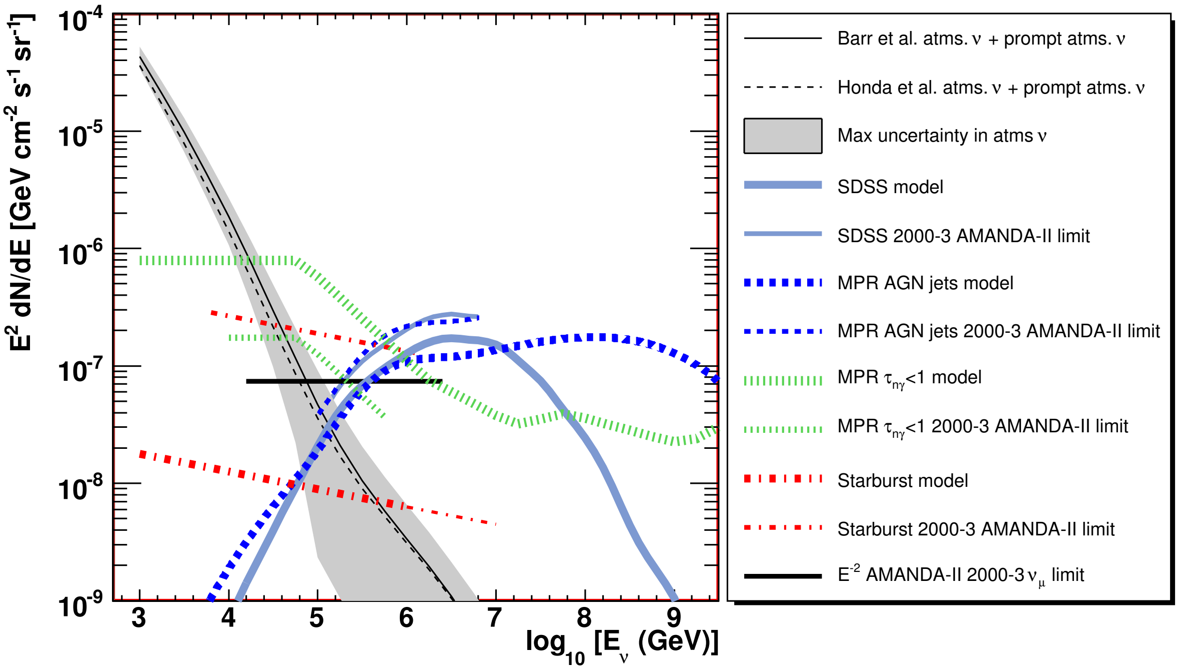

Figure 1.10: Models' predictions for diffuse astrophysical neutrino flux and upper limits established with AMANDA-II data analysis [A$^+$07c].

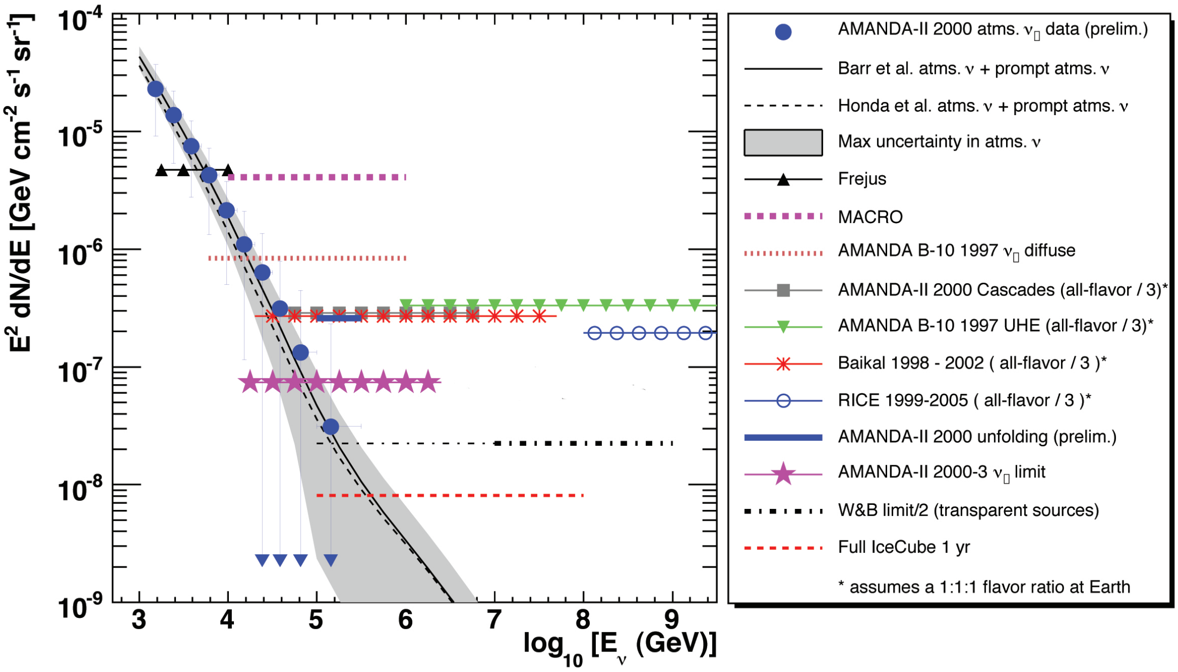

Figure 1.11: Upper limits on the diffuse ν_μ flux from sources with an E^{-2} energy spectrum are shown for different experiments. Figure from [A$^+$07c].

The recent experimental upper limits to the cosmic neutrinos diffuse flux are shown in Fig. 1.11. The AMANDA-II upper limit (pink stars) [A^+07c] is a factor of four above the Waxman-Bahcall upper bound and constrains the MPR upper bound for optically thick pion-photoproduction sources.

1.8 Multimessenger approach: cooperation of γ-ray and neutrino telescopes

The nature of the emission mechanisms in the galactic and extragalactic sources is still debated and it is clear that the information provided by photon observations are not enough to solve this problem. Detection of a point source of extraterrestrial neutrinos or cosmic rays would be the only indication of hadronic processes. As discussed in section 1.7.3 there is a strong connection between the VHE γ-ray and neutrino emission. A cooperation between γ-ray and neutrino telescopes which exploits this connection, can enhance a chance of a neutrino emitter discovery and in general shed more light on the behavior of the cosmic objects.

However, there is a serious drawback – sparse time and flux coverage of γ-ray data. While neutrino telescope observes simultaneously the whole hemisphere and have a duty cycle of $\sim$100% (excluding maintenance time and unexpected occurrences), a γ-ray telescope points to single source and has duty cycle of $\sim$10%. Therefore simultaneous data needed for trustworthy studies are rare.

This problem can be solved in two ways. One way is to ensure simultaneous source coverage by sending a trigger for a follow up observation when the neutrino telescope detects an interesting event. This type of observations are called Target of Opportunity (ToO) and are discussed in this work on the example of the Neutrino Target of Opportunity (NToO) program with AMANDA-II and MAGIC [A^+07d] (section 4.7). Second possibility, which aims rather on collecting large flux statistics independent of the source emission state, is to perform a regular monitoring of interesting γ-ray sources. This solution was addressed in this work by an analysis of historical γ-ray data from the public archive at DESY (Chapter 5) and of the recently obtained results from the MAGIC AGN monitoring program (Chapter 6).

2 Instruments

The first ever detector of Cherenkov radiation was the eye of Pavel Alekseyevich Cherenkov himself. He was working on his PhD, investigating the effect of Radium γ-rays on a luminescent liquid and comparing it to the known emission of luminophor light induced by visible light. The emission was so feeble, that he had to spend more than one hour in absolute darkness before starting the measurements. During his experiment Cherenkov observed a new and curious phenomenon: a faint blue light induced by γ-rays in the liquid [Che34][Che08].

This discovery brought him, Ilya Frank and Igor Tamm (who formulated the theoretical description of the radiation), the Nobel Prize in 1958. More importantly it became a powerful tool for particle detection for generations of nuclear, particle and astroparticle physicists.

In the next sections the mechanism of the emission of Cherenkov radiation will be described, along with its detection principle and how it can be used to detect neutrinos and γ-rays of cosmic origin. Two detectors which use this technique will be presented - the AMANDA-II neutrino telescope and MAGIC γ-ray telescope. Their cooperation can help to answer some of the important questions concerning the acceleration and emission mechanisms of AGN.

2.1 Cherenkov radiation

When a charged particle travels inside a transparent dielectric medium (like air or water) it interferes with the local electromagnetic field, displaces electrons in the atoms and causes their polarization. Then, the excited electrons emit photons and come back to equilibrium. When the particle velocity $v = \beta c$ is lower than the speed of light in the medium, photons interfere destructively with each other and no radiation is detected (Fig. 2.1 (left)). If the particle velocity is greater than the speed of light in the medium ($\beta > 1/n$, with n refraction index, Fig. 2.1 (middle)), the wavefronts can sum coherently and light is emitted Fig. 2.1 (right). This is the origin of the blue light which Cherenkov observed. He also noticed that photons are emitted in a narrow cone and further calculations showed that the emission angle θ_C is related to β and n by:

$$cos\theta_C = \frac{1}{\beta n}. \tag{2.1}$$

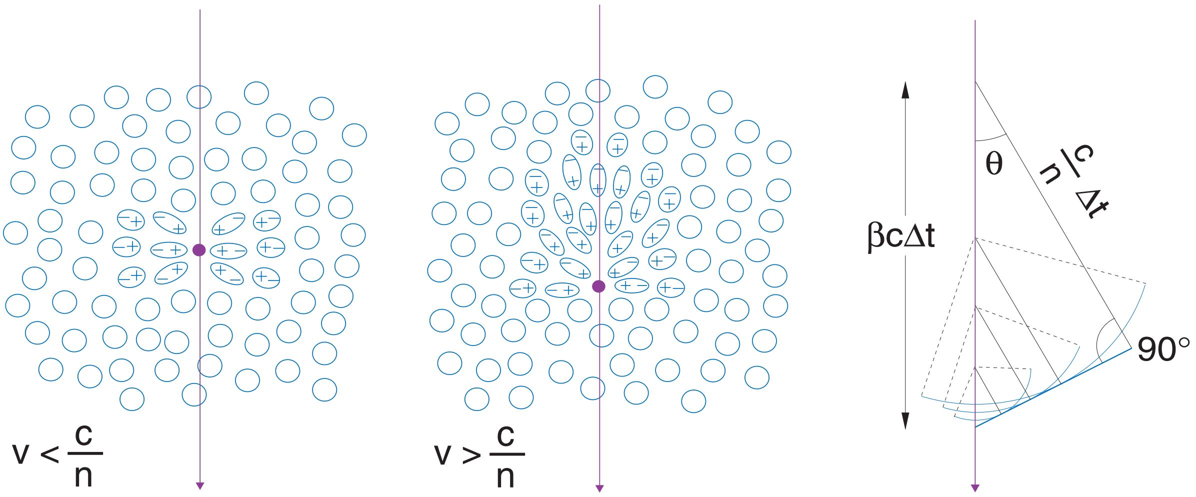

Figure 2.1: A charged particle traveling with a speed higher than the speed of light in the medium produces Cerenkov radiation. Right panel: Huygens' construction of Cherenkov waves. Figure from [Wag06].

As mentioned above, there is a threshold for the velocity of the particle for the production of Cherenkov light, which depends on the refraction index of the medium:

$$\beta_{min} = \frac{1}{n}. \tag{2.2}$$

This can be translated in an energy threshold for the involved particles:

$$E_{min} = \frac{m_0}{\sqrt{1-\beta_{min}^2}} = \frac{m_0}{\sqrt{1-n^{-2}}}. \tag{2.3}$$

2.2 Neutrino interactions

Neutrinos are very tricky particles to detect. They have no charge, very small mass and interact only weakly. The only evidence that a neutrino passed through the detector is a secondary particle created if the neutrino interacts with the media. There are two main processes in which neutrinos can be involved: a charge current (CC) and a neutral current (NC) interaction. In a CC interaction neutrino ν exchanges a $W^{\pm}$ boson with a nucleon N and a lepton l of the same flavor is produced:

$$\nu_l + N \to l + X \text{ (CC)}. \tag{2.4}$$

In the NC interaction neutrino and nucleon exchange a Z^0 boson and in the final state neutrino of the same flavor is found:

$$\nu_l + N \to \nu_l + X \text{ (NC)}. \tag{2.5}$$

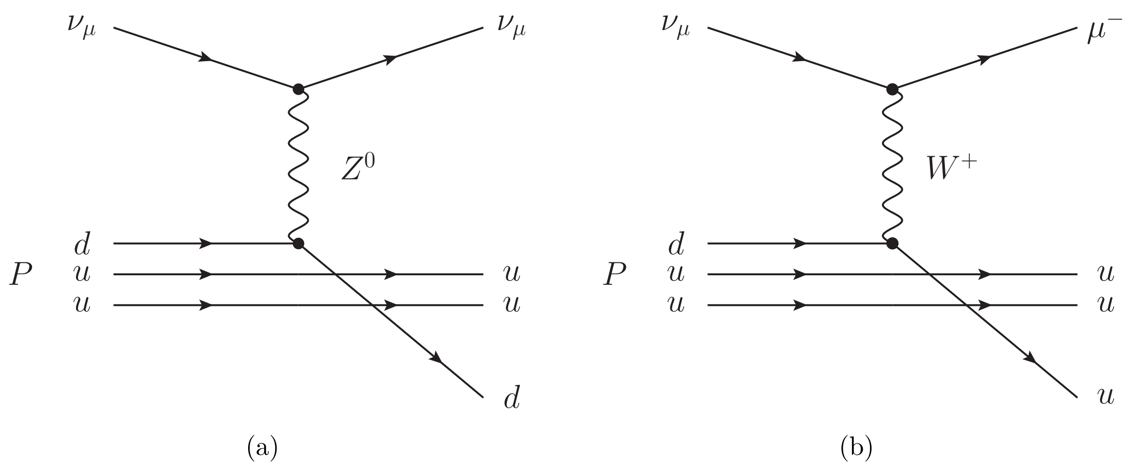

Figure 2.2: Examples of Neutral Current (NC) and Charged Current (CC) neutrino reaction diagrams.

In both cases X denotes the final hadronic state into which the nucleon N is transfered. In Fig. 2.2 examples of a CC and NC interaction for a proton p and muon neutrino ν_μ are given. The charged lepton produced in the CC reaction and the hadronic cascades (X) produced in NC reactions can be detected using the Cernenkov effect. In the discussed analysis only the neutrino induced muon events are used.

Both the cross sections for the CC and NC reactions are very small and it is evident that detectors with big volumes are needed. The cross sections are measured only up to some few tens of TeV, above that value an extrapolation based on the electroweak theory has to be used (Fig. 2.3).

One could argue that the steep rising of the cross section can partially compensate for the decrease of the cosmic neutrino flux. On the other hand one should not forget that an increment of the cross section means also an increment in the probability of the neutrino being absorbed in Earth before it reaches the detector. It can be seen from Fig. 2.4 that already at the energy of 50 TeV the mean free path of the neutrino is comparable with the Earth's diameter.

In neutrino telescopes there are two main neutrino detection channels: the muon channel (when a muon is produced in a CC reaction) and a cascade channel. With the currently operating detectors it is not possible to distinguish the electromagnetic cascades (from the CC interactions involving electron neutrino) from hadronic cascades (from NC interactions involving neutrino of any flavor). Since cascades usually deposit all their energy within a few meters, one can extract from them very precise information about the energy of the incident neutrino. Unfortunately the directional information is not well preserved.

On the contrary, high energy muons can travel long distances without suffering great energy losses. This allows to determine the direction of the incident neutrino with good precision, but not its energy. Fig. 2.5 shows energy losses of muons of different energies. As we can see at higher energies the most important processes are: bremsstralung, e^+e^-

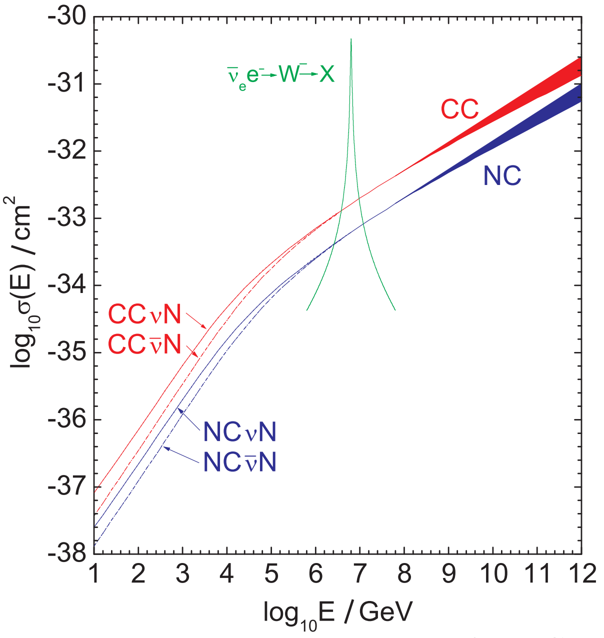

Figure 2.3: Neutrino and antineutrino cross sections for NC and CC reactions as a function of the neutrino energy E_ν. The green line depicts the Glashow resonance at $E_\nu = 6.3\,\text{PeV}$. Figure from [Lan05]

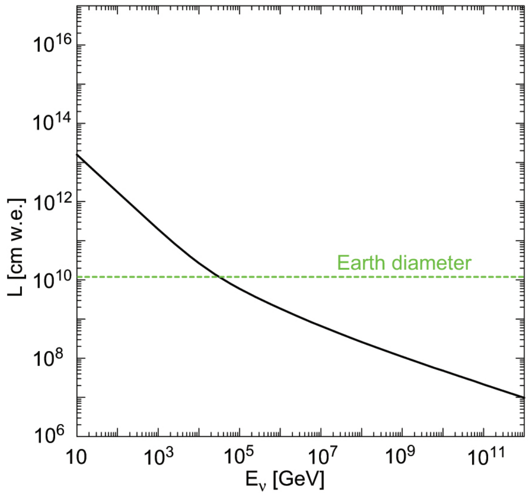

Figure 2.4: Mean free path of a neutrino given in units of cm water equivalent (i.e. in a medium with a density equivalent to the density of water). For E $\geq$ 50 TeV the mean free path becomes comparable to the diameter of the Earth indicated by the green dashed line. Figure from [Ack06].

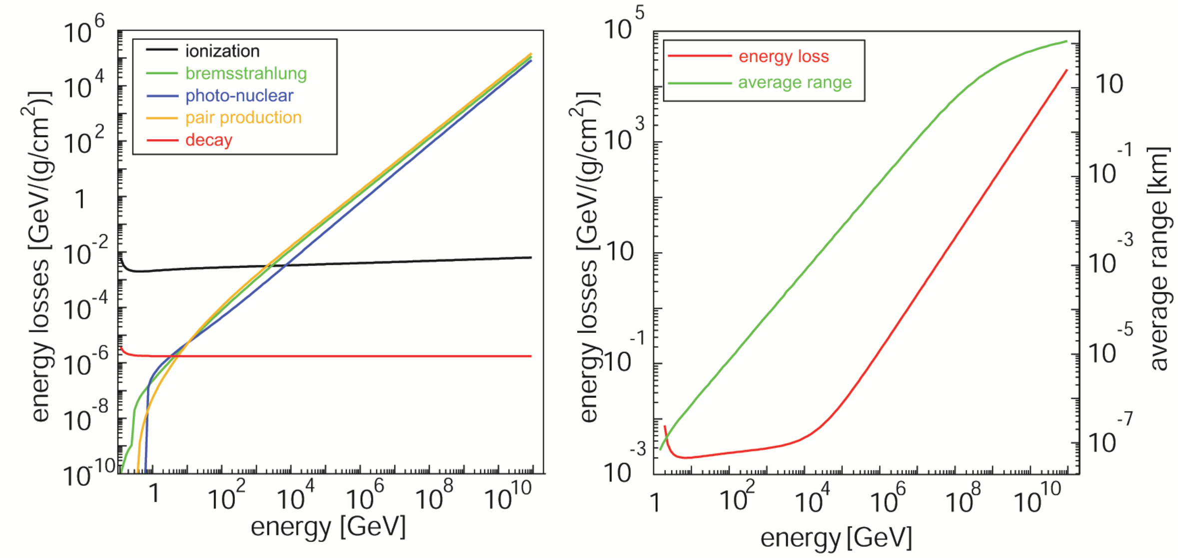

Figure 2.5: Energy losses for muons of different energies in a water equivalent (w.e.) medium. Left: contributions from different processes. Right: energy loss, all contributing processes added (red line) and average range of a muon in a w.e. medium (green line). Figure from [Ack06].

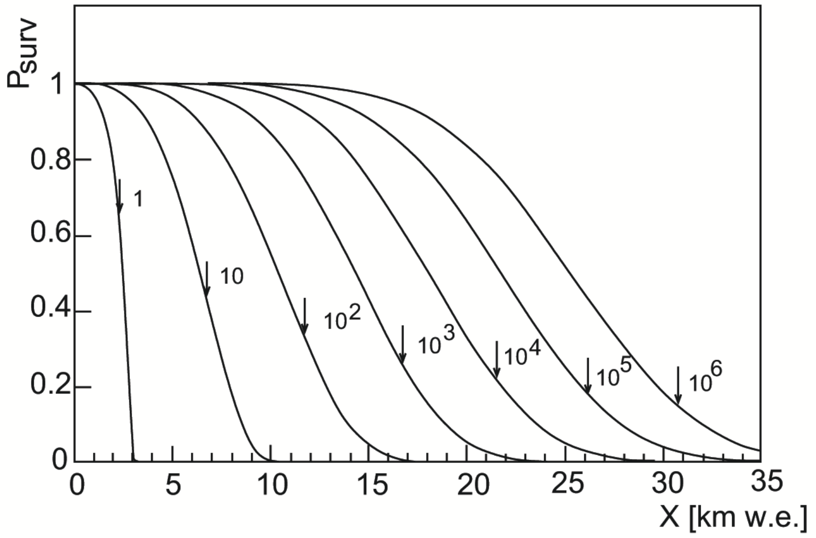

Figure 2.6: Survival probability P_{surv} of muons of different energies in a water equivalent medium. Figure adapted from [LS91].

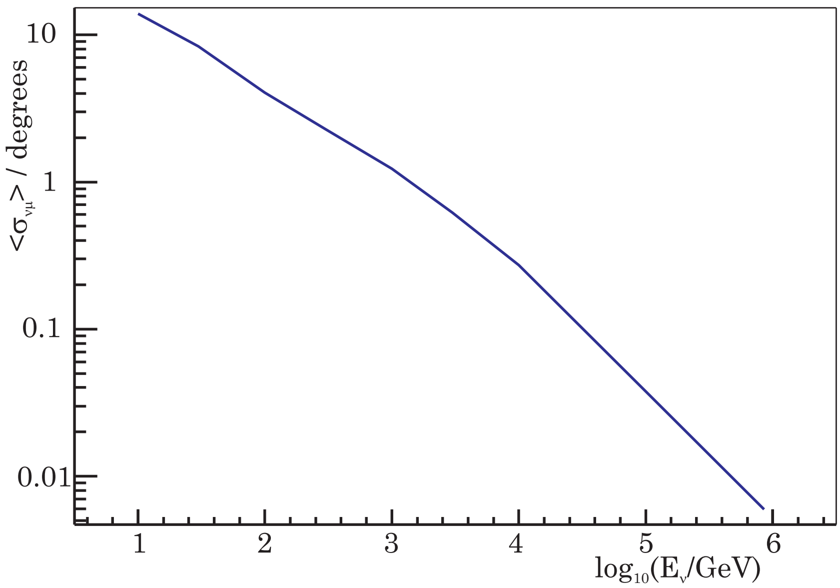

Figure 2.7: The mean scattering angle $\sigma_{\nu\mu}$ between neutrino and muon as a function of the neutrino energy. Figure from [Lan05]

pair production and photo-nuclear reactions. On Fig. 2.6 the survival probabilities for muons of different energies for a water equivalent medium is shown.

Another important factor in the search for cosmic neutrino point sources is the mean scattering angle $< \theta_{\nu\mu} >$ between the incident neutrino and the muon produced in the CC reaction (Fig. 2.7). It gives limits on the achievable angular resolution. According to Fig. 2.7 one can expect an angular resolution of 1° or less for muons with energies above 1 TeV.

2.3 Neutrino telescopes

When astrophysicists started to consider the idea of detecting neutrinos from cosmic sources [Mar60] they had to deal with two serious obstacles. First: according to model predictions high energy neutrino fluxes are very low. Second: the neutrino cross sections are also very small. Considering those two facts it became obvious that one needs huge detectors. Preferably filled with water or other transparent material if one wants to use Cherenkov light based detection technique. Since more than 70% of Earth's surface is covered with oceans, and lakes and there is almost $30 \times 10^6\,\mathrm{km}^3$ ice in Antarctica, an instrumentation of a natural water or ice volume is the best solution.

The first and unfortunately unsuccessful project which used natural water resources was the Deep Underwater Muon and Neutrino Detector (DUMAND) [Gri95]. It started in 1974 near the Big Island of Hawaii, but problems with the electronics led to the closing of the project in 1995. The next one was Baikal [A$^+$09f] deployed in 1993 in the Lake Baikal in Siberia and still operating. Other projects which are located on the northern hemisphere in the Mediterranean See are ANTARES [A$^+$06b], NEMO [Mig06] and NESTOR [Tza03]. The experience collected during their operation will be a valuable contribution to the planned one cubic kilometer detector KM3NeT [dW08].

2.3.1 Ice as a detection medium

The detectors enumerated above all use water as Cherenkov radiation medium and have to deal with some difficulties connected with this fact. For example the deployment of the detector is not as easy as in ice, and the distance to the shore might create problems with wires and readout electronics. In the sea water the noise rate (in the photomultiplier) is high (∼100 kHz) due to radioactive decays of ^{40}K and bioluminescence [A$^+$05b], and the movement of the water and changing temperature make the noise more time dependent. Also the Cherenkov radiation absorption length in water (∼20 m) is much shorter than in ice (∼100 m) [A$^+$05b].

On the other hand ice is also not the perfect and problemless medium. First of all, to have enough of it to build a 1 km^3 detector one has to go to the South Pole. Even with modern technology it is a challenge to transport all the needed equipment and people, and provide a suitable infrastructure. Once deployed all the parts of the detector which are under the ice surface are not accessible anymore and cannot be exchanged. Another disadvantage is the scattering length of the Cherenkov light in ice ∼20 m, rather short in comparison with the one in water ∼120 m [A$^+$06a].

The South Pole glacier is a very good source of knowledge of the Earth's climate history. Every year new snow which falls is compressed under its own weight and transformed into ice. At shallow depths the new formatted ice is full of air bubbles. The bubbles later (and deeper) undergo a phase transition to solid air hydrate crystals. Together with the snow all of the microscopic impurities (like mineral grains, acid droplets, salt crystals and soot) which the wind brings are compressed and forever preserved. This means that the ice properties such as scattering and absorption length are not uniform with depth. The properties of each ice layer have to be measured and properly accounted for in modeling of those parameters (Fig. 2.8 [A$^+$06a]). Glaciologists and climatologist use this information for their studies.

2.3.2 AMANDA-II

The AMANDA-II detector (Fig. 2.9) consists of 19 strings each one containing signal and power supply cables for the Optical Modules [Sch02] (OMs, in total 667) which are attached to them. The strings are separated from each other by 30 to 60 m and the OMs by 10 to 20 m. This configuration is optimal for detection of muons produced in CC interactions of neutrinos with energies above 1 TeV. The AMANDA-II angular resolution is in the range of 1.5° - 2.5°, depending on the energy and direction of the neutrino induced muon track [A$^+$07b].

The detector was deployed in the years 1995-2000 at the depth of 1500-2000 m with the center 1730 m below the surface. AMANDA-II predecessor AMANDA-A was deployed 800-1000 m below the surface. This turned out to be too shallow, because of numerous air bubbles still present at this depth. They cause strong light scattering and make the muon track reconstruction impossible.

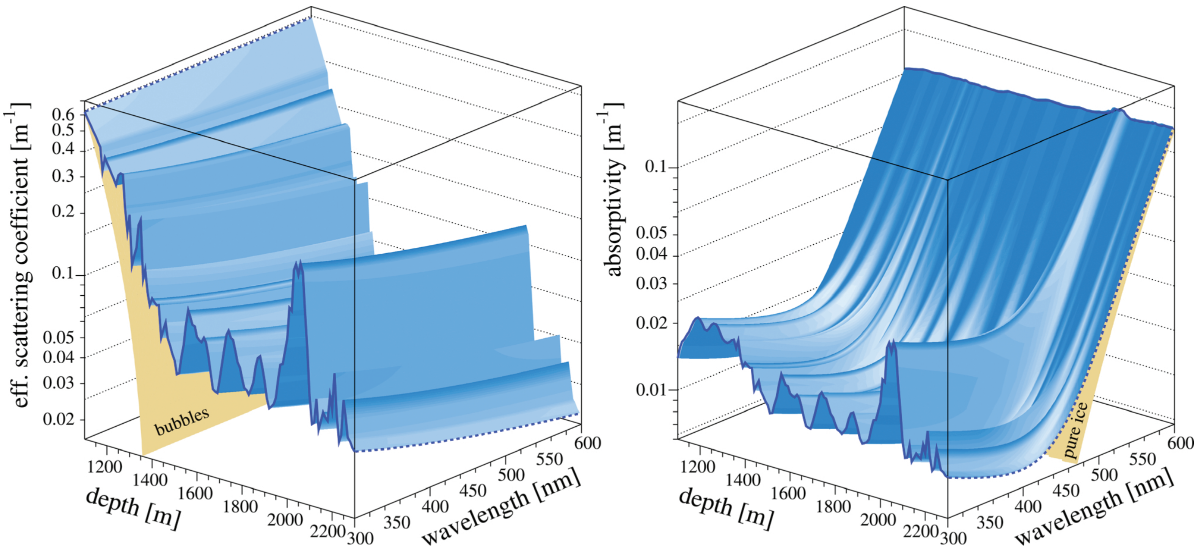

Figure 2.8: Maps of optical scattering and absorption for deep South Pole ice. The depth dependence between 1100 and 2300 m and the wavelength dependence between 300 and 600 nm for the effective scattering coefficient (left) and for absorptivity (right) are shown as shaded surfaces, with the bubble contribution to scattering and the pure ice contribution to absorption superimposed as (partially obscured) steeply sloping surfaces. Figure from [A$^+$06a].

The most important part of the AMANDA-II OM is the photomultiplier tube (PMT) which converts the incident Cherenkov photons into electric pulses. The PMTs were produced by Hamamatsu and have a diameter of 8 inches. A glass sphere protects them from the pressure of the ice. The PMT and glass surfaces are coupled with a transparent silicone gel with an adapted refraction index to obtain minimum refraction.

Since AMANDA-II grew over many years the detector topology is quite inhomogeneous. For example the center of string 17 is 500 m higher than the rest of the array because it got stuck while lowering it into the hole and froze in above the designated position. It is not used for the reconstruction of particle trajectories. The asymmetry of the detector layout has to be taken into account while estimating the expected background, especially if one wants to extract a signal which comes from a certain direction over a short period of time. This will be explained in more detail in Chapter 4.

2.3.3 Signal and background

The search for neutrino point sources of astrophysical origin is strongly affected by the background of events produced in the interactions of cosmic rays with the Earth's atmosphere. The most numerous, $O(10^9)$ per year, are the down-going atmospheric muons. They can be rejected by an angular cut on the declination of the incoming track. This limits the sensitivity of AMANDA-II to the northern sky only. The next major contribution comes from the atmospheric neutrinos which induce $O(10^3)$ of detected

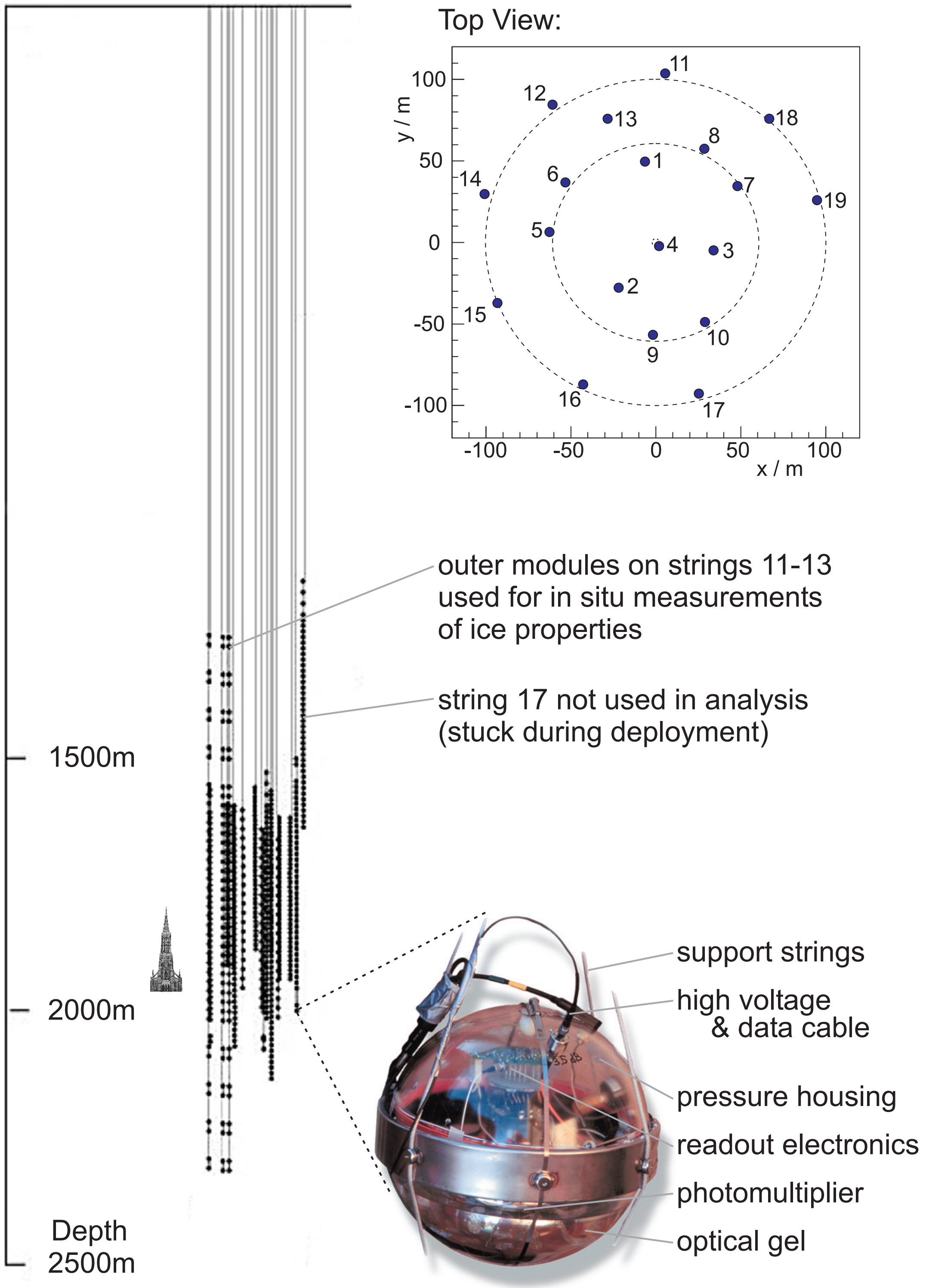

Figure 2.9: AMANDA detector layout. Figure from [Lan05].

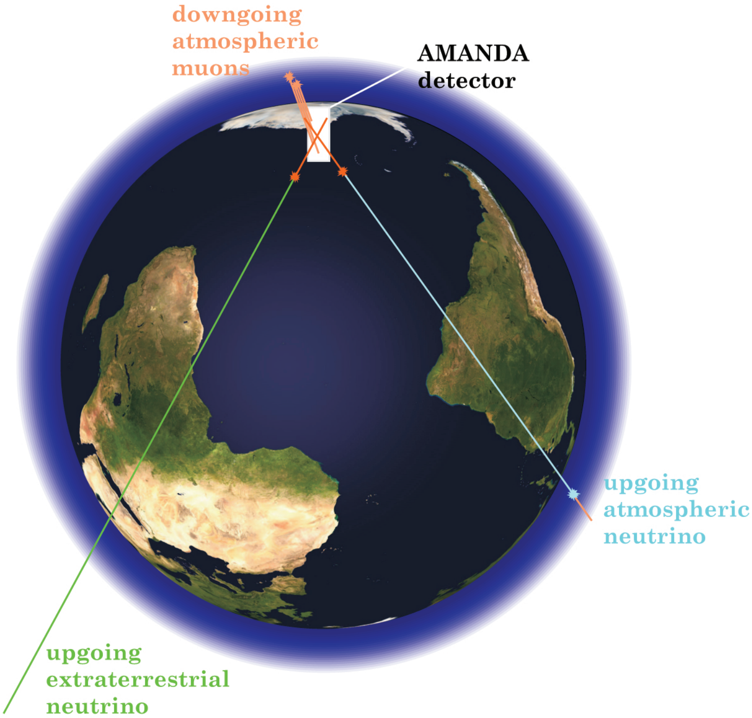

Figure 2.10: Sketch illustrating the definition of up-going and down-going tracks. The main background are the down-going tracks induced by muons from the atmospheric neutrinos' interactions. All muon up-going tracks are treated as a potential signal, since we cannot distinguish between an atmospheric and cosmic neutrino. Figure from [Lan05].

muon tracks per year. This is an irreducible background, since one cannot distinguish between a muon induced by an atmospheric or cosmic neutrino and all muons which have up-going tracks are treated as a potential signal. In Fig. 2.10 the concept of the up- and down-going track is illustrated.

2.3.4 Detector effective area

If one wants to compare the performance of different analyzes or experiments it is crucial to know their neutrino effective area A^{ν}_{eff}, which translates the incident neutrino flux Φ into the detectable neutrino rate R_{ν}. It depends on the neutrino energy E, because the CC cross section, muon range and detection efficiency vary with energy, but also on the direction from which the flux arrives. While the azimuthal dependence is averaged out by the yearly rotation of the Earth, the zenithal one persists because it is caused by factors like the fraction of neutrino and muons absorbed in the Earth and the geometry of the detector. The neutrino effective area is defined as:

$$dR_{\nu}(\delta) = A^{\nu}_{eff}(E,\delta)\frac{d\Phi}{dE}dE \tag{2.6}$$

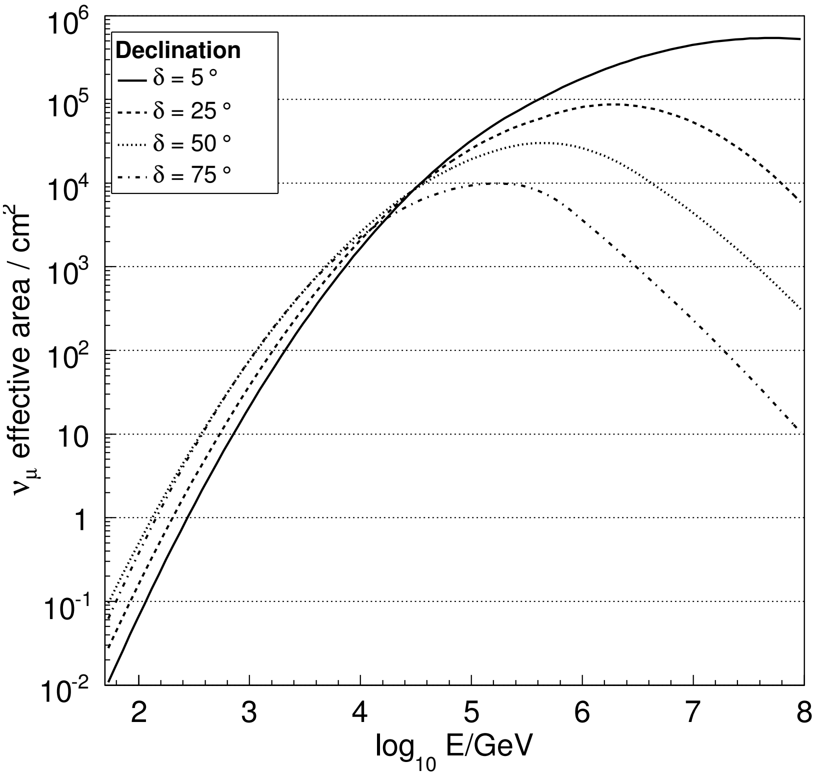

Figure 2.11: AMANDA-II effective area for ν_μ detection as a function of neutrino energy and declination δ. Figure from [A$^+$07b].

where δ stands for the declination of the neutrino source.

Fig. 2.11 shows the AMANDA-II A^{ν}_{eff} as a function of energy for different declinations as calculated using a complete simulation of the neutrino fluxes, neutrino interactions and detector response [A$^+$07b].

2.3.5 IceCube

From 2007 till March 2009, when it was shut down, AMANDA-II was fully integrated into the still growing IceCube detector. Till the year 2009 58 of IceCube strings were deployed and one of the low energy ($\leq$ 100 GeV) extension of the new detector, the so called DeepCore [Sch08]. It is planned to finish the construction of IceCube in 2011 with 80 strings and a volume of 1 km^3 (Fig. 2.12).

The main improvement over the AMANDA technology is the new Digital Optical Module (DOM) of 10 inch diameter, which houses all the electronics needed to digitize the signal [HT06]. This allows to minimize the noise and signal losses on the way to the surface data acquisition system.

Fig. 2.13 presents the comparison of the sensitivity to a point source with differential flux $\frac{d\Phi}{dE} = \Phi_0(\frac{E}{\text{TeV}})^{-2}$ as a function of the declination for AMANDA-II [D$^+$08a] and different IceCube configurations [A$^+$09a][A$^+$09b][J$^+$09] and ANTARES [A$^+$07a]. As one

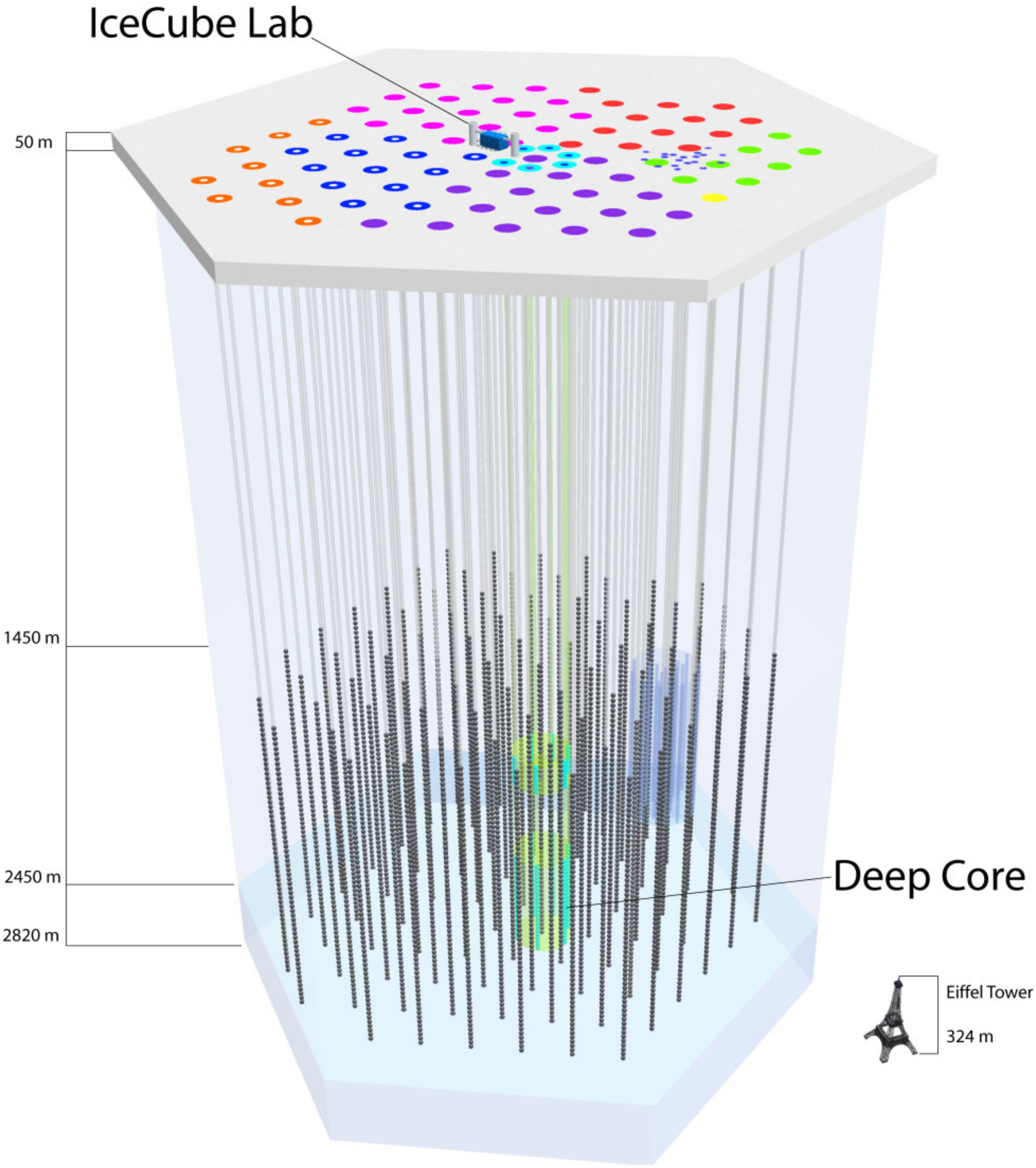

Figure 2.12: The IceCube telescope.

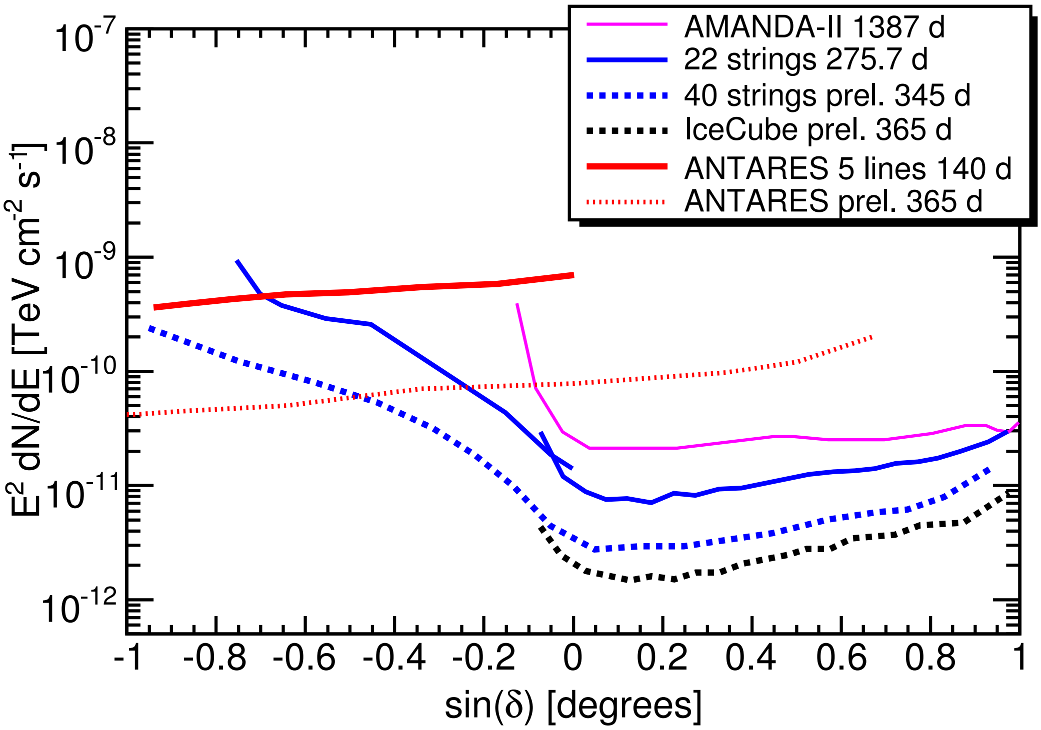

Figure 2.13: Sensitivity to a point source with differential flux $\frac{d\Phi}{dE} = \Phi_0(\frac{E}{\mathrm{TeV}})^{-2}$ as a function of the declination δ for AMANDA-II [D$^+$08a], different IceCube configurations: 22-strings [A$^+$09a][A$^+$09b], 40-strings and 80-strings [J$^+$09], and ANTARES [A$^+$07a]. Figure adapted from [J$^+$09].

can see, the full 80-strings IceCube is expected to be more than 10 times more sensitive than AMANDA-II. The angular resolution of IceCube should be better than 1°. It is also worth mentioning that, thanks to an innovative analysis which improves the sensitivity in the PeV-EeV enegy range, the FoV of IceCube can be extended to the southern hemisphere (declination from $-50°$ to $+85°$) [A$^+$09a].

2.4 Extensive Air Showers (EAS)

The Earth's atmosphere is constantly bombarded by an isotropic flux of high energy cosmic rays (protons, heavy nuclei) and photons. When they interact with air molecules they produce cascades of secondary particles known as Extensive Air Showers (EAS). The photon and hadron initiated showers differ in their geometrical (Fig. 2.14) and temporal properties. This allows one to differentiate the γ-ray showers from those coming from charged cosmic rays.

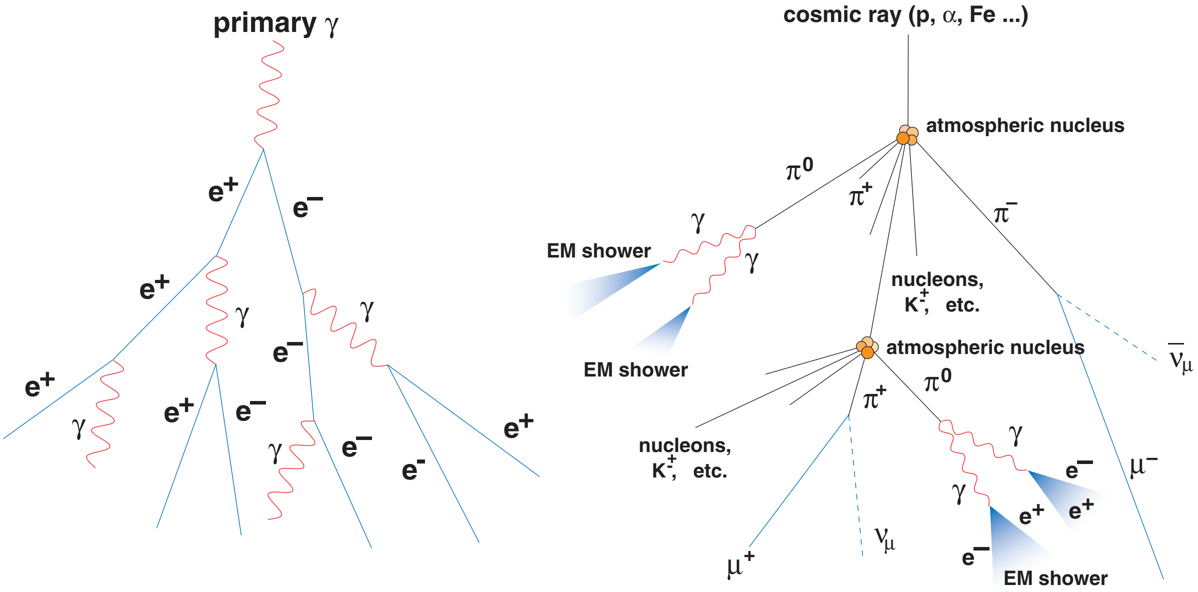

Figure 2.14: A sketch of development of electromagnetic (left) and hadronic (right) air showers. Figure from [Ott07].

Gamma-ray initiated showers

The main two processes involved in the electromagnetic shower development are pair creation and bremsstrahlung. After an initial pair creation they alternate: first, after traversing a characteristic distance, called radiation length X_0, the pair created electron and positron lose about 2/3 of their energy by photon emission (bremsstrahlung), then the bremsstrahlung photons again undergo pair creation after traversing an average distance of $\frac{7}{9}\,X_0$. As a consequence the number of particle doubles and the energy per particle halves after each unit length of $1\,X_0$ (Earth's atmosphere has $\sim$28 radiation lengths). This goes on until the average energy per particle reaches the so-called critical energy when the energy losses per unit length by bremsstrahlung and ionization are equal (83 MeV in air). After that point the shower rapidly dies out because the ionization losses for electrons start to dominate (this happens around 11 km above the ground level for a γ-ray of 100 GeV).

Hadron initiated showers

The primary hadron which collide with a nucleus can produce a great variety of secondary particles like pions (π), kaons (K), lighter nuclei, etc. The pions are usually the most numerous and produced with about equal numbers of π^+, π^- and π^0. Through the almost instantaneous decay of π^0 ($\tau = 10^{-16}\,$s) into two photons on average 1/3 of the energy in each hadronic EAS is transfered into the electromagnetic sub-showers. In the decay of charged pions muons and neutrinos are produced: $\pi^0 \rightarrow \mu^\pm + \nu_\mu$. The muons, which have a relatively long life time, usually penetrate deep into the atmosphere and if their energy is high enough ($> 2\,\mathrm{GeV}$) eventually reach the ground and beneath. As mentioned before, the muons and neutrinos from EAS are the main background components in searches for cosmic neutrino point sources.

In hadronic interactions, where the strong force plays the main role, the secondary particles receive on average higher transverse momenta than in the electromagnetic processes. There are also subcascades. As a result the hadronic showers are usually broader and less homogeneous than the electromagnetic ones (also in the temporal spread of the cascade). This is an important feature which allows the separation of the two shower types.

2.5 The Imaging Atmospheric Cherenkov Technique (IACT)

There are many detection techniques which allow one to reconstruct the energy, the arrival direction and the arrival time of cosmic rays or photons: direct detection of shower particles, fluorescent light, radio emission or Cherenkov light. But only the last one enables one to detect from ground the primaries with energies as low as few tens of GeV. If the primary energy is below ~20 TeV, the cascade dies out a few kilometers above the sea level. Still, most of the air shower particles are ultrarelativistic and produce Cherenkov radiation. As described in section 2.1 this radiation forms a narrow cone, for a particle with $\beta = 1$ and air refraction index $n_{air} = 1.0003$ the cone aperture angle is ~1°.

Cherenkov radiation penetrates the atmosphere to ground level, but on its way it suffers transmission losses. In Fig. 2.15 the differential Cherenkov photon densities are shown at the height near the maximum emission and at the 2200 m a.s.l. for shower induced by γ-rays of different energies. One can clearly see a sharp cutoff around 300 nm due to the absorption by Ozone. Other transmission losses are mainly caused by the Rayleigh scattering, which affects mostly the short wavelengths. Also the inclination of the shower influences the position of the peak of the emission - with higher zenith angles the peak shifts towards higher energies. The optimal optical observation window is a broad band in the blue and near UV (300-450 nm).

When it finally reaches the ground, Cherenkov radiation illuminates a circle of a radius of ~120 m – for a γ-ray primary of energy ~1 TeV (see Fig. 2.16)). The time spread of Cherenkov light pulses is of the order of 1-7 ns with the typical light pulse from hadronic shower (3-7 ns) being somewhat longer than from an electromagnetic one (1-3 ns).

The characteristics of the Cherenkov emission from an EAS given above indicates the constraints to the design of the telescope. For example the small time spread of Cherenkov light pulses requires the optics and readout electronics to be fast. In the next paragraphs some other requirements will be shortly presented and discussed in more detail later, based on the example of the MAGIC telescope (section2.7).

Due to the large area of the Cherenkov light pool ($\sim 10^5\,\mathrm{m}^2$) the light collection area should be as large as possible. This is usually achieved by a big (compared to optical

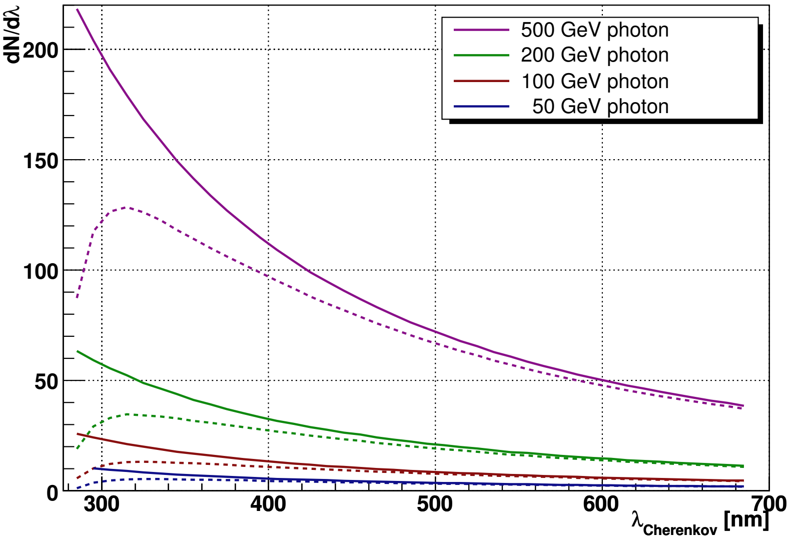

Figure 2.15: Differential Cherenkov photon densities $dN/d\lambda$ are shown at the height near the maximum emission (solid lines) and at the 2200 m a.s.l. (dashed lines) for shower induced by γ-rays of different energies. Figure from [Ott07].

telescopes) reflector diameter (≥10 m). To minimize the costs, such a reflector is made of an array of small tessellated mirrors of circular, hexagonal or square shape for close packing. The optimum image is achieved when the mirror curvature is the same as the focal length (so called Davies-Cotton design). To obtain the best reflectivity in the blue-UV part of the spectrum the glass mirrors are covered with an aluminum layer. Another layer of protective material is usually added, because the big size of the reflector makes it difficult to build a dome around it.

Reflected photons are collected by a camera placed in the focal plane of the telescope. It is an array of a few hundreds of photomultiplier tubes with a good (∼20%) quantum efficiency in the blue band and a diameter of ∼0.1°. The Field of View (FoV) obtained with such a camera is around 2°-5° and in a case of a single telescope the PMT size defines the minimal angular resolution.

Figure 2.16 shows the image formation scheme in the camera of a Cheren-kov telescope. Due to the changes of the refraction index of air with altitude and other minor factors, the angle of the emission of Cherenkov photons with respect to the shower axis also changes. The number of produced particle depends on the altitude too. Both factors are reflected in the longitudinal structure of the recorded Cherenkov image. The position of the image with respect to the camera center depends on the incident angle of the primary particle: the more inclined is the particle track, the more the image is shifted towards the camera border.

In 1985 Hillas defined a set of parameters [Hil85] describing the shape of shower image on the basis of the moment analysis of the signal amplitude recorded by the camera pixels. They allow to distinguish between the electromagnetic and hadronic showers, estimate the primary energy and, especially in the case of a single telescope, facilitate

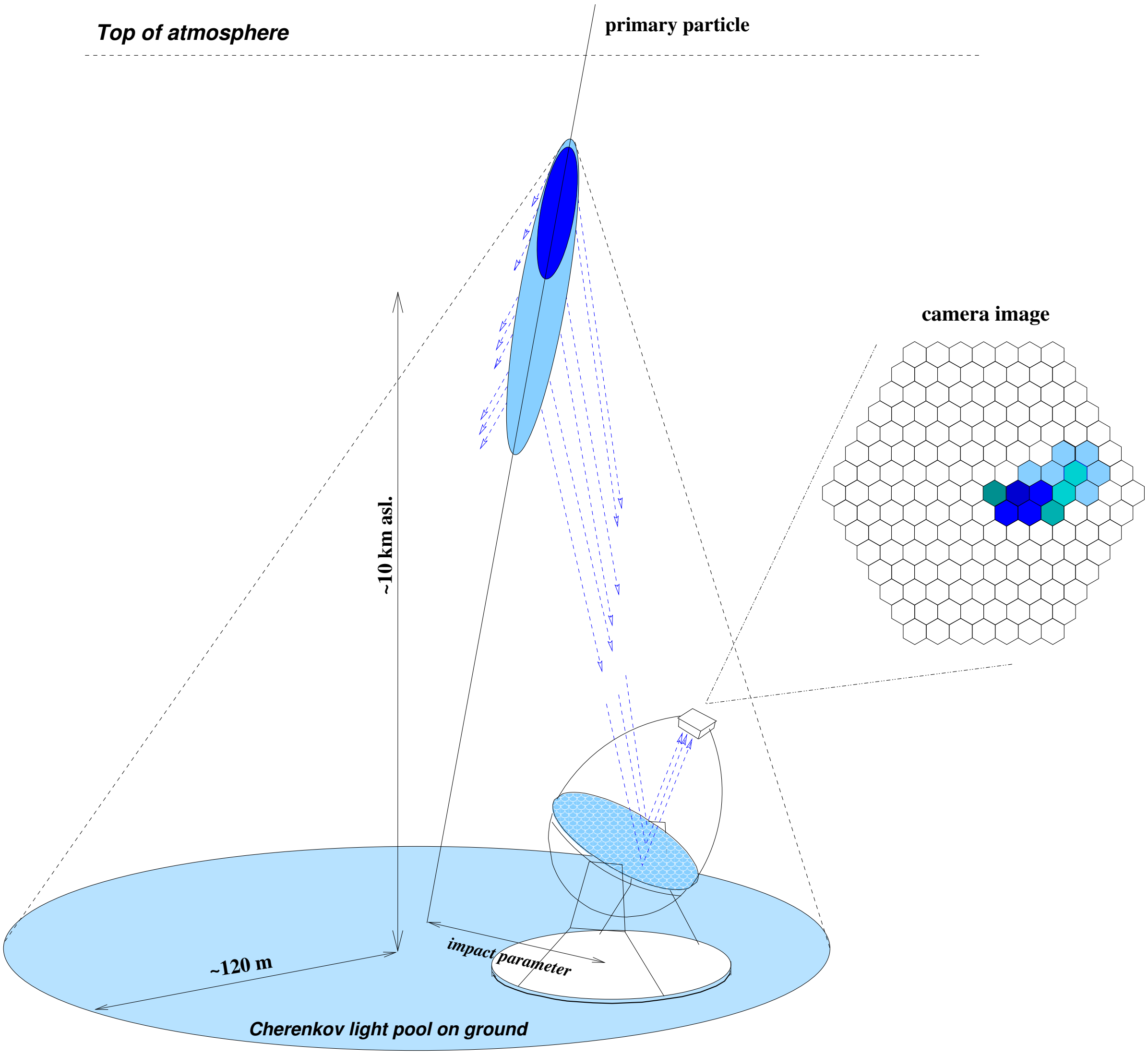

Figure 2.16: Image formation scheme in the camera of a Cherenkov telescope. Figure from [L$^+$09b].

the determination of the source position. More information on this and other aspects of the signal processing can be found in Chapter 3 consecrated to the MAGIC analysis chain.

2.6 Historical and modern gamma-ray telescopes

In 1968 the first IACT telescope, Whipple 10 m, was built on the top of Mount Hopkins in Arizona, but it did not start operation till 1982 when the first imaging camera was installed [W^+89]. This senior among the IACT telescopes is still in a good condition and after many years of successful operation and important discoveries serves mostly for monitoring of bright blazars. The Whipple follower, HEGRA CT1, started observations in 1992 at La Palma island [M^+94]. It was soon (1996) extended into an array by an addition of 4 IACT telescopes of the same type. During its operation (1996-2002) the HEGRA collaboration demonstrated that the IACT technique can be significantly improved by the use of multiple telescopes. Stereo shower detection offers many advantages such as: reduced energy threshold, better angular resolution, enhanced hadron discrimination and easier shower axis location. Other important telescopes belonging to the same generation are: CAT (1996-2003) in France, TACTIC in India (2000-present) and, first one on the southern hemisphere, CANGAROO (1992-1998) in Australia. In Table 2.1 one can find a summary of their dimensions and performance.

In comparison to the first generation the modern Cherenkov telescopes are capable of observing lower energy showers and have much higher sensitivity. It was possible thanks to larger collection areas (bigger reflectors) and improvements in the camera design. Most of the currently operating experiments are telescope arrays (HESS, VERITAS, CANGAROO-III). Till 2009 MAGIC was the only single telescope experiment, but recently MAGIC-II telescope came into operation. Also the HESS collaboration is working on an extension of their array. In order to improve the performance at lower energies a 28 m HESS-II telescope will be placed in the center of the array, the start of data taking is planned in 2010.

The next big step in the development of the ground-based VHE γ-ray physics will be the Cherenkov Telescope Array (CTA) of $\sim$100 telescopes of different sizes. The collective efforts of scientists from different IACT collaborations aims at lowering the energy threshold down to $\sim$10 GeV and improving the sensitivity by a factor of 10. CTA is supposed to be an open observatory providing observation time for the whole astrophysics community.

In Table 2.1 the second generation IACTs are compared. In the following section one of them – the MAGIC telescope – will be described in more detail.

2.7 The MAGIC telescope

MAGIC is located on one of the Canary Islands, La Palma, and started operation in 2004. Although it is a single telescope its sensitivity is comparable to the array experiments

Figure 2.17: Operating Cherenkov telescopes. Top: the VERITAS array. Middle: the HESS array. Bottom, from left to right: MAGIC, CANGAROO-III, TACTIC, Whipple. Figure from [Gru07b].

Table 2.1: Comparison of the first generation of the IACT telescopes. Table contains: the name of the *Experiment*, its *Location*, *Elevation* in km a.s.l., period of *Operation*, number of *Telescopes* × *Mirror diameter* in m, *Field of View* in degrees, number of *Camera pixels*, energy threshold E_{th}, *Sensitivity* to Crab flux in $\sigma/\sqrt{h}$, *Energy resolution* in %, *Angular resolution* in degrees, *Reference*

Experiment	Location	Elev. [km a.s.l.]	Operation	Tel. × Mir. diam. [m]	FoV [deg]	Camera pixels	E_{th} [TeV]	Sens. [$\sigma/\sqrt{h}$]	E res. [%]	Ang. res. [deg]	Ref.
Whipple	Arizona, USA	2.3	1982-now	1×10	2.6	467	0.25	5	30	0.1-0.2	[W$^+$89]
HEGRA	La Palma, Spain	2.2	1992-2002	6×3.4	4.3	271	0.5	16	10-20	0.09	[P$^+$03]
CANGAROO	Woomera, Australia	0.2	1992-1998	1×3.8	3.0	256	0.4	1	25	0.25	[T$^+$98a]
CAT	Pyrenees, France	1.6	1996-2003	1×5	4.8	600	0.25	4.6	20-25	0.15	[B$^+$98] [B$^+$97a]
TACTIC	Mt. Abu, India	1.3	2000-now	1×9.5	6.0	349	0.3	1	40	0.3	[K$^+$07]

Table 2.2: Comparison of the second generation of the IACT telescopes. Table content - see caption in Tab. 2.1, *Sensitivity* is given in % Crab/50 h/5 σ

Experiment	Location	Elev. [km a.s.l.]	In operation since	Tel. × Mir. diam. [m]	FoV [deg]	Camera pixels	E_{th} [TeV]	Sens. [% Crab/50 h/5 σ]	E res. [%]	Ang. res. [deg]	Ref.
CANGAROO-III	Woomera, Australia	0.2	2004	4×10	4.0	427	0.4	10.0	10-15	0.15	[K$^+$04c]
HESS	Namibia	1.8	2004	4×13	5.0	960	0.2	$\leq$1.0	20	0.12	[A$^+$06c]
MAGIC	La Palma, Spain	2.2	2004	1×17	3.5	577	0.1	1.6	20	0.10	[A$^+$08e])
VERITAS	Arizona, USA	1.3	2007	4×12	3.5	499	0.15	1.0	15	0.10	[H$^+$09]

and the energy threshold is lower. It also possesses some unique features like a low weigth construction which allows for fast repositioning, low gain PMTs for observations under moderate moonlight and very fast readout electronics which enhances the precision of reconstruction of the time structure of Cherenkov pulses.

2.7.1 Drive system and frame

One of the important criteria for the MAGIC desing, was to make it as light as possible in order to enable fast repositioning for follow-up observations of Gamma Ray Burst (GRB). This was achieved by using a very light (∼5 t) carbon fiber structure for mounting the reflector. It rests on a steel ring which allows to move the reflector in elevation and an undercarriage which moves in azimuth. This kind of mount is called alt-azimuth-mount.

The total weigth of the MAGIC telescope is ∼ 64 t and its drive system is powerful enough for moving it with both: a fast slew of ∼90°/10 s and a slow source tracking mode of ∼90°/6 h. The position of the telescope is measured with 14 bit resolution absolute precision shaft encoders with a frequency of 1 kHz. There are two of them in the elevation axis (they also serve for checking possible torsion of the telescope dish caused by the weight of the reflector) and one in the azimuth axis. A measurement of telescope position with accuracy better than 0.02° is possible in this configuration. With a bending correction algorithm a tracking precision of 1.5 arcmin is achieved and a further improvement up to 0.25 arcmin (15 arcsec) is possible using the information from a star guider system. More detailed description of the MAGIC drive system as well as the pointing model can be found in [B$^+$09a].

2.7.2 Reflector

The Cherenkov pool on the ground level illuminates a circle of ∼100-120 m and in order to detect low energy showers (<100 GeV) the reflector area should be as big as possible to collect as much light as possible. MAGIC with its 17 m diameter dish has a collection area of 236 m^2 (so far the largest one for a single dish telescope).

The reflector is octagonally shaped and consists of 964 square mirrors measuring 49.5 × 49.5 cm^2 each. They are lightweight sandwich aluminum panels with a high reflectivity over a broad range of wavelengths ($>$ 80% between 250 and 750 nm). They are covered with a quartz coating layer for weather protection and internal heating is installed to prevent dew and ice deposits. A detailed description and study of the performance of the reflecting elements is given by [D$^+$08b].

Although the individual mirror panels are spherically shaped the general curvature of the reflector is parabolic. This geometry allows one to avoid a dispersion in the arrival times of the Cherenkov photons in the plane of the camera and to reduce the time window, from which the signal is extracted. Preservation of the intrinsic time structure of the Cherenkov pulse is very useful for the separation of gamma and hadron induced showers as well as reducing the signal contamination with the Night Sky Background (NSB) events.

An Active Mirror Control (AMC) system was designed for compensating the degradations of the optical performance of the telescope due to the deformations of the telescope structure which occur while tracking. A laser pointer is attached in the middle of each mirror panel and a light spot from each laser is visible on the camera shield. The position of the spots is recorded by a video camera located in the place of the central mirror panel of the telescope. If defocused, the individual mirror elements are readjusted. [Gar06] gives a detailed description of the AMC and its performance.

2.7.3 Camera

The MAGIC camera [S^+02] is located in the focal plane of the telescope. It has hexagonal shape and a Field of View (FoV) of 3.5°. It is equipped with two types of PMTs: 397 of the type ET9116A with 0.1° diameter are installed in the inner part of the camera (radius ∼1.25°), the outer part (radius ∼1.25°-1.8°) consists of 180 PMTs of type ET9116B with a diameter of 0.2°. This design, while reducing the costs, allows for a good imagining of low energy showers which are usually more compact and occur closer to the camera center. On the other hand the camera is big enough to record the more extended high energy showers.

Both types of pixels have 6 dynodes and operate under low gain in order to prevent degradation due to bright NSB, moon light or accidental light flashes (e.g. from passing cars). Their surface is coated with a wavelength shifter which enhances their quantum efficiency up to ∼28% and extends its range to the UV region. In order to compensate for the dead space between the pixels so called Winstone cones are installed on top of each pixel. They provide a nearly 100% light collection efficiency by focusing the light on the most sensitive region of the PMT. For environmental protection (dust, humidity) a 2 mm thick, UV transmitting plexiglass window covers the camera front.

The humidity and temperature inside the camera are constantly controlled by a dedicated system. It prevents temperature dependent fluctuations of the readout channels. The camera is cooled by a water-based cooling system.

2.7.4 The trigger and Data AQusition (DAQ) system

The signal digitization, trigger and readout electronics of the MAGIC telescope is located in the near-by counting house. Low-weight optical fibers are used to transmit the signal from the camera. They minimize the noise and time dispersion of the signal. In the counting house the signals are split. One branch goes to a discriminator, and if the pulse height exceeds a certain threshold a signal for the trigger system is generated. The signal in the second branch is delayed and directed to the digital converters (Fig. 2.18).

The discriminator thresholds (DT) can be adjusted individually for each pixel by a control system called IPR (Individual Pixel Rate). This circuit loops continuously over all channels and registers the individual pixel rate after the discriminator thresholds (DT). If the rate is too high, the DT for any individual pixel is increased to set back the first level trigger (L1T) rate to around 200 Hz. This algorithm was initially developed

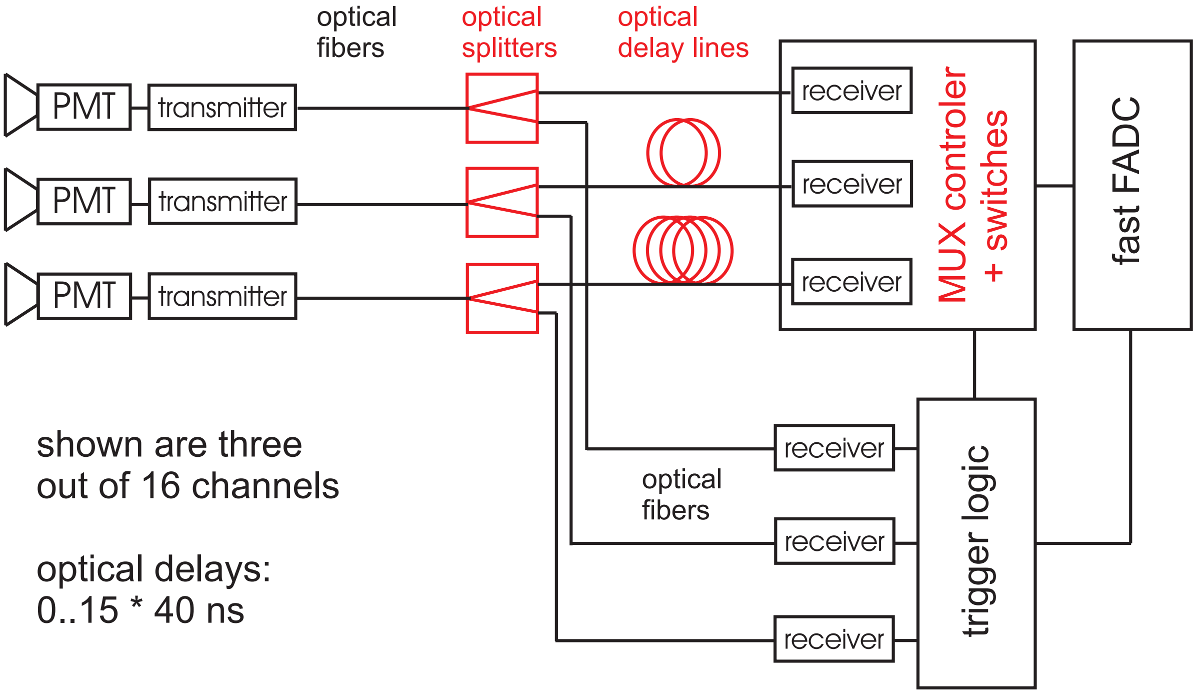

Figure 2.18: MAGIC DAQ system. The signal is transmitted from a PMT in the camera to the counting house via optical fibers. In the counting house the signals are split by fiber-optic light splitters. Then one branch is delayed using optical fibers and directed to the digital converters (FADC). Each of 16 channels is delayed by 40 ns with respect to the previous channel. The other branch goes to a discriminator and, if the pulse height exceeds a certain threshold, a signal for the trigger system is generated. Figure from [G^+07c].

to decrease accidental triggers in channels with a bright star in the field of view but it turned out useful also for the observations during moonlight and twilight.

Until the end of January 2007 the signals were digitized by 300 MHz Flash Analogue to Digital Converters (FADCs). In February 2007 the data acquisition was upgraded with FADCs capable to digitize at the ultra-high speed of 2 GSample/s [T$^+$07a, G$^+$07c]. Thanks to a smaller width of the pulse ($\sim$2.3 ns FWHM) a shorter integration window can be used and the amount of the NSB (Night Sky Background) light integrated with the real signal is reduced. Moreover the new configuration allows to reconstruct the timing characteristics of the Cherenkov shower with a good time resolution.

The readout and trigger system of the camera is divided into 19 overlapping sectors (trigger macrocells) of $\sim$37 pixels each and defines the camera trigger radius of $\sim$0.8°. The first level trigger (L1T) applies time coincidences and a simple 4-next-neighbor (4NN) logic in the trigger macrocells in order to reduce the random coincidence rate [M$^+$04]. The average trigger rate of MAGIC is $\sim$200 Hz (for low zenith angle observations) and the peak of the distribution of the energy of the triggered events lies $\sim$60 GeV.

In 2007 an innovative trigger [R$^+$08] was developed with the aim of lowering the energy threshold by a factor of two and allowing for detection of the signal from the Crab and other pulsars [A$^+$08f]. The new trigger concept was based on the analog summation of the signals coming from clusters of 18 pixels (hence the name "Sum Trigger"). The DAQ is triggered if the signal exceeds a threshold of 26 coinciding photoelectrons in the cluster. To prevent accidental triggers from frequent large afterpulses, the signal of each pixel is clipped at the 6 photoelectron level. This approach was proven to cope better with the discrimination of the faint flashes of Cherenkov photons from the NSB at low energies. The two triggers can be used together and later the analyzer can decide to use events triggered by both or only one of them.

All events which successfully pass the trigger are digitized and written out into a FiFo (First In First Out) buffer. Then the data is saved to a RAID disk system. The average raw data production is around 73.0 GBytes/h and per year up to 100 TBytes are collected. An on-line analysis starts immediately after the data is taken. It allows one to monitor on-line the source state and in case of an interesting behavior prolong the observation or send an alert for further observations by other telescopes.

3 MAGIC data analysis chain

Results form the MAGIC observations presented in this work were analyzed using the MAGIC Analysis and Reconstruction Software (MARS). It is a collection of programs written in C++ in the framework of the ROOT data analysis software maintained at CERN [1]. The repository of the MARS code and the MAGIC data center are both located at PIC (Port d'Informació Cientifica) in Barcelona[2]. MARS allows the user to do a complete data analysis, from the extraction of the signal, to the calculation of observed flux values and spectral energy distribution.

3.1 Observation modes

There are two different modes of observing sources (see Fig. 3.1). In the ON mode the camera center points to the source. It is usually used for tracking faint objects, since the camera efficiency is highest in the center. The ON observation is usually accompanied by an OFF observation with camera pointing to a sky region with similar background light conditions, but no γ-ray source in the field of view. This data is used as a background sample for the analysis. Ideally OFF observation should be performed for the same amount of time and under the same atmospheric conditions as the ON one. If no OFF data are available, background has to be estimated using a fit to the ON data recorded by a camera region where no showers from the source are expected (usually 30° - 90° from the camera center), the fit is extrapolated to the source region.

The second observation mode is called wobble mode [F^{+}94]. In this mode the source position is shifted by a fixed distance (in MAGIC usually 0.4°) from the camera center. The point opposite to the source position is called "anti-source position" (180° w.r.t. the camera center) and it is used for background determination. Often two more background regions, lying ±90° away from the source position, are also used for the analysis. During tracking the source and anti-source positions are regularly swapped (this is called "wobbling") in order to avoid systematic errors that might arise from the inhomogeneities in the camera. The big advantage of the wobble mode is simultaneous recording of signal and background, a disadvantage is a slightly lower efficiency in the camera regions away from the center.

Data taken in the two different modes require a slightly different analysis. This will be explained in more detail below.

---

[1] http://root.cern.ch/

[2] http://magic.pic.es

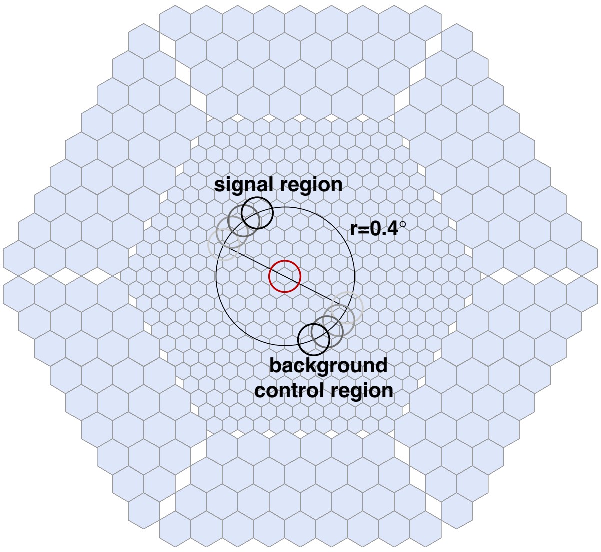

Figure 3.1: Observation modes: during ON/OFF observations the source is positioned in the center of the camera (red circle); during wobble observations the source and background control regions are displaced by 0.4° from the camera center and observed simultaneously. Figure from [Wag06].

3.2 Signal extraction and calibration

The first step of the event reconstruction is to determine its arrival time and amplitude recorded by the MAGIC camera pixels. This information is extracted from the FADC sample using a digital filter which fits a fixed pulse shape to the recorded signal and returns the signal amplitude in FADC counts and the amplitude peak position in time. The normalized signal shape used for fitting is determined from Monte Carlo simulations. In [Gau06] it was shown that this method of signal extraction is very reliable unless the pulses appear very early in the FADC digitization window or have small amplitude i.e. can be mistaken with the Night Sky Background fluctuation.

In the next step the extracted amplitude in FADC counts and the signal time in FADC clock ticks are converted to amplitude in photoelectrons (phe) and absolute time, assuming a linear relation between the number of phe in the camera pixel and the extracted FADC amplitude. For the calibration of the data presented in this thesis the so-called F-factor method (excess noise factor method) [RM97] was used. These conversion factors are obtained by measuring the single photoelectron response of PMTs in the laboratory. In addition a few calibration runs before each source observation and interleaved calibration events at a rate of 50 Hz during observation are taken. They allow to correct the conversion factors for short term fluctuations in the optical signal transmission.

An alternative method of a global absolute light collection efficiency calibration is the analysis of muon images (rings) in the camera. The energy of single muons which hit the detector is reconstructed and compared to Monte Carlo predictions. Muon ring images are also used for deriving the optical point spread function (PSF) of the telescope.

3.3 Image cleaning

Since, for a single event, most of the pixels in the camera contain only the information about the NSB fluctuations and not the actual Cerenkov shower image they have to be eliminated from further analysis. This is done during a procedure called ”image cleaning”. In the MARS framework two image cleaning methods are implemented: the Standard Image Cleaning and the Time Image Cleaning which uses additionally the timing information of the event and allows for a better reconstruction of the low energy events.

3.3.1 Standard Image Cleaning

In the first stage of this procedure the so called ”core pixels” are selected. A pixel is tagged as a core pixel when its charge exceeds a fixed threshold value q_1 (in phe) and has at least one neighbor fulfilling the same condition. Then all pixels which have at least one core neighbor and charge above q_2 ($q_2 < q_1$) are also selected and included in the image as the ”boundary pixels”. To determine the optimal threshold values for q_1 and q_2 one has to make a compromise between relaxing the cleaning levels to effectively lower the analysis energy threshold, and the fact that too low values result in including pixels only due to noise. The standard values of q_1 and q_2 used in MAGIC before the upgrade of the FADC system were 10 phe and 5 phe respectively.

3.3.2 Time Image Cleaning

As mentioned before, during the extraction of the signal both the amplitude and the arrival time of the Cerenkov pulse are assigned to each pixel. With the new FADC system the accuracy of the arrival time assignment was substantially improved (from 3.3 ns to 0.5 ns) and this information is used for more advanced selection of the core and boundary pixels. The Time Image Cleaning relies on the fact that the Cerenkov flashes are very short and that the NSB photons produce pulses which are asynchronous with the respect to the pulses from the shower image. If one introduces a time coincidence window between the mean arrival time and single pixel arrival time most of the NSB generated pulses can be rejected and the cleaning levels q_1 and q_2 relaxed.

The procedure is the same as in the Standard Image Cleaning, with the addition of two time coincidence windows: δt_1 for core pixels and $\delta t_2 < \delta t_1$ for boundary pixels, into which the arrival time of the signal has to fall in order to be accepted. A study based on Monte Carlo simulations (for more details see [Tes07]) was performed in order to find the optimal values of the new parameters and the cleaning thresholds are now set to $q_1 = 6$ phe, $q_2 = 3$ phe, $\delta t_1 = 4.5$ ns and $\delta t_2 = 1.5$ ns.

Fig 3.2 illustrates the different cleaning methods and the efficiency of the Time Image Cleaning.

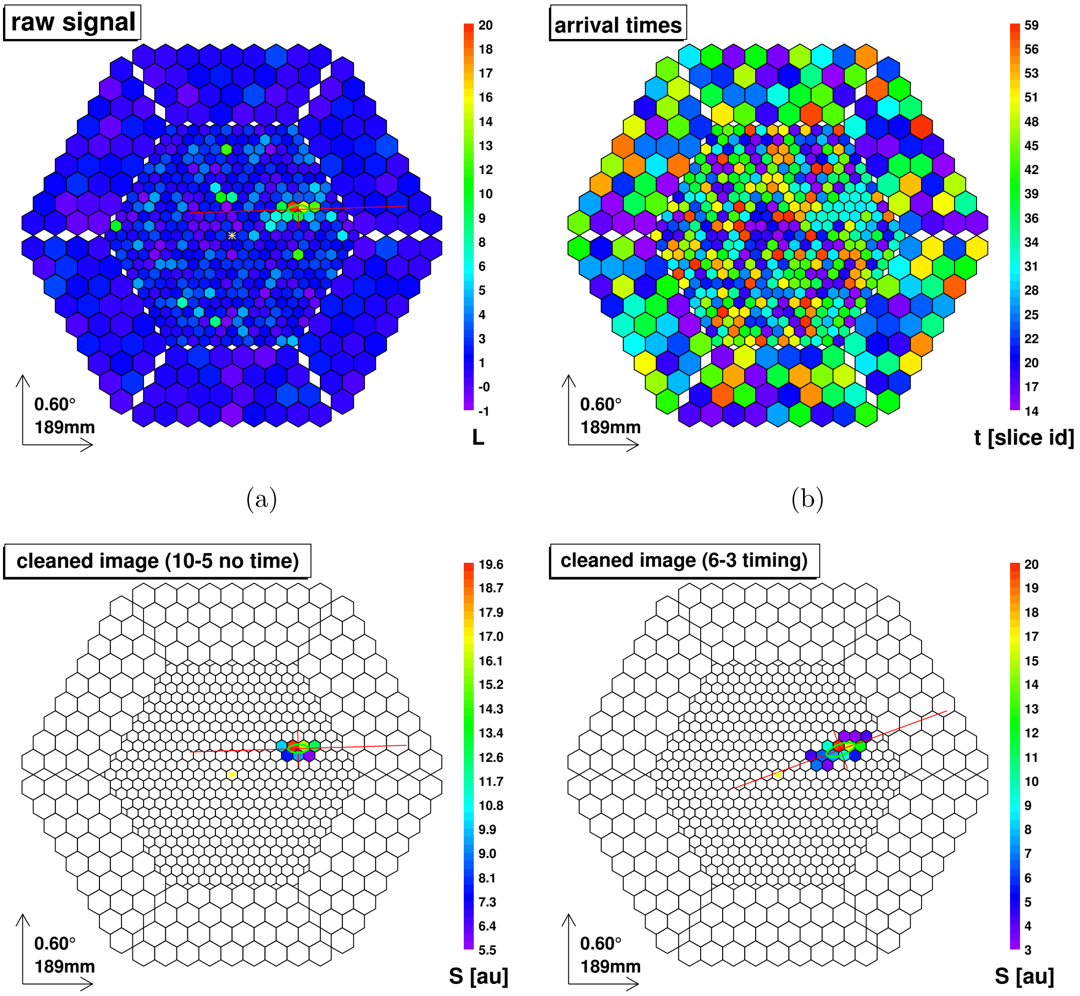

(a)

(b)

(c)

(d)

Figure 3.2: Illustrative event images (MC γ-ray, Energy=71 GeV, Impact Parameter= 111 m). First row: display of raw recorded data (left) and arrival times information (right). Second row: comparison of Standard Image Cleaning with 10-5 phe minimum charge levels (left) and the Time Image Cleaning (right) with 6-3 phe minimum charge levels and 4.5 ns and 1.5 ns as time constrains. The simulated gamma-ray source is located in the center of the camera (yellow star). Figure adapted from [A^+09e].

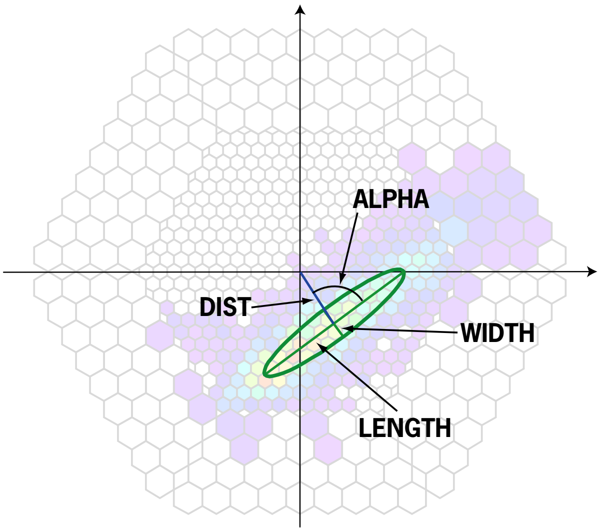

Figure 3.3: The Hillas parameters: Length, Width, Alpha and Dist. Figure from [Ott07]

3.4 Image parameters

After cleaning the shower image it has to be decided wether it was induced by a γ-ray or hadron. This decision is based on a geometrical analysis of the image first introduced by [Hil85]. The so-called Hillas (or image) parameters are obtained from the moments of the light distribution in the camera pixels and their distributions differ for γ-ray and hadron events. They are shown in Fig 3.3.

3.4.1 The standard Hillas parameters

The parameters which describe the shape and the light content of the shower are: Size, Conc, Length, Width, M3Long and Leakage.

1. Size: the total charge (number of phe) contained in the shower image. It is, in the first approximation, proportional to the primary energy.

2. Conc(n): the ratio of the light content of the n pixels with the highest light yield to the total light content of the shower. It describes the compactness of the shower maximum region. Gamma-ray induced showers are usually more compact than those induced by hadrons.

3. Length: the RMS spread of the charge along the major axis of the image. It carries the information about the longitudinal development of the shower and is usually larger for the hadron-induced showers.

4. Width: the RMS value of the charge distribution along the minor axis of the image. It carries the information about the lateral development of the shower. Since the hadron-induced showers have usually larger transverse momentum it is one of the key parameters in γ-hadron separation.

5. M3Long: the third moment (asymmetry) of the light distribution along the major axis. It is positive when the image points in the direction of the source position in the camera.

6. Leakage: the ratio between the number of phe in the 2 outermost rings of the camera and the total light yield of the shower. This parameter is important for estimating the energy of the shower, since the high energy events might not be fully contained in the camera.

The parameters which describe the orientation of the shower image in the camera are Alpha and Dist.

1. Alpha: the angle between the main shower axis and the line connecting the source position in the camera with the center of gravity of the image.

2. Dist: the distance between the source position in the camera and the center of gravity of the image. It is correlated to the impact parameter of the shower produced by a γ-ray coming form a point source.

3.4.2 The time-parameters

As mentioned before, the timing characteristics of the Cerenkov showers are different for different types of primaries. In [H$^+$99b] it is explained that the most important discriminating factor is the dependence of the timing profile along the major axis of the image on the impact parameter of the shower. If the impact parameter is small (below 60 m) the light emitted in the higher part of the shower (shower head) arrives later than the light emitted in the lower part of the shower (shower tail), because the photons emitted at the beginning travel slower (with a speed of c/n) then the ultra relativistic particles of the shower which produce photons closer to the ground. In case of a large impact parameter (over 120 m) this effect is reduced or even inverted, since the arrival time from the tail becomes the sum of the times spent in the paths of particles and photons respectively.

Relying on the model described above two new time-related image parameters have been introduced in the MAGIC analysis: Time Gradient and Time RMS.

1. Time Gradient: describes how fast the arrival time changes along the major axis of the image. In order to reduce the problem to one dimension the pixel coordinates are projected onto this axis. Then a linear function is fitted to the arrival time t versus the space coordinate x along the major axis: $t = m \cdot x + q$. The slope m measures the Time Gradient, it is positive if the arrival time increases with the distance of the pixel from the source position in the camera. The parameter q is a free parameter and do not have any physical meaning.

2. Time RMS: the root mean square of the arrival times of all pixels which belong to the image (after cleaning). It measures the spread of the arrival times.

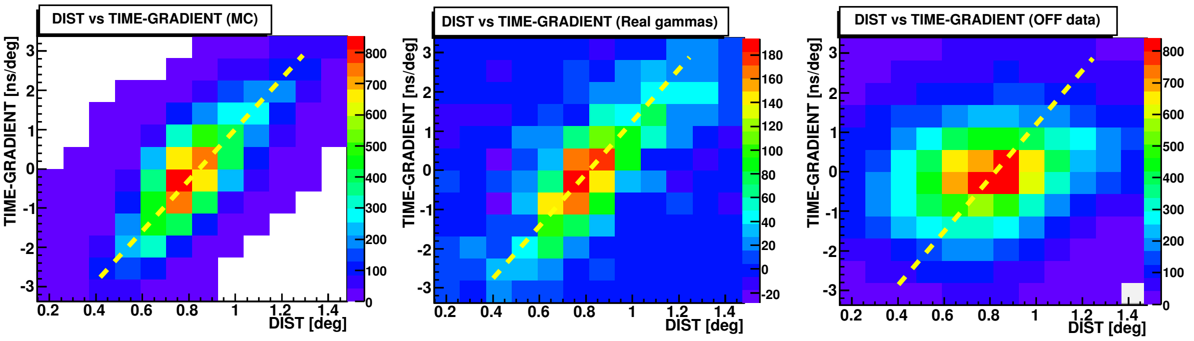

Figure 3.4: Correlation of Time Gradient with Dist for MC γ-rays (left), real γ-rays (center) and background (right) data [A+09e].

The above mentioned correlations of Time Gradient with impact parameter and impact parameter with Dist (for γ-rays) induce a Time Gradient-Dist correlation which improves the separation of hadron- and γ-like events (Fig 3.4). It is especially helpful for single dish experiments (like MAGIC) where the shower direction is not as well determined as in the stereoscopic systems. A further improvement using the Time RMS comes from the fact that the Time RMS distribution for hadron initiated showers usually has a longer tail towards large values.

A detailed study in [A+09e] showed that, in case of MAGIC, the analysis which uses both the Time Image Cleaning and Time Parameters results in an enhancement of about a factor of 1.4 of the flux sensitivity to point like sources.

3.5 Separation of the γ- and hadron-like events using the Random Forest method

In Fig 3.5 selected image parameter distributions are compared for MC (γ events) and background. One can clearly see the differences which are used for the discrimination of the γ- and hadron-like events. The most popular methods among different IACT experiments relies on a set of independent cuts (one for each image parameter) which rarely take into account all of the existing correlations. The cuts are optimized on a strong γ-ray source or on a MC sample.

In the analysis presented in Chapter 6 a different approach, exploiting the concept of a decision tree, is used. The Random Forest (RF) is a flexible multivariable selection method which uses all parameters at once and automatically accounts for the correlations [A+08d].

In the first step the decision trees are trained with shower images of a known nature: γ events from a MC sample and hadron events, usually from data taken with the telescope pointing away from a source (OFF data) or to a very weak source (in raw data hadron events are $\sim 10^4$ times more numerous than the γ ones). The trees are created in the following manner: a subsample of γ and hadron events is randomly chosen from the

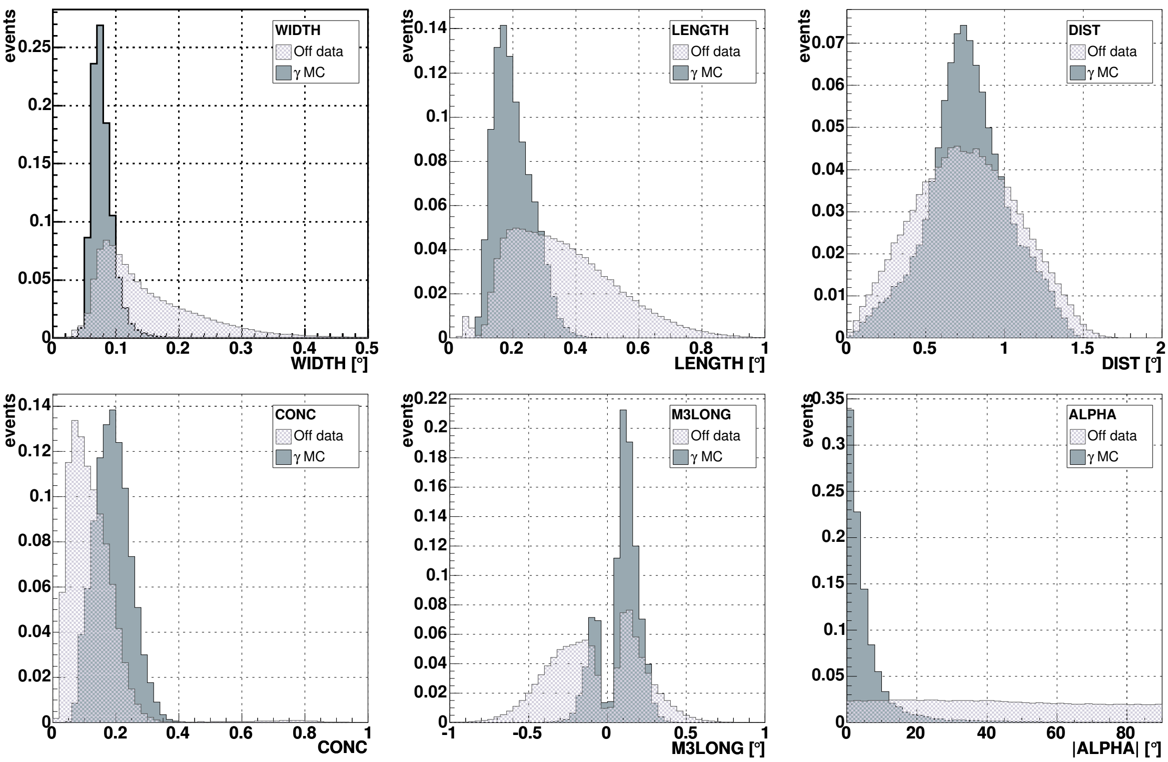

Figure 3.5: Comparison of the Hillas parameter distributions of MC generated γ events and background. Figure from [Wag06].

data provided by the user, then a separation variable (image parameter) is also chosen at random and a cut in this variable is applied. The cut value is optimized such as to minimize the Gini index [Gin21]:

$$Q_{Gini} = 2\left(\frac{N^{survived}_{signal}N^{survived}_{background}}{N^{survived}} + \frac{N^{rejected}_{signal}N^{rejected}_{background}}{N^{rejected}}\right) \tag{3.1}$$

where the $N^{survived}$ denotes the number of all events that survived the cut and $N^{rejected}$ the ones that were rejected, the $N^{survived}_{signal}$ means the number of signal events which survived the cut, the $N^{survived}_{background}$ means the number of background events which survived the cut, the $N^{rejected}_{signal}$ the number of rejected signal events and the $N^{rejected}_{background}$ the number of rejected background events. In this way the event sample is split into two subsamples which in general still contain γ and hadron events. The procedure is repeated iteratively till in the final subsamples (leafs) only one kind of events is left. Each leaf is then labeled with 1, if it contains background events, or 0, if it is composed of signal events. Normally a forest of 100 trees is built during this procedure.

The choice of Hillas parameters used to grow the trees depends mostly on the mode in which the data was taken and on the planned analysis type (see section 3.8). Alpha is always excluded from the RF training. Alpha is very weakly correlated with other parameters and, as mentioned above, serves later as a final cut in the rejection of irreducible background. Also the possible differences of the Size distributions of the starting samples are reduced by choosing the events in a way to make the distributions equal. The individual discriminating power of the parameters is characterized by the Gini index. As illustrated by the Fig 3.6 the Width and Length are the strongest discriminating parameters.

After the creation of the forest (also called "γ-hadron separation matrices") each of the events from the data sample one wants to analyze is passed through all the trees. Depending on the image parameter values of the event it will finally arrive in one of the leafs and be given an according score of 0 or 1. Then all scores are added and divided by the number of trees the event went through. This average number is called Hadronness and is related to the probability of the event not being a γ-ray. Its value lies between 0 and 1, where 0 denotes a γ-ray event and 1 a hadronic one. A cut in Hadronness is equivalent to a cut in the multidimensional space of the image parameters included in the RF training. Figure 3.7 shows the Hadronness distributions for MC γ and background (OFF data) events.

3.6 Estimation of the primary's energy

As mentioned above the Size of the image is directly correlated to the energy of the primary, but additional dependencies on such parameters as the zenith angle of the observation, the impact parameter of the shower and applied image cleaning have to be taken into account when estimating the energy of the primary.

Similarly to the γ-hadron separation, the energy estimation in this thesis was also

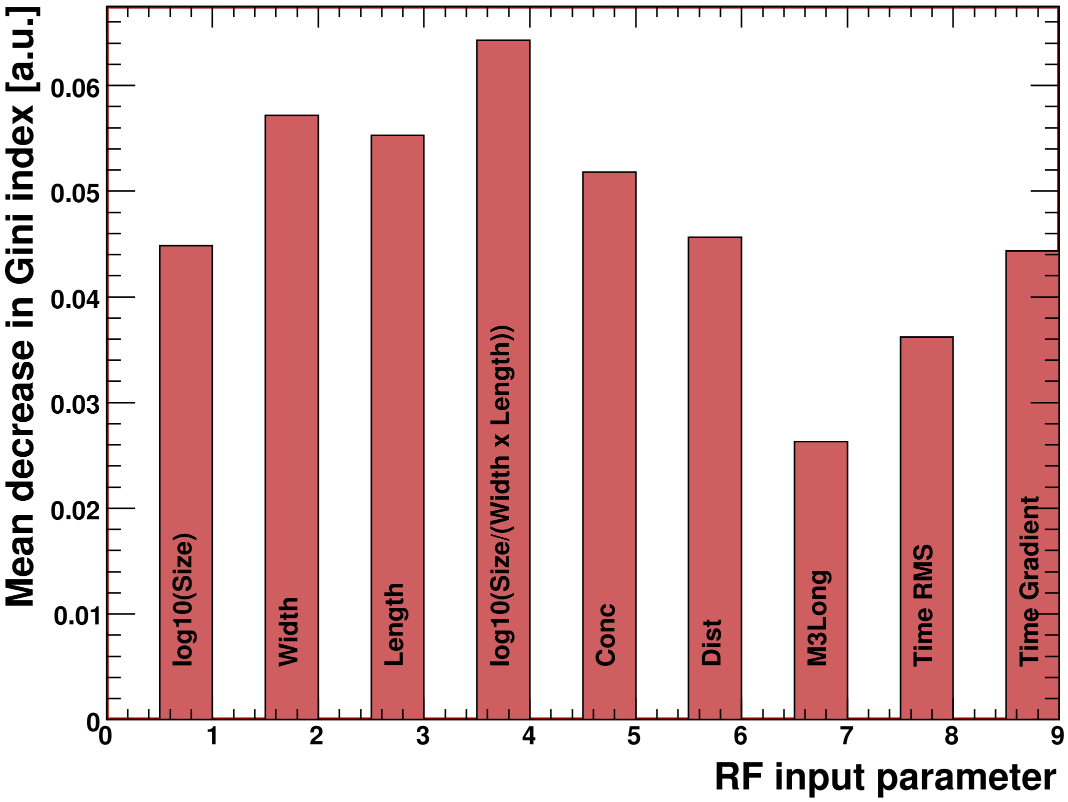

Figure 3.6: Importance of Random Forest input parameters measured by the mean decrease of the Gini index. Figure plotted during the analysis of Mkn 501 data described in section 6.4.2.

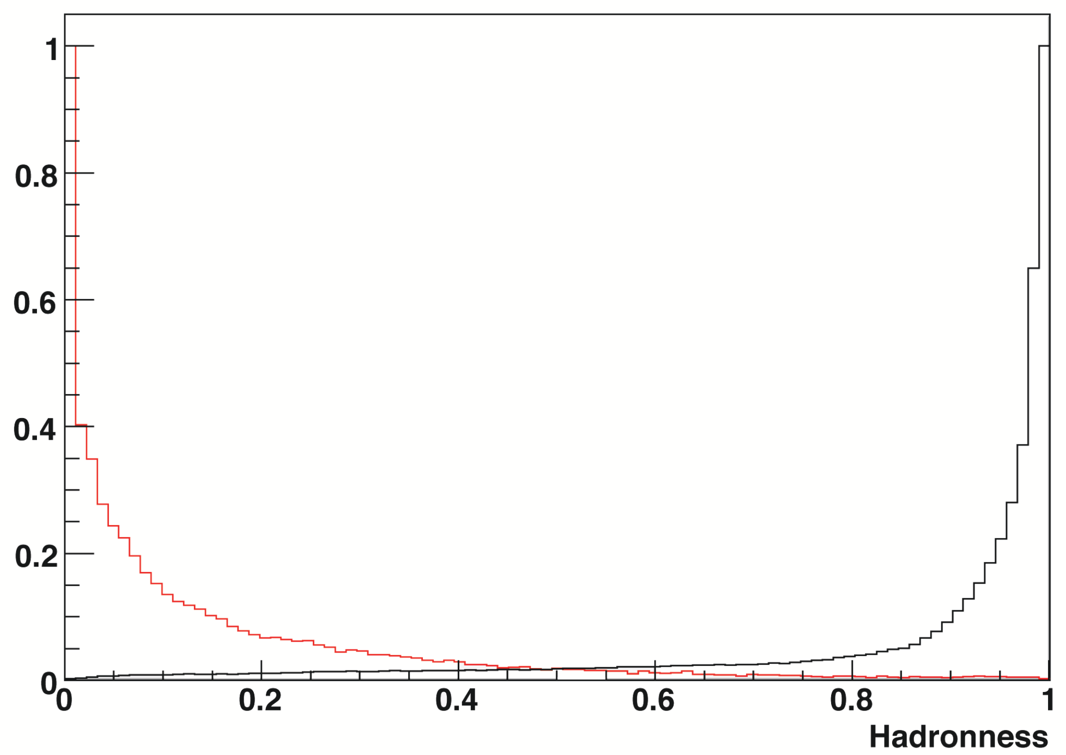

Figure 3.7: Normalized Hadronness distributions for MC generated γ events (red line) and OFF data (black line).

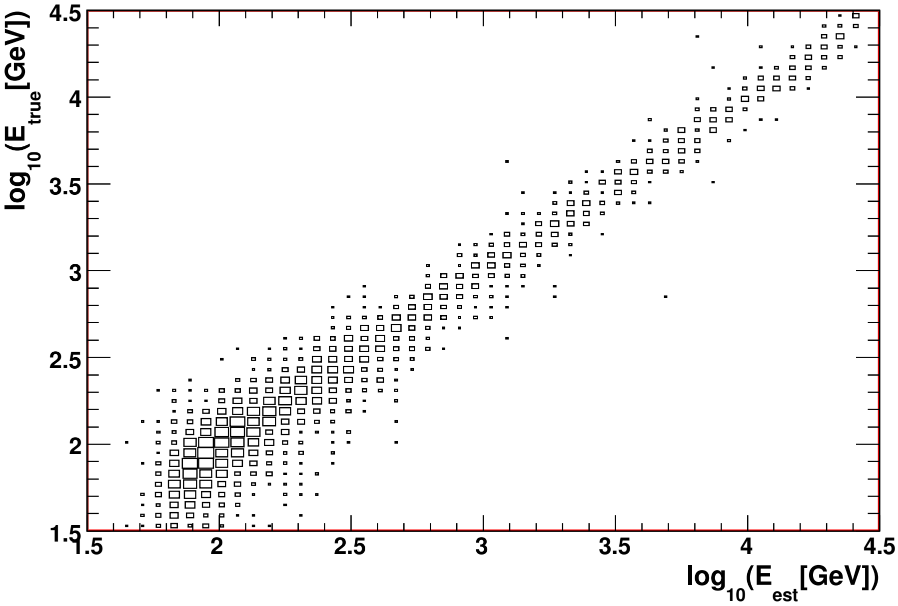

Figure 3.8: Energy migration matrix: the estimated energy as a function of the true (simulated MC) energy.

done using the RF method. A sample of MC γ-ray images, with known primary energy, is used to build a histogram with fine bins in the logarithm of the simulated energy. For each of these bins a a forest is trained that separates γ-rays with energies that fall within the bin from those with energies outside of the bin. The parameters given to the RF for training are: log(Size), Dist, Width, Length, log(Size(Length×Width)), Conc$n$, Leakage and the zenith angle.

After the training for each event from the analyzed data sample a parameter analogous to Hadronness is calculated. It is related to the probability of a given event to fall into a given energy bin, and the event is assigned an energy of the bin into which it falls with the highest probability.

Fig 3.8 shows the estimated energy as a function of the true (simulated MC) energy. The energy resolution obtained by this method does not exceed 25% for E > 100 GeV.

3.7 Arrival direction reconstruction

The arrival direction of the shower is relatively easy to reconstruct if one performs the observations with a telescope array. With a single telescope a more sophisticated geometrical construction has to be used, namely the "Disp method" [L$^+$01]. The Disp parameter is defined as the distance between the reconstructed source position and the center of the gravity of the shower image, measured along its major axis (see Fig.3.9). Fig.3.9 shows also the Dist parameter, which is defined as the distance between the source position in the camera (in Fig.3.9 it is in the camera center) and the center of gravity

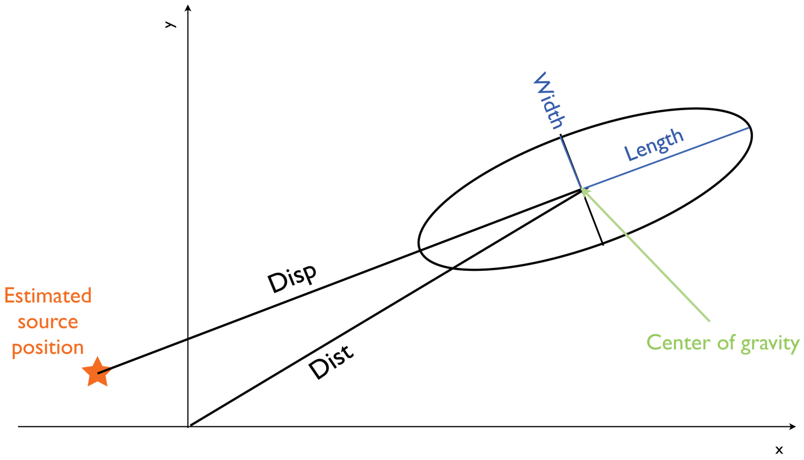

Figure 3.9: The Disp parameter is defined as the distance between the reconstructed source position and the of gravity of the shower image, measured along its major axis.

of the image. The "Disp method" uses the fact that the ellipticity of a shower image depends on the image distance from the source position. For a given primary energy and interaction height, the closer the shower is to the source position the more circular image is observed in the camera. Disp is calculated using the parameters describing the image ellipticity (Width and Lenght) and scales with the Size of the event:

$$\mathrm{Disp} = A(\mathrm{Size}) + B(\mathrm{Size}) \cdot \left(\frac{\mathrm{Width}}{\mathrm{Length} + \eta(\mathrm{Size}) \cdot \mathrm{Leakage}} \right) \tag{3.2}$$

The coefficients A and B are calculated using those MC γ events for which Disp $=$ Dist, i.e. when the reconstructed source position is in the center of the camera. The definition given above does not include the information on which side of the image lies the arrival direction. It has to be obtained from the image asymmetry parameter M3Long.

3.8 Signal significance

When all events from the data sample have their properties reconstructed and the γ/hadron separation cuts are applied N_{ON} γ-ray event candidates are left. This number contains the excess events, but also the irreducible hadronic background. In order to estimate the number of background events a sample of background data, taken under the same conditions as the assumed source data, is analyzed in an identical way and the number of background events N_{OFF} is calculated. The two data sets have to be normalized by their observation times or the number of events in a chosen normalization region. Depending on the observation mode and type of the analysis one chooses there are two possibilities to do the normalization.

Alpha analysis. The isotropic background has a nearly flat distribution in the Alpha parameter, while the showers coming from the source direction should have small Alpha values. According to the MC studies no showers coming from the source direction are expected for $|\mathrm{Alpha}| > 30°$ and the normalization region is defined as $30° < |\mathrm{Alpha}| < 90°$. Since the accuracy of Alpha is mainly constrained by the finite size of the pixels and signal fluctuations, the width of the excess distribution in Alpha depends strongly on the Size cut chosen for the analysis, and is broader for smaller Size values.

θ^2 analysis. The θ^2 parameter is defined as the quadratic angular distance between the estimated shower direction and the direction of the source. It is calculated using the Disp parameter defined in section 3.7 . Usually the $0.1^{\circ 2} < \theta^2 < 0.2^{\circ 2}$ region is chosen for normalization.

In the RF training the source independent parameters (i.e. those describing the image without any assumption on the source position, e.g. Size, Width and Length) are usually used for the θ^2 analysis, while the source dependent parameters (most importantly Dist and Time Gradient) for the Alpha analysis. It is due to the fact that the θ^2 cut constrains two spatial directions in the camera (along and perpendicular to the main axis of the image), while Alpha constrains only one (perpendicular). The usage of source dependent parameters allows for a constraint in the second dimension. On the other hand if one decides to use source dependent parameters to calculate the Hadronness, one has to take into account that for the events with small Hadronness the estimated Disp value is very close to the real Dist value. This results in a strong correlation between θ^2 and Hadronness and a broad peak in the background distribution around $0^{\circ 2}$. For faint sources it can mimic the true signal. For a source independent Hadronness this effect does not appear. The Alpha analysis is usually associated with data taken in the ON/OFF mode and the θ^2 analysis with data taken in wobble mode.

The number of excess events is calculated according to

$$N_{EXC} = N_{ON} - \eta N_{OFF}, \tag{3.3}$$

where η is the normalization factor. The method proposed by Li and Ma in [LM83] is used to calculated the significance S of the excess,

$$S = \sqrt{2}\sqrt{N_{ON} \cdot \ln\left(\frac{(1-\eta)N_{ON}}{\eta(N_{ON}+N_{OFF})}\right) + N_{OFF} \cdot \ln\left(\frac{(1+\eta)N_{OFF}}{N_{ON}+N_{OFF}}\right)}. \tag{3.4}$$

3.9 Spectrum and light curve determination

In order to properly define the spectrum and flux one has to first introduce the definition of the effective area A_{eff} and the effective time t_{eff}.

3.9.1 Effective area

The effective area of the detector A_{eff} (Fig. 3.10) is estimated from MC simulation in a similar way as described in section 2.3.4. In case of a γ-ray telescope it is defined as the

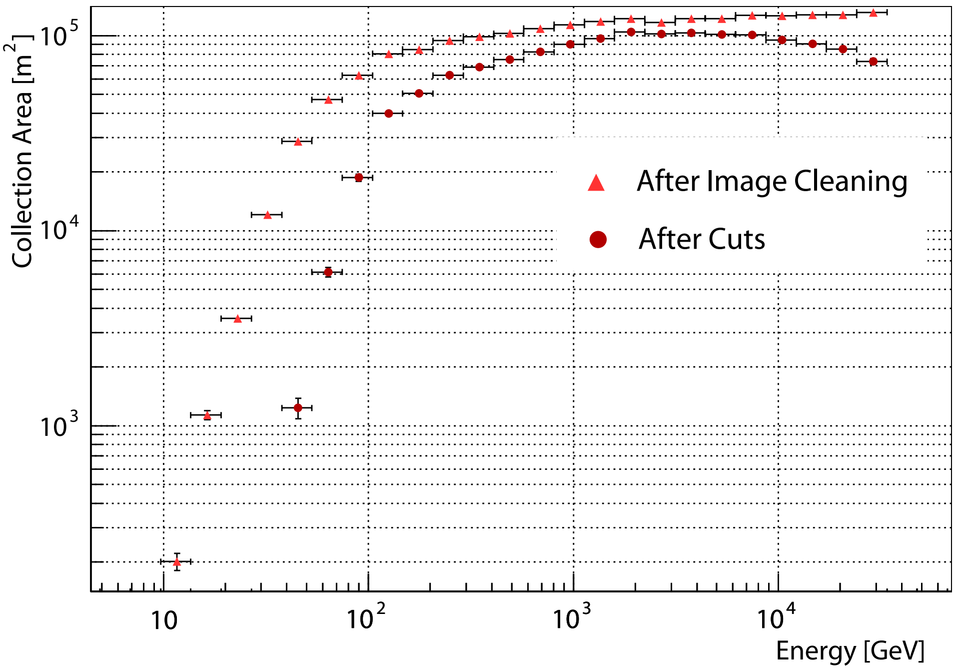

Figure 3.10: MAGIC effective area as a function of the energy after image cleaning (orange triangles) and after cuts (red circles) for low zenith angle observations ($< 20°$) [A$^+$08e].

area in which the showers can be observed folded with the efficiency of the detector ϵ:

$$A_{eff}(E,\theta) = \int_0^{2\pi}\int_0^{\infty} \epsilon(E,b,\theta,\phi) b db d\phi. \tag{3.5}$$

The detection efficiency is calculated after all cuts and depends on the energy of the primary E, the impact parameter b and the azimuth ϕ and zenith θ observation angles (which depend on time). Typically the effective area of an IACT is constant for θ<30° and starts to decrease for higher zenith angles. This effect must be taken into account when analyzing data sets with large zenith angle spread.

3.9.2 Effective time

In order to estimate the effective time t_{eff} (i.e. the dead time corrected live time) a distribution of the time differences between the consecutive (measured) events is constructed and then fitted by an exponential function:

$$\frac{dn}{dt} = n_0 \cdot R \cdot e^{-Rt}, \tag{3.6}$$

where n is the number of observed events and R is the event rate. Then the t_{eff} is calculated as:

$$t_{eff} = \frac{n}{R}. \tag{3.7}$$

The differential photon flux (differential photon energy spectrum) is defined as the number of photons dN_γ (the number of excess events), per energy bin dE, effective area dA_{eff} and life time dt_{eff}:

$$\frac{dF}{dE} = \frac{dN_\gamma}{dEdA_{eff}dt_{eff}} \tag{3.8}$$

Integrating the differential flux above an energy threshold E_{th} one obtains an integrated photon flux. A light curve is defined as an evolution of the integral flux in time bins. The integrated flux observed from the Crab Nebula, the standard candle of the γ-ray astronomy, was chosen in this work as the unit for the observed integrated fluxes (Crab).

3.9.3 Unfolding of the energy spectrum

The spectra are determined in bins of estimated energy. The estimated energy is derived from the image parameters as described in section 3.6 . Like all experiments MAGIC has to cope with finite energy resolution and a bias in the energy estimation. The low energy showers are more difficult to reconstruct and, especially near the trigger threshold, the event energy is on average overestimated. On the other end of the spectrum the high energy events are very sparse and a difference of one or two in an energy bin can change the spectral shape quite significantly. The estimated energy E_{est} distribution is therefore a convolution of the true energy E_{true} distribution and a migration matrix $M_{i,j}$ which describes the effect of the finite detector resolution and the bias on the true energy spectra:

$$N(E^i_{est}) = \sum_j M_{i,j} N(E^j_{true}) \tag{3.9}$$

In order to calculate the true energy spectra one has to invert this relation, by an unfolding. More detail on the unfolding procedures used in the MAGIC analysis can be found in [A$^+$07i].

3.10 Systematic errors

Apart from statistical errors the analysis and final results (flux, energy spectrum) are affected by systematic errors. Here only the most important ones will be described, a full account of the systematic effects is given in [A$^+$08e].

Photon detection efficiency

The so-called photon detection efficiency (PDE), i.e. the uncertainty in the conversion from real photons to photoelectron units, is the dominant systematic error. It is dominated by the gain variations of the first PMT dynode, but many other small effects like the PMT geometry, angular effects on the PMT surface, QE spread etc. also contribute. The PDE can be estimated using a calibrated blue or UV light source which uniformly illuminates the camera, although this procedure unavoidably introduces another small systematic error. Also the F-factor method [RM97], used to determine the number of detected photoelectrons, adds another uncertainty. Overall the systematic error on PDE was estimated to be ∼10-12%.

Mirror reflectivity and other optical losses

The nominal mirror reflectivity of 85% and other optical properties of the system (e.g. the point spread function) change with time. This affects mainly the estimation of the energy and the numbers given in the brackets describe the uncertainty on the energy scale resulting from a given effect. The mirror surface ages (7%), the AMC control system needs regular updates (3%), the temperature, humidity and dust change the mirror reflectivity and the plexiglass camera cover transparency on daily basis (2%). The mirror reflectivity and the PSF fluctuations are monitored regularly and the necessary changes are introduced into the detector simulations.

Atmospheric conditions and the atmospheric model

The atmospheric model used in MC simulations uses the U.S. standard atmosphere. It does not account for the daily changes of pressure, temperature, humidity and presence of high clouds or calima which can lead to an underestimation of the measured γ-ray flux. The systematic uncertainty on the measured flux due to the atmospheric effects described above is 3%. The photon scattering due to the Mie effect introduces an uncertainty on the energy scale of 5%.

Analysis chain

The overall systematic error on the measured flux, resulting from different cuts and methods used by different analyzes ranges from 5% to 30% and is strongly energy dependent. At low energies it is mainly due to bad reconstruction and event losses, in the high energy range the analysis is more affected by low statistics.

In summary, if one takes into account all of the systematic effects as given in [A^{+}08e], the systematic uncertainty on the calculated flux normalization is of the order of 11%, (this does not include the energy scale error of ∼16%) and the systematic error on the spectral index is ±0.2 .

4 Search for neutrino flares from predefined directions

4.1 Introduction

Observations of some candidate neutrino sources indicate that their electromagnetic emission is very variable and often shows a flare-like behavior. According to several models one can expect that the neutrino emission from these sources have a similar character [AD03] [M+03]. Time integrated analyses [A+07b] [B+07] [F+07] are not always sensitive to this behavior: if signal events are emitted in flares, the integrated background is higher due to the typically longer exposures (see Fig. 4.1). Therefore a dedicated time variable analysis was developed with the goal of improving the discovery chance.

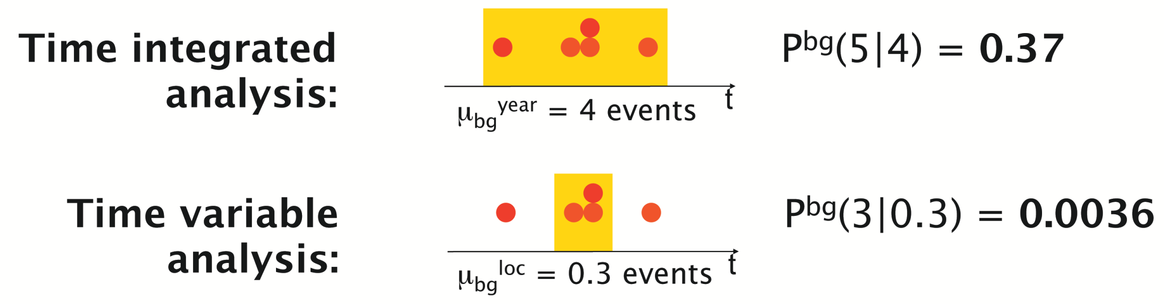

Figure 4.1: A simple comparison of a time integrated a time variable analysis. Time integrated analysis: $m = 5$ neutrinos are observed from a source during the whole year, with a typical background of $\mu_{bg}^{year} = 4$ events the Poisson probability of observing m events over a μ_{bg}^{year} background equals: $P^{bg}(m|\mu_{bg}^{year}) = 0.37$. Time variable analysis found a flare of $m = 3$ over a background of $\mu_{bg}^{loc} = 0.3$, the $P^{bg}(m|\mu_{bg}^{loc}) = 0.0036$, which is a much more significant result.

This analysis is discovery oriented, based on the experience gained during the previous time-variable analysis [A+05a]. The newly developed algorithm (time-clustering algorithm) looks for structures (clusters) in the time distribution of the neutrino events from certain directions. Since no a priori assumption on the time structure of the potential signal is made this approach is model independent, but due to testing all possible combinations of the arrival times of neutrino events it is affected by a high trial factor.

A critical point for this type of analysis is the reliability of the background estimation over short time scales. So far the expected background was estimated from the event density, as a function of the declination (similar to the ON/OFF-source approach of γ-ray astronomy), integrated over long time (e.g. a year or more) [A+07b]. This method however fails when applied to short time scales due to the limited event statistics. A good solution to this problem is a parameterization of the background which reduces its statistical uncertainty. Additionally, to take into account the asymmetrical shape of the detector, a correction for azimuth non-uniformity is applied depending on each specific cluster time window. As shown in the section 4.3 for short time scales the new method has up to 10% smaller statistical errors, while for longer time periods it is in a very good agreement with the old method.

In order to investigate the discovery potential of the time-clustering algorithm a series of MC simulations was performed, simulating variable neutrino point-sources of different signal strength and duration - see section 4.6.

In what follows the principle of this analysis and its performance in comparison to previous analyses is discussed. The results obtained on data collected with AMANDA-II in 2004 to 2006 are given in section 4.6.5.

As explained in section 1.7.3 according to hadronic models neutrino and γ-ray emission from cosmic sources are closely connected. Two kinds of correlation studies can be performed: an "off-line" search for neutrino events in coincidence with γ-ray flares using separately collected data and an "on-line" approach where the simultaneous neutrino and γ-ray time coverage is secured by a neutrino trigger (Neutrino Target of Opportunity - NToO). In this work only the first approach was tested, but since the new background estimation method was also used in the analysis of the data from the NToO program with AMANDA-II and MAGIC this program is also briefly discussed in section 4.7.

The analysis presented here is realized in two steps. In order to prevent a posteriori observations of coincidences with γ-ray flares the neutrino event sample is first tested for a coincident enhanced γ-ray emission for those sources and periods when the γ-ray data is available. The outcome of this test is declared positive if an excess of neutrino events of significance equal or higher than $5\,\sigma$ is found during the chosen periods. If in this first step none of the observations shows a significance of $5\,\sigma$ or higher (or if there are not enough γ-ray data for a coincidence study) the time-clustering algorithm is applied to the whole analysis period for a set of selected sources. Three types of sources were chosen for this analysis: blazars, XRBs and one radio loud galaxy (see Tab. 4.2).

4.2 The neutrino data sample

The input data samples for this analysis for 2004 and 2005 were taken from [A+07b] and [B+07] respectively. For 2006 the results of the AMANDA on-line event reconstruction and filtering chain, which was implemented following the scheme reported in [A+07b], were used as the final neutrino sample. After excluding periods of detector calibration with an artificial light source (so-called "flasher runs") and selecting high quality data we used 247.5 / 199.9 / 239.5 effective days of data taking for the year 2004 / 2005 / 2006 respectively.

4.3 Background estimation

Two methods of background estimation are presented and compared here: a previously used ON/OFF-source method: "counting method", and the one developed for this analysis: "fit + azimuth method", which is more reliable for short time scales (as shown in sections 4.3.3 and 4.6).

4.3.1 Counting method

In the first method, the arrival times of possible background events from the whole northern sky, from the whole period of time in which the analyzed data were taken, are collected. In the first step the number of events N_t falling into the analyzed time interval is calculated and normalized to the number of all events N_{All} from the whole northern sky, from the whole period of time in which the analyzed data were taken. In the second step the number of events falling into a declination band defined by the angular search bin N_{band} is calculated and normalized to the ratio of the bin to the band area A_{bin}/A_{band}. In the end the expected number of background events μ_{bg} is calculated as:

$$\mu_{bg} = \frac{N_t}{N_{All}} \frac{N_{band} A_{bin}}{A_{band}}. \tag{4.1}$$

This method is simple and fast, however as shown in section 4.6.4 due to the low statistics it fails to properly describe the background in a case of short time scales (less then 10 days). One can expect that a neutrino flare can happen over a very short time period (few days or even less than one day) and have a low multiplicity. In this case, because of the low statistics and background fluctuations, N_t is in the order of a few events and μ_{bg} often has a very large uncertainty. As a consequence the significance of the flare is also affected by a large uncertainty.

4.3.2 Fit+azimuth method

A different approach to estimate the background was developed for this work. It will be explained for the example of the data from the year 2004.

Detector up-time and the Very Low Frequency (VLF) veto

First the detector's "up-time" (i.e. the dead time corrected live time) development is tabularised. This takes into account the inefficiency periods and data gaps after the data quality selection.

The detector's up-time was calculated using the trigger level data (Fig 4.2 upper panel). An additional correction for the operation of the VLF antenna was applied. The VLF antenna started operating in the end of 2003 and continued trough the whole 2004. It induced a very low frequency wave component to the AMANDA-II data and a veto had to be implemented. The regular pattern of the VLF veto is clearly visible in the up-time of the detector: every 15 min there's a 1 min break in the operation of the detector. It gives an overall 7% decrease of the effective up-time per day (Fig 4.2 lower panel).

Fit to the event rate

Once corrected for the detector exposure one can calculate the expected neutrino rate from the whole northern sky[1] by fitting the event rate versus time (Fig 4.3) - this way we obtain the average number of events per day for each year (μ_{bg}^{year}): 4.13±0.13 for 2004, 3.7±0.13 for 2005 and 4.30±0.13 for 2006. For each sky angular bin the number of expected background events μ_{bg}^{loc} in the whole data period (i.e year 2004, 2005 or 2006) is then calculated as:

$$\mu_{bg}^{loc} = \mu_{bg}^{year} \frac{N_{band} A_{bin}}{N_{All} A_{band}}, \tag{4.2}$$

where N_{band} is the number of events in the declination band of the hight defined by the bin size, N_{All} is the number of all events in the sample for each year, A_{bin} is the area of the angular search bin, and A_{band} is the area of the declination band defined by the size of the angular search bin. The ratio N_{band}/N_{All} allows to account for the different background density at different declinations.

Azimuth angle non-uniformities

The next problem to consider is the non-uniformity in the azimuth angle Φ introduced by the asymmetry of the detector. For flares that last a non-integer number of days the effect of the asymmetry of the detector does not average out. This effect (azimuth efficiency) is clearly visible in Fig 4.4. If the detector was fully symmetrical the distribution would be flat. There exists also another, smaller effect due to the differences between the solar and sidereal time. The solar (24h) and sidereal day (23h 56') are not equal: during one day the blind regions of the detector seen by the source shifts 4 minutes (1 degree) forward with the respect to the solar time.

Till now all of the calculations were done assuming that the acceptance of the detector is uniform in Φ (equation 4.2). In fact, this assumption is valid for the integrated time analysis, but for short time periods the real dependence of the efficiency of the detector on Φ should be taken into account. As one can see in Fig 4.4 the non-uniformities in the azimuth angle have a big influence on the number of the background events (±40%).

---

[1] No dependency of the results on different choices in the binning of the event rates or angular regions of the sky (e.g. estimating the expected rate for different declination regions) was observed.

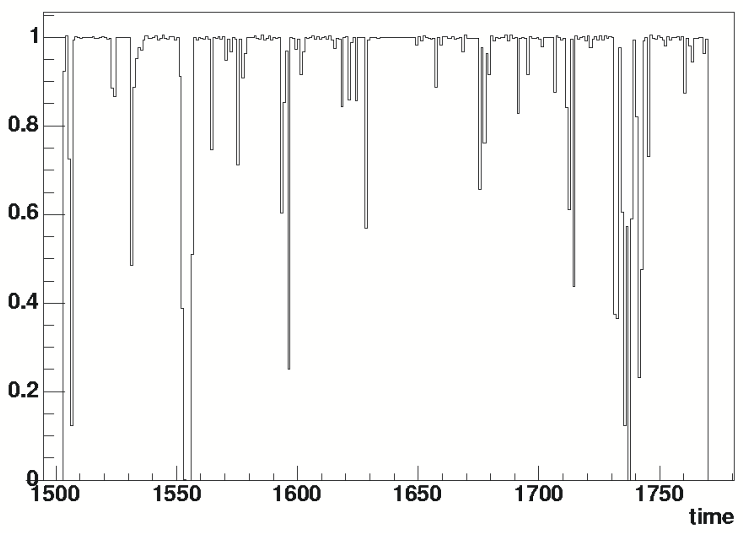

(a)

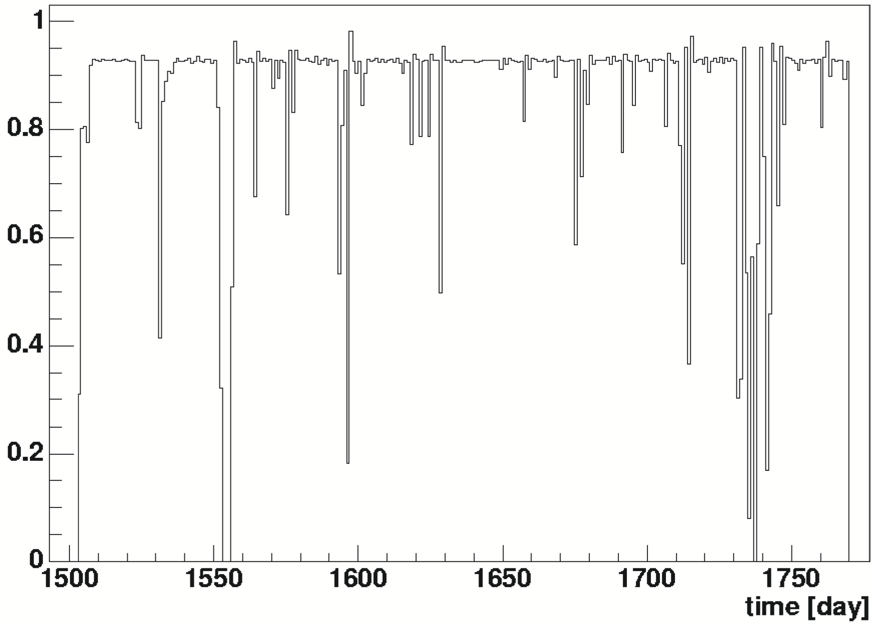

(b)

Figure 4.2: (a) Detector up-time in 1 day bins in 2004. (b) VLF corrected up-time in 1 day bins in 2004. X-axis: time in 1 day bins (day 0 = 01.01.2000). Y-axis: up-time per 1 day.

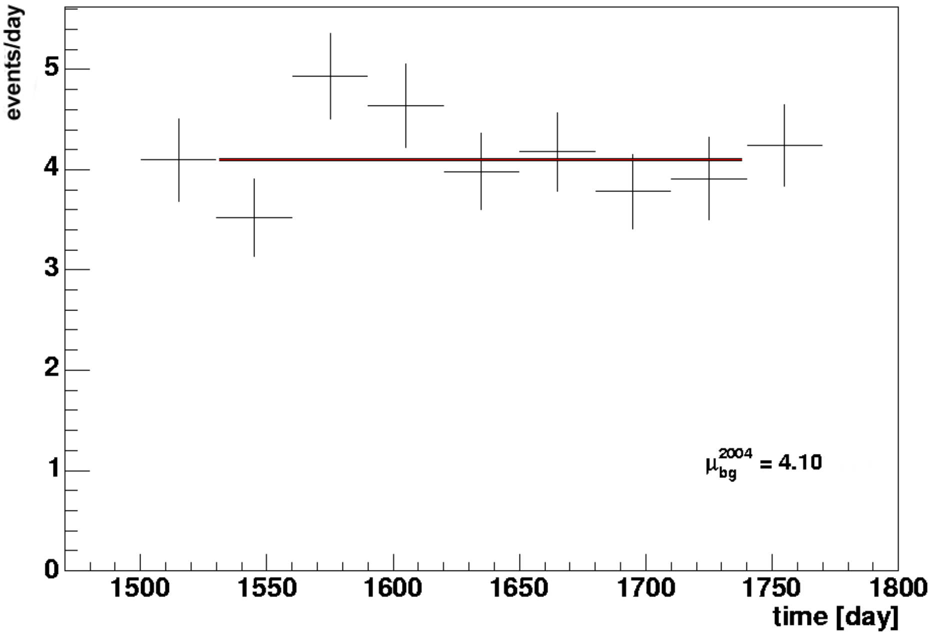

Figure 4.3: The up-time corrected background (i.e. background divided by the up-time of the detector) in 30 day bins, for the year 2004. The X-axis shows the time in days (day 0 = 01.01.2000), the Y-axis the number of events per day. A flat function is fitted (solid line), its value μ_{bg}^{2004} (mean background per day for 2004) is printed on the picture.

Background calculation

The value estimated in equation (4.2) is corrected for the acceptance of the detector in azimuth, which needs to be calculated for each individual time cluster. This correction is given by the integral of the azimuth distribution over the time period of a cluster. The up-time of the detector is also taken into acount.

The number of expected background events for each individual cluster μ_{bg}^{loc}, is then given by:

$$\mu_{bg}^{loc} = I_{UT} I_{\Phi} \frac{N_{band} A_{bin}}{A_{band}}. \tag{4.3}$$

In this value the correction for the up-time of the detector I_{UT} and the correction for the acceptance of the detector in azimuth I_{Φ} are taken into account.

The overall error in the background estimation is a combination of a statistical uncertainty, the error of the fit and the uncertainty introduced by the azimuth corrections.

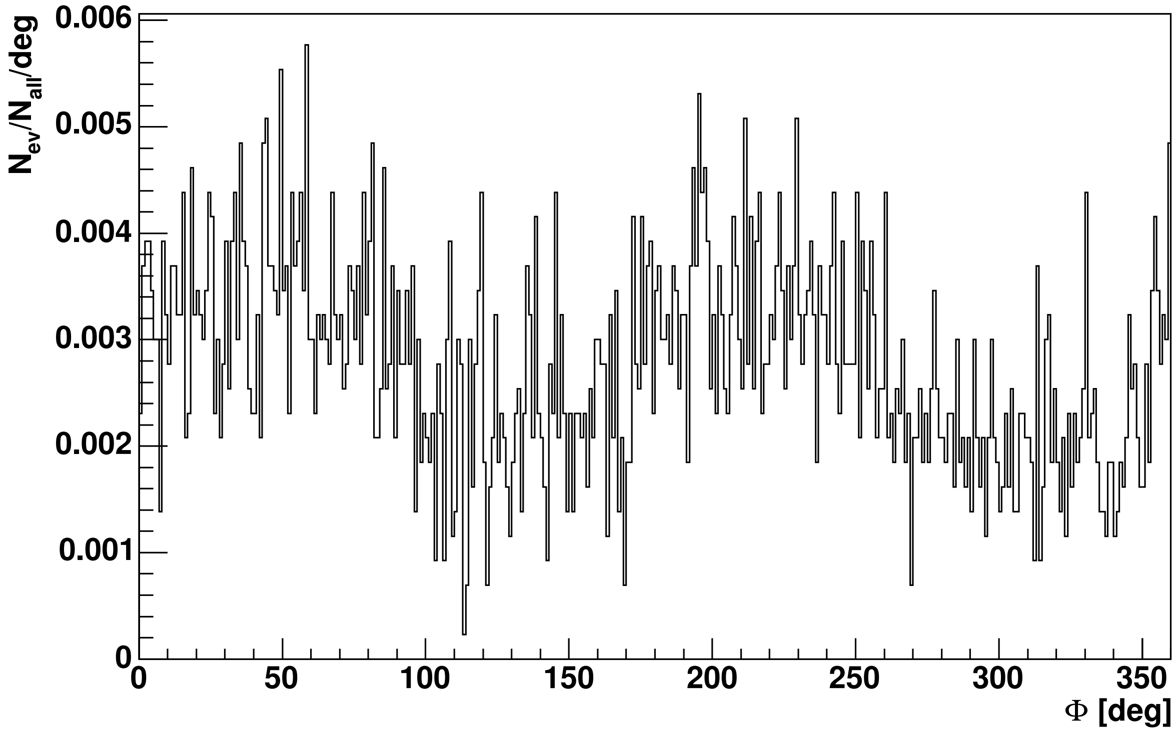

Figure 4.4: Normalized Φ distribution of the final sample of neutrino candidate events from the AMANDA-II data sample reported in [A+07b].

4.3.3 Comparison of the background estimation methods

In order to compare the "counting" and the "fit+azimuth" methods a large number of MC simulations were performed. For every cluster in each simulated experiment the μ_{bg}^{loc} values according to both methods were calculated and then compared (Fig 4.5 black dots). The red squares with error bars refer to a few characteristic points (time periods) chosen to show the general trend of the uncertainties of each method[2]. As one can see from the plots and the accompanying tables the agreement of the two methods is very good. On the other hand, calculations for short time scales show that the "fit+azimuth" method have smaller errors and is more reliable. For example for $\Delta t = 3$ days, an error of 20% was achieved in this analysis compared to 30% in previous works.

For more arguments in favor of the fit+azimuth method see section 4.6.

---

[2] Note, that the calculated points are correlated since they correspond to different combinations of multiplets out of a randomized sample of real event times. Therefore the errors are much larger than the width of the band (for example - there is only one point μ_{bg}^{loc} for the whole year period, while for shorter time scale one can simulate more independent clusters).

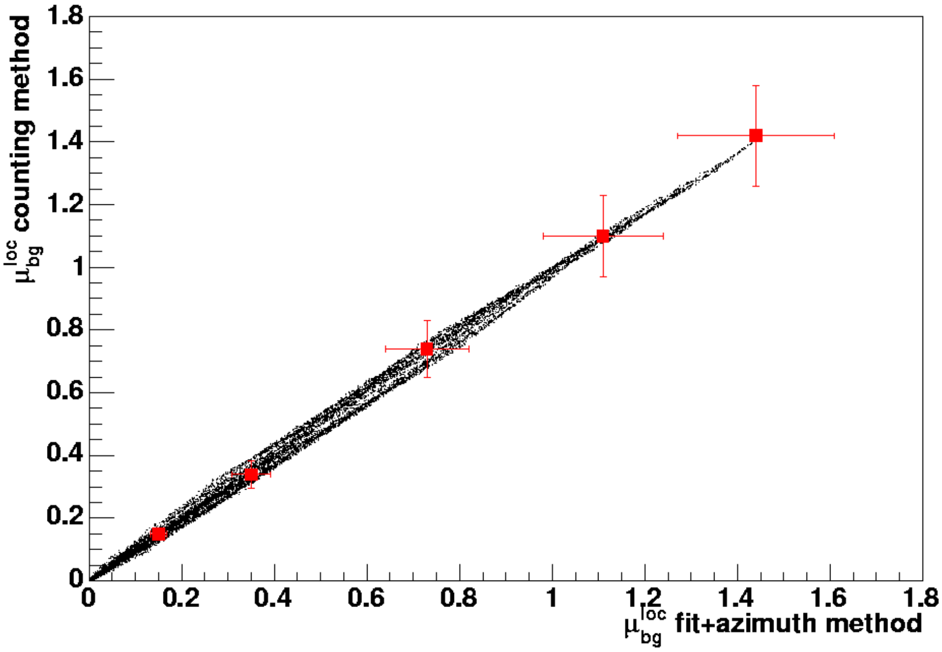

Figure 4.5: Comparison of the "counting" and "fit+azimuth" methods for 2004. The X-axis shows the μ_{bg}^{loc} calculated according to the "fit+azimuth" method, the Y-axis the μ_{bg}^{loc} calculated according to the "counting" method. Each black point denote the values of the μ_{bg}^{loc}, calculated with both methods, for simulated clusters. The red points refer to the Table 4.1.

4.4 Search for neutrino events in coincidence with gamma-ray flares

Observations of strong variability in the high energy (TeV) γ-ray emission exist for various TeV neutrino candidate sources. However, often there is no long coverage of their flux and also a very limited knowledge exists on the frequency of γ-ray flares, as well as on their eventual time correlation with neutrino flares. Nevertheless, a search for coincidences between high energy neutrinos and γ-rays can possibly increase the chance of discovery of a neutrino point source.

A test for correlation of neutrino events with a high state of γ-ray emission was performed for a sub-sample of objects for which γ-ray data for the years 2004 to 2006 are published (Table 4.2). For each selected source a flux threshold was established to select the periods of interest. The number of neutrino events observed, n_{obs}, in the sum of the chosen periods was compared to the expected background, μ_{bg}, and the

Table 4.1: Comparison of the μ_{bg}^{loc} calculated according to the "counting" and "fit+azimuth" methods for 2004 data, for different flare duration times Δt

Δt [days]	μ_{bg}^{loc} counting	μ_{bg}^{loc} fit+azimuth
3	0.022±0.006	0.017±0.002
7	0.044±0.009	0.041±0.005
10	0.068±0.013	0.058±0.007
27	0.15± 0.02	0.15±0.02
67	0.34±0.05	0.35±0.04
134	0.74±0.09	0.73±0.09
201	1.1±0.1	1.1±0.1
309	1.4±0.2	1.4±0.2

significance was calculated. For most of the sources the collected γ-ray data was enough to establish the flux threshold using the method proposed in section 4.4.1. In the case of Cygnus X-1 only one day of significant measurement was available so the sensitivity of the experiment (MAGIC) was considered as the flux threshold.

An example of a long term VHE γ-ray light curve of one of the objects (Mrk 421) with the chosen threshold (flux at the level of 1.0 Crab Nebula flux) is presented in the Fig 4.6. More information on collection and studies of the light curves can be found in Chapter 5.

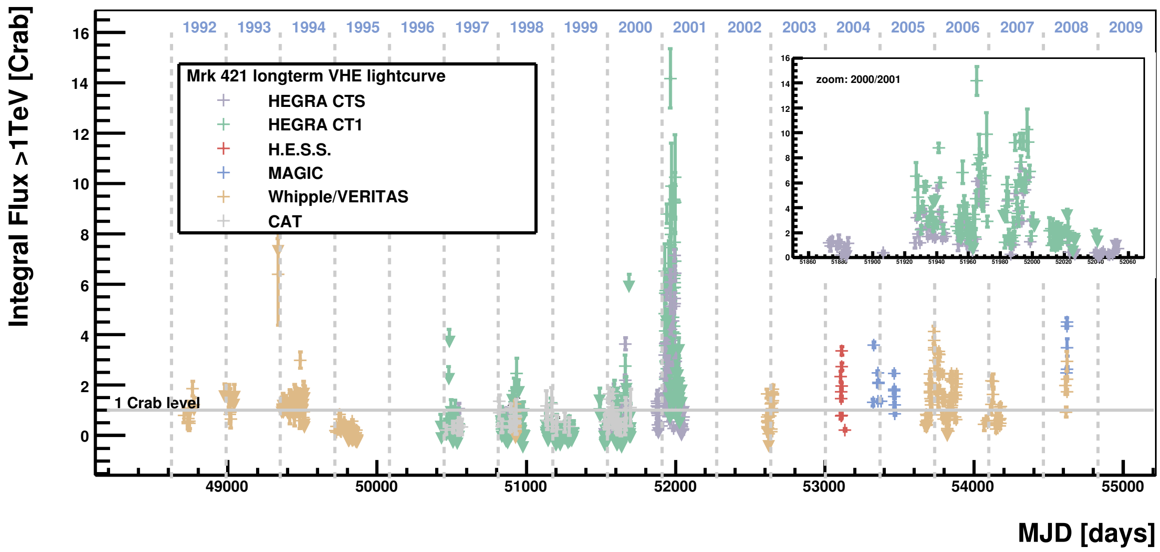

Figure 4.6: Longterm light curve of Mrk 421 spanning 17 years of observations performed by different IACT telescopes. For more details see Chapter 5 or [T$^+$07b].

4.4.1 Defining the gamma-ray flux high state threshold

The threshold for the γ-ray flux was chosen based on the analysis of combined light curves presented in Chapter 5 and [T$^+$07b]. This analysis was done with the assumption that the γ-ray and neutrino emission are strictly correlated in time and amplitude. Therefore, if one looks for the periods of time with the best ratio of signal to square root of background $S/\sqrt{B}$ for the observed γ-ray emission one can expect that those periods of time will have the best $S/\sqrt{B}$ for the neutrino emission too.

For each source the integral γ-ray flux (S) above several thresholds was considered. The threshold value was optimized for the best $S/\sqrt{B}$, where B is the total time span of the periods above threshold. Periods of measurement gaps longer than one week as well as periods with only upper limits on the flux were excluded, in order to avoid making any unjustified assumptions or extrapolations of the flux values on periods about which there is no information.

Two approaches to optimize the high state flux threshold were used. They are presented here on the example of Mkn 421. In the first approach the signal is defined as the sum of the integral fluxes, measured in one day bins above a certain level and the background, as the time in which the measurements took place (Fig 4.7 (a)).

In the second approach (Fig 4.7 (b)) the signal is defined as an average of the integral fluxes measured above a certain level. That means their sum is divided by the number of points above threshold and multiplied by the time in which the measurement took place. The background is defined as in the first approach.

Both methods give a stable maximum of the $S/\sqrt{B}$ ratio around the flux level of 1.0 Crab Nebula flux and therefore this value is defined as the flux threshold, above which Mkn 421 is consider as being in a state of enhanced emission.

The considerably high values of the $S/\sqrt{B}$ below 0.5 Crab can be explained by the fact that the observations are biased towards higher flux values due to external triggers. The second reason is that periods with no measurements longer than one week were excluded from the calculations of the background.

Note that this simplified method of defining the γ-ray flux high-state threshold gave almost identical results as a more sophisticated one presented in the next chapter. For Mrk 421 the obtained values are 1.0 Crab and 0.9 Crab and for Mrk 501 in both cases the threshold value is 1.5 Crab.

4.4.2 Results

The search for coincidence of neutrinos with γ-ray flares was performed on a sub-sample of 7 sources, for which the collected γ-ray data allowed to define states of enhanced emission.

For Mkn 501 one event was observed on a background of 0.13 ± 0.02 events in 2005. For the rest of the sources no events were observed in correlation with high state of γ-ray flux. The results of the search for neutrino events in coincidence with γ-ray flares are reported in Table 4.3.

Since no significant excess of neutrino signal correlated with a γ-ray flare was found the time-clustering analysis was performed on all selected sources. If such a correlation is found the probability of a random coincidence of the γ-ray flares with atmospheric neutrinos must be calculated. Without the full knowledge about the probabilities of finding the selected sources in a γ-ray flux state above a certain threshold a proper calculation of a significance of a neutrino-γ-ray flare correlation is impossible. This problem is discussed in the following chapter.

4.5 Time-clustering algorithm

For each preselected direction all combinations (clusters) of the arrival times of events within a certain angular bin are constructed. For each cluster its multiplicity (m) is compared to the expected background (μ_{bg}^{loc}) and the significance of the cluster (S_{bg}) is calculated. The cluster with the highest significance (S_{bg}^{best}) is chosen as the "best". The overall probability (P, trial factor corrected) to observe a cluster of significance S_{bg}^{best} or higher is calculated based on a series of Monte Carlo (MC) experiments (Fig 4.8).

The algorithm works according to the following scheme:

1. An angular search bin around the investigated source is defined.

2. Two samples of the arrival times of the neutrino events are collected:
   a) neutrinos registered in the search bin - called "on-source";
   b) neutrinos registered in the declination band which contains the search bin (the events in the search bin are included) - called "background".

3. The mean number of background events μ_{bg} for the on-source region, for the complete data set (integrated in time), is calculated:

$$\mu_{bg} = N_{band} \frac{A_{bin}}{A_{band}}, \tag{4.4}$$

   where: N_{band} is the number of background events in the declination band, A_{bin} the area of the search bin, A_{band} the area of the declination band.

4. A search for interesting time clusters in the on-source sample is performed.
   a) The events are grouped into ordered clusters starting from the first one and subsequently adding the second one (a doublet), then the third one (a triplet), etc. Then the procedure is repeated starting from the second event, then from the third, etc., so all of the possible combinations are created.
   b) For each cluster a "local" background μ_{bg}^{loc} is calculated - see the description of the background estimation in section 4.3.2.
   c) For each cluster of multiplicity m the probability for the events in the cluster to be background events is calculated:

$$P_{bg}(m|\mu_{bg}^{loc}) = \sum_{j=m-1}^{\infty} \frac{e^{-\mu_{bg}^{loc}} \cdot (\mu_{bg}^{loc})^j}{j!}, \tag{4.5}$$

the number of events in the cluster is reduced by 1 in order to reduce the bias coming from the fact that $P_{bg}(m|\mu_{bg}^{loc})$ is only calculated when a signal candidate is detected.
d) The significance of this observation is defined as:

$$S_{bg} = -\log_{10}(P_{bg}). \tag{4.6}$$

e) The "best cluster" is defined as the one with the highest S_{bg}: S_{bg}^{best}.

5. In the last step the probability for the "best cluster" to be compatible with the background hypothesis is estimated.
   a) A MC sample of N background events is generated randomly from a Poisson distribution with a mean μ_{bg} - see section 4.6.1.
   b) Then the procedure described in point 4. is applied to them.
   c) Points a) & b) are repeated N_{iter} times (e.g. 10000) and the number of samples with a cluster which $S_{bg} \geq S_{bg}^{best}$ is calculated (N_{best}).
   d) The probability P for the "best cluster" to be compatible with the background hypothesis is defined as:

$$P = \frac{N_{best}}{N_{iter}}. \tag{4.7}$$

The main difference between this analysis and what was presented in [A$^+$05a] is that in this work no assumption is made on the duration of signal flares and different time scales are simultaneously tested. Moreover, a correct background estimation over short time scales was developed, in order to properly calculate the significance of the potential signal and its compatibility with the background hypothesis.

4.6 Algorithm performance study

In this part some details about the algorithm performance are presented. The neutrino flare detection chance was investigated, depending on the strength and duration of the signal generated using a toy MC, described below. This study was performed for the cases of fixed [A$^+$07b] and variable angular search bin size. In the last case the angular size of the bin was chosen among the angles between the arrival directions of the neutrino induced muons and the direction of the assumed neutrino source.

4.6.1 Toy MC description

A toy MC is used to produce on-source events with randomly distributed arrival times and arrival directions. There are two different procedures to generate background and signal events.

Background

The mean background in the angular search bin μ_{bg} is calculated like in the time integrated analysis. The number of background events b is picked up randomly from a Poisson distribution of a mean μ_{bg}. The arrival time of the background events is picked up randomly, from the up-time distribution. In order to attribute an arrival direction to the background events first all the right ascensions (α) and declinations (δ) of the recorded muon tracks for the chosen angular search bin around the chosen direction are collected. Then the arrival direction of a background event to the source is calculated from randomly picked up α and δ. In this way a set of b background events is obtained, described by their arrival time and arrival direction. Both are distributed uniformly.

Signal

The procedure for generating signal events is very similar. The number of signal events s is picked up randomly from a Poisson distribution of a mean μ_{sig} which is an arbitrary number defined by the user. The time of the first event t_0 is picked up randomly, using the up-time distribution. Starting from t_0 a sample of events which arrival times are contained in an interval Δt - the desired duration time of the neutrino flare - is collected. From this sample s events are picked up randomly. Then the arrival direction of each signal event is randomly selected from the Point Spread Function (PSF). The PSF is calculated for each potential neutrino source direction using MC simulations as described in [Ack06]. In this way a set of s signal events described by their arrival time and arrival direction is obtained. The time is distributed uniformly over a chosen flare duration period Δt. The arrival direction is distributed according to the PSF.

On-source

In general the on-source sample is a combination of signal and background events and has $s + b$ events in total. However, to estimate the probability of the background hypothesis the on-source sample is constructed from the background events only.

4.6.2 Excess parameter

An excess parameter ξ is defined as: $\xi = -\log_{10}(P_{bg}^{best})$. A large number of independent experiments (of background events) was simulated, on which the time-clustering search was applied. In each of the experiments the best cluster was found and its P_{bg}^{best} was calculated. Then the P_{bg}^{best} is translated into the excess parameter ξ and filled into a histogram (Fig. 4.9 - an example for a fixed angular search bin). Then the histogram is integrated and the ξ value which gives 99.78% (3σ one side) of the integral is calculated. For example for the fixed angular search bin at declination 50^o it was $P_{bg}^{best} = 10^{-7.2}$, so $\xi_{th} = 7.2$. In order to calculate the detection chance a cluster is accepted only if its $\xi \geq \xi_{th}$ - this way the trial factors due to looking on all possible combinations of events (clusters) coming from a certain direction are automatically accounted for.

4.6.3 The probability to detect a neutrino flare

In order to investigate the discovery potential of the time-clustering algorithm a few thousands MC experiments were performed, simulating variable neutrino point-sources of different signal strength and duration. The signal was generated according to the Point Spread Function. The background events are distributed uniformly in time and their arrival direction is generated using the δ and α distributions of the real events.

Figures 4.10 and 4.11 show the probability of detecting a neutrino flare with a significance of 99.87% or higher for a fixed and variable angular search bin respectively. The time-variable analysis and the standard time integrated analysis are compared. Different curves are related to different time duration of the flare (1, 3, 5, 10 weeks or the whole year). Comparison of both plots shows that the best detection chance is obtained with a variable bin size. What is also interesting is the fact that in case of a fixed bin analysis the time integrated search has a better discovery potential than the time-clustering search, if the neutrino flare lasts longer than 1-2 weeks.

Figure 4.12 shows the "best bin" size, i.e the size of the angular search bin in which the biggest number of "best clusters" was found, for a source located at the declination of 50°. An average "best bin" size is very similar to the bin size chosen for the time integrated analysis in [A^{+}07b], which for the sources at this declination equals 2.5°. On the other hand one still gains by varying the bin size because the events which lie on the border of the "best bin" are included in the analysis.

4.6.4 Performance study of the counting method

The upper panel of Figure 4.13 shows a good example of the main drawback of the counting method. Due to the low statistics and the fact, that the number of events in the cluster is discrete the μ_{bg}^{loc} and P_{bg} distributions are not continuous and the ξ plot shows spikes. This effect is less prominent in the ξ distribution for the free angular search bin size (Fig 4.13 lower panel) simply because the statistics is much higher. In Fig 4.14 one can see a comparison of the excess parameter ξ, mean cluster background μ_{bg}^{loc} and cluster P_{bg} distributions for the "counting" (left) and "fit+azimuth" (right) methods. The ”spikiness” of the ξ distribution results in an underestimation of ξ_{th}. For the "counting" method in this example ξ_{th} equals 5.4, while for the "fit+azimuth" method it is 7.2 (both values calculated in the same simulation conditions) which results in two orders of magnitude difference in the P-value. As one can see, the problem with a proper ξ_{th} estimation in the "counting" method is another serious argument for using the "fit+azimuth" method.

Table 4.2: The columns show: sources selected for this analysis, available γ-ray data with references (all Whipple data were taken from: http://veritas.sao.arizona.edu/content/blogsection/6/40/) and the chosen ”high state” flux threshold (in Crab units).

Source	Available γ-ray data	Flux threshold [Crab]
Mrk 421	2004: HESS [A^+05c], MAGIC [A^+07h] 2005: MAGIC [A^+07h], Whipple 2006: Whipple	1.0
Mrk 501	2005: MAGIC [A^+07j], Whipple 2006: Whipple	1.5
Mrk 180	2006: MAGIC [A^+06d]	-
1ES 1959+650	2004: MAGIC [A^+06f] 2005: Whipple 2006: Whipple, MAGIC (preliminary)	0.8
1ES 2234+514	2005: MAGIC [A^+07g], Whipple 2006: Whipple	-
1ES 1218+30.4	2005:MAGIC [A^+06e]	-
BL Lac	2005: MAGIC [A^+07f]	0.07
H1426+428	2006: Whipple	0.15
3C 66A	2004: Whipple (U.L.), STACEE (U.L.) [B^+05a]	-
3C 454.3	not observed in VHE γ-rays	-
GRO J0422+32	not observed in VHE γ-rays	-
GRS 1915+150	2004: HESS (U.L.) [Ce05]	-
LSI+61 303	2005: MAGIC [A^+06g] 2006: MAGIC [A^+06g]	-
Cyg X-1	2006: MAGIC (1 day flare) [A^+07k]	-
Cyg X-3	not observed in VHE γ-rays	-
XTE J1118+480	not observed in VHE γ-rays	-
3C 273	2004: HESS (U.L.) [A^+05e]	-
M87	2005: HESS [Aha06]	0.08

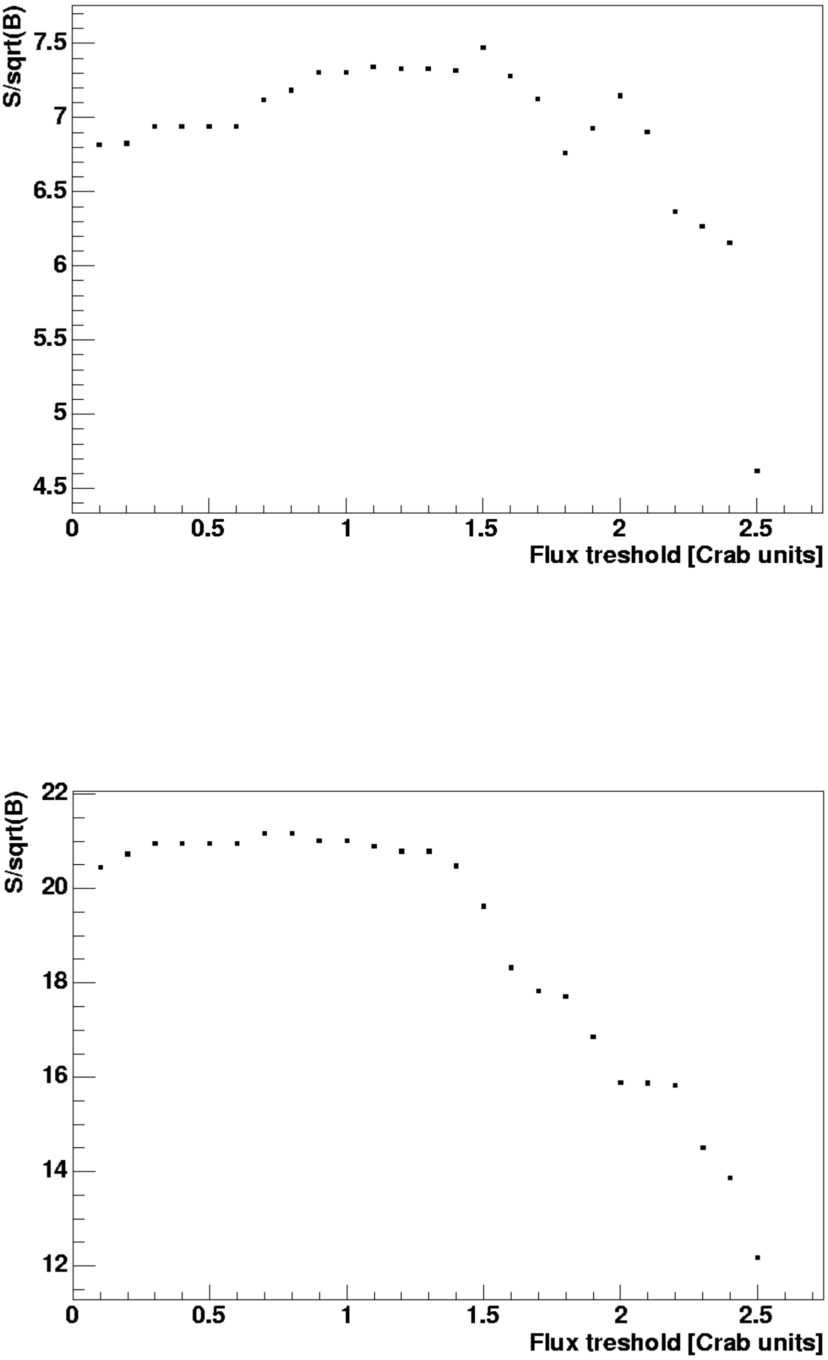

Figure 4.7: Mkn 421 $S/\sqrt{B}$ ratio - (Y axis) for different flux levels (X-axis): (a) "sum approach" for 1992-2006 data, (b) "average approach" for 1992-2006 data.

Table 4.3: Results of the search for neutrino events in coincidence with γ-ray flares. Column "Selected periods" give the year and integrated up-time of the detector in days.

Source	Selected periods	n_{obs} / μ_{bg}
Mkn421	2004 (7.6)	0 / 0.057±0.007
	2005 (1.0)	0 /0.0067±0.0008
	2006 (10.8)	0 / 0.078±0.009
Mkn501	2005 (21.1)	1 / 0.13±0.02
1ES1959+650	2005 (0.95)	0 / 0.0040±0.0007
BL Lac	2005 (2.0)	0 / 0.008±0.001
H1426+428	2006 (3.0)	0 / 0.018±0.002
Cyg X-1	2006 (1.0)	0 / 0.0070±0.0008
M87	2005 (4.7)	0 / 0.033±0.004

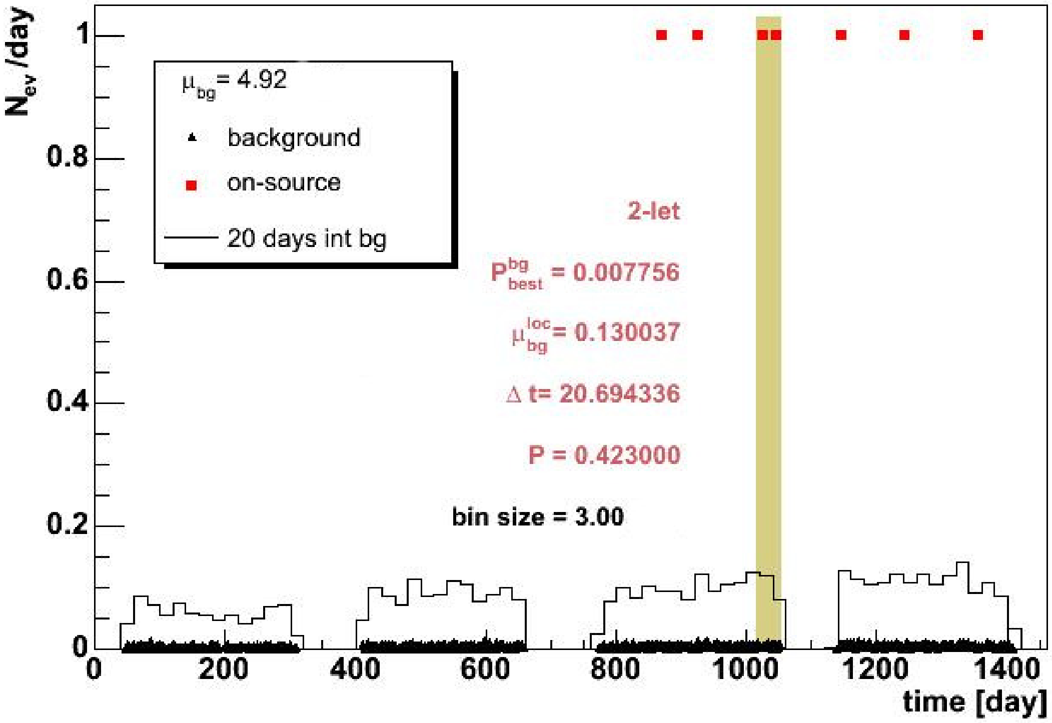

Figure 4.8: Simulated variable neutrino point-source: Dec = 40^o, RA = 12.5 h; search bin radius: 3^o (position in the sky and distribution of the on-source events randomly generated). X-axis: time in days (day 0 = 01.01.2000),Y-axis: number of events per day. Red squares: on-source events, black triangles: expected background per day (including the on-source sample), black histogram - expected background in 20 days. The yellow stripe highlights the position of the "best cluster", and μ_{bg} - mean background in the search bin, n-let - cluster multiplicity, P_{bg}^{best} - cluster "P-value", μ_{bg}^{loc} - cluster mean background, Δt - cluster size in time, P - probability to find a cluster of this or lower probability P_{bg}^{best} at any time in the whole period of data considered.

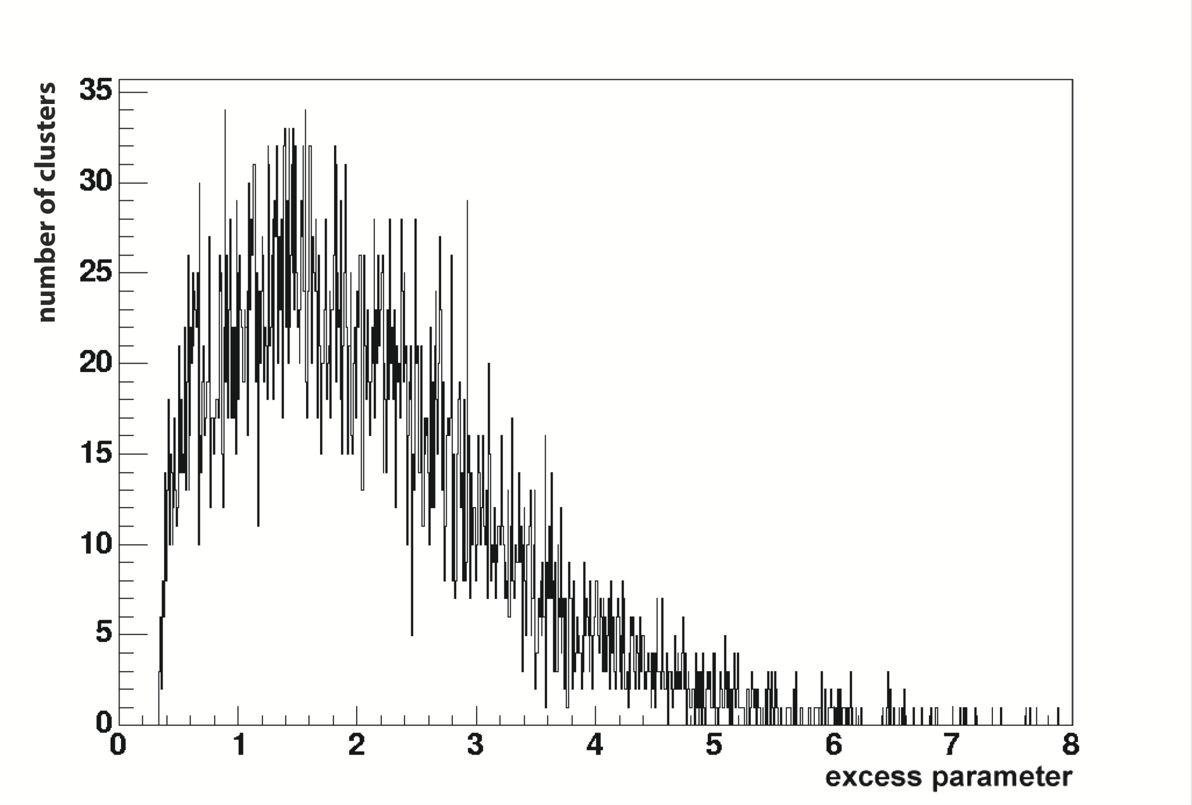

Figure 4.9: Distribution of the excess parameter ξ for 10,000 MC generated experiments. The search bin radius was fixed to 2.5^o (declination 50^o). The X-axis shows the value of the excess parameter. The confidence level was set to 99.87% which, in this case, corresponds to the excess parameter value of about 7.2.

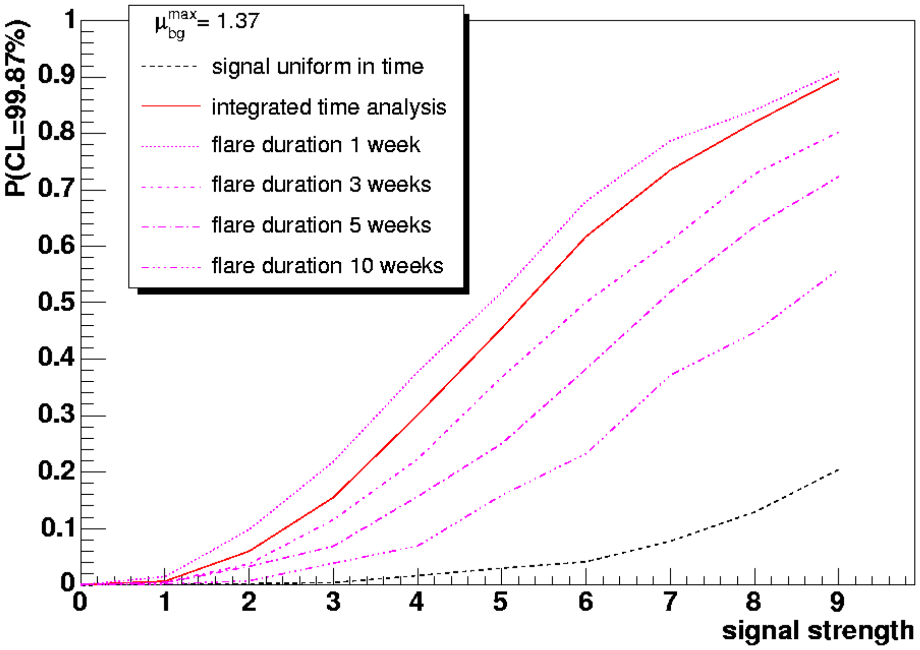

Figure 4.10: Probability of detecting a neutrino flare with a significance of 99.87% or higher, with an angular search bin radius fixed to 2.5^o. The X-axis shows the signal strength (number of signal events). The pink curves were calculated for different time duration of the signal (1, 3, 5 or 10 weeks) and applying the time clustering algorithm, the black (dashed) curve - for a signal uniformly distributed over the year 2004 also applying the time clustering algorithm, the red (continuous) curve - for a signal uniformly distributed over the year 2004, but without applying the time clustering algorithm (integrated analysis). Calculations made for 10,000 MC experiments simulating a variable neutrino point-source of a certain signal strength, on a background of μ_{bg}^{max}, at Dec = 50^o, RA = 12.5 h (position in the sky and distribution of the on-source events were generated randomly).

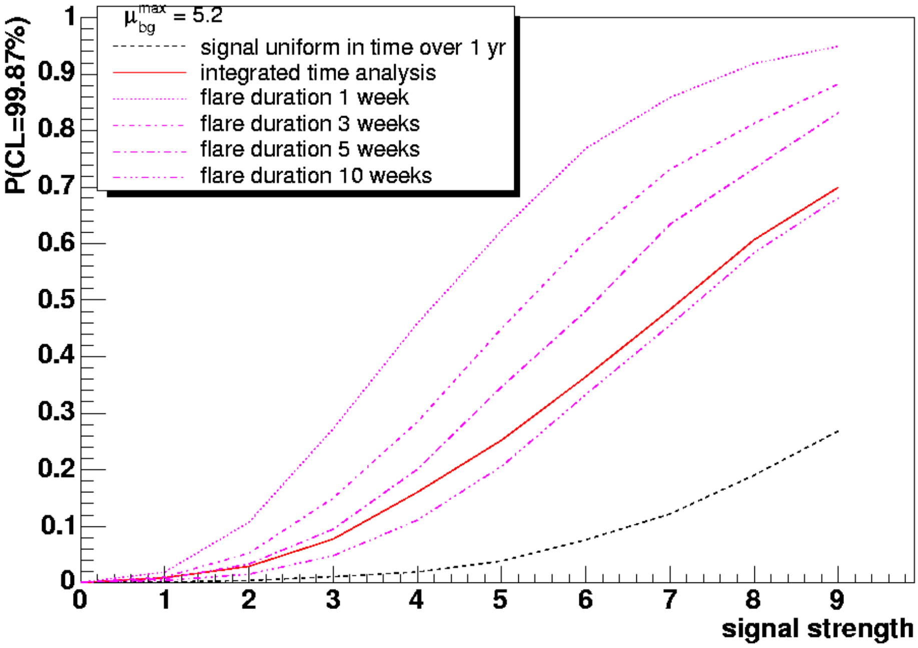

Figure 4.11: Probability of detecting a neutrino flare with a significance of 99.87% or higher, with an angular search bin radius varied from 0^o to 5.0^o . The X-axis shows the signal strength (number of signal events). The pink curves were calculated for different time duration of the signal (1, 3, 5 or 10 weeks) and applying the time clustering algorithm, the black (dashed) curve - for a signal uniformly distributed over the year 2004 also applying the time clustering algorithm, the red (continuous) curve - for a signal uniformly distributed over the year 2004, but without applying the time clustering algorithm (integrated analysis). Calculations made for 10,000 MC experiments simulating a variable neutrino point-source of a certain signal strength, on a background of μ_{bg}^{max}, at Dec = 50^o, RA = 12.5 h (position in the sky and distribution of the on-source events were generated randomly).

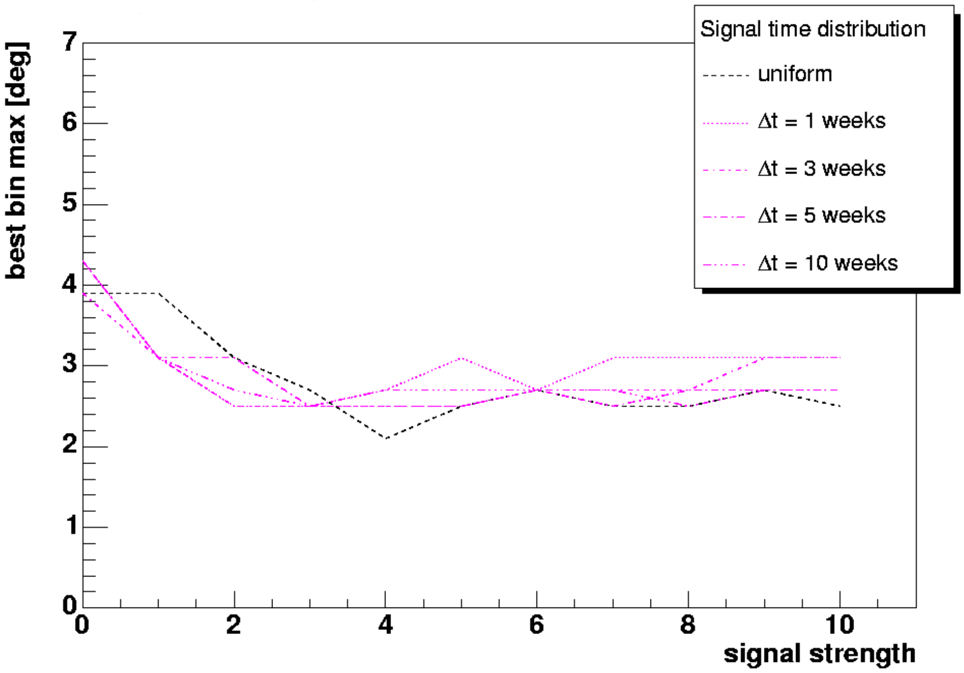

Figure 4.12: "Best bin" size, i.e. size of the angular search bin in which the biggest number of "best clusters" was found. The angular search bin radius was varied from 0^o to 5.0^o. The X-axis shows the signal strength (number of signal events). The pink curves were calculated for different time duration of the signal (1, 3, 5 or 10 weeks) and applying the time clustering algorithm, the black (dashed) curve - for a signal uniformly distributed over the year 2004 also applying the time clustering algorithm, the red (continuous) curve - for a signal uniformly distributed over the year 2004, but without applying the time clustering algorithm (integrated analysis). Calculations were made for 10,000 MC experiments simulating a variable neutrino point-source of a certain signal strength, on a background of $\mu_{bg}^{max} = 5.2$ events, at Dec $= 50^o$, RA $= 12.5\,\mathrm{h}$ (position in the sky and distribution of the on-source events were generated randomly).

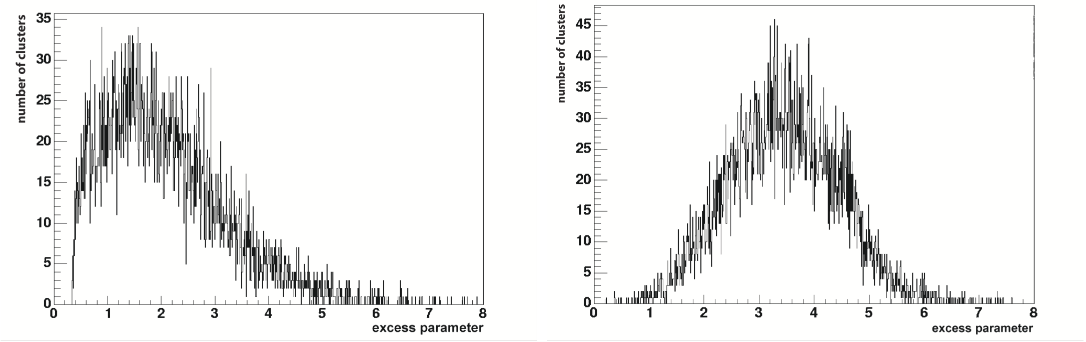

(a) (b)

Figure 4.13: Distribution of the excess parameter for 10,000 MC experiments: (a) the search bin radius was fixed to 3^o, the confidence level of 99.87% in this case corresponds to the excess parameter value of about 7.2; (b) the search bin radius was varied up to 6^o, the confidence level of 99.87% corresponds to the excess parameter value of about 8.4.

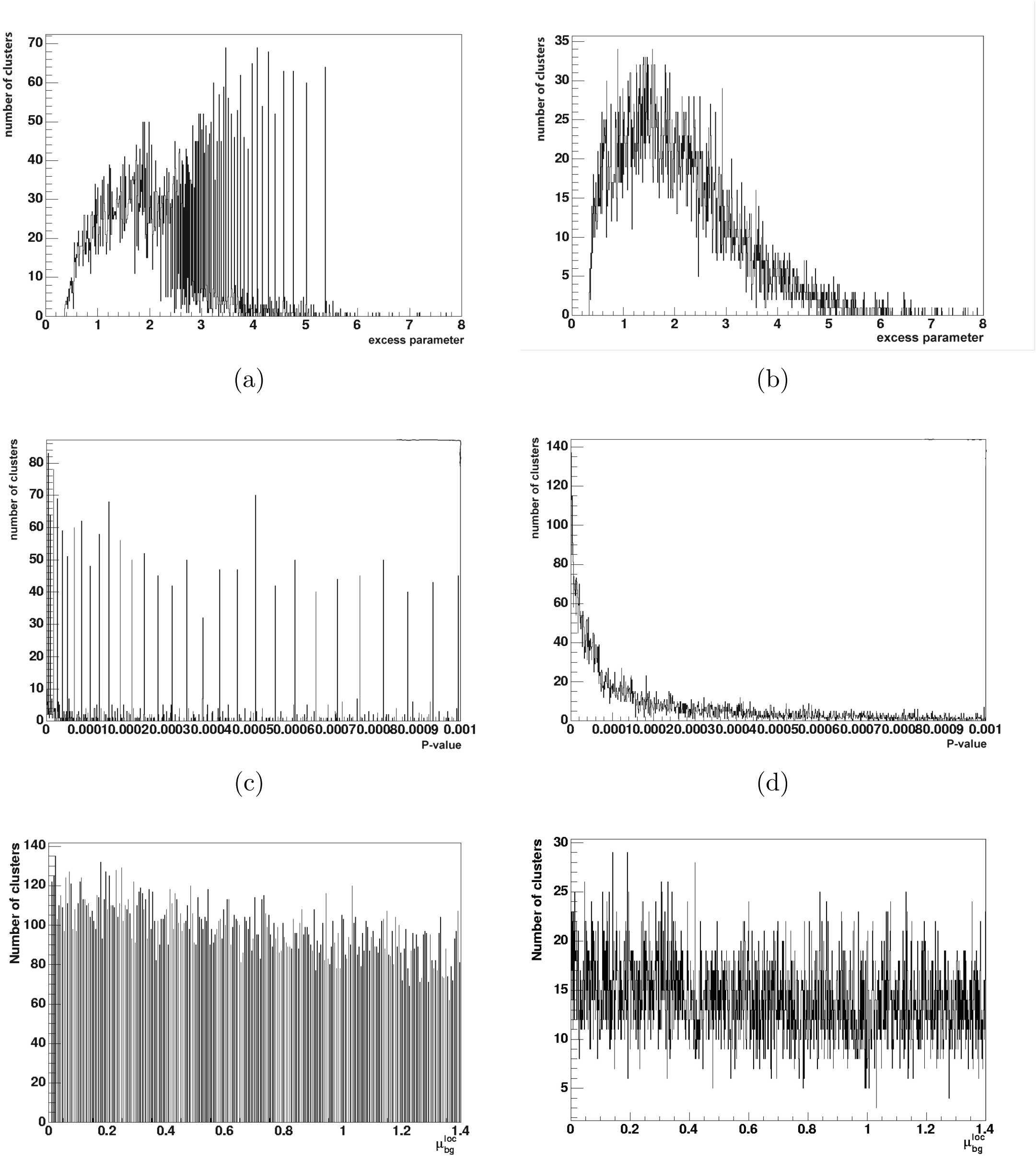

(a) (b)

(c) (d)

(e) (f)

Figure 4.14: Comparison of calculations using the "counting method" (left) and the "azimuth + fit method" (right): the excess parameter - plots (a) and (b), the P_{bg} of the cluster - (c) and (d), the background of the cluster μ_{bg}^{loc} - (e) and (f).

4.6.5 Results of the time-clustered search for neutrino bursts

Eighteen sources were chosen for this analysis. Since no significant excess in coincidence with enhanced γ-ray emission was found (for those objects for which the γ-ray data were available) the time-clustering analysis with a variable angular search bin size was applied to all of them.

Table 4.4 reports the results of the cluster search for neutrino flares for combined data sets of 2004, 2005 and 2006. The highest excess observed (for Cygnus X-3) corresponds to $3.56\,\sigma$. The overall probability to observe a cluster of this significance or higher at any time in the whole periods analyzed equals 5.9% (not including the trial factors due to looking on several sources) and is therefore compatible with the background hypothesis.

Table 4.4: Results of the search for neutrino clusters: duration Δt [days], angular bin size $\Delta\psi$ [deg], significance of the best cluster found S_{bg}^{best} [σ] and the overall probability to observe a cluster of this significance or higher at any time in the whole period analyzed P [%] .

Source	Δt [days]	$\Delta\psi$ [deg]	S_{bg}^{best} [σ]	P [%]
Mkn 421	3.9	5.2	1.6	95.0
Mkn 501	26.5	4.8	3.2	14.5
Mkn 180	0.35	2.2	2.92	30.0
1ES 1959+650	11.2	2.8	2.82	29.0
1ES 2234+514	42.2	3.4	2.7	35.0
1ES 1218+30.4	5.0	6.0	1.4	95.0
BL Lac	51.6	4.6	2.45	46.0
H1426+428	4.4	5.2	1.5	92.0
3C 66A	7.7	5.0	2.45	44.0
3C 454.3	8.1	4.8	2.7	33.0
GRO J0422+32	19.5	5.8	1.75	90.0
GRS 1915+150	94.4	2.0	3.2	8.4
LSI+61 303	0.2	4.5	2.9	31.0
Cyg X-1	27.5	6.37	3.2	15.0
Cyg X-3	**8.8**	**4.3**	**3.56**	**5.9**
XTE J1118+480	31.1	4.5	2.25	64.0
3C 273	194.5	6.1	2.88	9.1
M87	11.1	6.6	2.0	69.0

4.7 Neutrino Target of Opportunity

The Neutrino Trigger of Opportunity (NToO) program proposed in [Ber05] addresses the problem of the lack of simultaneous γ-ray and neutrino data. By sending a trigger after observing a neutrino event from a candidate source direction a follow up observation by γ-ray telescope can be performed and the amount of simultaneous data increases. A short

	LSI+61 303	GRS 1915+105	1ES 2344+514	1ES 1959+650	Mrk 421
n_{bck}	0.86	1.26	0.99	0.92	1.51
n_{obs}	0	1	1	0	3
n_{fo}	0	0	1	0	1
n_γ	–	–	0	–	0
F_{thr} [C.U.]	0.2	0.2	0.5	1.0	4.0
p_γ	–	–	–	< 0.15	< 0.05
P_ν	1.0	0.7	0.6	1.0	0.2

Table 4.5: List of sources selected for the NToO test run. Given are preliminary numbers for expected (n_{bck}) and observed (n_{obs}) neutrino triggers, the number of follow up observations by MAGIC n_{fo}, the number of observed coincidences (n_γ), the γ-ray high-state probability p_γ and the probability P_ν for observing n_{obs} neutrinos or more. The error on n_{bck} is typically ~10%.

test run of NToO with AMANDA-II and MAGIC was performed from September until November 2006 [A$^+$07d]. The AMANDA-II data were analyzed using the background estimation method presented here (section 4.3.2). Table 4.5 shows the obtained results. Although no significant coincidences between the neutrino events and VHE γ-ray flares were found the technical feasibility of the set up was successfully tested. Again, as in the case of any correlation study, a probability of a random coincidence should be assessed. Here the γ-ray high-state probability p_γ was calculated using the flux frequency distribution of the object fitted with an exponential function, an alternative method is discussed in the next chapter.

An extension of this program to IceCube was proposed in [FB09]. The main modification concerns implementing a fast "on-line" analysis of neutrino signal including the time-clustering algorithm. The trigger is sent only when the significance of the observed neutrino cluster exceeds a predefined threshold (e.g. $5\,\sigma$). The software for neutrino event selection is implemented and ready to be deployed and tested at the South Pole. The program was approved by the MAGIC Collaboration and the first results with the IceCube configuration of 79 strings and two MAGIC telescopes can be expected at the end of this year.

4.8 Summary

This chapter reported on the first search for neutrino flares from pre-selected sources with no a priori assumption on the time structure of the signal. In order to prevent a posteriori findings of coincidences with γ-ray flares a pre-test was performed, to look for correlations between the high energy neutrinos and high states of γ-ray emission of selected sources. In both cases no significant excess above the expected background was found. To accomplish the time-clustered search a new background estimation method was developed. It allows to reduce the statistical uncertainties up to 10% as compared to the classical ON/OFF-source approach. The method presented here also properly takes into account the effects caused by the detector asymmetries arising from a non-homogeneous detector. This approach becomes relevant when analyzing data for IceCube, a detector under construction with a non-homogeneous distribution of the strings before completion. The modified version of the algorithm, using an improved version of the background estimation (likelihood method) and additional information on the energy of the neutrino events was applied to IceCube 22-strings data [L$^+$09a], no neutrino point-sources were found.

5 Historical Gamma-ray Light Curves

The, not yet thirty years old, ground-based VHE γ-ray astronomy belongs to one of the youngest branches of physics and most of the efforts of different collaborations was put into discovering new classes of sources, or detecting the γ-ray counterparts of the known ones. In the recent years the interest shifted towards more detailed, statistical studies. For example some part of the observational time is now spent on regular monitoring of the established emitters. Comparing with other wavelengths the number of discovered sources[1] (~ 50) or the length of the longest light curve ($\sim 1500\,\text{hours}$) might not be impressive, but some interesting results might be derived even from this limited statistics. This chapter introduces the public archive of published long term γ-ray light curves maintained at DESY [T^{+}07b] and presents a statistical study of the flux states on the example of two objects Markarian 421 (Mrk 421) and Markarian 501 (Mrk 501).

5.1 Purpose and limitations

This analysis is a continuation of the work reported in [T^{+}07b]. The information collected in the archive was intended to be used mainly for investigating the correlations of neutrino events and γ-ray flares (see section 4.4 or [S^{+}07]). There are many statistical problems connected with such a study. For example: how to define a “flare” (or high state), how often it occurs, how many accidental correlations with other signals (e..g neutrino flare) one can expect from a certain source? These questions are addressed in the last section of this chapter.

By now the archive contains the light curves of some of the extragalactic objects of the Northern Hemisphere which lie in the IceCube FoV. The most frequently observed among them were those early discovered: Mrk 421, Mrk 501 and 1ES 1959+650 which belong to the HBL class of the AGN. By looking through the published articles and contacting the authors as much information as possible concerning the observations was collected.

A new data format, so called Simple Light curve Format (SLF) was introduced in order to order the information. The standard SLF is an ASCII file with 12 columns (this can be extended if needed) which contain the following:

1. The start time of the observation in MJD: MJD_{start}.
2. The end time of the observation in MJD: MJD_{end}.

---

[1] for an actual number see e.g. the on-line catalogues at http://www.mppmu.mpg.de/ rwagner/sources/ or http://tevcat.uchicago.edu/

3. The measured integral flux in Crab units: F.
4. The statistical error on F: ΔF_{stat}.
5. The systematic error on F: ΔF_{sys}.
6. The differential spectral index: α.
7. The statistic error on α: $\Delta\alpha_{stat}$.
8. The systematical error on α: $\Delta\alpha_{sys}$.
9. The energy threshold in TeV: $E_{Th.}$.
10. The spectral cut-off in TeV, if the spectrum is described by a power law with an exponential cut-off: E_{cutoff}.
11. The experiment identification number.
12. The duration of the observation: Δt.
13. Additional entry 1
14. Additional entry 2...

The combination of data coming from many different experiments is not a trivial task. During the building and updating of the archive several problems occurred which can influence the results of the analysis.

The most important of them is the incompleteness of available data. Since some of the measurements were made long ago it is unavoidable that part of the information (for example the exact start and end times of the observation) is missing or was never derived and published (e.g. the spectral indices).

In many cases due to a low sensitivity of the telescope and/or the source being in a low state, the measurements are given as upper limits. They are calculated using different methods and a statistically correct way to include them in this analysis has not yet been found, since the original information (number of excess events, number of background events, etc.) cannot be reconstructed.

Duty cycle of the IACT telescopes ($\sim 10\%$) and restricted visibility periods of many sources create irregular gaps in the light curves - another limiting factor to any time variability analysis.

Different sensitivities (see Tables 2.1 and 2.2) of the experiments permit them to give flux levels above different energy thresholds. Also during the life time of a telescope its sensitivity changes. It can be improved by a hardware upgrade or more sophisticated analysis techniques, but after a certain time it usually diminishes due to the degradation of the mirror reflectivity, aging of the PMTs etc. In order to convert different measurements to a common energy threshold one needs to know the shape of the spectral distribution of the source. The common unit for the observed integrated flux was chosen to be the flux observed from the Crab Nebula F_{Crab}, the standard candle of the γ-ray astronomy. In Table 5.1 the differential energy spectra of Crab $\Phi_{Crab}(E)$ as measured by different telescopes are listed. An integral flux above an energy threshold of E_{th} is given by:

$$F(E > E_{th}) = \frac{\int_{E_{th}}^{\infty} \Phi(E)dE}{\int_{E_{th}}^{\infty} \Phi_{Crab}(E)dE} = \frac{\int_{E_{th}}^{\infty} \Phi(E)dE}{F_{Crab}(E > E_{th})}. \tag{5.1}$$

For a pure power law differential energy spectrum the calculation is straight forward:

$$F(E > E_{th}) = \frac{E_{th}}{E_0}^{-\alpha+1} \frac{F(E > E_0)}{F_{Crab}(E > E_{th})} \tag{5.2}$$

otherwise, for example if the measured spectrum is described by a power law with a cut-off at E_{cutoff}, the equation (5.1) has to be evaluated numerically.

Last but not the least important issue is the systematic error on the relative flux normalization of the combined data. In many cases (especially for the data from the pioneering experiments) the energy threshold and measured spectral shape are affected by large and not well known experimental uncertainties such as aging effects and changes in the atmospheric conditions. Very often one spectral index is given for long term measurements (e.g. data collected over the whole observational cycle) not taking into account the intrinsic variability of the observed object. Also the assumption on the spectral shape is often simplified: a pure power law or a power law with a cut off might describe the spectrum well in a certain energy range, but in reality a log-parabola is better suited to model the inverse Compton emission especially in the vicinity of the peak. Therefore data extrapolation to lower than original energy threshold is quite critical. For example a change from the E_{th} value of 1 TeV to 100 GeV with a typical systematic error on the spectral index of 0.1 leads to a relative systematic error on the integral flux of 30%.

At present any statistical study of the data is affected by large uncertainties. Nevertheless, the amount of good quality data from the second generation of IACTs is increasing every year and soon the proposed methods and hypotheses can be tested with a much higher precision.

5.2 Collected data

In Fig. 5.1 the combined light curves of the three BL Lac objects: Mrk 421, Mrk 501 and 1ES 1959+650 are shown. Data from different experiments (see Table 5.2 for references) was combined and normalized to a common threshold of 1 TeV according to the procedure described above. The light curves of Mrk 501 and 1ES 1959+650 include MAGIC data from this work (see Chapter 6).

Table 5.1: Differential energy spectra of Crab as measured by different experiments.

Experiment	Differential Crab spectrum $\frac{dF}{dE}$ [cm^{-2}s^{-1}TeV^{-1}]	Reference
CAT	$(2.21 \pm 0.05 \pm 0.60) \times 10^{-11}(\frac{E}{TeV})^{(-2.80 \pm 0.03 \pm 0.06)}$	[Pir00]
HEGRA	$(2.83 \pm 0.04 \pm 0.6) \times 10^{-11}(\frac{E}{TeV})^{(-2.62 \pm 0.02 \pm 0.05)}$	[A$^+$04b]
Whipple	$(3.19 \pm 0.07) \times 10^{-11}(\frac{E}{TeV})^{(-2.64 \pm 0.03)}$	[Gru07a]
MAGIC	$(6.0 \pm 0.2) \times 10^{-10}(\frac{E}{0.3TeV})^{((-2.31 \pm 0.06)-(0.26 \pm 0.07)log10(E/0.3TeV))}$	[A$^+$08e]
HESS	$(3.45 \pm 0.05) \times 10^{-11}(\frac{E}{1TeV})^{(-2.63 \pm 0.01)}$	[A$^+$06c]
VERITAS	$(3.19 \pm 0.07 \pm 0.70) \times 10^{-11}(\frac{E}{1TeV})^{(-2.40 \pm 0.03 \pm 0.17)}$	[Cel08]

Table 5.2: Reference list for the combined light curves.

Experiment	Mrk 421	Mrk 501	1ES 1995+650
CAT	[P+01] [Pir00]	—	[Khe02]
HEGRA	[A+02] [A+03b] [K+01] [Kes01] [R+06]	[A+99b] [A+99a] [A+01]	[A+03a]
Whipple	[K+95] [S+96] [B+96] [M+99] [R+06]	[G+06a]	[H+03] [K+04b] [G+06b]
MAGIC	[A+07h] [D+09]	[A+07j]	[T+08a] [A+06f]
HESS	[A+05c]	—	—
VERITAS	[D+09]	—	—

5.3 Statistical study of the integral flux distribution

The top panel of Fig. 5.2 shows the distribution of VHE γ-ray flux values integrated above 1 TeV in one day bins for Mrk 421. In the low flux range (below 0.5 Crab) the distribution is very well described by the Gauss distribution whose mean μ_{Gauss} can be interpreted as the baseline constant flux. Above 0.5 Crab a log-normal distribution was fitted:

$$f(x) = \frac{N_{Ln}}{x\sigma_{Ln}\sqrt{2\pi}} \exp\left(-\frac{(\log(x) - \mu_{Ln})^2}{2\sigma_{Ln}^2}\right) \tag{5.3}$$

It can be an indication of multiplicative processes being responsible for the source flux variability and the observed flares. In order to make sure that the overall fit is continuous the sum of both functions is fitted to the integral flux distribution. All calculations are done using the parameters derived from the fit with the sum of both functions. The middle and bottom panels of Fig. 5.2 display the integral flux distributions of Mrk 501 and 1ES 1959+650 respectively. In case of Mrk 501, the fit is still relatively good, although the ligh curve is not as well sampled as the one of Mrk 421. Due to very low statistics it was impossible to perform a reliable fit to the 1ES 1959+650 data. Here the detector sensitivity starts to play a significant role - most of the measurements are upper limits, which are not taken into account in this analysis. At high flux values the collected data is biased due to external- or self-triggers issued during multiwavelength campaigns or in order to expand the observation window during monitoring.

In Fig. 5.3 the probability of finding the source in a flux state above a certain threshold (p_γ) is shown, calculated using the collected data and the fit discussed above. In case of Mrk 421 the fit and the experimental data agree very well with each other. For Mkn 501 the fit overestimates the probability calculated using the data in the region below 1 Crab and underestimates it for higher flux values.

Using the Gauss distribution parameters one can define the source as being in a high state when the flux level exceeds the μ_{Gauss} by $5\,\sigma_{Gauss}$. For Mrk 421 this will happen above ~0.9 Crab for Mkn 501 above ~1.5 Crab. Although the values of μ_{Gauss} and σ_{Gauss} are similar for both sources the probabilities of finding those objects in a high state are different: ~50% for Mrk 421 and ~30%-40% for Mrk 501.

Examining the light curves, integral flux distributions and p_γ distributions one comes to the conclusion that Mrk 421 seems to show flaring behavior more often than Mrk 501, this source is characterized by longer periods of low state with only occasional flares. Those differences in the behavior of objects which belong to the same class are very important for investigating the correlations of γ-ray outbursts and other signals. The most important statistical question concerning such a correlation is its significance. In order to estimate it properly one has to know the probability of a random coincidence between the two types of signals.

In this work two kinds of correlation studies have been presented (see Chapter 4): an "off-line" search for neutrino events in coincidence with γ-ray flares using the data collected in the light curve archive and an "on-line" approach where the simultaneous neutrino and γ-ray time coverage is secured by a neutrino trigger (Neutrino Target of Opportunity - NToO). The importance of a correct p_γ estimation will be discussed here for the example of the NToO. As proposed in [A$^+$07d] the chance probability of detecting at least n_{obs} neutrinos and observing at least n_γ coincident γ-ray flares, under the hypothesis that all the neutrinos detected from the direction of the source are atmospheric, is given by:

$$P = \sum_{i=n_{obs}}^{+\infty} \frac{(n_{bg})^i}{i!} e^{-n_{bg}} \sum_{j=n_\gamma}^{i} \frac{i!}{j!(i-j)!} (1-p_\gamma)^{i-j}. \tag{5.4}$$

The first term describes the Poisson probability of observing at least n_{obs} neutrinos with n_{bg} expected background events. This is a straightforward calculation and the n_{bg} can be estimated as shown in Chapter 4 with a good accuracy even for very short periods. The second term describes the probability of observing at least n_γ coincident γ-ray flares out of the $i \geq n_{obs}$ issued neutrino triggers, here the probability to detect a flare in a time Δt (e.g. 1 day), once the trigger is issued (p_γ) plays a crucial role. Considering the present status of VHE γ-ray observations this value can be only calculated for very few sources - those observed frequently over a long time period - and is affected by a large uncertainty. Regular monitoring programs performed by high sensitivity instruments, like the MAGIC AGN monitoring program described in Chapter 6, are essential for future studies.

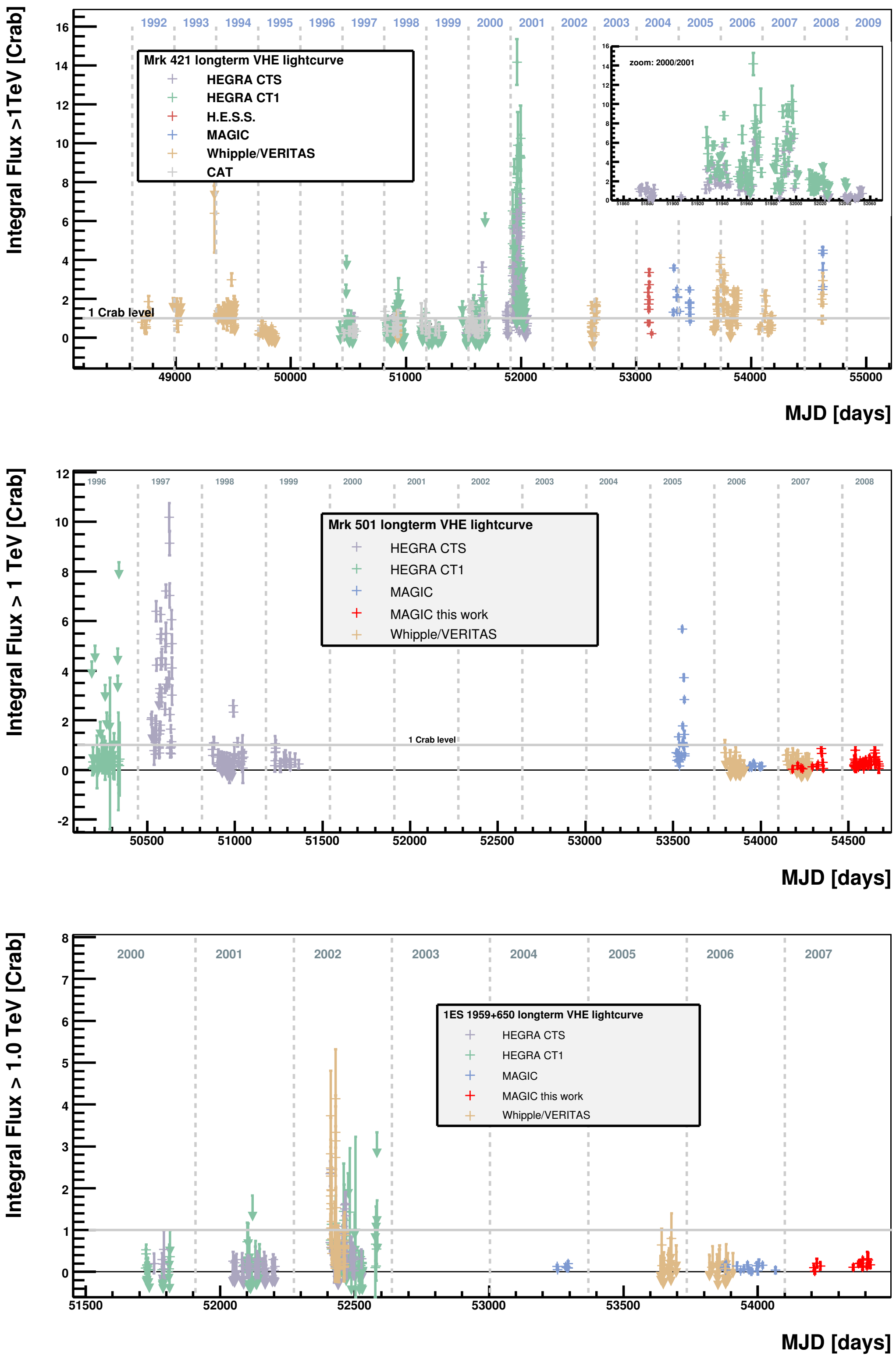

Figure 5.1: Long term light curves of BL Lac objects: Mrk 421 (top), Mrk 501(middle) and 1ES 1959+650 (bottom).

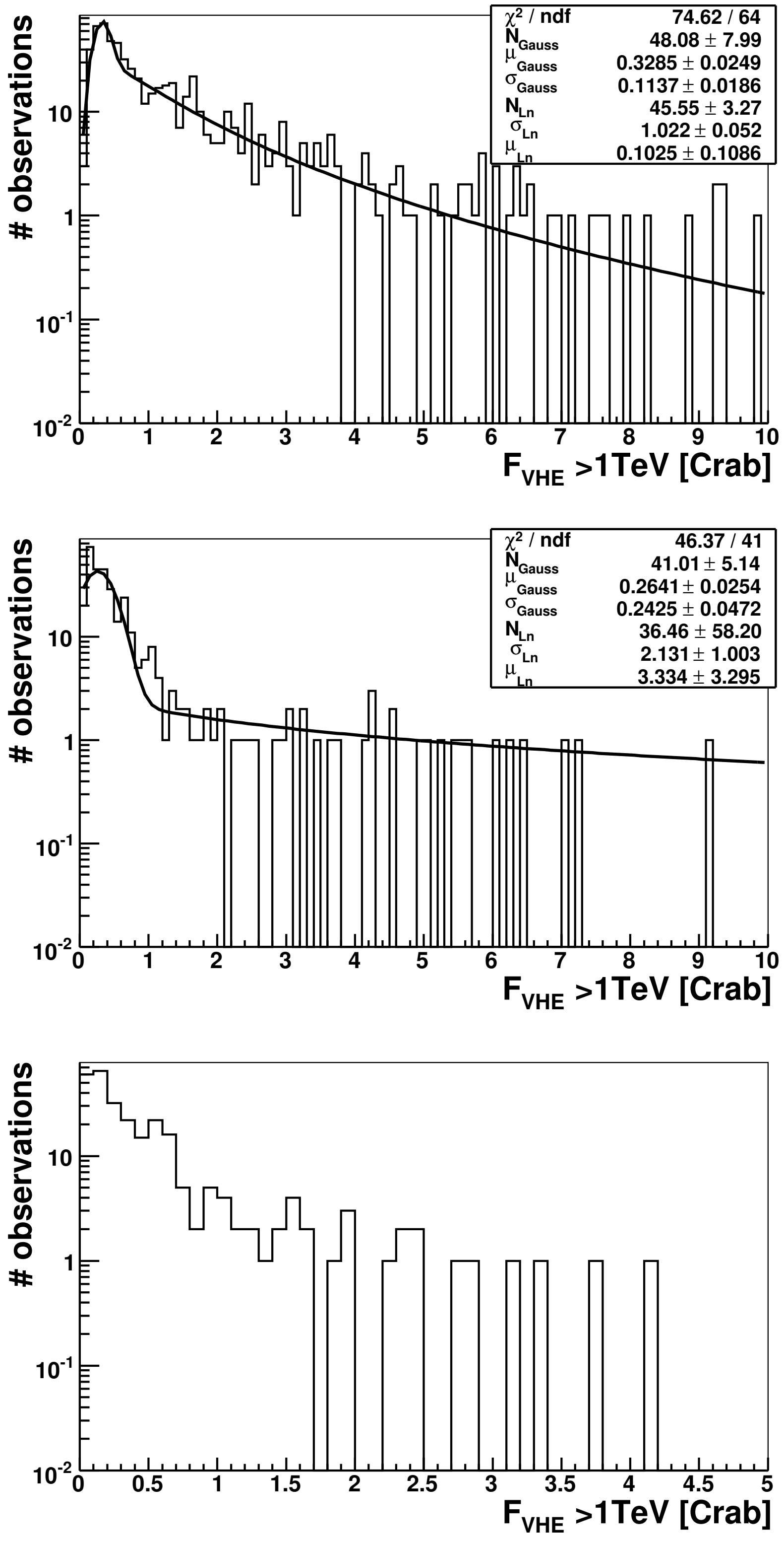

Figure 5.2: Distribution of flux values integrated above 1 TeV in one day bins for: Mrk 421 (top), Mrk 501(middle) and 1ES 1959+650 (bottom). See text for details.

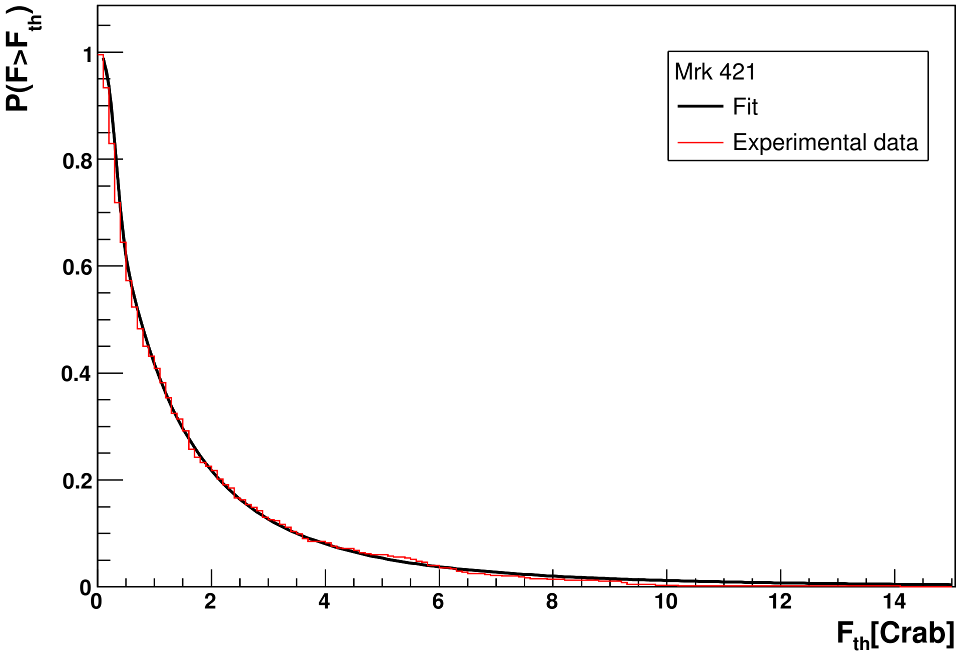

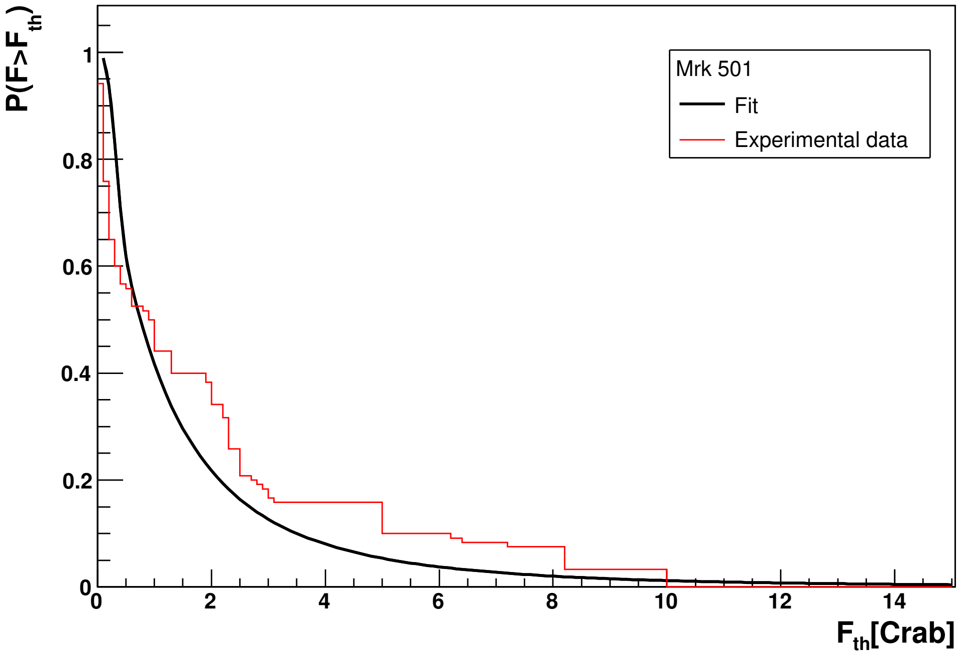

Figure 5.3: Probability (p_γ) of finding a source in a flux state above a certain threshold (F_{th}) for Mrk 421 (top) and Mkn501 (bottom). See text for details.

6 AGN monitoring with MAGIC

Almost one third of the objects detected in VHE γ-rays are blazars, i.e. Active Galactic Nuclei (AGN) which contain relativistic jets pointing approximately in the direction of the observer. Their energy spectra show no or very weak emission lines, but a continuous distribution with two broad peaks: one in the UV to soft X-ray band and a second one in the GeV-TeV range. One of the most interesting aspects of blazars is their flux variability, observed in all frequencies and on different time scales ranging from weeks to minutes [A$^+$07e] [A$^+$07j] with hints of associated spectral variability.

In recent years numerous multiwavelength campaigns (see section 1.5) were performed with the aim of explaining the acceleration and emission mechanisms in blazars. In many campaigns the new generation of Imaging Atmospheric Cerenkov Telescopes (IACTs) like HESS [A$^+$06c], MAGIC [A$^+$08e] and VERITAS [A$^+$08c] also took part which allows one to have a deeper look at the highly variable VHE (E>100 GeV) γ-ray emission. Unfortunately the data collected so far is not yet enough to fully constrain the theoretical models. In particular it is not yet clear if the leptonic or hadronic processes play a decisive role. For example, the Synchrotron-Self Compton (SSC) or External Compton (EC) leptonic models can successfully describe most of the existing data and offer a reasonable explanation of the fast flux variability of blazars (see section 1.6). On the other hand, hadronic models can also very well describe the SED structure. Additionally they explain the "orphan" gamma-ray flares (like the one observed for 1ES 1959+650 in 2002 [K$^+$04b]) and predict emission of high energy neutrinos (see section 1.7).

6.1 The aim of the AGN monitoring

As mentioned before the new generation IACTs can give valuable input for understanding the emission mechanism in blazars, not only by participation in multiwavelength observations, but also by performing an emission state independent, long term monitoring of the most interesting brighter γ-ray sources.

There are many advantages of such observations which allow to obtain an unbiased distribution of flux states. Many of the previously performed measurements were triggered by an observed enhancement of flux state in other wavebands. Therefore, observations of AGN during low flux states are still sparse. Consequently any statistical study which requires high statistics on various flux levels is difficult. An example of such a study is the determination of flaring state probabilities. It is essential for estimation of the statistical significance of possible (anti)correlations between flaring states and other observables, such as neutrino events (see section 4.4 or [S$^+$07]). Here, a long term monitoring plays a crucial role, especially in view of the results expected from the IceCube neutrino observatory [A+04c].

Another interesting application is the investigation of spectral changes during periods of different source activity, which can improve our knowledge about the acceleration and emission processes.

Last but not least AGN monitoring can serve to trigger Target of Opportunity (ToO) observations. The ToO observations may be performed by the IACT issuing the ToO trigger but may also include other IACTs, thus allowing to increase the time coverage of the observations, or telescopes and satellites observing other wavelengths. X-ray observations are especially interesting in the context of ”orphan” TeV flares.

6.2 Monitoring strategy and observational limitations

Due to the low duty cycle (∼10%) the operation time of IACTs is very precious and the observations have to be scheduled very carefully in order to achieve the right balance between the high priority programs, deep observations and AGN monitoring. Therefore usually previous generation IACTs which are still operational are used for this purpose. For example the Whipple[1] telescope, which is leading a monitoring program since 2005 for five well established TeV sources, or DWARF, one of the former HEGRA telescopes currently being refurbished and brought back into operation on La Palma [B+08]. In the case of MAGIC a large part of the monitoring program (∼60%) has been performed under moderate moonlight or twilight, keeping the impact on the overall observation schedule low and allowing to increase the available duty cycle up to ∼12%. The above enumerated IACTs observe the northern hemisphere, on the southern hemisphere, since 2004, the HESS Collaboration is monitoring the blazar PKS 2005-489 [A+09d]. The radio galaxy M87 is also regularly observed in a framework of a joined monitoring program of HESS, MAGIC and VERITAS.

For MAGIC, in order to achieve a dense sampling, up to 40 short observations per source are scheduled, evenly distributed over the MAGIC observation time. Each pointing should be long enough to detect a given minimum flux level taking into account the sensitivity of the telescope. Fig. 6.1 shows the sensitivity of the MAGIC telescope as a function of observation time for energies above 300 GeV. MAGIC is able to detect fluxes at the level of 30% Crab during 0.5 h observation, at a significance of $5\,\sigma$. Three sources were chosen for a regular monitoring: Mrk 421, Mrk 501 and 1ES 1959+650. The first two are relatively bright and usually 15-30 min observations are scheduled for them. 1ES 1959+650, being fainter, requires longer observation times, at least 30 minutes per single exposure.

6.3 Data analysis

In general, the same scheme was applied to analyze data sets from different observation periods. Any deviation from this scheme is explained in the section dedicated to the

---

[1] http://veritas.sao.arizona.edu/content/blogsection/6/40/

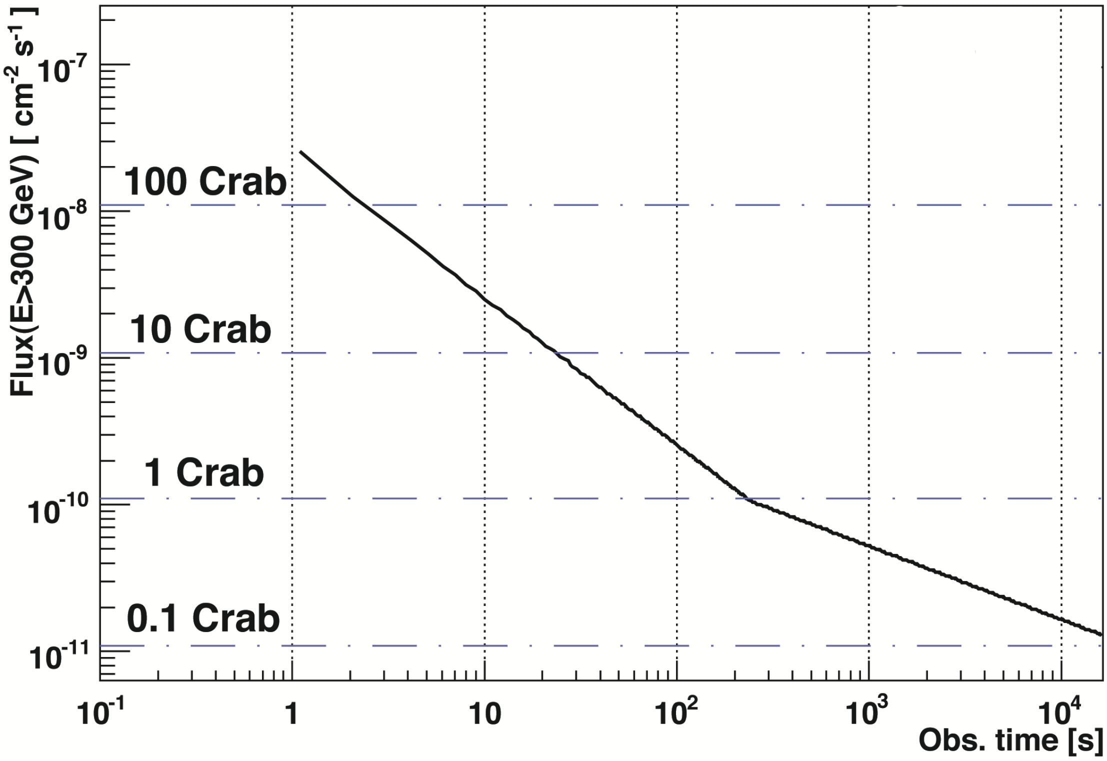

Figure 6.1: Sensitivity of the MAGIC telescope as a function of observation time for energies above 300 GeV. Figure adapted from [G$^+$08].

particular data set.

Data and MC files

All data and MC files used for this analysis were processed using standard, automatized scripts at the PIC data repository, up to the level on which the image parameters are calculated. If not otherwise explicitly mentioned in the text, the Time Image Cleaning (see section 3.3.2) was performed and time image parameters (section 3.4.2) were calculated and included in the RF training.

Data quality selection

The main criterion for run selection is the stability of the telescope event rate. During a moonless, clear night one should expect a zenith dependence of the rate as shown in Fig 6.2. The solid line shows a fit to the measured event rate where the rate is proportional to the square of the cosine of the zenith angle under which the observation was performed. Due to the atmospheric conditions and telescope performance the observed data rate usually differs from the ideal case. In this analysis a 10% difference from the expected rate is allowed. Sometimes part of the data had to be rejected if the weather conditions (clouds, changing humidity, calima etc.) caused large rate variations (example Fig 6.3). Also excluded from the analysis were very short runs or runs with small number of events, both types characterized by a large statistical error on the estimated event rate.

Most of the monitoring data were taken during moonlight or twilight and the discriminator thresholds (DT) settings were different than for the dark night observations, in order to account for a higher Night Sky Background (NSB) level. High values of DT result in a decrement of the event rate and a correction to the measured flux has to be applied. A detailed model of the influence of moonlight on the observations with MAGIC has been proposed after this analysis was completed. An analysis of Crab data and dedicated MC with different levels of NSB presented in [B$^+$09b] showed that up to a NSB level 2.5 times higher than for dark nights, even with mean DT values above 20, no corrections to the calculated flux level are needed. In this analysis all data taken with mean DT values above 20 (in arbitrary units) were excluded, and no corrections to the fluxes values were applied. In a view of a future publication a reanalysis of the data rejected due to high DT is considered.

Separation of γ- and hadron-like events and energy estimation using the RF algorithm

In order to create the γ-hadron separation matrices one needs a sample of γ-ray and a sample of hadron events. In the case of ON/OFF observations a part of the OFF data can serve as a good hadron sample. Sometimes data taken from another, fainter source are used provided they were taken under similar conditions. If this is not possible, one can use part of the data one wants to analyze, since typically only 1 in 10000 events is a real γ-ray event. Another possibility is to use the data rejected from the analysis. In this case one has to make sure that the distributions of the image parameters from

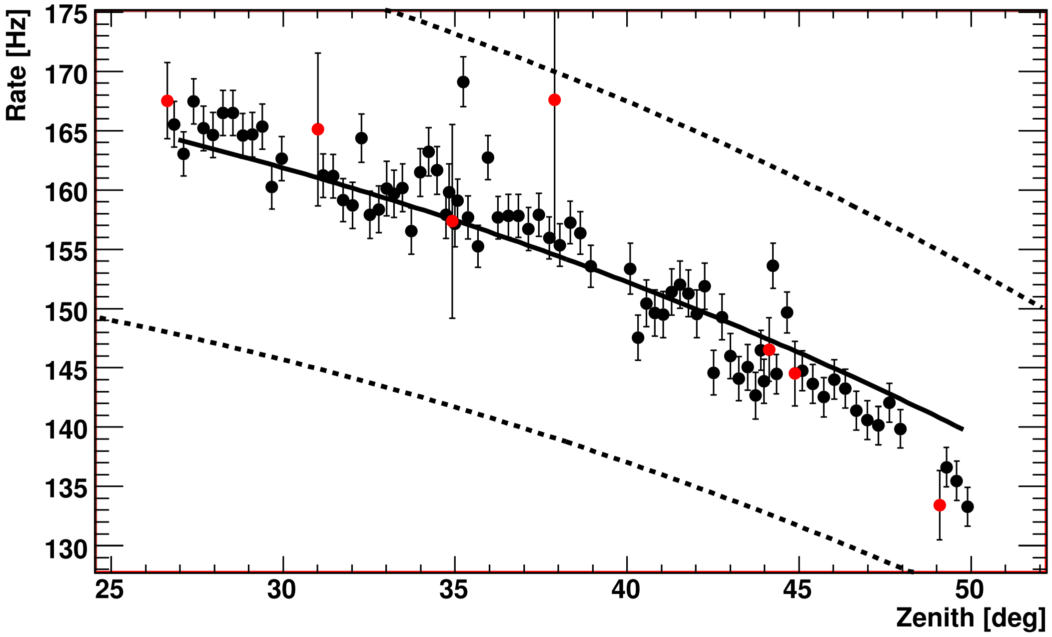

Figure 6.2: Event rate as a function of the zenith angle. The solid line shows the mean value and the dashed lines the 10% difference from the expected rate. The red points depict rejected runs. Crab Nebula observations performed on MJD 54382.

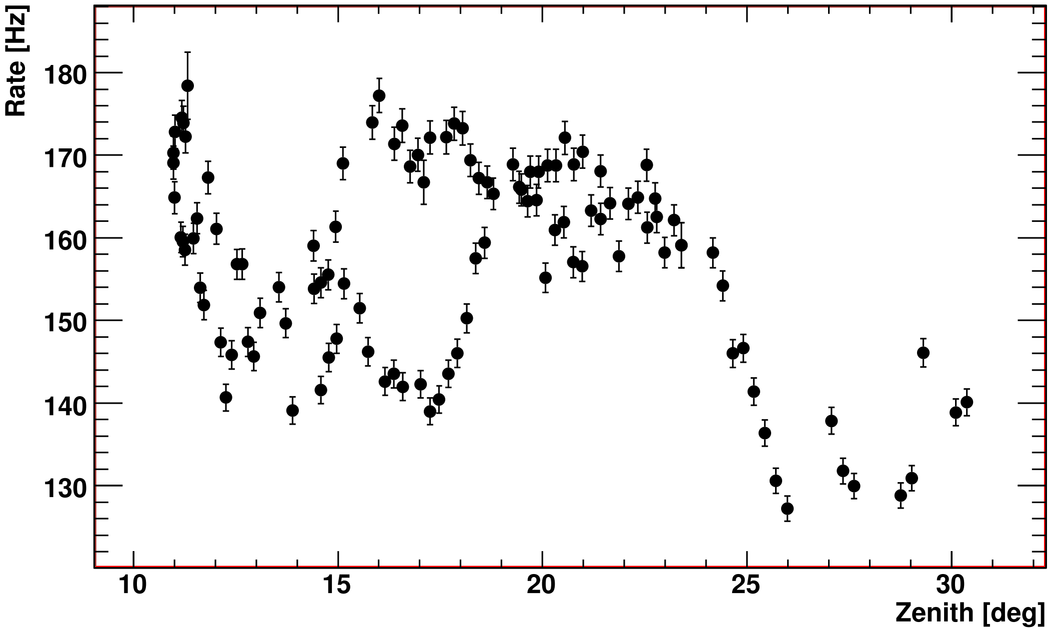

Figure 6.3: An example of unstable event rates due to bad weather. Mrk 501 observations performed on MJD 54588.04.

the rejected files agree with those from the data accepted for further analysis. As γ-ray samples MC generated γ-ray samples were used, the simulated zenith angle range, PSF and other parameters (cleaning type etc.) were adequate to the observation conditions (and preprocessing type) in each period. The MC sample was divided into three sub samples: "train1" for creating the γ-hadron separation matrices, "train2" for creating the energy estimation matrices and "test" for calculating the effective area of the telescope in the later analysis stage.

During the training one can apply cuts to reject events with unphysical parameter values or events which may be badly reconstructed because they are not fully contained, have too few core pixels or to many disconnected groups of pixels (”islands”). One can also set the image parameters which will be used for training. The choice of cuts and Hillas parameters depends mostly on the mode in which the data was taken and on the planned analysis type (*Alpha analysis* or θ^2 *analysis*, see section 3.8).

In this analysis default cut values were used to reject badly reconstructed events:

- Size < 80 and Size > 80000,
- image compactness:1.5 - 4.0 $\cdot$ $\log_{10}$(Conc(5)) < $\log_{10}$(Size),
- Leakage > 0.2,
- Number of Core Pixels < 3,

- Number of Islands > 3,
- Dist < 40 and Dist > 340 - only for ON data.

And the following image parameters are then used for γ-hadron separation:

- Width,
- Length,
- Log_{10}(Size),
- Log_{10}(Size)/(Width $\cdot$ Length),
- Zenith Angle ϕ,
- image compactness: Conc(5),
- image asymmetry: M3Long $\cdot$ sgn(cos($Alpha$)),
- Time RMS ,
- Time Gradient,
- Dist - only for ON data.

For energy estimation the same cuts and a similar set of image parameters was used:

- Width,
- Length,
- Log_{10}(Size),
- Log_{10}(Size)/(Width $\cdot$ Length),
- Zenith Angle ϕ,
- Conc5,
- Leakage,
- Time Gradient,
- Dist - only for ON data.

Cut optimization

Since the Crab Nebula is the standard candle of γ-ray astronomy, data taken from this source were used for optimizing the final signal/background separation cuts. For each period Crab data taken under conditions as similar to the analyzed source as possible were selected, that means with the same zenith angle range and period of observation (detector conditions).

In order to find the cuts which would give the best sensitivity, after applying the RF matrices to the Crab data, all combinations of Hadroness, Size and α values in given ranges were tested:

- Hadronness: 0.05 - 0.5 in steps of 0.05,
- Size: 50 - 450 phe in steps of 50 phe,
- α: 6.0° - 12.0° in steps of 2.0°.

All other cuts are set to default values (the same as used to calculate the flux and spectrum in MARS):

- Leakage > 0.2,
- Number of Core Pixels > 3,
- Number of Islands < 3,
- Zenith angle cut - to make sure that the zenith range used for optimization is the same as for the analyzed data,
- Energy cut for the flux estimation: 300 GeV to 50 TeV.

The cut values which give the best sensitivity according to the eq. 3.4 were chosen as the optimal ones. The resulting Crab flux above 300 GeV and spectrum were compared to the values reported in [A^{+}08e]:

$$\frac{dF}{dE} = (5.7 \pm 0.2_{stat}) \times 10^{-10} \left(\frac{E}{300\mathrm{GeV}}\right)^{(-2.48 \pm 0.03_{stat} \pm 0.2_{sys})} \mathrm{cm}^{-2}\mathrm{s}^{-1}\mathrm{TeV}^{-1} \tag{6.1}$$

$$F(> 300\mathrm{GeV}) = (1.16 \pm 0.10_{stat}) \times 10^{-10} \mathrm{ph\,cm}^{-2}\mathrm{s}^{-1} \tag{6.2}$$

The integral flux from Crab Nebula is used in this work as an integral flux unit (denoted Crab).

Calculation of flux and spectra

All fluxes were calculated for energies larger than 300 GeV using the procedure described in section 6.3. This energy threshold was chosen on the basis of the distributions of the estimated energy E_{est} for MC γ-ray events after training and application of all cuts (see e.g. Fig. 6.4). For the low zenith angle observations the energy threshold could be lower (∼200 GeV), but it was set to 300 GeV for the sake of consistency with the high zenith angle observations. If the significance of the measurement was below $1\,\sigma$ it was converted to 90% C.L. upper limits using the method proposed in [R+05].

For each day on which the flux was measured with a significance higher than $5\,\sigma$ (and for each Crab data sample) a spectrum was determined. The spectra were unfolded (see section 3.9.3) using two independent unfolding methods by Bertero [Ber89] and by Tikhonov [TA79] in order to check the stability of the results. If not explicitly indicated, usually a simple power law fit in the form of $dN/dE = N_0 \times (E/E_0)^{-\alpha}$ was used and the fit values obtained with the method proposed by Bertero are quoted.

The spectra used for modeling the broad band SED were, apart from unfolded, also corrected for the γ-ray absorption in the EBL (see section 1.3).

6.4 Markarian 501 - analysis results

The BL Lac object Mrk 501 is the second established TeV-blazar [Q+96] [B+97b]. MAGIC has been observing this source since 2005 when it was found in a flaring state and doubling times as short as a few minutes were observed [A+07j].

Presented here are results based on observations performed between February 2007 and August 2008. In order to maximize the time coverage for this source, observations were carried out mostly in the presence of moderate moonlight or twilight (56% of the observation time). Part of this data was taken during a multiwavelength campaign (MJD 54550-54602) described in more detail in [K+09]. The summary of the observations performed by MAGIC as well as data selection for the analysis is presented in Tables 1 and 2 in Appendix A.

6.4.1 Data collected in 2007

In 2007 Mrk 501 was observed for 25.5 h. All observations were taken in wobble mode: 8.94 h during dark nights, 16.56 h during twilight or moderate moonlight. Because of the dependence of the effective area on the zenith angle the data sample was divided into two subsamples: 14 h of high zenith angle data (30°- 45°) and 11.5 h of low zenith angle data (11°- 29°).

High zenith angles

After data quality selection 7.23 h (433.6 min) of high zenith angle (HZA) data were left for further analysis. The γ-hadron separation and energy estimation was done using matrices trained on data from 0.85 h of observation of a faint blazar 1ES 0235+164 taken

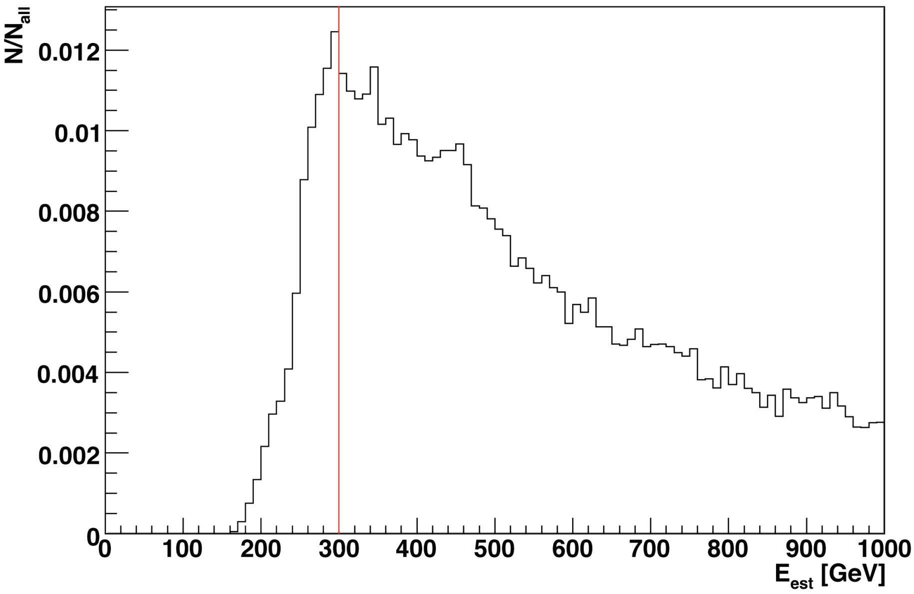

Figure 6.4: Distribution of the estimated energy (E_{est}) of the MC γ-ray events after training and applying the optimal cuts for the high zenith angle data sample of Mrk 501 collected in 2007: Hadronness < 0.15, Size > 250 and Alpha $< 8°$. The Y-axis gives the number of events in each energy bin normalized to the number of all events which passed the cuts. The red line marks the analysis threshold.

in the end of February 2007 (Table 6.1). During the data taking period from February till October 2007 there were very few nights when the Crab Nebula was observed in the zenith angle range 30°- 45°. For the cut optimization data taken from this source on MJD 54141 was used. The resulting cuts: Hadronness < 0.15, Size > 250 and Alpha $< 8°$ were tested on Crab Nebula data taken on MJD 54382. Table 6.2 gives the details of the measured Crab flux and spectral parameters from power law fit. The measured spectra are in agreement with those measured in [A$^+$08e]. The distribution of the estimated energy E_{est} for MC γ-ray events after training and application of the "optimal cuts" is shown in Fig. 6.4.

The results of the analysis can be found in Table 6.3. Figure 6.5 shows the Alpha distributions of the most and least significant measurements. On two days the significance of the measurement exceeded $5\,\sigma$ and the spectra were calculated. They are shown in Fig. 6.6, the values of the fit parameters can be found in Table 6.4. While the fit to the data collected on MJD 54344.91 has a good quality, the fit to the data taken on MJD 54348.9 is affected by large uncertainties on both the spectral index and normalization, due to the low statistics of high energy events.

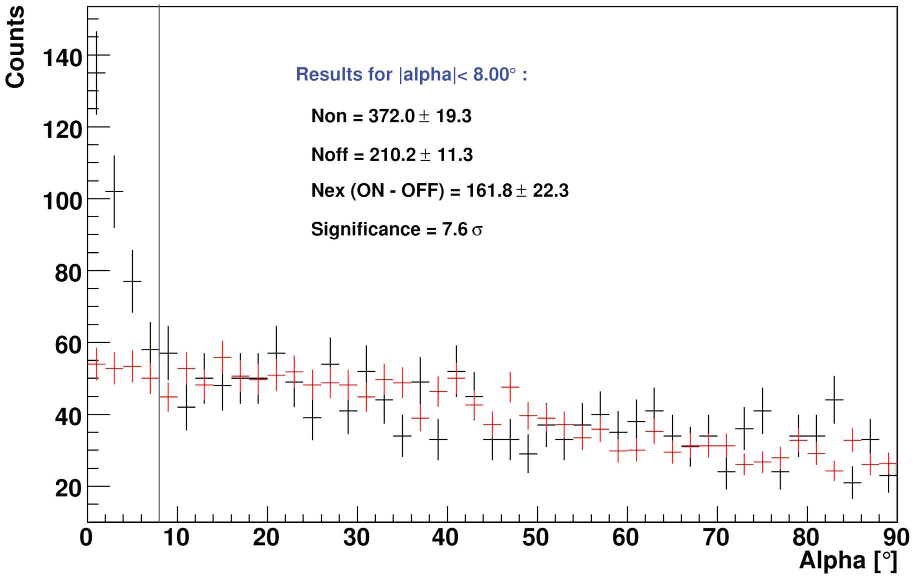

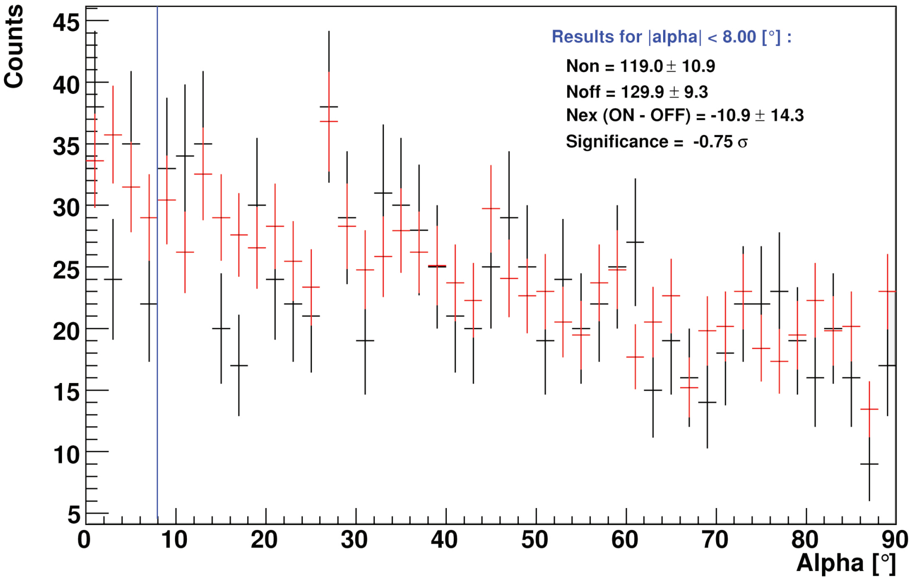

Figure 6.5: Alpha distributions for the most (MJD 54344.91) and least (MJD 54226.99) significant measurements taken form Mrk 501 observations in 2007 under high zenith angles. The red data points denote the background sample, the black points the data sample containing the γ-ray candidate events.

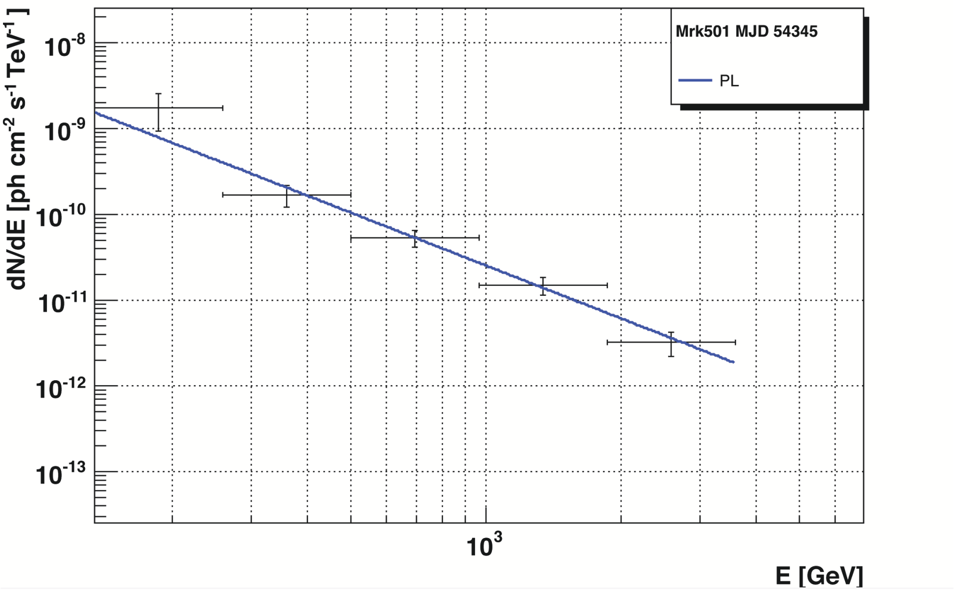

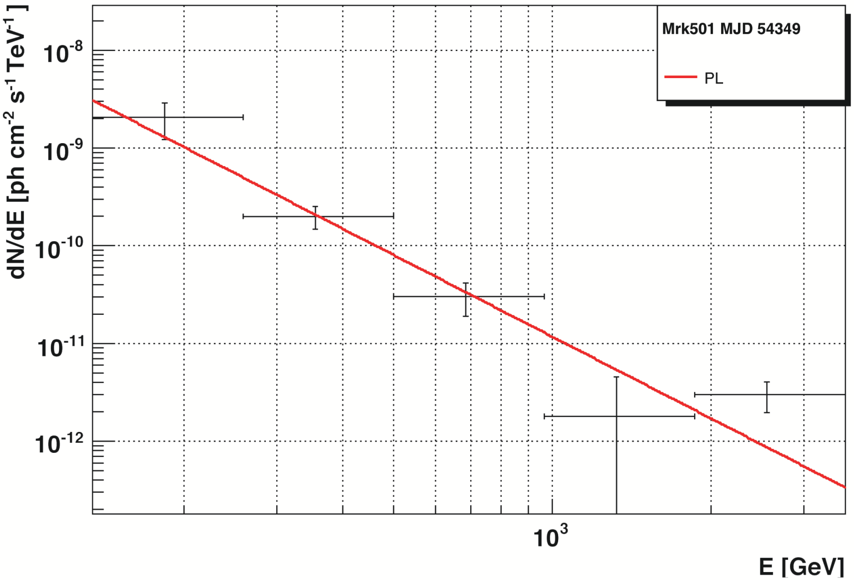

Figure 6.6: Mrk 501 spectrum as measured on MJD 54344.91(top) and MJD 54348.90 (bottom), fitted with a simple power law (PL). Fit parameters are given in Table 6.4.

Table 6.1: Observation parameters for the1ES0235+164 data after quality selection, used as hadron sample for the Mrk 501 high zenith angle data collected in 2007. The table contains: *MJD start* - the MJD date of the start of the observation, *Time* [min] - the duration of the observation in minutes, *DT* [a.u.] - the mean discrimination threshold in arbitrary units and the information of the light conditions during the observation: *D* - dark, *T* - twilight, *M* - moon, *ZA* [deg] - the zenith angle of the observation in degrees, *Mean rate* [Hz] - the mean rate in Hz given with an accuracy of 5.0 Hz.

MJD start	Time [min]	DT [a.u.]	ZA [deg]	Mean rate [Hz]
54143	27.35	15.4 (D)	29-35.7	190
54144	23.70	16.2 (D)	30-35.8	195

Low zenith angle

Rejection of bad quality data left 2.7 h (162.8 min) of low zenith angle (LZA) data for further analysis. Matrices for γ-hadron separation and energy estimation were trained on data taken on the faint blazar PKS 1424+240 (Table 6.5). The cuts were optimized on Crab Nebula data taken on MJD 54147. The optimal cut values are: Hadronness $<$ 0.1, Size $>$ 200 phe and Alpha $< 6°$, yielding a significance of $17.7\,\sigma$. This configuration was tested on Crab Nebula data taken on MJD 54382. Results are presented in Table 6.6. The distribution of the estimated energy E_{est} for MC γ-ray events after training and application of the "optimal cuts" is shown in Fig. 6.7. The blue dashed line marks the analysis threshold of ~200 GeV, but in order to be consistent with the high zenith angle measurements all fluxes were calculated for energies above 300 GeV (red line).

Results of the Mrk 501 analysis are shown in Table 6.7. Figure 6.8 shows the Alpha distributions for the most and least significant measurements.

6.4.2 Data collected in 2008

In the year 2008 MAGIC observed Mrk 501 for 63.1 h. A part of this data (49.5 h) was taken in ON mode during a multiwavelength campaign (MJD 54550-54602) [K$^+$09] while the rest was taken during a regular monitoring program performed in wobble mode mostly during twilight. The data from the MW campaign was included in the monitoring data because the campaign was scheduled beforehand and therefore the choice of the time period is not biased by a trigger issued because of an interesting event (e.g. X-ray flare).

Table 6.2: Results of the analysis of the Crab Nebula data sample used for optimization and test of cuts for the analysis of Mrk 501 high zenith angle data collected in 2007. The table contains: *MJD start* - the MJD date of the start of the observation, *Time* [min] - the duration of the observation in minutes, the measured number of ON, OFF and excess events, the significance of the measurement [σ], the integral flux above 300 GeV and its statistical error [ph cm^{-2} s^{-1}], the spectral index and its statistical error, the normalization of the spectra at 1 TeV and its statistical error [ph cm^{-2} s^{-1} TeV^{-1}] , the χ^2 of the spectral fit.

MJD start	Time [min]	N_{ON}	N_{OFF}	N_{EXC}	Significance [σ]	Flux > 300 GeV [ph cm^{-2} s^{-1}]	Spectral index	Normalization [ph cm^{-2} s^{-1} TeV^{-1}]	χ^2/ndf
54141	55.9	585.0	208.3	376.7	16.1	$(1.19 \pm 0.09)\times10^{-10}$	2.61±0.14	$(0.25\pm0.03)\times10^{-10}$	5.11/3
54382	65.7	859.0	457.0	402.0	12.5	$(1.09 \pm 0.10)\times10^{-10}$	2.38±0.15	$(0.28\pm0.03)\times10^{-10}$	2.95/5

Table 6.3: Results of the Mrk 501 high zenith angle observations in 2007. The table contains: *MJD start* - the MJD date of the start of the observation, *Time* [min] - the duration of the observation in minutes, the measured number of ON, OFF and excess events, the significance of the measurement [σ], the upper limit on the integral flux above 300 GeV calculated with a confidence level of 90% [ph cm^{-2} s^{-1}], the integral flux above 300 GeV and its statistical error [ph cm^{-2} s^{-1}].

MJD start	Time [min]	N_{ON}	N_{OFF}	N_{EXC}	Significance [σ]	UL(90%) [ph cm^{-2} s^{-1}]	Flux > 300 GeV [ph cm^{-2} s^{-1}]
54182.12	30.1	185.0	179.7	5.3	0.3	2.67×10^{-11}	$(0.3\pm1.1)\times10^{-11}$
54211.06	27.2	117.0	92.4	24.6	1.9	—	$(2.0 \pm 1.1)\times10^{-11}$
54226.99	20.1	119.0	129.9	-10.9	-0.75	1.65×10^{-11}	$(-1.0 \pm1.4)\times10^{-11}$
54231.01	22.8	72.0	63.2	8.8	0.85	3.15×10^{-11}	$(0.8 \pm 1.0)\times10^{-11}$
54238.98	30.4	109.0	102.6	6.4	0.5	2.47×10^{-11}	$(0.4 \pm 0.9)\times10^{-11}$
54295.04	35.8	171.0	147.7	23.3	1.4	—	$(1.4 \pm 1.0)\times10^{-11}$
54321.97	27.6	123.0	100.7	22.3	1.7	—	$(1.7 \pm 1.0)\times10^{-11}$
54325.96	25.3	112.0	82.5	29.5	2.4	—	$(2.4 \pm 1.1)\times10^{-11}$
54344.91	35.5	372.0	210.2	161.8	7.6	—	$(9.4 \pm 1.3)\times10^{-11}$
54348.90	35.7	347.0	219.2	127.8	6.0	—	$(7.2 \pm 1.2)\times10^{-11}$
54353.89	37.5	317.0	254.2	62.8	2.9	—	$(3.4 \pm 1.2)\times10^{-11}$
54356.87	31.1	176.0	164.9	11.1	0.7	3.42×10^{-11}	$(0.8 \pm 1.2)\times10^{-11}$
54372.84	41.8	405.0	335.7	69.3	2.8	—	$(3.3 \pm 1.2)\times10^{-11}$
54375.84	8.5	86.0	56.2	29.8	2.8	—	$(7.1 \pm 2.6)\times10^{-11}$
54381.84	23.5	259.0	188.4	70.6	3.7	—	$(5.7 \pm 1.6)\times10^{-11}$

Table 6.4: Parameters of the power law (PL) fits to Mrk 501 spectra for data taken in 2007. Table contains: *MJD start* - the MJD date of the start of the observation, the spectral index and its statistical error, the normalization of the spectra at 1 TeV and its statistical error [ph cm^{-2} s^{-1} TeV^{-1}] , the χ^2/ndf of the spectral fit.

MJD start	Spectral index	Normalization [ph cm^{-2} s^{-1} TeV^{-1}]	χ^2/ndf
54344.91	-2.05 ± 0.18	$(0.10 \pm 0.02)\times10^{-9}$	2.63/3
54348.90	-2.78 ± 0.45	$(0.79 \pm 0.15)\times10^{-10}$	7.36/3

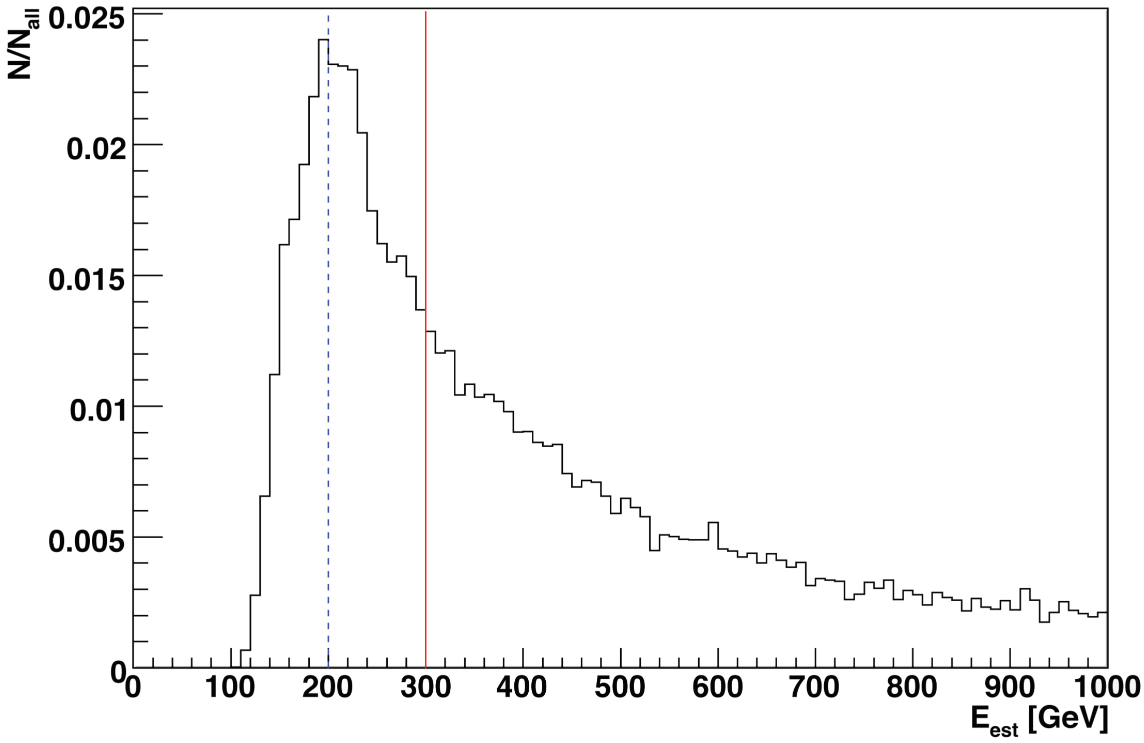

Figure 6.7: Distribution of the estimated energy (E_{est}) of the MC γ-ray events after applying the optimal cuts for the low zenith angle data sample of Mrk 501 collected in 2007: Hadronness < 0.1, Size > 200 and Alpha < 6°. The Y-axis gives the number of events in each energy bin normalized to the number of all events which passed the cuts. The blue dashed line marks the analysis threshold of ~200 GeV, the red solid line marks the chosen threshold above which all flux values are calculated.

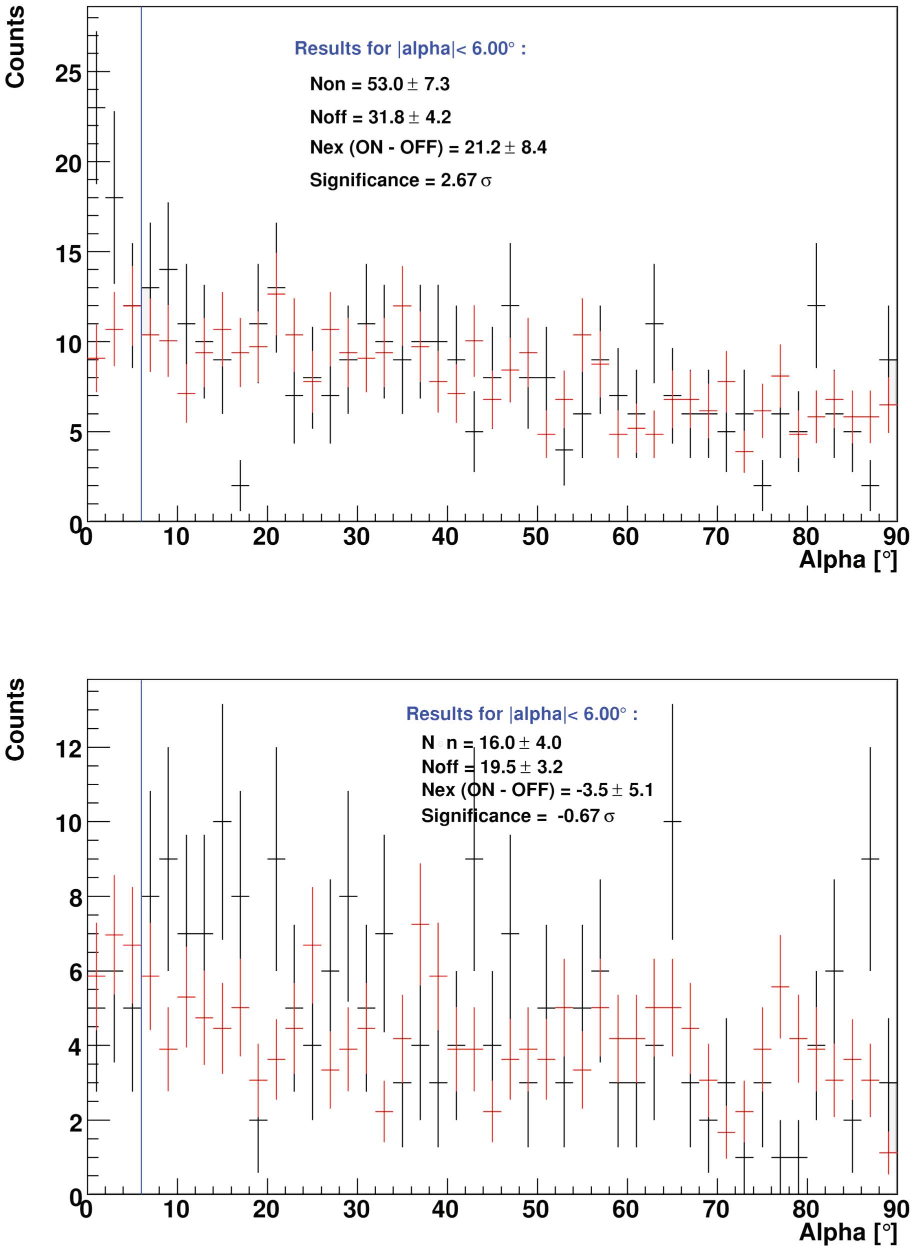

Figure 6.8: Alpha distributions for the most (MJD 54211.08) and least (MJD 54269.91) significant measurements taken from Mrk 501 observations in 2007 under low zenith angles. The red data points denote the background sample, the black points the data sample containing the γ-ray candidate events.

Table 6.5: Observation parameters for PKS1424+240 data after quality selection, used as hadron sample for the analysis of Mrk 501 low zenith angle data collected in 2007. Table content - see caption of Tab. 6.1.

MJD start	Time [min]	DT [a.u.]	ZA [deg]	Mean rate [Hz]
54152	91.0	14.0 (D)	10 - 30	235
54155	87.6	14.4 (D)	10 - 30	220

Monitoring data

In 2008 Mrk 501 monitoring data was taken in wobble mode, mostly during twilight (7.84 h) or moderate moonlight (4.37 h). After a quality selection 534.4 min (8.9 h), of low zenith angle (11°- 29°) data were analyzed. The γ-hadron separation and energy estimation was done using matrices trained on the events from part of the rejected files (with DT $<$ 20).

The Hadronness, Size and Alpha cuts were optimized on Crab data taken on MJD 54491 and tested on MJD 54798 (Tab. 6.8). The resulting optimal cuts are: Hadronness < 0.05, Alpha$< 6°$, Size > 450 phe. In order not to loose low energy events a lower size cut of 250 phe was applied. Table 6.8 summarizes the results obtained on Crab data (with Size $>$ 250 phe). In Fig. 6.9 the distribution of the estimated energy E_{est} for MC γ-ray events after training and application of the "optimal cuts" is shown. The analysis threshold of $\sim$200 GeV is marked with the blue dashed line, but in order to be consistent with the high zenith angle measurements all fluxes were calculated for energies above 300 GeV (red line).

Table 6.9 reports the results for Mrk 501. The mean flux measured above 300 GeV equals $3.20 \pm 1.71 \times 10^{-11}$ ph cm^{-2} s^{-1}, i.e. $\sim$40% of the Crab Nebula flux. Figure 6.10 shows the Alpha distributions of the most and least significant measurements.

Multiwavelength campaign

Mrk 501 was a target of many multiwavelength campaigns mainly in flaring states. The MAGIC data reported here were taken between MJD 54550 and 54602 during extensive MW observations covering radio (Effelsberg, IRAM, Medicina, Mets ahovi, Noto, RATAN-600, VLBA), optical (GASP-WEBT), UV (Swift/UVOT), X-ray (Swift/XRT, XRTE/PCA, Swift/BAT) and γ-ray (MAGIC, Whipple, VERITAS) frequencies. A short report from the campaign can be found in [K$^+$09], it will be presented in more detail in an upcoming paper. The results reported in this section, especially the spectral energy distribution, are discussed in section 6.4.4 .

MAGIC data was taken in ON mode during dark nights (32.5 h), twilight (0.13 h) and moderate moonlight (16.9 h). After quality selection 1835.78 min (30.6 h) of low zenith angle data (11°- 30°) were analyzed. The γ-hadron separation and energy estimation was done using matrices trained on events from part of the rejected files (with DT $<$

Table 6.6: Results of the analysis of the Crab Nebula data sample used for optimization and test of cuts for the analysis of Mrk 501 low zenith angle data collected in 2007. Table content - see caption of Tab. 6.2.

MJD start	Time [min]	N$_{ON}$	N$_{OFF}$	N$_{EXC}$	Significance [σ]	Flux > 300 GeV [ph cm^{-2} s^{-1}]	Spectral index	Normalization [ph cm^{-2} s^{-1} TeV^{-1}]	χ^2/ndf
54147	83.3	501.0	124.0	377.0	17.7	$(1.25 \pm 0.09)\times10^{-10}$	2.54±0.11	$(0.27 \pm 0.03)\times10^{-10}$	3.44/5
54382	76.5	513.0	188.7	324.3	14.7	$(1.21 \pm 0.10)\times10^{-10}$	2.36±0.13	$(0.30 \pm 0.03)\times10^{-10}$	5.40/5

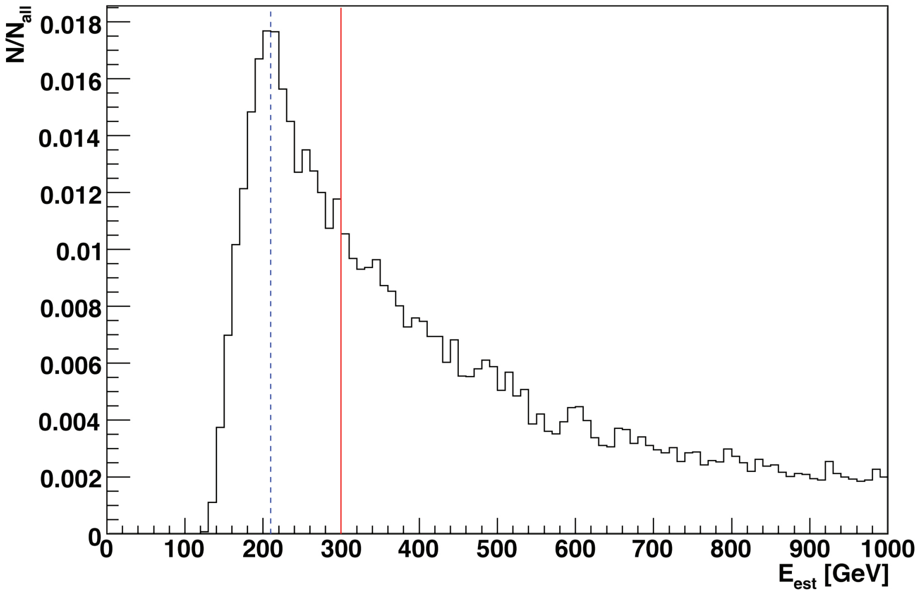

Figure 6.9: Distribution of the estimated energy (E_{est}) of the MC γ-ray events after applying the optimal cuts for the data sample of Mrk 501 collected in 2008 during the AGN monitoring program: Hadronness < 0.05, Size > 250 and Alpha $< 6°$. The Y-axis gives the number of events in each energy bin normalized to the number of all events which passed the cuts. The blue dashed line marks the analysis threshold, the red solid line marks the chosen threshold above which all flux values are calculated.

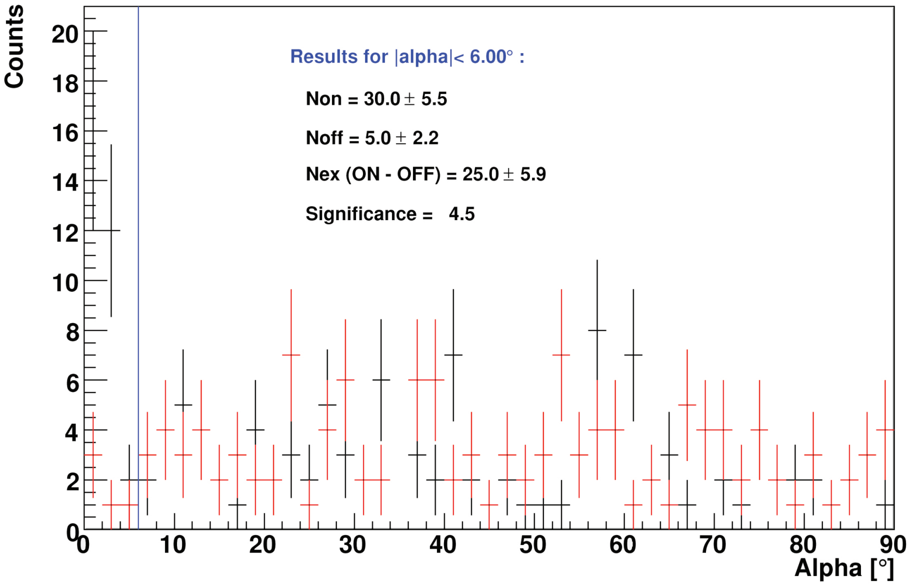

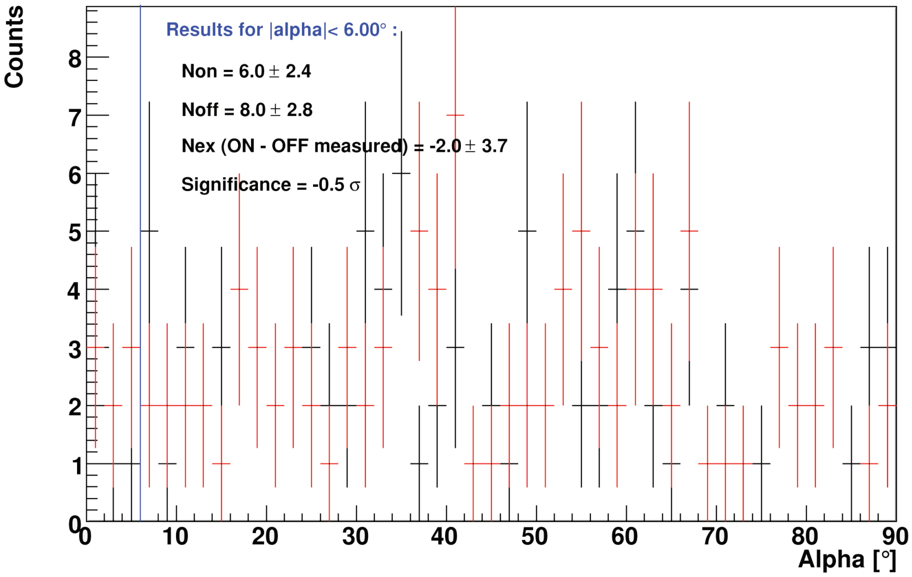

Figure 6.10: Alpha distributions for the most (MJD 54540.26) and least (MJD 54677.89) significant measurements taken from Mrk 501 observations in 2008 during the AGN monitoring program. The red data points denote the background sample, the black points the data sample containing the γ-ray candidate events.

20). Since Crab is not visible for MAGIC in May, in order to optimize the cuts for the dark (moon) observations the Mrk 501 data from MJD 59591 (MJD 54554) were divided into two samples (odd and even run numbers). To find the cuts which would give the best sensitivity all combinations of Hadroness, Size and Alpha values were applied to the "odd sample". Additional cut of Dist $< (1.0 + (\log_{10}(\text{Size}) - 2.5) \cdot 0.2)$ was also used in order to reject the events which could artificially broaden the Alpha distribution and fake the signal . The resulting optimal cuts are:

- odd sample MJD 59591: Hadroness < 0.1, $\alpha < 8.0°$, Size > 200 phe → Significance $= 7.2\,\sigma$,
- odd sample MJD 54554: Hadroness < 0.1, $\alpha < 6.0°$, Size > 250 phe → Significance $= 6.6\,\sigma$.

Those cuts were tested on the "even sample", and gave similar results:

- even sample MJD 59591: Hadroness < 0.1, $\alpha < 8.0°$, Size > 200 phe → Significance $= 7.7\,\sigma$,
- even sample MJD 54554: Hadroness < 0.1, $\alpha < 6.0°$, Size > 250 phe → Significance $= 5.4\,\sigma$.

Fig. 6.11 shows the distributions of the estimated energy E_{est} for MC γ-ray events after training and application of the "optimal cuts". The blue dashed line marks the analysis threshold ~180 GeV, but in order to be consistent with the high zenith angle measurements all fluxes were calculated for energies above 300 GeV.

Unfortunately no suitable OFF data was taken in this period, since it was important to maximize the observation time on the source. In order to calculate the flux values a polynomial (maximally 3^{rd} order) fit to the distributions of ON events in the Alpha region 30° - 90° away from the source position was performed and then extrapolated to the source region. The number of excess events N_{EXC} was calculated as the difference between the N_{OFF} predicted by the fit and the measured N_{ON}. The measured fluxes are reported in Table 6.10, the mean flux value above 300 GeV was found to be $(2.6 \pm 0.7) \times 10^{-11}$ cm^{-2} s^{-1}, i.e. did not exceed 40% of the Crab Nebula flux. Figure 6.12 shows the Alpha distributions with background fits with the highest (MJD 54557.16) and lowest (MJD 54597.06) probability from all of the measurements taken during this multiwavelength campaign. The fit probability is calculated using a maximum likelihood method, i.e. a higher fit probability indicates a better fit. The fit is rejected if the probability value is below 0.01 and the measurement is discarded from the analysis.

6.4.3 Light curve

Figure 6.13 and 6.14 show the light curves of Mrk 501 obtained from the analysis of the data taken between February 2007 and August 2008. The source was found in a rather low state with flux values rarely exceeding 0.5 Crab level. An important quality of this

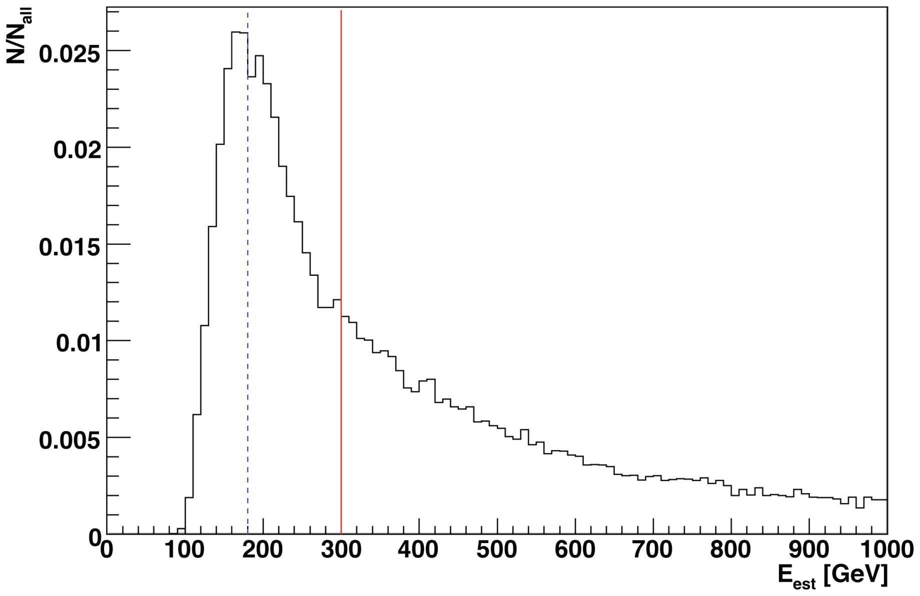

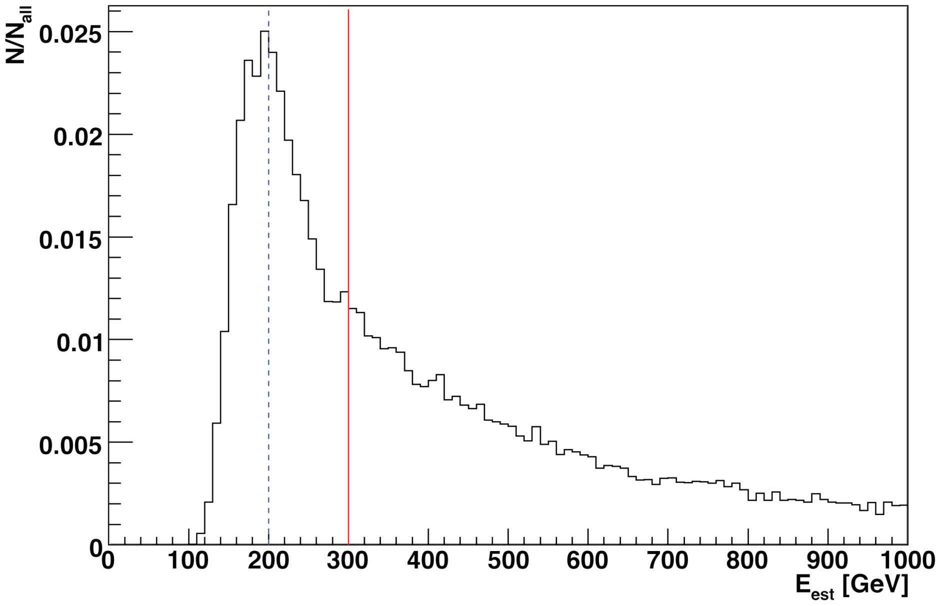

Figure 6.11: Distributions of the estimated energy (E_{est}) of the MC γ-ray events after applying the optimal cuts for the dark (top) and moon/twilight (bottom) data sample of Mrk 501 collected during the multiwavelength campaign in 2008. The Y-axis gives the number of events in each energy bin normalized to the number of all events which passed the cuts. The blue dashed line marks the analysis threshold, the red solid line marks the chosen threshold above which all flux values are calculated.

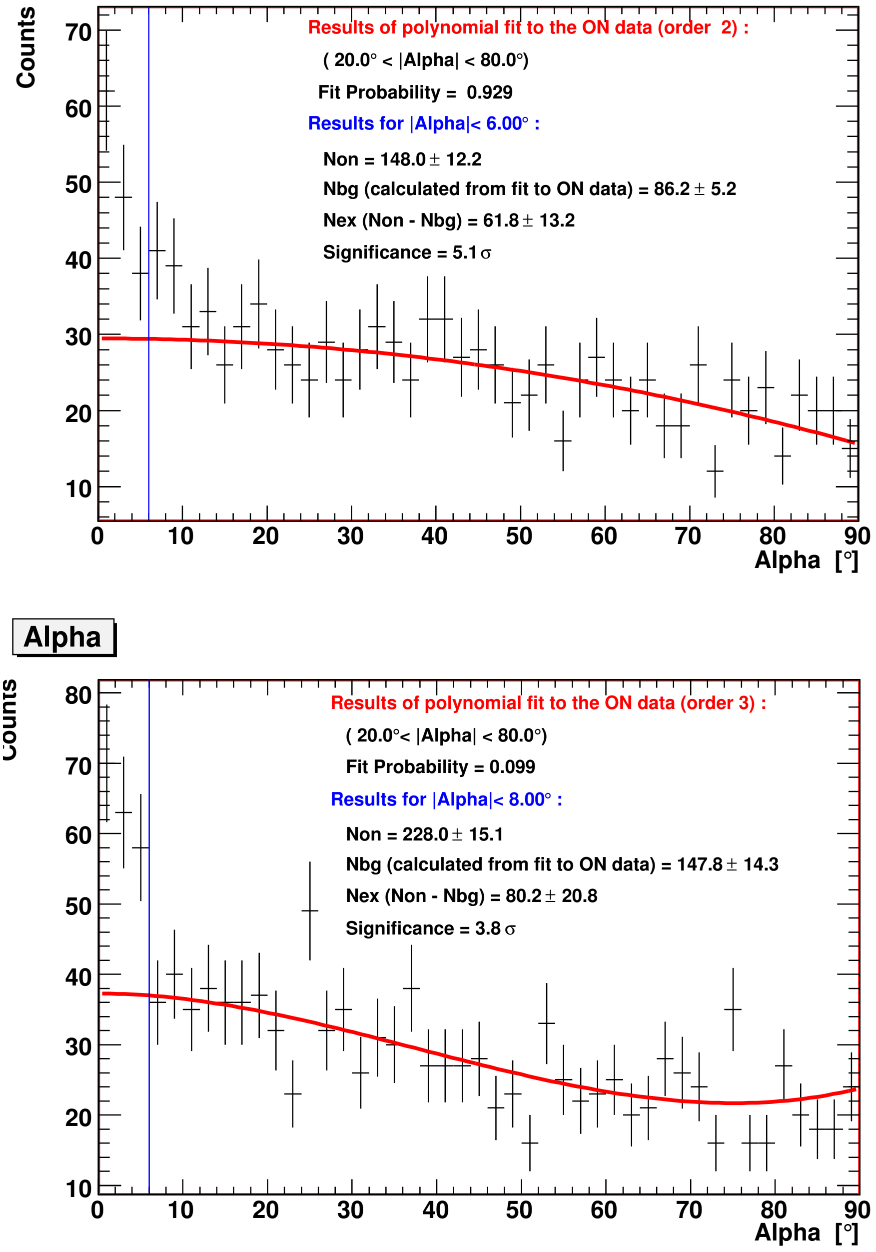

Figure 6.12: Alpha distributions with background fits with the highest (MJD 54557.16) and lowest (MJD 54597.06) probability of describing the data correctly, from all of the measurements taken in 2008 during the multiwavelength campaign. The red data points denote the background sample, the black points the data sample containing the γ-ray candidate events.

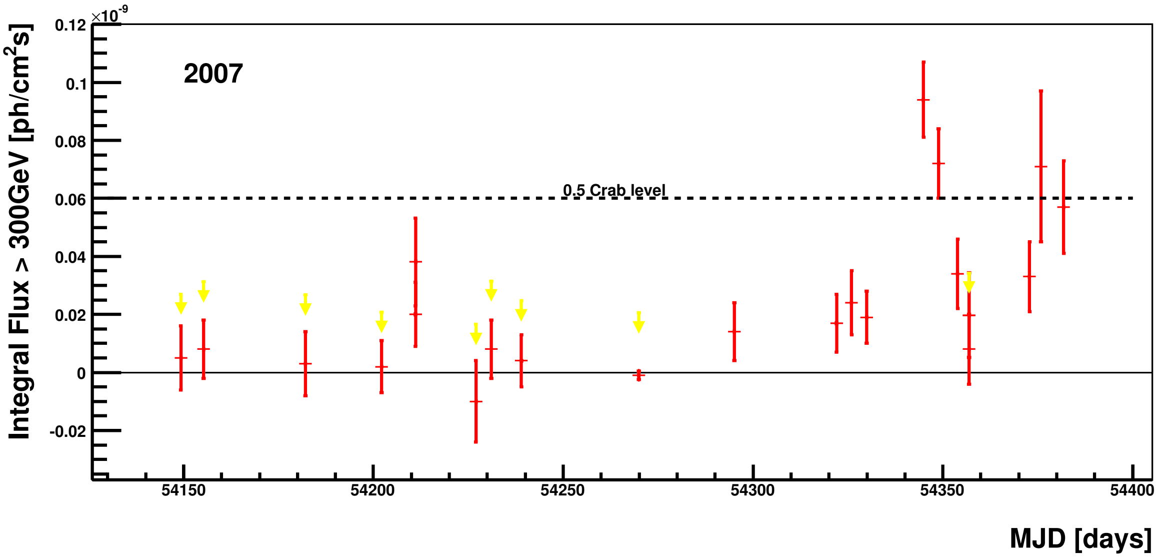

Figure 6.13: Mrk 501 light curve for the year 2007. The red points denote the flux values measured above 300 GeV, the yellow arrows 90% C.L. upper limits calculated using the Rolke method (see section 6.3 for details).

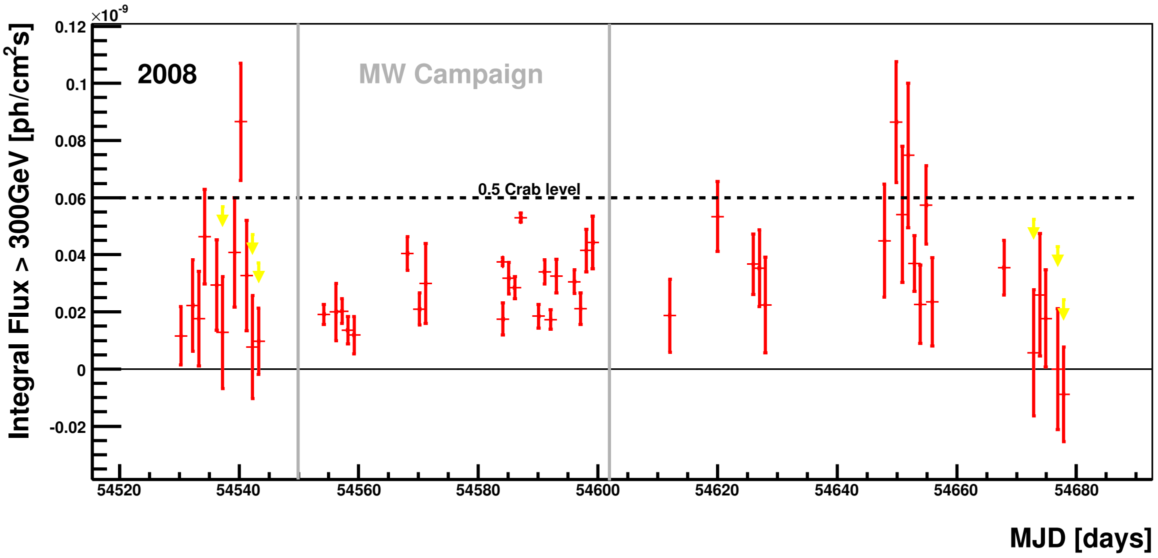

Figure 6.14: Mrk 501 light curve for the year 2008. The red points denote the flux values measured above 300 GeV, the yellow arrows 90% C.L. upper limits calculated using the Rolke method (see section 6.3 for details).

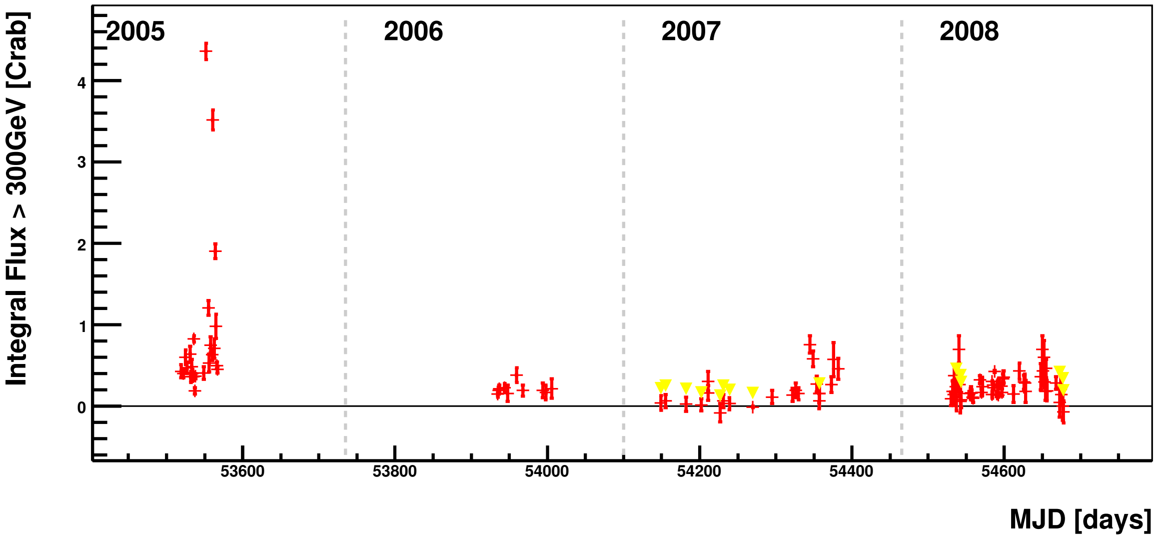

Figure 6.15: Mrk 501 light curve for the period from 2005 untill 2008 as measured by the MAGIC telescope. The 2005 data are taken from [A+07j] and 2006 from [G+07b].

light curve is quite a dense sampling which is very important for statistical studies, such as the one reported in Chapter 5.

The light curve with all MAGIC data from 2005 untill 2008 is shown in Fig 6.15. Since 2005 no flares were observed for this source.

6.4.4 The broad band Spectral Energy Distribution

The multiwavelength campaign performed between MJD 54550 and 54602 covered a large part of the energy spectrum of Mrk 501 from radio to γ-ray frequencies. Figure 6.16 shows the measured light curves normalized to the average flux observed by each experiment (some of the instruments were excluded from the plot for clarity). One can immediately see that in the low energy range the source emitted a rather constant flux and that the variability is more pronounced at higher energies. In order to quantify the flux variability, for measurements from each instrument which took part in the campaign, the fractional variability parameter F_{var} was calculated according to the method of [V+03]. The F_{var} is defined as:

$$F_{var} = \sqrt{\frac{S^2 - < \sigma_{err}^2 >}{< F_\gamma >}} \tag{6.3}$$

where $< F_\gamma >$ denotes the average photon ßux, S the standard deviation of the N flux measurements and $\sigma_{err}^2 >$ the mean squared error. As reported in [K+09] the F_{var} seems to increase with energy (see Fig. 6.17), although in the VHE γ-ray range it is affected

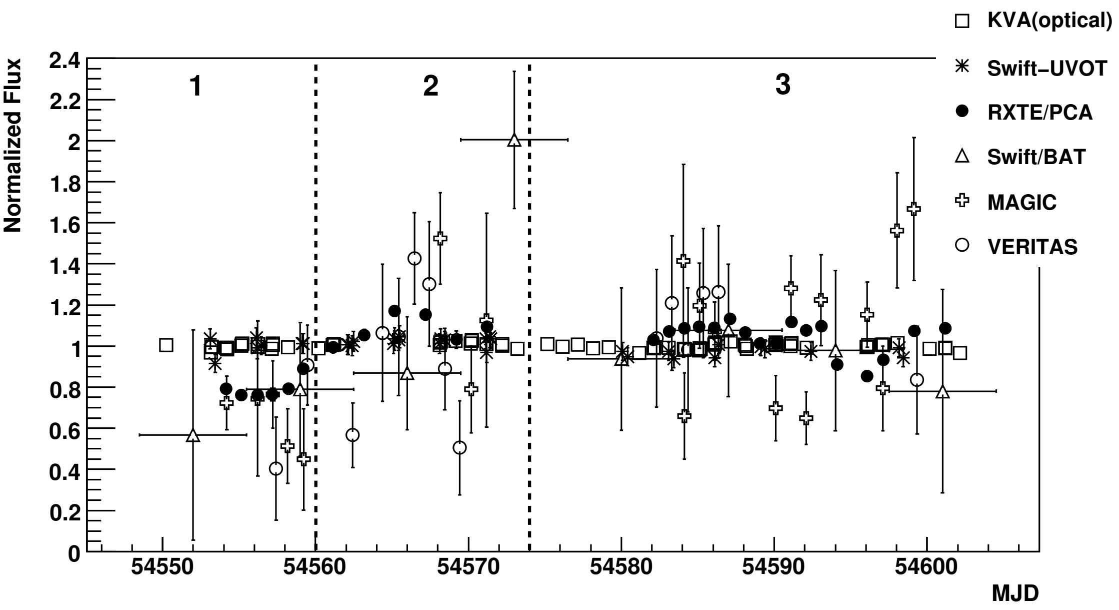

Figure 6.16: Mrk 501 multifrequency light curve as measured during the multiwavelength campaign in 2008. The flux values for each instrument were normalized to the mean flux value. Some instruments were omitted in the plot for clarity. In order to analyze the spectral behavior of the source, the data was divided into three periods denoted by numbers and vertical, dashed lines. Figure from [K$^+$09].

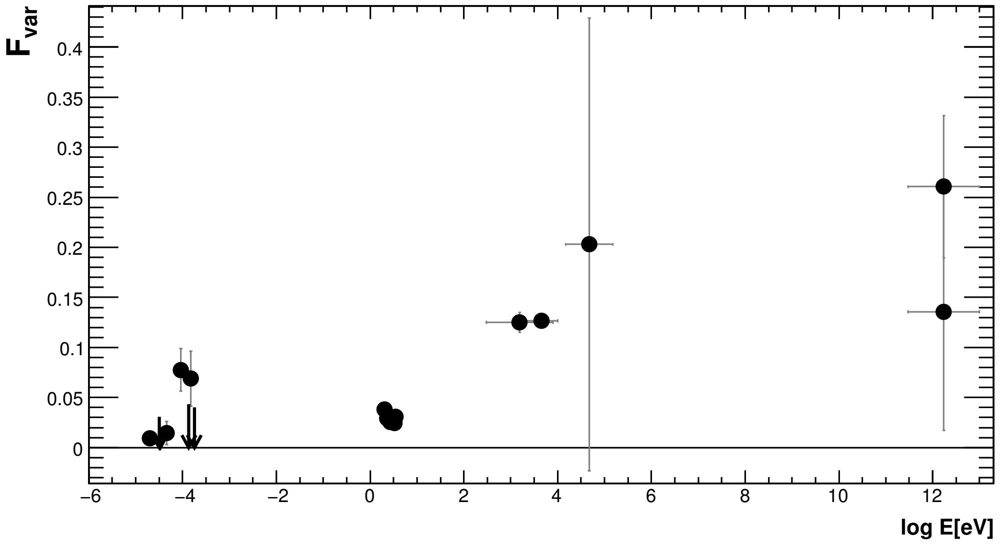

Figure 6.17: Mrk 501 fractional variability parameter F_{var} for all the instruments participating in the campaign. F_{var} was derived using the individual single-night flux measurements except for Swift/BAT for which data integrated over one week was used. Vertical bars denote $1\,\sigma$ uncertainties, horizontal bars indicate the approximate energy range covered by the instrument. The arrows indicate 95% confidence level upper limits. Figure from [K$^+$09].

by a large uncertainty, due to large errors on the measured flux.

Search for correlated variability using the Discrete Correlation Function (DCF) proposed in [EK88] revealed a significant correlation for RXTE/PCA - Swift/XRT (hard - soft X-ray) with the DCF maximum of 0.87 ± 0.28 with no time lag. A less significant correlation was found for RXTE/PCA - MAGIC and VERITAS pairs (hard X-ray - VHE γ-rays) with a value of 0.5 ± 0.19, also with no time lag (see Fig.6.18). Taking into account the large flux errors and rather moderate flux variability it is difficult to draw a strong conclusion from this analysis.

Table 6.11 presents the spectral fit values to data collected by MAGIC. In Fig 6.19 they are plotted against the measured fluxes. The two measurements from the year 2007 are also shown. Due to large uncertainties on both the measured fluxes and spectral indices and the small range of flux values no firm conclusion about a correlation between the flux state and the hardness of the spectra in the VHE γ-ray region can be made.

For the modeling of the spectra the data was divided into three periods according to the activity in the X-ray energy range (see Fig. 6.16). In period 1 Mrk 501 was less active than in periods 2 and 3 which show similar flux states (period 3 was defined because of a time gap in the observations of some of the instruments). The average spectra for each period as measured by MAGIC are reported in Table 6.12 and Table 6.13 - after EBL correction using the Kneiske Low model [K$^+$04a]. All photon indices values are compatible within the errors.

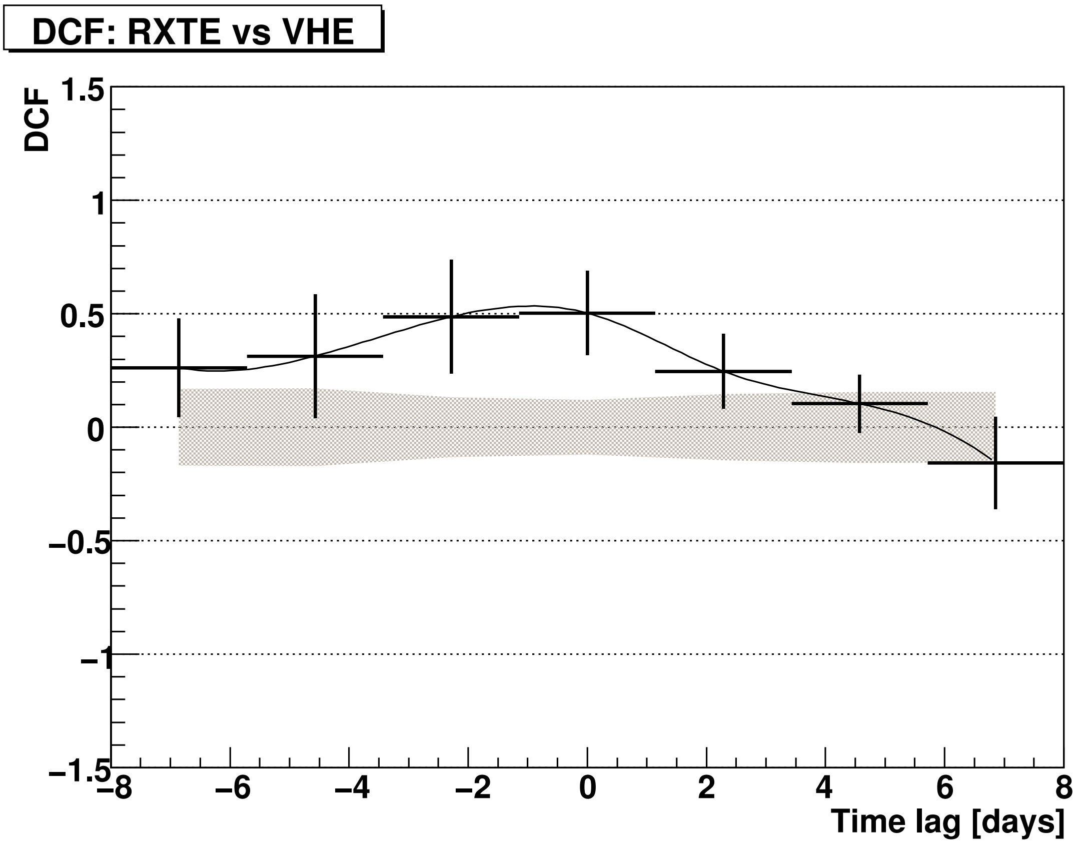

Figure 6.18: Mrk 501 Discrete Correlation Function for the VHE γ-ray (combined MAGIC and VERITAS measurements) and hard X-ray (RXTE), for time lags from −8 to +8 days in steps of ∼2 days. The grey band represents the expected fluctuation of the DCF values in the case of completely uncorrelated time series, given the error bars from the actual observations. Figure from [K+09].

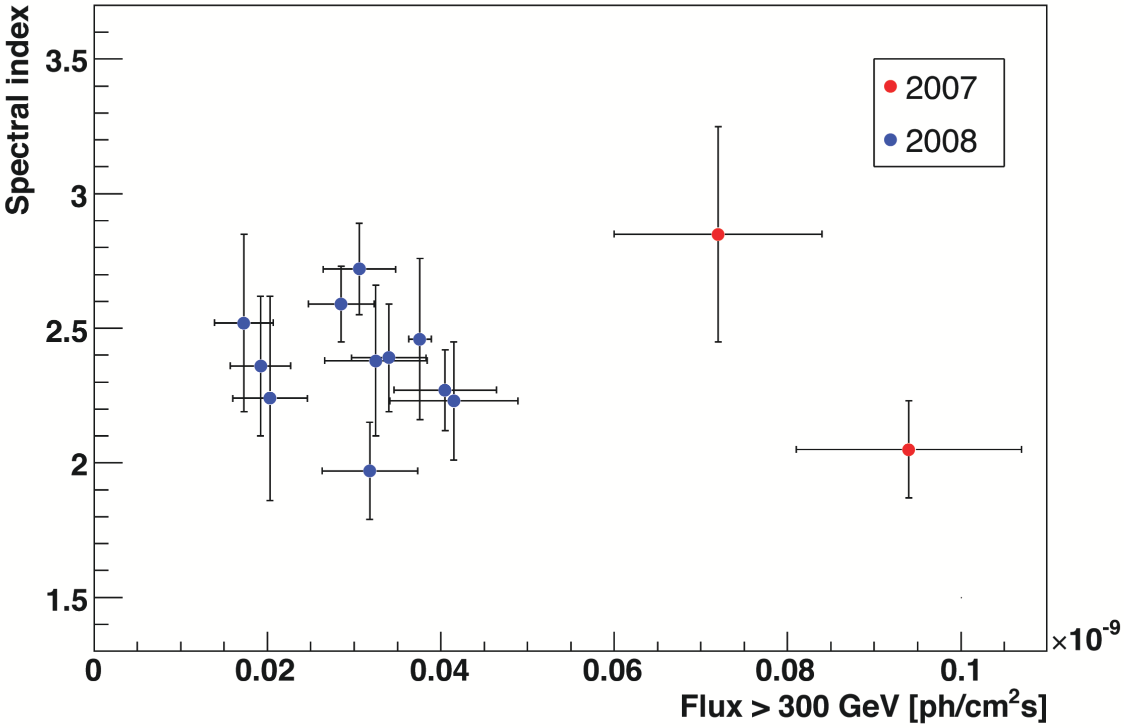

Figure 6.19: Mrk 501 F(>300 GeV) plotted against the photon index measured on the same day by MAGIC.

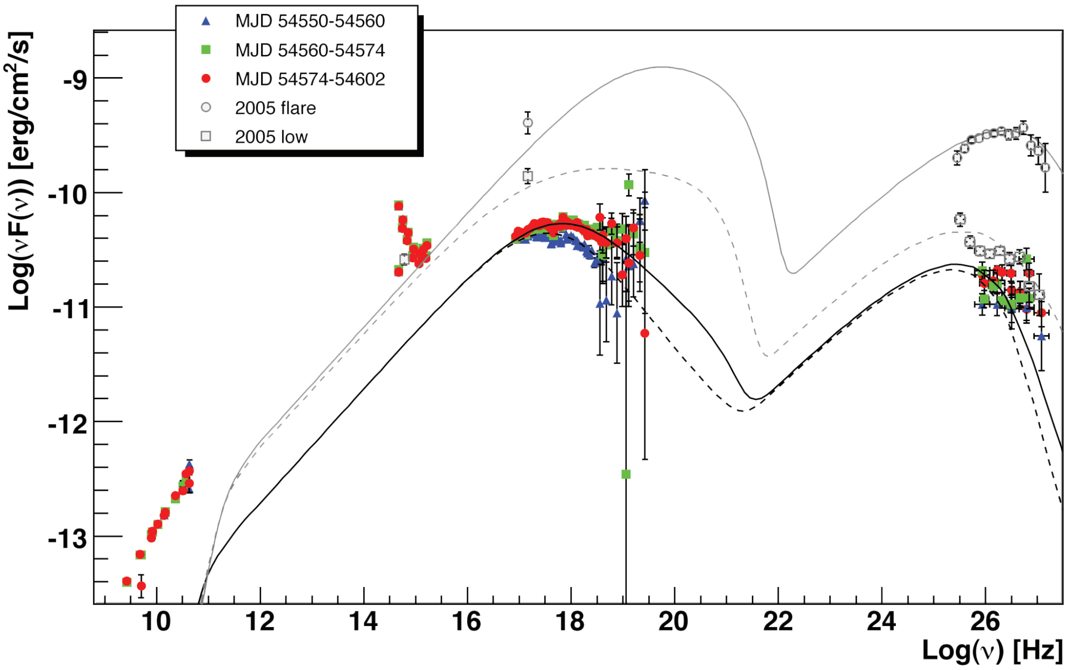

Figure 6.20: Broadband SED for Mrk 501 as obtained during the multiwavelength campaign in 2008 in comparison to those from a past low and high state from 2005. The results from a SSC model fit to the low state 2008 data (dot-dashed cuve), the high state 2008 data (heavy-dashed curve), the 2005 low state (light-dashed curve) and the 2005 high state (solid curve) are shown. The parameters of the fits are given in Table 6.14.

The broadband SED for each of the periods and the historical data from 2005 [A^{+}07j] are shown in Fig 6.20. The lines in the figure depict the results of a 1-zone SSC leptonic model fit to the data.

The model was developed by [T^{+}98b] (see section 1.6.1). It assumes a spherical emission region of radius R moving with a Lorenz factor Γ and observed at an angle θ resulting in a Doppler factor δ. The magnetic field of strength B is tangled and uniform. The injected electron population has a broken power law distribution with a particle density K, spectral indices n_1 and n_2 and break energy γ_{break}. The parameter values for the two different emission states during this campaign and the campaign in 2005 are given in Table 6.14. The model reproduces the X-ray data very well. The transition from the low to high emission state can be explained by an injection of fresh high energy electrons, which lead to the shift of the break energy to higher values and hardening of the electron spectrum. Also the hints of variability increasing with energy and correlation between the emission states in X-ray and TeV bands seems to support this model.

Nevertheless, the significant discrepancy between the model prediction and the measurements in the low energy range cannot be ignored. It could be due to the fact that the intrinsic photon absorption processes, like the synchrotron self absorption were not taken into account in this model. Earlier studies of the Mrk 501 SED [KSK01][VR99] suggest that a radiation from a different emission region can be responsible for the fluxes observed at the radio-optical frequencies. This hypothesis seems to be supported by the fact that the model parameters for fits to the data from the year 2005 differ significantly from the ones derived in this work. The SED coverage was much sparser in 2005 and allows for larger degeneracies in the parameter space, but while the the X-ray and γ-ray fluxes changed substantially between those two epochs, the fluxes at optical frequencies remained approximately the same. This observation fits especially well into the "blob-in-the-jet" model by [KSK01] where the authors assume that the low frequency radiation comes from a slowly changing jet while the rapid flux variations and flares observed in X-ray and γ-rays are due to a blob of relativistic plasma moving along the jet. In Fig 6.21 a fit to historical Mrk 501 data using this model is presented.

6.5 1ES1959+650 - analysis results

The source was discovered already in 1998 by the Utah Seven Telescope Array [N^{+}99], which reported a signal with a significance of $3.9\,\sigma$ after 56.7 hours of observation. Detection of an ”orphan” TeV flare in 2002 [K^{+}04b] made 1ES 1959+650 one of the most interesting VHE γ-ray sources. MAGIC is observing this object since 2004 [A^{+}06f], and a regular monitoring was first performed in 2005 [G^{+}07b]. Unfortunately, the source position allows observations only under a relatively high zenith angles (35-50 deg). Moreover, when not in a high state the source is rather faint in comparison with Mrk 501.

MAGIC monitored 1ES 1959+650 from April 2007 until October 2008 for 30.7 hours under large zenith angle (35°-50°). The source was observed in wobble mode. The summary of the observations performed by MAGIC as well as data selection for the analysis is presented in Tables 3 and 4 in Appendix B.

6.5.1 Data collected in 2007

After the quality selection 12.7 h (out of 18.1 h) of data taken from 1ES 1959+650 in 2007 were left for analysis. The matrices for γ-hadron separation and energy estimation were trained using data taken from the faint extragalactic source 1ES0235+164 considered as a hadron sample (see Table 6.15).

The cuts were optimized on data taken from Crab Nebula on MJD 54141 and then tested on MJD 54382. The combination of Hadroness < 0.2, Alpha $< 6°$ and Size $>$ 300 phe yielded the highest significance. Details can be found in Table 6.16. In Fig. 6.22 the distributions of the estimated energy E_{est} for MC γ-ray events after training and application of the "optimal cuts" is shown. The red solid line marks the analysis threshold $\sim 300\,\text{GeV}$.

Table 6.17 presents the results of the 1es1959+650 data analysis. The overall significance of the signal from this data sample is 6.44 σ (see Fig. 6.23 for the Alpha

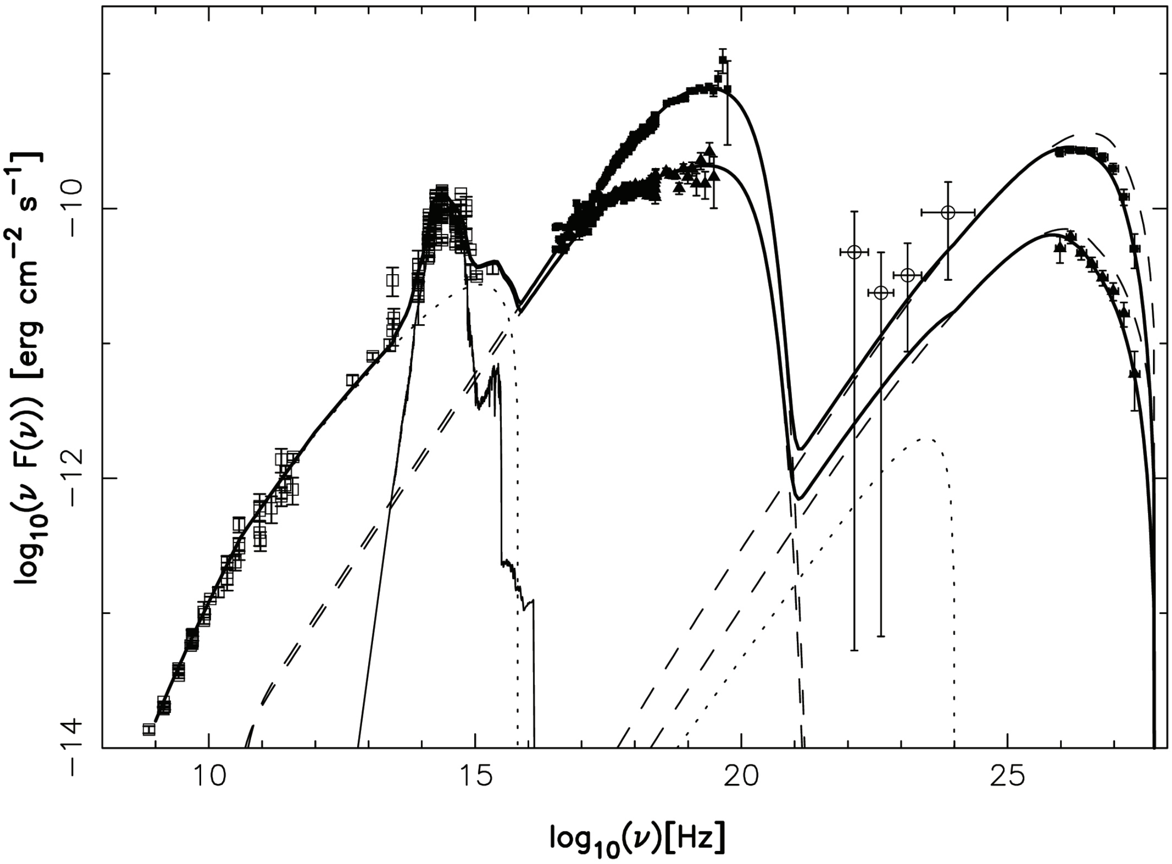

Figure 6.21: Mrk 501 broadband SED model by Katarzynski et al. [KSK01]. The authors assume that the low frequency radiation comes from a slowly changing jet while the rapid flux variations and flares observed in X-ray and γ-rays are due to a blob of relativistic plasma moving along the jet. The dashed line depicts the contribution from the blob, the dotted line from the jet, the thin continuous line from the host galaxy and the solid line the sum of all three.

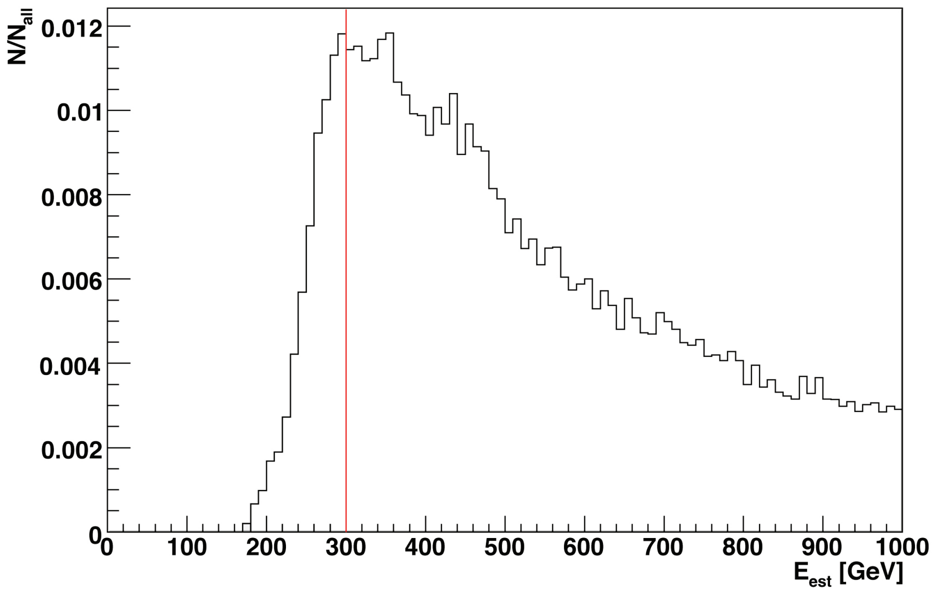

Figure 6.22: Distribution of the estimated energy (E_{est}) of the MC γ-ray events after applying the optimal cuts for the data sample of 1ES 1959+650 collected in 2007 during the AGN monitoring program: Hadronness < 0.2, Size $>$ 300 phe and Alpha $< 6°$. The Y-axis gives the number of events in each energy bin normalized to the number of all events which passed the cuts. The red line marks the analysis threshold.

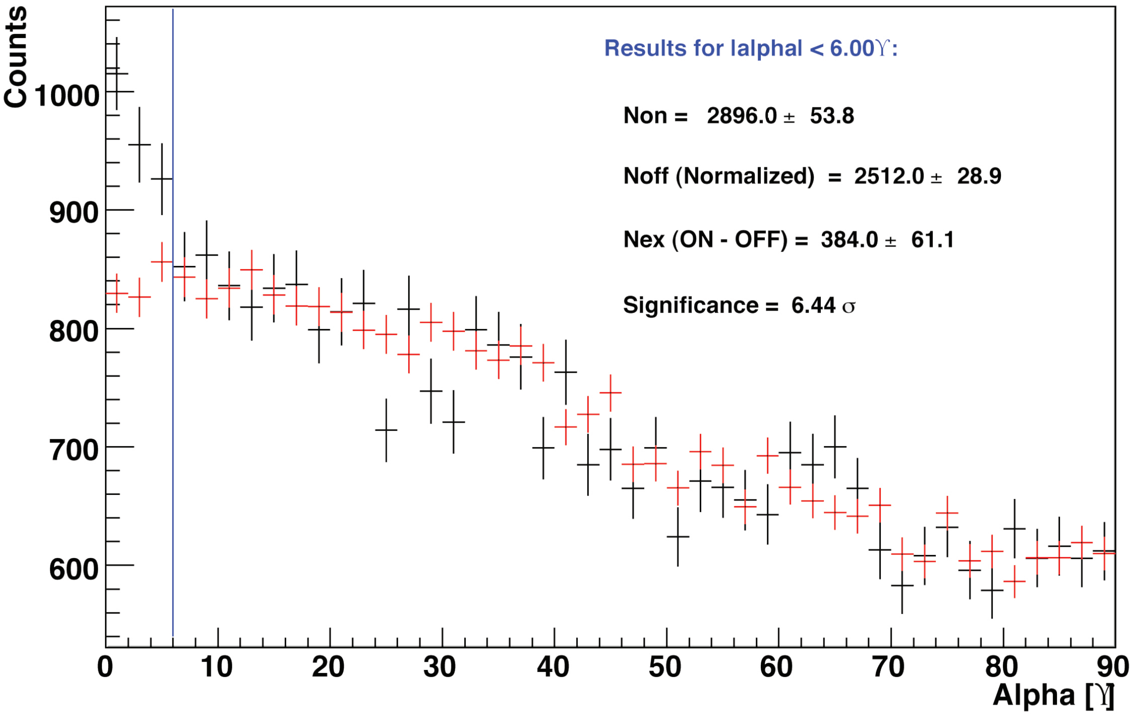

Figure 6.23: Alpha distribution for the 1ES1959+650 data collected in 2007. Red data points denote the background sample, the black points the data sample containing the γ-ray candidate events.

distribution), so an average spectrum for the observation period April - November 2007 was derived, it is discussed in section 6.5.4.

6.5.2 Data collected in 2008

The observations of 1ES1959+650 in 2008 were performed during dark nights (6.44 h), twilight (4.34 h) and moderate moonlight (1.88 h). After the quality selection only 3.4 h of data were left for further analysis.

The γ-hadron separation and energy estimation was done using matrices trained on part of the rejected files (with DT<20). The optimal cuts: Hadronness < 0.05, Alpha$<$ $6°$, Size > 250 phe were determined using Crab data from MJD 54448 and tested on MJD 54444 (Table 6.18). Distributions of the estimated energy E_{est} for MC γ-ray events after training and application of the "optimal cuts" is shown in Fig. 6.24. The analysis energy threshold $\sim$ 300 GeV is indicated with the red solid line.

The overall significance of the signal from the 1ES1959+650 data sample from 2008 is $2.5\,\sigma$ (see Fig. 6.25 for the Alpha distribution) which allows to set an upper limit on the flux above 300 GeV of: F(E$\geq$ 300 GeV) $\leq 2.53\times10^{-11}$ ph/cm^2/s ($\sim$20% Crab flux),

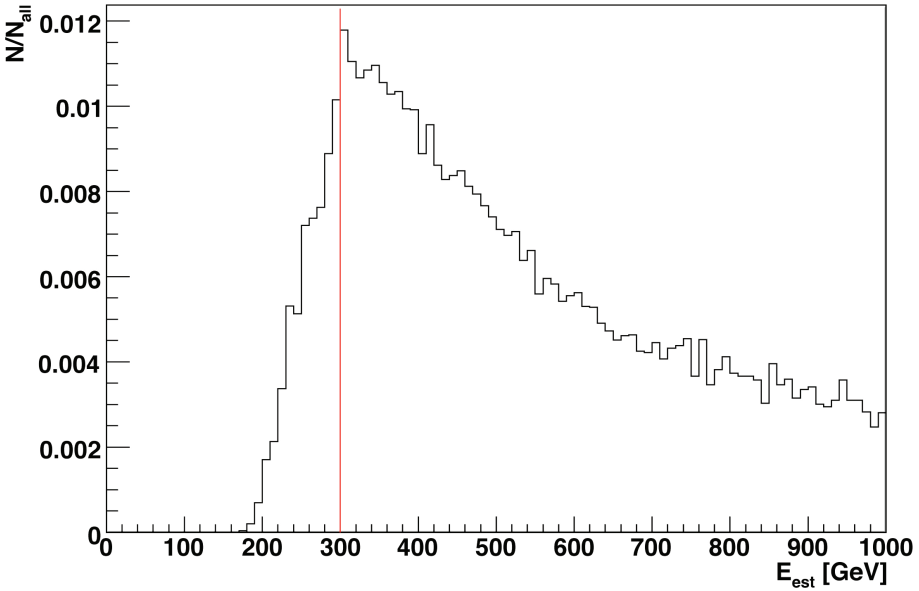

Figure 6.24: Distribution of the estimated energy (E_{est}) of the MC γ-ray events after applying the optimal cuts for the data sample of 1ES 1959+650 collected in 2008 during the AGN monitoring program: Hadronness < 0.05, Size $>$ 250 phe and Alpha $< 6°$. The Y-axis gives the number of events in each energy bin N normalized to the number of all events which passed the cuts N_{All}. The red line marks the analysis threshold.

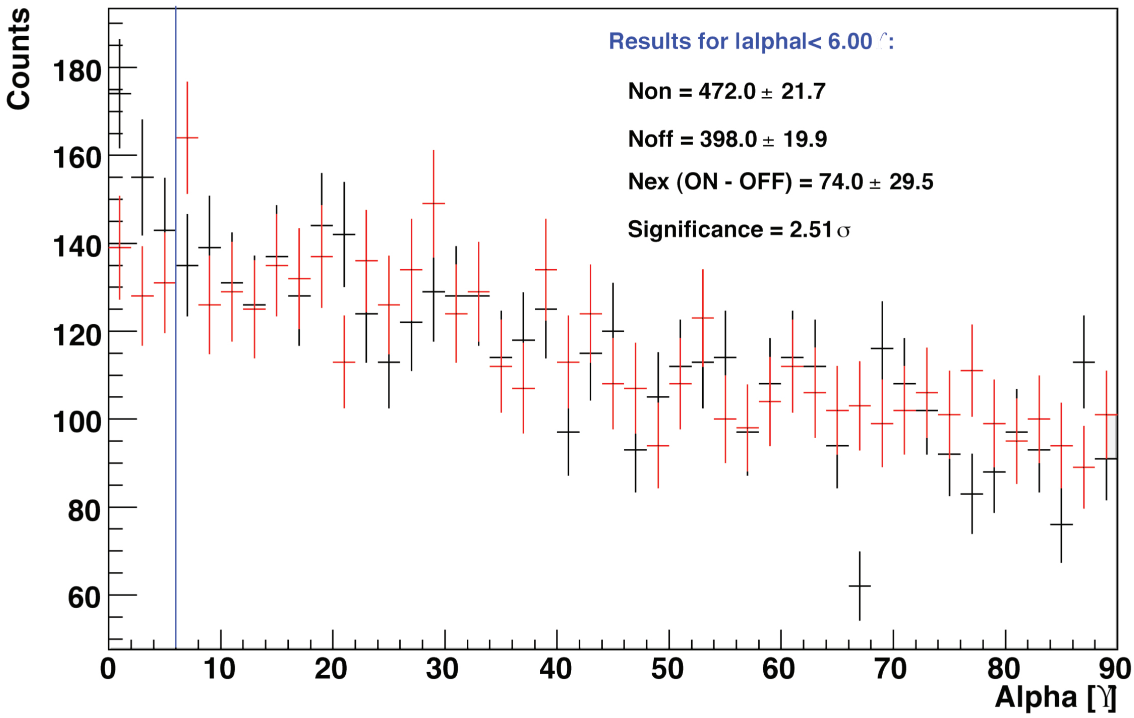

Figure 6.25: Alpha distribution for the 1ES1959+650 data collected in 2008. Red data points denote the background sample, the black points the data sample containing the γ-ray candidate events.

at 90% C.L.

6.5.3 Light curve

In 2007 the average 1ES1959+650 γ-ray flux above 300 GeV observed by MAGIC was only $(1.43\pm\ 0.34)\times10^{-11}$ ph cm^{-2} s^{-1}, i.e. ~12% of Crab. The light curve for 1ES1959+650 in 2007 is shown in Fig. 6.26, all measurements with significances 1 σ were converted to flux upper limits. The light curve does not indicate major changes of the flux level or flares. Previous MAGIC observations in 2004 [A+06f] and 2006 [T+08a] also found the source in a non variable low state with mean fluxes above 300 GeV of ~17% Crab and ~10% Crab respectively (see Fig 6.27). Since the outburst in 2002 no flares were observed for this source.

6.5.4 VHE gamma-ray spectrum

The average spectrum for the 1ES1959+650 data from 2007 was unfolded using both the Bertero and Tikhonov methods. The results agree within error, but the second method

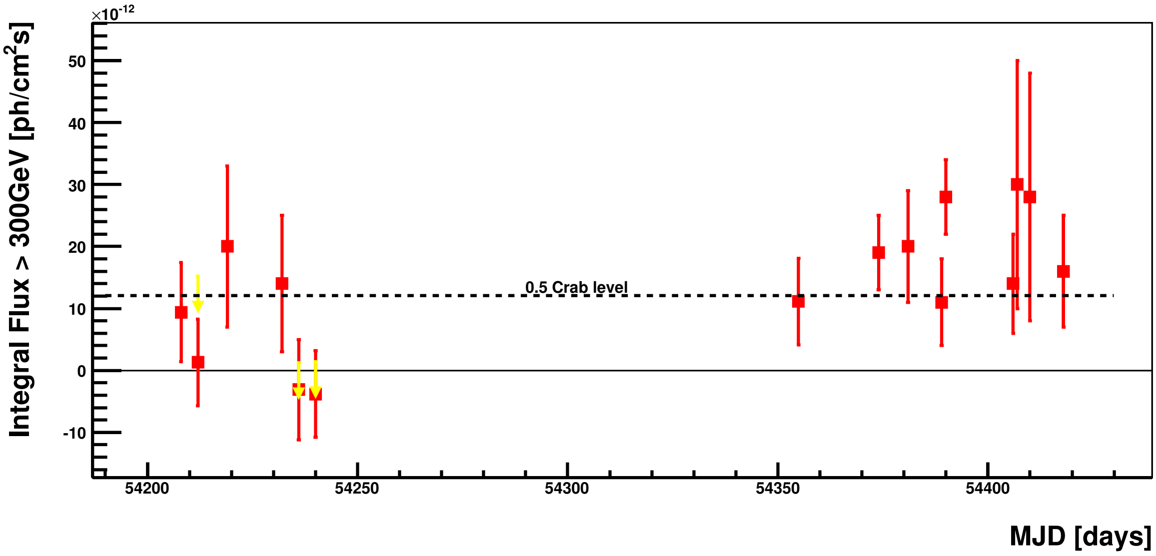

Figure 6.26: 1ES1959+650 light curve measured in 2007. The red points denote the flux values measured above 300 GeV, the yellow arrows 90% C.L. upper limits calculated using the Rolke method (see section 6.3 for details).

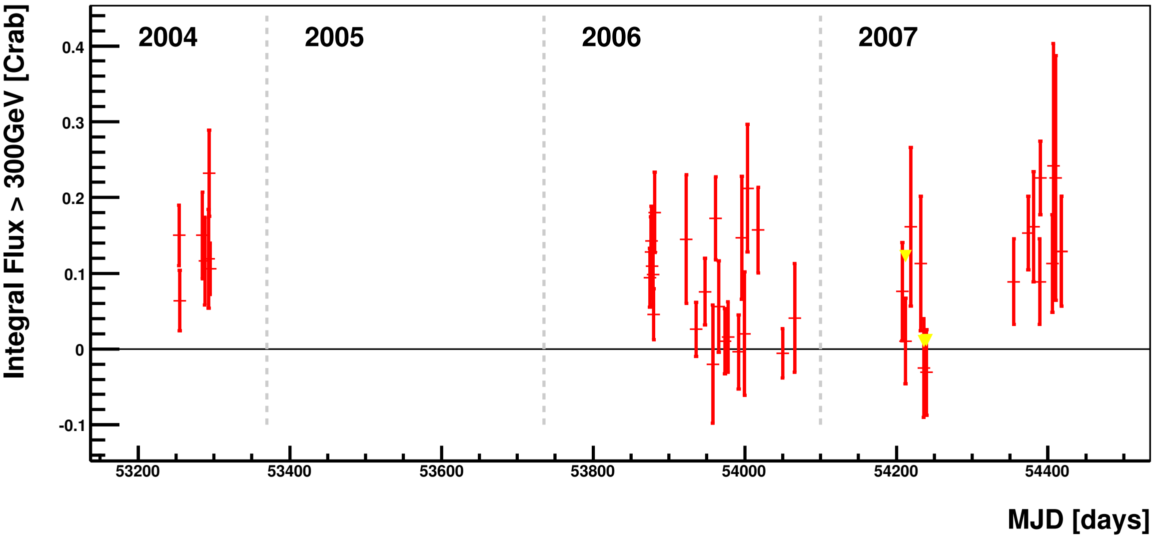

Figure 6.27: 1ES1959+650 light curve as measured by the MAGIC telescope from 2004 until 2007.

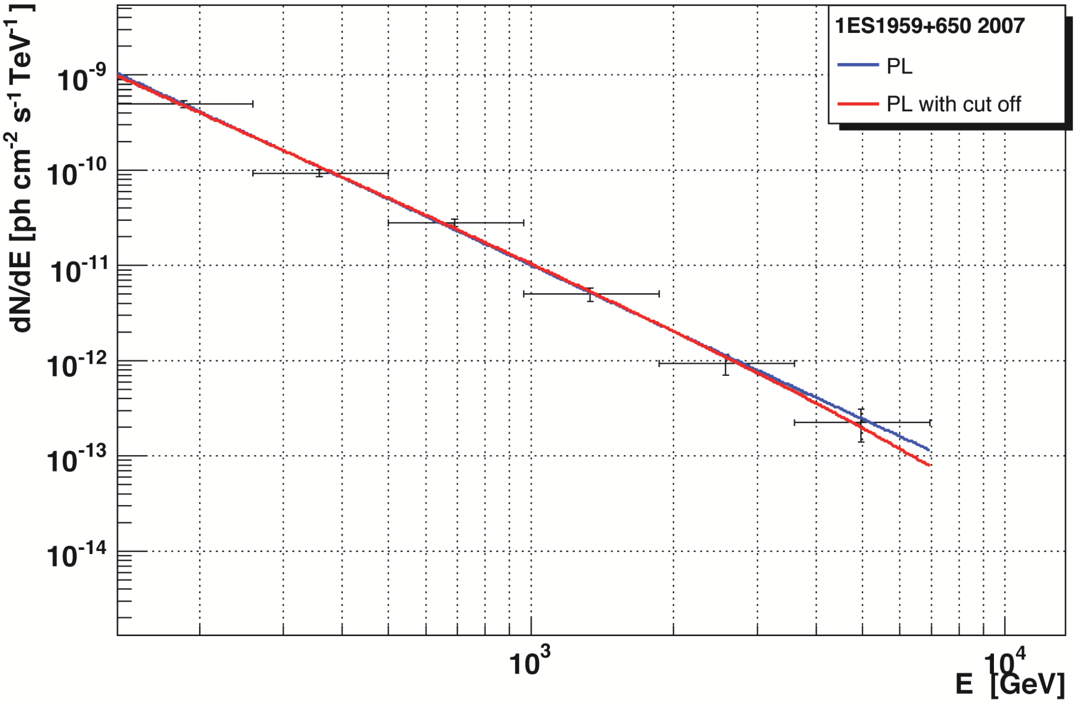

Figure 6.28: Average energy spectrum for 1ES1959+650 from data taken in 2007 and unfolded using the Bertero method. The blue line depicts a fit with a power law (PL) and the red line a fit with a power law with a cutoff (PL with cutoff). The parameters of the fits can be found in Table 6.20.

yielded an additional point at the energy of 9.6 TeV. The shape of the distribution before unfolding suggested a fit with a power law with a cut off (PLwC). After the unfolding the spectrum was fitted with both the PLwC and a simple power law (PL). The PL fit resulted in a better χ^2. Table 6.20 and Figure 6.28 show the results obtained with both unfolding methods and both fit functions. The derived spectral indices are harder than the ones measured by MAGIC in 2004 ($\alpha_{2004} = -2.72 \pm 0.14$) and 2006 ($\alpha_{2006} = -2.58 \pm 0.18$) when the source was in a similarly low state.

6.6 Summary

In the years 2007 and 2008, in the framework of the AGN monitoring program, MAGIC observed Mrk 501 for 88.6 h (including 30.7 h of data collected during the MW campaign in 2008) and 1ES1959+650 for 30.7 h. Around 60% of these observations were performed during twilight or moderate moonlight. For Mrk 501 44% of the collected data, and for 1ES1959+650 48%, were excluded from this analysis because of unstable or too low event rate and too high discriminator thresholds.

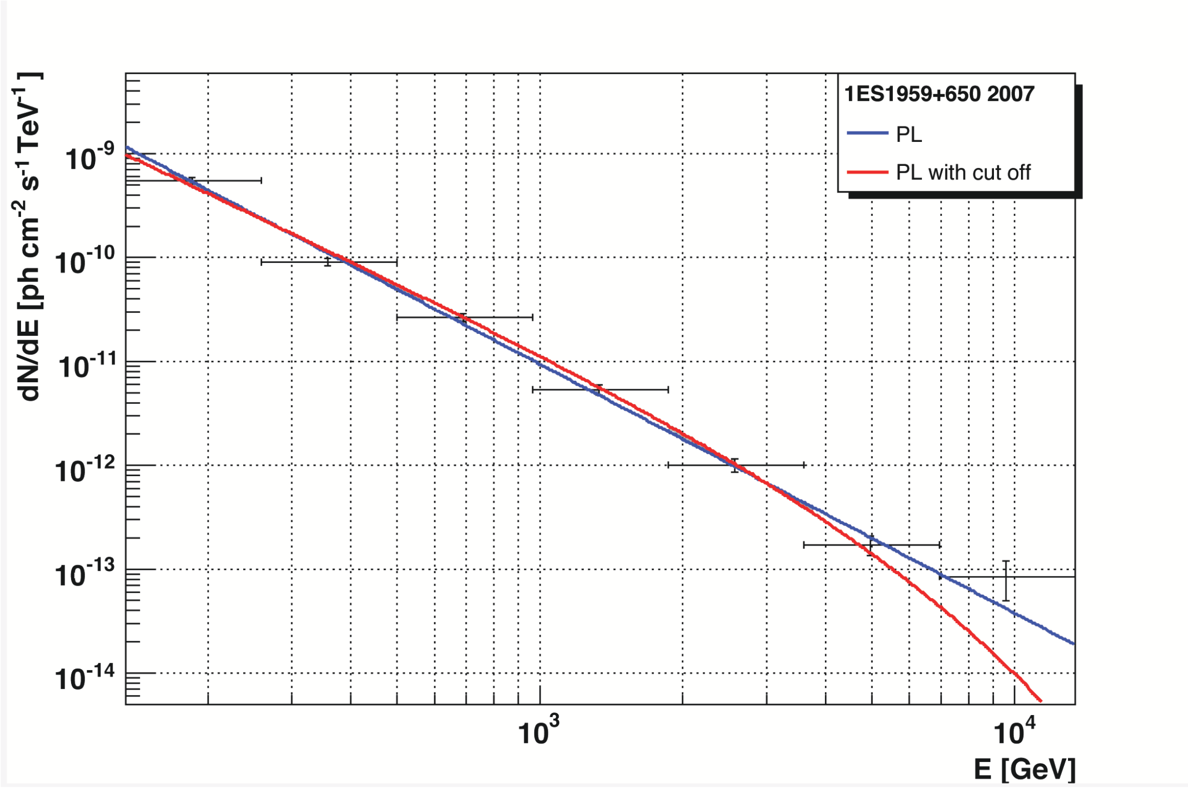

Figure 6.29: Average energy spectrum for 1ES1959+650 from data taken in 2007 and unfolded using the TIkhonov method. The blue line depicts a fit with a power law (PL) and the red line a fit with a power law with a cutoff (PL with cutoff). The parameters of the fits can be found in Table 6.20.

Both sources were found in a low state and showed moderate (Mrk 501) or no variability (1ES1959+650) with no prominent flares. The average flux of Mrk 501, integrated above 300 GeV, was ~0.19 Crab in 2007 and ~0.24 Crab in 2008. For Mrk 501 spectra were calculated for all data sets with a signal significance exceeding $5\,\sigma$. Due to large uncertainties on both the measured fluxes and derived spectral indices no firm conclusion about a correlation between the flux state and the hardness of the spectra can be made. The broad-band SED of the source, measured during a MW campaign in 2008, was modeled with a 1-zone SSC leptonic model [T^{+}98b], which reproduced the X-ray data very well. Observed hints of variability increasing with energy and the correlation between the emission states in X-ray and TeV bands are also in agreement with this model. Still, a significant discrepancy exists between the model prediction and the measurements in the radio-optical range, which can point to a different emission region as a source of the radiation in the low energy range (see e.g. [KSK01]).

The average flux measured from 1ES1959+650 in 2007 was ~0.12 Crab. For the observations in 2008 an upper limit for the average flux of ~0.20 Crab was set. An average spectrum for the year 2007 was calculated and fitted with two different functions: a simple power law and a power law with a cut-off. The power law function with the spectral index of -2.31 ± 0.05 gave the best quality fit.

The MAGIC AGN monitoring program aims at collecting large and un-biased data samples for sources which are potential neutrino emitters. This is very important for any reliable statistical study. In the discussed observational period this goal was achieved for Mrk 501, the light curve of which was very densely sampled. 1ES1959+650 is a faint source and MAGIC can observe it mostly under rather unfavorable conditions (moonlight, high zenith angle), therefore a large portion of the data was excluded from this analysis. Nevertheless, one should expect that, with the recently introduced model of the moonlight influence on the MAGIC observations [B^{+}09b] , the efficiency of the analysis of the data, collected when the NSB level is high, will increase. Also the stereo observations, with both MAGIC telescopes, will significantly improve the sensitivity of the instrument for faint sources.

Table 6.7: Results of the Mrk 501 low zenith angle observations in 2007. Table content - see caption of Tab. 6.3.

MJD start	Time [min]	N$_{ON}$	N$_{OFF}$	N$_{EXC}$	Significance [σ]	UL(90%) [ph cm^{-2} s^{-1}]	Flux > 300 GeV [ph cm^{-2} s^{-1}]
54149.26	28.1	72.0	67.1	4.9	0.5	2.7×10^{-11}	$(0.5 \pm 1.1)\times10^{-11}$
54155.25	31.6	75.0	66.0	9.0	0.9	3.12×10^{-11}	$(0.8 \pm 1.0)\times10^{-11}$
54202.16	41.3	69.0	66.1	2.9	0.3	2.07×10^{-11}	$(0.2 \pm 0.9)\times10^{-11}$
54211.08	17.1	53.0	31.8	21.2	2.7	—	$(3.81 \pm 1.51)\times10^{-11}$
54269.91	9.8	16.0	19.5	-3.5	-0.7	2.05×10^{-11}	$(-1.0 \pm 1.5)\times10^{-12}$
54329.88	51.8	140.0	106.2	31.8	2.3	—	$(1.9 \pm 0.9)\times10^{-11}$
54356.85	21.1	69.0	55.5	13.5	1.4	—	$(1.97 \pm 1.46)\times10^{-11}$

Table 6.8: Results of the analysis of the Crab Nebula data sample used for optimization and test of cuts for the analysis of Mrk 501 data collected in 2008 during the AGN monitoring program. Table content - see caption of Tab. 6.2.

MJD start	Time [min]	N_{ON}	N_{OFF}	N_{EXC}	Significance [σ]	Flux > 300 GeV [ph cm^{-2} s^{-1}]	Spectral index	Normalization [ph cm^{-2} s^{-1} TeV^{-1}]	χ^2/ndf
54491	61.2	322.0	61.7	260.3	14.3	$(1.48 \pm 0.11)\times10^{-10}$	-2.54 ±0.12	$(0.37 \pm 0.04)\times10^{-10}$	0.86/3
54798	60.6	295.0	67.1	227.9	15.1	$(1.37 \pm 0.11)\times10^{-10}$	-2.51 ± 0.11	$(0.30 \pm 0.03)\times10^{-10}$	1.17/4

Table 6.9: Results of Mrk 501 observations taken in 2008 during the AGN monitoring program. Table content - see caption of Tab. 6.3.

MJD start	Time [min]	N_{ON}	N_{OFF}	N_{EXC}	Significance [σ]	Flux > 300 GeV [ph cm^{-2} s^{-1}]	UL(90%) [ph cm^{-2} s^{-1}]
54530.26	22.13	17.0	11.0	6.0	1.1	$(1.16 \pm 1.02) \times10^{-11}$	—
54532.26	14.4	16.0	9.0	8.0	1.4	$(2.22 \pm 1.60) \times10^{-11}$	—
54533.26	15.6	19.0	13.0	6.0	1.1	$(1.76 \pm 1.66) \times10^{-11}$	—
54534.26	11.9	19.0	7.0	12.0	2.4	$(4.63 \pm 1.66) \times10^{-11}$	—
54536.26	17.1	23.0	12.0	11.0	1.9	$(2.94 \pm 1.58) \times10^{-11}$	—
54537.26	11.0	12.0	9.0	3.0	0.7	$(1.28 \pm1.96) \times10^{-11}$	5.69×10^{-11}
54539.26	9.2	11.0	3.0	9.0	2.2	$(4.08 \pm 1.91) \times10^{-11}$	—
54540.26	13.5	30.0	5.0	25.0	4.5	$(8.66 \pm 2.05) \times10^{-11}$	—
54541.26	11.4	15.0	7.0	8.0	1.7	$(3.28 \pm 1.93) \times10^{-11}$	—
54542.26	12.1	12.0	10.0	2.0	0.4	$(0.77 \pm 1.80) \times10^{-11}$	4.71×10^{-11}
54543.25	14.6	8.0	5.0	3.0	0.8	$(0.97 \pm 1.16) \times10^{-11}$	3.71×10^{-11}
54612.04	25.9	34.0	23.0	11.0	1.5	$(1.87 \pm 1.28) \times10^{-11}$	—
54620.00	38.6	85.0	37.0	48.0	4.4	$(5.34 \pm 1.23) \times10^{-11}$	—
54625.98	41.3	76.0	39.0	37.0	3.5	$(3.67 \pm 1.06) \times10^{-11}$	—
54626.98	28.4	54.0	30.0	24.0	2.6	$(3.53 \pm 1.35) \times10^{-11}$	—
54627.99	17.2	27.0	18.0	9.0	1.35	$(2.24 \pm 1.67) \times10^{-11}$	—
54647.89	9.8	20.0	8.0	12.0	2.3	$(4.49 \pm 1.98) \times10^{-11}$	—
54649.89	8.6	22.0	2.0	20.0	4.4	$(8.64 \pm 2.12) \times10^{-11}$	—
54650.90	8.3	20.0	8.0	12.0	2.3	$(5.41 \pm 2.38) \times10^{-11}$	—
54651.89	8.5	25.0	8.0	17.0	3.0	$(7.48 \pm 2.53) \times10^{-11}$	—
54652.90	46.4	86.0	43.0	43.0	3.8	$(3.70 \pm 0.98)\times10^{-11}$	—
54653.90	23.6	43.0	29.0	14.0	1.7	$(2.27 \pm 1.37) \times10^{-11}$	—
54654.89	25.1	50.0	22.0	38.0	4.3	$(5.74 \pm 1.37) \times10^{-11}$	—
54655.89	17.9	32.0	21.0	9.0	1.5	$(2.35 \pm 1.55) \times10^{-11}$	—
54667.89	37.2	47.0	17.0	30.0	3.8	$(3.55 \pm 0.95) \times10^{-11}$	—
54672.89	8.0	8.0	7.0	1.0	0.3	$(0.57 \pm 2.21) \times10^{-11}$	5.25×10^{-11}
54673.89	9.0	11.0	6.0	5.0	1.2	$(2.60 \pm 2.14) \times10^{-11}$	—
54674.89	13.2	14.0	9.0	5.0	1.0	$(1.77 \pm 1.70) \times10^{-11}$	—
54676.89	7.7	6.0	6.0	0.0	0.0	$(0.0 \pm 2.11) \times10^{-11}$	4.28×10^{-11}
54677.89	10.6	6.0	8.0	-2.0	-0.5	$(-0.88 \pm 1.66) \times10^{-11}$	2.42×10^{-11}

Table 6.10: Results of Mrk 501 observations performed during the multiwavelength campaign in 2008. Table content - see caption of Tab. 6.3.

MJD start	Time [min]	N_{ON}	N_{OFF}	N_{EXC}	Significance [σ]	Flux > 300 GeV [ph cm^{-2} s^{-1}]
54554.14	132.4	177.0	97.5	79.5	6.1	$(1.92 \pm 0.35)\times10^{-11}$
54556.21	16.0	48.0	30.8	17.2	2.00	$(2.0 \pm 1.0)\times10^{-11}$
54557.16	102.7	148.0	86.2	61.8	5.1	$(2.03 \pm 0.43)\times10^{-11}$
54558.13	150.7	276.0	207.6	68.4	2.8	$(1.36 \pm 0.48)\times10^{-11}$
54559.21	24.2	17.0	8.8	8.2	2.0	$(1.19 \pm 0.65)\times10^{-11}$
54568.12	124.8	343.0	177.8	165.2	6.6	$(4.05 \pm 0.59)\times10^{-11}$
54570.14	114.7	199.0	126.0	73.0	3.7	$(2.10 \pm 0.56)\times10^{-11}$
54571.19	11.2	18.0	8.5	9.5	2.6	$(3.0 \pm 1.4)\times10^{-11}$
54584.06	14.4	38.0	18.8	19.2	3.6	$(3.76 \pm 0.13)\times10^{-11}$
54584.08	55.0	88.0	49.5	38.5	4.5	$(1.75 \pm 0.56)\times10^{-11}$
54585.05	86.6	204.0	112.4	91.6	6.3	$(3.18 \pm 0.55)\times10^{-11}$
54586.05	152.0	300.0	155.8	144.2	8.3	$(2.85 \pm 0.38)\times10^{-11}$
54587.05	104.7	29.0	10.4	18.6	3.8	$(5.3 \pm 1.6)\times10^{-12}$
54590.04	136.0	290.0	206.0	84.0	4.6	$(1.85 \pm 0.42)\times10^{-11}$
54591.04	137.3	331.0	171.	160.0	8.7	$(3.40 \pm 0.43)\times10^{-11}$
54592.05	108.9	121.0	59.6	61.4	5.6	$(1.73 \pm 0.34)\times10^{-11}$
54593.03	75.4	213.0	123.2	89.8	6.0	$(3.25 \pm 0.59)\times10^{-11}$
54596.03	143.0	352.0	201.9	150.1	7.9	$(3.06 \pm 0.42)\times10^{-11}$
54597.06	121.2	228.0	147.8	80.2	3.8	$(2.11 \pm 0.55)\times10^{-11}$
54598.03	48.8	122.0	55.8	66.2	6.4	$(4.15 \pm 0.74)\times10^{-11}$
54599.10	55.8	147.0	71.9	75.1	4.7	$(4.43 \pm 0.92)\times10^{-11}$

Table 6.11: Parameters of the power law (PL) fits to Mrk 501 spectra from data taken during the multiwavelength campaign in 2008. Table content - see caption of Tab. 6.4.

MJD start	Spectral index	Normalisation [$\text{cm}^{-2}\text{s}^{-1}\text{TeV}^{-1}$]	χ^2/d.o.f
54557.16	-2.24 ± 0.38	$(0.71 \pm 0.08)\times10^{-10}$	0.22/3
54568.12	-2.27 ± 0.15	$(0.16 \pm 0.01)\times10^{-9}$	1.43/4
54584.08	-2.46 ± 0.30	$(0.12 \pm 0.02)\times10^{-9}$	0.33/3
54585.05	-1.97 ± 0.18	$(0.11 \pm 0.02)\times10^{-9}$	2.97/3
54586.05	-2.59 ± 0.14	$(0.16 \pm 0.02)\times10^{-9}$	0.79/4
54591.04	-2.39 ± 0.20	$(0.16 \pm 0.02)\times10^{-9}$	1.48/2
54592.05	-2.52 ± 0.33	$(0.69 \pm 0.03)\times10^{-10}$	0.93/2
54593.03	-2.38 ± 0.28	$(0.20 \pm 0.03)\times10^{-9}$	0.01/1
54596.03	-2.72 ± 0.17	$(0.17 \pm 0.02)\times10^{-9}$	0.04/3
54598.03	-2.23 ± 0.22	$(0.19 \pm 0.01)\times10^{-9}$	1.52/3

Table 6.12: Parameters of the power law (PL) fits to Mrk 501 spectra measured by MAGIC for the three periods of the multiwavelength campaign in 2008, not corrected for attenuation on the Extragalactic Background Light. Table content - see caption of Tab. 6.4.

MJD start - end	Spectral index	Normalisation $[\mathrm{cm^{-2}s^{-1}TeV^{-1}}]$	χ^2/d.o.f
54554-54559	-2.44 ± 0.18	$(0.46 \pm 0.08)\times10^{-11}$	3.67/3
54568-54571	-2.37 ± 0.16	$(0.75 \pm 0.11)\times10^{-11}$	5.69/3
54575-54602	-2.50 ± 0.05	$(0.70 \pm 0.04)\times10^{-11}$	5.18/4

Table 6.13: Parameters of the power law (PL) fits to Mrk 501 spectra measured by MAGIC for the three periods of the multiwavelength campaign in 2008, corrected for attenuation on the Extragalactic Background Light with the Kneiske Low model [K$^+$04a]. Table content - see caption of Tab. 6.4.

MJD start - end	Spectral index	Normalisation $[\mathrm{cm^{-2}s^{-1}TeV^{-1}}]$	χ^2/d.o.f
54554-54559	-2.11 ± 0.16	$(0.63 \pm 0.08)\times10^{-11}$	0.30/3
54568-54571	-2.01 ± 0.22	$(0.11 \pm 0.01)\times10^{-10}$	4.31/2
54575-54602	-2.29 ± 0.07	$(0.97 \pm 0.05)\times10^{-11}$	6.26/3

Table 6.14: The SSC model parameters used to describe the broadband SED for different flux states of the multiwavelenght campaigns in 2005 and 2008 [T$^+$98b] [A$^+$07j] .

parameter	2008 low state	2008 high state	2005 low state	2005 high state
γ_{break}	2.2×10^5	2.6×10^5	1.0×10^6	1.0×10^5
n_1	2.0	2.0	2.0	2.0
n_2	4.2	3.9	3.9	3.2
B [G]	0.19	0.19	0.23	0.31
K [cm^3]	1.8×10^4	1.8×10^4	7.5×10^4	4.3×10^4
R [cm]	3×10^{15}	3×10^{15}	1×10^{15}	1×10^{15}
δ	12	12	25	25

Table 6.15: Observation parameters for 1ES0235+164 data after quality selection, used as a hadron sample for 1ES 1959+650 observations in 2007. Table content - see caption of Tab. 6.1

MJD start	Time [min]	DT [a.u.]	ZA [deg]	Mean rate [Hz]
54143	27.3	15.4 (D)	29-35.7	190
54144	23.7	16.2 (D)	30-35.8	195

Table 6.16: Results of the analysis of the Crab Nebula data sample used for optimization and test of cuts for the analysis of 1ES1959+650 data collected in 2007. Table content - see caption of Tab. 6.2.

MJD start	Time [min]	DT [a.u.]	N_{ON}	N_{OFF}	N_{EXC}	Flux (>300 GeV) [ph cm^{-2} s^{-1}]	Signif. [σ]	Spectral index	Normalization [ph cm^{-2} s^{-1} TeV^{-1}]	χ^2/ndf
54141	36.5	16.5	294.0	113.3	180.7	$(1.13\pm0.1)\times10^{-10}$	11.6	-2.51±0.29	$(0.33\pm0.07)\times10^{-10}$	6.00/4
54382	35.5	16.5	380.0	163.7	216.3	$(1.47\pm0.14)\times10^{-10}$	12.0	-2.48±0.23	$(0.35\pm0.05)\times10^{-10}$	6.24/4

Table 6.17: Results of 1ES1959+650 observations performed from April untill October 2007. Table content - see caption of Tab. 6.3.

MJD start	Time [min]	N_{ON}	N_{OFF}	N_{EXC}	Flux > 300 GeV [ph cm^{-2} s^{-1}]	Significance [σ]	UL(90%) [ph cm^{-2} s^{-1}]
54208	44.7	161.0	144.0	17.0	$(9.4 \pm 8.0)\times10^{-12}$	1.2	—
54212	54.25	180.0	177.0	3.0	$(1.3 \pm 7.0)\times10^{-12}$	0.2	1.52×10^{-11}
54219	16.0	62.0	48.7	13.3	$(2.0 \pm 1.3)\times10^{-11}$	1.6	—
54232	24.4	90.0	76.0	14.0	$(1.4 \pm 1.1)\times10^{-11}$	1.3	—
54236	39.6	127.0	132.0	-5.0	$-(3.1 \pm 8.1)\times10^{-12}$	-0.4	1.25×10^{-12}
54240	43.8	132.0	132.7	-0.7	$-(3.8 \pm 7.0)\times10^{-12}$	-0.05	1.41×10^{-12}
54355	53.6	237.0	212.7	24.3	$(1.1 \pm 0.7)\times10^{-11}$	1.4	—
54374	85.9	383.0	326.3	66.7	$(1.9 \pm 0.6)\times10^{-11}$	3.1	—
54381	40.5	175.0	140.7	34.3	$(2.0 \pm 0.9)\times10^{-11}$	2.4	—
54389	63.6	272.0	242.3	29.7	$(1.1 \pm 0.7)\times10^{-11}$	1.6	—
54390	90.5	471.0	336.3	104.7	$(2.8 \pm 0.6)\times10^{-11}$	4.5	—
54406	58.4	314.0	280.7	33.3	$(1.4 \pm 0.8)\times10^{-11}$	1.7	—
54407	8.3	43.0	32.3	10.7	$(3.0 \pm 2.0)\times10^{-11}$	1.5	—
54410	9.2	49.0	38.0	11.0	$(2.8 \pm 2.0)\times10^{-11}$	1.5	—
54418	41.9	188.0	161.0	27.0	$(1.6 \pm 0.9)\times10^{-11}$	1.8	—
54208-54418 (2007)	897.6	2896.0	2512.0	384.0	$(1.38 \pm 0.22)\times10^{-11}$	6.44	—

Table 6.18: Results of the analysis of the Crab Nebula data sample used for optimization and test of cuts for the analysis of 1ES1959+650 data collected in 2008. Table content - see caption of Tab. 6.2.

MJD	Time [min]	DT [a.u.]	N_{ON}	N_{OFF}	N_{EXC}	Flux (>300 GeV) [ph cm^{-2} s^{-1}]	Significance [σ]
54448	52.5	17.4	413.0	141.0	272.0	$(1.29 \pm 0.11)\times10^{-10}$	11.8
54444	38.0	17.2	318.0	130.0	188.0	$(1.22 \pm 0.14)\times10^{-10}$	9.0

Table 6.19: Results of 1ES1959+650 high zenith angle observations performed from March until October 2008. Table content - see caption of Tab. 6.3.

MJD start-end	Time [h]	N$_{ON}$	N$_{OFF}$	N$_{EXC}$	Significance [σ]	Flux > 300 GeV [ph cm^{-2} s^{-1}]	UL(90%) [ph cm^{-2} s^{-1}]
54559-54663 (2008)	3.41	472.0	398.0	74.0	2.5	$(0.88 \pm 0.35)\times10^{-11}$	2.53×10^{-11}

Table 6.20: Spectral parameters obtained for the measured spectrum for 1ES1959+650 from fits to a power law with a cut off (PLwC) or a simple power law (PL) and two different unfolding methods. Table contains: type of the $Fit/Unfolding$, the spectral index and its statistical error, the normalization of the spectra at 1 TeV and its statistical error [ph cm^{-2} s^{-1} TeV^{-1}] , the cutoff energy E_0, the $\chi^2/d.o.f.$ of the spectral fit.

Fit/Unfolding	Spectral index	Normalisation [10^{-11} cm^{-2}s^{-1}TeV^{-1}]	E$_0$ [TeV]	χ^2/d.o.f
PL/Bertero	-2.31 ± 0.05	(0.98 ± 0.06)	—	6.72/4
PL/Tikhonov	-2.40 ± 0.05	(0.92 ± 0.05)	—	19.81/5
PLwC/Bertero	-2.22 ± 0.13	(5.2 ± 0.6)	9.90 ± 13.86	6.19/3
PLwC/Tikhonov	-2.13 ± 0.13	(6.0 ± 0.6)	4.19 ± 2.05	15.56/4

7 Summary and Outlook

This work aims at exploring the multimessenger approach, i.e. connections between the observed very high energy γ-ray emission and expected neutrino emission from cosmic sources. In this context several points were investigated. New methods of enhancing the chance of detection of neutrino point sources, by improving the signal-to-background ratio were developed: a time variable analysis and a correlation study using data form neutrino and VHE γ-ray telescopes. The long term behavior of selected VHE γ-ray emitters was investigated using historical and recently collected data. The analysis of observations performed during the AGN monitoring program with the MAGIC telescope, including SED modeling, was made.

Under the assumption that the neutrino emission, like the electromagnetic one, could be variable and could show a flare-like behavior, a new algorithm (time-clustering algorithm) was developed to look for structures (clusters) in the time distribution of the neutrino events detected from certain directions by the AMANDA-II telescope at the South Pole. Along with this algorithm a new background estimation method, based on a parameterization of the up-time of the detector and the detection efficiency, was proposed. It proved to be affected by smaller (up to ~10%) statistical uncertainty and thus more reliable for shorter time scales than the previously used approach [A$^+$07b]. A study of the algorithm performance showed that the analysis developed for this work improves the detection chance by up to ~40% for neutrino flares lasting less than 7 days in comparison with the time integrated analysis. The search for neutrino flares from predefined directions was performed on 18 sources (galactic and extragalactic) using data collected by the AMANDA-II neutrino telescope in the years 2004-2006. No significant deviation from the background hypothesis was found.

Cosmic ray observations indicate that hadronic processes are responsible for, at least some part of, the emission observed from cosmic sources. The observed power-law like behavior of the CR spectrum can be explained by stochastic shock acceleration of particles in collision-less plasma. If indeed, those particles are protons they can later loose their energy by synchrotron radiation or by collisions with photons and other protons leading to emission of very high energy γ-rays and neutrinos. Therefore a correlation of the neutrino and VHE γ-ray signal is expected in many models. Motivated by this assumption, a test for correlation of neutrinos (from AMANDA-II data) with high states of γ-ray emission was performed for 7 objects for which γ-ray data for the years 2004 to 2006 were published. No significant correlation was found.

The main difficulty connected with this type of analysis is the sparse time and flux state coverage of the VHE γ-ray data. It not only decreases the chance of finding such a correlation (lack of simultaneous data to be tested), but also makes the estimation of the probability of a random coincidence of γ-ray flare with atmospheric neutrinos and therefore a proper calculation of significance of such a correlation (if observed) very difficult.

The Neutrino Trigger of Opportunity program proposed in [A^{+}07d] addresses the first issue: by sending a trigger after observing a neutrino event from a candidate source direction a follow up observation by a γ-ray telescope is secured and the amount of simultaneous data increases. A test run of NToO with AMANDA-II and MAGIC was performed in 2006. Although no significant coincidences between the neutrino events and VHE γ-ray flares were found the technical feasibility of the set up was successfully tested.

A way to obtain a long term exposure of γ-ray sources is a combination of all existing (historical) data. In parallel a regular monitoring of the selected sources is promoted. The public γ-ray light curves archive maintained at DESY collects published data from the IACT telescopes. Based on this data, a statistical analysis of different emission states of two extragalactic VHE γ-ray sources, Mrk 421 and Mrk 501, was performed. In this work an attempt was made to calculate the probability of finding those sources in a flux state above a certain threshold. The collected flux statistics is not yet sufficient to draw final conclusions. One can only state that, although belonging to the same class of object, they show different behavior: Mrk 421 seems to be more often in a flaring state, while Mrk 501 is characterized by longer periods of moderate activity.

The only solution to overcome the problem of limited time and flux state coverage of the VHE γ-ray data is to perform dedicated long term monitoring observations of interesting objects. Such programs are already performed by the HESS, MAGIC and VERITAS (with the Whipple telescope) collaborations. In this work results of the MAGIC AGN monitoring program from the observational season 2007/2008 were obtained for two sources: Mrk 501 and 1ES1959+650. Both sources were found in a rather low state. The average flux of Mrk 501, integrated above 300 GeV, was $(1.95\pm0.85)\times10^{11}$ ph cm^{-2} s^{-1} ($\sim$19% of the Crab Nebula flux) in 2007 and $(2.90\pm1.35)\times10^{11}$ ph cm^{-2} s^{-1} ($\sim$24% of the Crab Nebula flux) in 2008. The source shows moderate variability with no prominent flares. For the 13 measurements with the highest signal significance the spectra were calculated, but due to large uncertainties on both the measured fluxes and derived spectral indices no firm conclusion about a correlation between the flux state and the hardness of the spectra can be made. The average flux measured from 1ES1959+650 in 2007 was $(1.43\pm\ 0.34)\times10^{-11}$ ph cm^{-2} s^{-1} ($\sim$12% of the Crab Nebula flux), for 2008 observations an upper limit of 2.53×10^{-11} ph cm^{-2} s^{-1} ($\sim$20% of the Crab Nebula flux) was set. An average spectrum for the year 2007 was calculated with the resulting spectral index of -2.40 ± 0.05, in agreement within errors with the one derived from the MAGIC observations in 2006, when the source was found in a similarly low state.

Part of the 2008 monitoring data of Mrk 501 was collected during a multiwavelength campaign. The energy spectrum of Mrk 501 was very well covered from radio to very high energy γ-rays by different instruments, which allowed for variability study in different energy ranges and SED modeling. Hints of variability increasing with energy and correlations between the emission states in X-ray and TeV bands were found. The SED was modeled with a 1-zone SSC leptonic model [T^{+}98b]. The model reproduces the X-ray data very well. The transition from the low to high emission state can be explained by an injection of fresh high energy electrons, which lead to the shift of the break energy to higher values and hardening of the electron spectrum. Unfortunately there is a significant discrepancy between the model prediction and the measurements in the radio-optical range. It is beyond the scope of this thesis to develop a different model, but very probably, as proposed by [KSK01] the radiation from a different emission region can be responsible for the fluxes observed in the low energy range.

From the phenomenological point of view even a multiwavelength campaign with the best possible energy coverage cannot fully address the question of the leptonic or hadronic origin of the observed electromagnetic emission from cosmic sources. Only a multimessenger approach, involving observations of neutrinos (and cosmic rays) can solve this dilemma. Although none of the analyses in this work resulted in a significant detection of a neutrino point source the improvements proposed in [FB09] and [L^{+}09a] and the rapid development of both the neutrino and γ-ray astronomy promise more spectacular results in the near future.

Appendix A: Observations of the blazar Mrk 501 performed by the MAGIC telescope from February 2007 until August 2008

The tables in this Appendix summarize the observations of the blazar Mrk 501 performed by the MAGIC telescope from February 2007 until August 2008: Table 1 - the year 2007, Table 2 - the year 2008. The double horizontal lines in Table 2 indicate the period when the multiwavelength campaign took place. The columns in each table contain:

- *MJD start* - the MJD date of the start of the observation,
- *Time* [h] - the duration of the observation in hours,
- *DT* [a.u.] - the mean discrimination threshold in arbitrary units and the information of the light conditions during the observation: *D* - dark, *T* - twilight, *M* - moon,
- *ZA* [deg] - the zenith angle of the observation in degrees,
- *Mean rate* [Hz] - the mean rate in Hz given with an accuracy of 5.0 Hz, or *U* - unstable,
- *Comments* - acceptance (*OK*) or exclusion of the data from the analysis due to: *R* - unstable or too low rates, *DT* - too high DT threshold or other reasons explained in the table; *OK* means that all or a large part of the data was accepted and only few files rejected due to too low/high rate etc.

Table 1: Observational parameters and data quality selection for Mkn 501 data collected in 2007

MJD start	Time [h]	DT [a.u.]	ZA [deg]	Mean rate [Hz]	Comments
54149.26	0.47	14.6445 (D/T)	21.9 - 28.0	225	OK
54155.25	0.53	14.4675 (D/T)	18.8 - 25.3	215	OK
54159.23	0.42	14.5407 (D)	19.7 - 26.6	210	OK
54170.17	0.61	22.8608 (M)	26.4 - 34.4	110	DT
54182.12	0.52	15.9255 (D)	34.6 - 41.4	195	OK
54202.16	1.42	15.295 (M)	11.0 - 16.0	190/235	data with R∼190Hz excluded
54203.18	0.54	14.9644 (M)	11.0 - 12.3	U	R
54211.06	0.75	15.592 (D)	24.8 - 34.5	190	OK
54215.11	0.24	17.7586 (M)	17.1 - 19.5	U	R
54226.99	1.01	16.8383 (D/M)	30.9 - 43.8	180/U	moon data excluded - unstable rates
54231.01	0.39	15.0573 (D)	29.6 - 34.4	165	OK
54234.99	0.63	14.7918 (D)	27.8 - 34.4	205	OK
54238.98	0.62	15.4224 (D)	28.7 - 35.0	190	OK
54253.90	0.19	18.987 (D)	44.6 - 46.6	135	R
54269.91	0.72	17.8034 (M)	21.6 - 31.5	190/140	data with R∼140Hz excluded
54274.92	0.40	34.4928 (M)	22.7 - 26.1	35	DT
54283.92	0.87	22.2583 (D/M)	12.3 - 20.8	U	DT, R
54288.04	0.20	17.7506 (M)	26.0 - 32.2	U	R
54295.04	0.64	14.1757 (D)	29.7 - 37.3	220	OK
54298.89	0.78	15.143 (M/T)	11.0 - 15.4	105	R
54302.90	0.54	22.4668 (M)	11.0 - 12.4	110	DT
54321.97	0.47	16.6285 (D)	31.5 - 37.9	205	OK
54325.96	0.44	16.1872 (D)	31.6 - 37.9	195	OK
54329.88	0.89	19.6453 (M/T)	14.0 - 22.5	195	OK

54333.88	0.61	25.4209 (M)	16.6 - 23.8	125	DT
54344.91	0.92	19.0265 (D/M)	32.0 - 43.2	235/100	data with R∼100 Hz excluded
54348.90	0.62	16.6656 (D)	33.0 - 40.5	215	OK
54353.89	0.63	16.6962 (D)	33.2 - 39.7	215	OK
54356.85	0.90	16.7834 (D/T)	25.1 - 35.4	215	OK
54360.85	1.36	18.838 (M/T)	29.5 - 46.1	U	R
54372.84	0.72	17.4797 (T)	33.3 - 41.9	220	OK
54373.84	0.16	17.982 (T)	34.5 - 36.3	210	excluded
54375.83	0.21	18.6876 (D/T)	34.1 - 36.5	200/U	data with unstable rate excluded
54376.83	0.22	20.663 (T)	35.1 - 37.2	U	DT , R
54377.83	0.26	21.669 (T)	34.0 - 37.0	140	DT
54378.83	0.19	21.6449 (T)	35.9 - 37.9	150	DT
54379.83	0.09	19.7993 (T)	36.9 - 37.8	160	very short - excluded
54381.83	0.65	18.2171 (D/T)	37.0 - 45.8	140/200	data with R∼140 Hz excluded
54382.83	0.16	21.0934 (T)	37.4 - 39.2	135	DT
54383.83	0.16	21.5281 (T)	38.0 - 39.7	130	DT
54386.83	0.18	19.2529 (T)	41.1 - 43.0	140	R
54387.82	0.65	21.3632 (T)	40.2 - 47.5	115	DT
54390.83	0.48	20.1648 (T)	45.6 - 50.4	130	DT

Table 2: Observational parameters and data quality selection for Mkn 501 data collected in 2008. The double horizontal lines indicate the period when the multiwavelength campaign took place.

MJD start	Time [h]	DT [a.u.]	ZA [deg]	Mean rate [Hz]	Comments
54501.28	0.28	20.1 (T)	28.5 - 31.5	160	DT
54502.28	0.28	20.2 (T)	27.9 - 30.0	U	DT
54503.28	0.02	18.6 (T)	30.5	142.0	very short - excluded
54504.28	0.27	21.9 (T)	25.7 - 28.7	160.0	DT
54507.28	0.22	21.1 (T)	25.0 - 26.6	160.0	DT
54523.27	0.28	30.2 (T)	16.8 - 19.1	45.0	DT
54526.26	0.41	21.8 (T/M)	15.3 - 18.3	110.0	DT
54527.26	0.33	20.7 (T/M)	14.6 - 18.0	125.0	DT
54529.26	0.11	14.6 (M)	17.8 - 18.7	U	R
54530.26	0.37	19.4 (T/M)	13.3 - 16.9	190	OK
54532.26	0.24	20.0 (T)	12.6 - 14.1	150	OK
54533.26	0.26	20.9 (T)	12.2 - 13.8	145	OK
54534.26	0.20	19.6 (T)	12.5 - 13.7	150	OK
54536.26	0.28	16.6 (T)	11.8 - 13.5	205	OK
54537.26	0.18	19.4(T)	11.4 - 12.2	150	OK
54538.26	0.14	19.9 (T)	11.6 - 12.1	U	R
54539.26	0.16	20.4 (T)	11.1 - 11.5	120	OK
54540.26	0.23	16.4 (T)	11.2 - 12.1	180	OK
54541.26	0.19	19.0 (T)	11.0 - 11.3	175	OK
54542.26	0.20	18.0 (T)	11.0 - 11.3	170	OK
54543.26	0.24	18.0 (T)	11.0 - 11.5	170	OK
54553.19	1.07	33.8 (M/T)	11.0 - 16.3	60	DT
54554.14	2.43	19.1 (M/T)	11.0 - 30.6	190	OK

54555.14	1.56	19.2(M)	11.0 - 30.0	U	R
54556.21	0.57	19.2 (M)	11.0 - 12.5		OK
54557.16	1.71	18.9 (M/D)	11.0 - 20.7	150	OK
54558.12	2.65	15.9 (D/M/T)	11.0 - 30.8	165	OK
54559.21	0.46	16.0 (D/M)	11.0 - 11.9	200	OK
54568.08	2.27	16.0 (D)	11.0 - 34.8	200	OK
54570.14	1.97	15.8 (D)	11.0 - 18.0	205	OK
54571.19	0.19	15.8 (D)	11.1 - 11.5	210	OK
54572.19	0.84	16.0 (D/T)	11.0 - 15.7	U	R
54583.09	2.15	28.6 (M)	11.0 - 28.6	U	DT, R
54584.06	0.32	15.8 (D)	24.2 - 30.3	170	OK
54584.08	0.99	19.3 (M)	11.2 - 24.0	140	OK
54585.05	2.18	16.3 (D/M)	17.3 - 30.6	190	OK
54586.05	2.60	15.7 (D/M)	12.3 - 30.2	155	OK
54587.05	2.58	15.8(D/M)	11.0 - 29.8	160	OK
54588.04	3.41	15.8 (D/M)	10.9 - 30.2	U	R
54589.04	2.84	15.8 (D/M)	11.0 - 30.5	U	R
54590.04	2.57	15.7(D)	11.0 - 31.2	185	OK
54591.04	2.39	15.7 (D)	11.0 - 29.9	190	OK
54592.05	2.10	15.8(D)	11.0 - 25.1	165	OK
54593.03	1.48	15.7(D)	15.7 - 31.2	175	OK
54596.03	2.48	14.8(D)	11.0 - 29.9	210	OK
54597.05	2.65	14.8(D/M)	11.0 - 27.7	190	OK
54598.02	1.13	18.7 (M)	16.3 - 21.3	130	OK
54599.10	0.94	14.8(D)	11.0 - 18.9	195	OK
54601.18	0.07	14.6 (D)	24.4 - 25.0	U	R
54612.03	0.48	17.7 (M)	12.4 - 16.5	155	OK

54616.04	0.64	14.8 (D)	11.0 - 12.9	U	R
54620.00	0.66	14.8 (D)	12.7 - 18.2	210	OK
54625.98	0.72	14.8 (M)	13.1 - 19.2	200	OK
54626.98	0.54	17.4 (M)	14.4 - 18.4	155	OK
54627.98	0.35	19.6 (M)	14.2 - 16.4	120	OK
54637.92	1.24	25.2 (M)	14.5 - 27.9	U	R
54638.89	0.17	18.0 (T)	31.6 - 33.0	U	R
54639.89	0.19	18.0 (T)	31.7 - 33.2	U	R
54641.89	0.25	17.9 (T)	29.0 - 31.3	U	R
54642.89	0.19	17.9 (T)	29.5 - 31.0	U	R
54646.89	0.07	17.8 (T)	26.3 - 28.3	80	R
54647.89	0.17	18.0 (T)	24.9 - 26.1	200	OK
54649.89	0.15	17.9 (T)	24.2 - 25.2	123	OK
54650.89	0.14	17.9 (T)	22.6 - 23.6	137	OK
54651.89	0.17	17.9 (T)	22.9 - 24.2	135	OK
54652.90	0.80	17.8 (D/T/M)	14.0 - 21.2	145	OK
54653.89	0.42	19.0 (T)	18.2 - 21.4	130	OK
54654.89	0.44	18.0 (T/M)	17.5 - 22.2	130	OK
54655.89	0.31	19.0 (T)	18.1 - 20.6	120	OK
54657.89	0.17	22.4 (T)	17.3 - 18.3	70	DT, R
54667.89	0.64	18.3 (T/M)	11.1 - 15.2	170	OK
54668.89	0.60	18.8 (T/M)	11.3 - 13.5	90	R
54670.89	0.17	17.9 (T)	13.7 - 14.0	U	R
54671.89	0.17	17.8 (T)	11.9 - 12.6	U	R
54672.89	0.13	17.9 (T)	12.3 - 12.8	140	OK
54673.89	0.18	18.0 (T)	11.5 - 12.0	130	OK
54674.89	0.22	17.8 (T)	12.2 - 13.7	135	OK

54676.88	0.18	.17.9(T)	11.3 - 12.1	145	OK
54677.89	0.18	.17.7 (T)	11.1 - 11.5	135	OK
54678.89	0.07	26.7 (T)	11.0 - 11.1	100.0	DT
54679.88	0.10	44.0 (T)	11.0	125.0	DT
54680.88	0.28	43.8 (T)	11.0 - 11.2	130.0	DT
54681.88	0.24	44.1 (T)	11.0 - 11.3	140.0	DT
54682.88	0.27	39.2 (T/M)	11.1 - 14.1	215.0	DT
54684.88	0.18	45.1 (T)	11.0 - 11.5	15.0	DT
54686.88	0.25	53.1 (T)	11.5 - 12.6	55.0	DT
54687.89	0.26	58.7 (M)	13.3 - 15.2	50.0	DT
54688.88	0.18	42.0 (T/M)	12.9 - 14.0	45.0	DT
54700.87	0.10	44.5 (T)	17.1 - 17.6	140	DT
54701.87	0.12	42.8 (T)	15.5 - 16.1	110	DT
54702.87	0.16	44.0 (T)	17.3 - 18.3	100	DT
54703.87	0.02	43.9 (T)	16.8 - 17.9	150	DT
54704.87	0.05	44.1 (T)	18.9	150	DT
54705.86	0.10	26.4 (T)	17.7 - 18.6	U	DT, R
54706.86	0.10	42.6 (T)	18.7 - 19.7	155	DT

Appendix B: Observations of the blazar 1ES 1959+650 performed by the MAGIC telescope from April 2007 until October 2008

The tables in this Appendix summarize the observations of the blazar 1ES 1959+650 performed by the MAGIC telescope from April 2007 until October 2008: Table 3 - the year 2007, Table 4 - the year 2008. The columns in each table contain:

- *MJD start* - the MJD date of the start of the observation,
- *Time* [h] - the duration of the observation in hours,
- *DT* [a.u.] - the mean discrimination threshold in arbitrary units and the information of the light conditions during the observation: *D* - dark, *T* - twilight, *M* - moon,
- *ZA* [deg] - the zenith angle of the observation in degrees,
- *Mean rate* [Hz] - the mean rate in Hz given with an accuracy of 5.0 Hz, or *U* - unstable,
- *Comments* - acceptance (*OK*) or exclusion of the data from the analysis due to: *R* - unstable or too low rates, *DT* - too high DT threshold or other reasons explained in the table; *OK* means that all or a large part of the data was accepted and only few files rejected due to too low/high rate etc.

Table 3: Observational parameters and data quality selection for 1ES 1959+650 data collected in 2007.

MJD start	Time [h]	DT [a.u.]	ZA [deg]	Mean rate [Hz]	Comments
54203.20	0.70	18.8 (M/T)	41.5-45.5	U	R
54208.19	0.82	15.2 (D)	41.5-46.0	180	OK
54212.18	0.95	15.2 (D)	40.0-45.0	175	OK
54219.21	0.42	16.0 (D/T)	38.0-41.0	170	OK
54232.11	0.72	14.8 (D/M)	43.0-48.0	180	OK
54236.10	0.81	14.8 (D)	42.0-47.0	180	OK
54240.08	0.95	16.0 (D)	42.0-47.0	165	OK
54263.15	1.03	22.85 (M/T)	36.0-37.0	100	DT
54354.86	0.92	17.1 (D/T)	36.0-38.0	210	OK
54361.85	1.22	22.4 (D/M)	36.0-37.0	130	DT
54373.85	1.46	19.6 (D/T)	36.0-38.0	220	OK
54380.84	1.13	17.2 (M)	36.0-38.0	200	OK
54388.84	1.08	19.2 (M)	36.0-39.0	150	OK
54389.83	1.77	19.1 (M)	36.0-43.0	150	OK
54404.82	0.07	19.4 (T)	37.6-37.7	160	rejected: very short
54405.81	1.35	16.3 (D/T)	38.0-43.0	200	OK
54406.81	0.19	19.1 (T)	37.0-38.0	155	OK
54409.81	0.21	19.0 (T)	38.0-38.5	155	OK
54410.81	0.19	19.1 (T)	38.0-39.0	96	R
54413.82	1.13	16.2 (D/T)	40.0-45.0	U	R
54414.81	0.15	19.1 (T)	39.0-40.0	55	R
54415.81	0.28	18.9 (T)	39.0-40.0	100	R
54417.81	1.24	16.0 (M/T)	39.0-46.0	165	OK

Table 4: Observational parameters and data quality selection for 1ES 1959+650 data collected in 2008.

MJD start	Time [h]	DT [a.u.]	ZA [deg]	Mean rate [Hz]	Comments
54553.25	0.06	34.45 (T)	44.4-44.5	U	R, DT
54554.24	0.25	26.4 (T)	43.6-44.7	70	DT
54555.24	0.19	24.6 (T)	44.0-44.9	90	DT
54557.24	0.24	22.1(T)	43.6-44.7	115	DT
54558.24	0.24	20.6 (T)	42.6-43.8	140	DT
54559.24	0.24	19.1 (T)	43.1-44.2	135	OK
54561.24	0.24	19.3 (T)	42.1-43.2	165	OK
54568.23	0.23	19.3 (T)	40.8-41.7	155	OK
54570.23	0.24	19.1 (T)	40.3-41.3	160	OK
54571.23	0.22	18.7 (T)	40.7-41.6	160	OK
54572.23	0.27	16.6 (T)	40.0-41.0	U	R
54573.23	0.19	19.1 (T)	40.4-41.2	160	OK
54588.21	0.31	22.0 (T)	37.5-38.6	120	DT
54589.21	0.31	17.9 (T)	37.5-38.3	125	
54597.21	0.23	20.1(T)	36.7-37.4	130	DT
54599.21	0.24	20.2 (T)	36.6 -37.0	130	DT
54612.07	1.18	25.2 (M)	39.7 -45.9	60	DT
54616.07	0.86	14.9 (D)	41.3 -45.5	U	R
54620.06	0.86	15.4 (D)	41.5 -45.8	165	OK
54661.10	0.22	19.4 (M)	37.0-37.3	120	OK
54662.13	0.25	19.5 (M)	39.7-40.3	80	R
54663.17	0.23	20.0 (M)	43.5-44.3	70	DT
54683.98	1.70	36.1(D)	36.4 -39.7	70	DT
54686.10	0.89	36.8 (D)	42.2 -49.1	75	DT
54687.01	3.13	36.3 (D)	36.6 -48.9	60	DT

List of Abbreviations

1ES	1^{st} Einstein Survey
AGASA	Akeno Giant Air Shower Array
AGILE	Astro-rivelatore Gamma a Immagini LEggero
AGN	Active Galactik Nucleus
AMANDA	Antarctic Muon And Neutrino Detector Array
AMC	Active Mirror Control
ANTARES	Astronomy with a Neutrino Telescope and Abyss enviromental RESearch
a.s.l.	above see level
ASM	All Sky Monitor on board RXTE
BAT	Burst Alert Telescope on board Swift
BH	Black Hole
BLR	Broad Line Region
CANGAROO	Collaboration of Australia and Nippon (Japan) for a GAmma-Ray Observatory in the Outback
CAT	Cherenkov Array at Themis
CC	Charged Current
CMB	Cosmic Microwave Background
CGRO	Compton Gamma-Ray Observatory
COMPTEL	COMPton TELescope
CR	Cosmic Rays
CTA	Cherenkov Telescope Array
DAQ	Data AQuisition
DCF	Discrete Correlation Function
(D)OM	(Digital) Optical Module
DT	Discriminator Threshold
DUMAND	Deep Underwater Muon and Neutrino Detection
EAS	Extended Air Shower
EBL	Extragalactic Background Light
EC	External Compton
EGRB	Extragalactic Gamma-Ray Background
EGRET	Energetic Gamma-Ray Experiment Telescope
FADC	Flash Analog to Digital Converter

FSQR	Flat Spectrum Radio Quasar
GASP-WEBT	GLAST-AGILE Support Program of the Whole Earth Blazar Telescope
GLAST	Gamma-ray Large Area Space Telescope
GRB	Gamma-Ray Burst
GZK cutoff	Greisen-Zatsepin-Kuzmin cutoff
HBL	High frequency peaked BL Lac object
HE	High Energy
HEGRA	High Energy Gamma-Ray Astronomy
HESS	High Energy Stereoscopic System
HiRes	High Resolution Fly's Eye Detector
HZA	High Zenith Angle
IACT	Imagining Atmosperic Cherenkov Technique/Telescope
IC	Inverse Compton
INTEGRAL	INTErnational Gamma-Ray Astrophysics Laboratory
IR	Infra Red
IRAM	Institut de Radioastronomie Millimetrique
KM3NeT	KM^3 (cube kilometer) Neutrino Telescope
LBL	Low frequency peaked BL Lac object
LC	Light Curve
LZA	Low Zenith Angle
MAGIC	Major Atmospheric Gamma Imagining Cherenkov Telescope
MARS	MAGIC Analysis and Reconstruction Software
MC	Monte Carlo
MJD	Modified Julian Date
MM	MultiMessenger
MPR	Mannheim, Protheroe and Rachen
Mrk	Markarian
MW	MultiWavelenght
NC	Neutral Current
NEMO	NEutrino Mediterranean Observatory
NESTOR	Neutrino Extended Submarine Telescope with Oceanographic Research
NSB	Night Sky Background
(N)ToO	(Neutrino triggered) Target of Opportunity
PCA	Proportional Counter Array on board RXTE
phe	photoelectrons
PIC	Proton Initiated Cascades
PMT	Photo-Multiplier Tube

PSF	Point Spread Function
QE	Quantum Efficiency
RATAN-600	600-meter RAdio Telescope ANtenna
RF	Random Forest
RIQ	Radio Intermediate Quasar
RXTE	Rossi X-ray Timing Explorer
SDSS	Stecker, Done, Salamon and Sommers
SED	Spectral Energy Distribution
SLF	Simple Light curve Format
SMBH	Super Massive Black Hole
SN(R)	Super Nova (Remnant)
SPB	Synchrotron-Proton Blazar
SSC	Synchrotron Self-Compton
SSRQ	Steep Spectrum Radio Quasars
TACTIC	TeV Atmospheric Cherenkov Telescope with Imaging Camera
UHE	Ultra High Energy
UV	UltraViolet
UVOT	UltraViolet and Optical Telescope on board Swift
VERITAS	Very Energetic Radiation Imagining Telescope Array System
VHE	Very High Energy
VLBA	Very Long Baseline Array
W&B	Waxman and Bahcall
w.e.	water equivalent
XRB	X-Ray Binary
XRT	X-Ray Telescope on board Swift

Bibliography

[A$^+$99a] Aharonian, F.; et al. (HEGRA): The temporal characteristics of the TeV gamma emission from Mkn 501 in 1997. II. Results from HEGRA CT1 and CT2. In: *Astron. Astrophys.*, volume 349:pp. 29–44, 1999. `astro-ph/9901284`.

[A$^+$99b] Aharonian, F.; et al. (HEGRA): The temporal characteristics of the TeV gamma radiation from Mkn 501 in 1997. I. Data from the stereoscopic imaging atmospheric Cherenkov telescope system of HEGRA. In: *Astron. Astrophys.*, volume 342:pp. 69–86, 1999. `arXiv:astro-ph/9808296`.

[A$^+$99c] Aharonian, F.; et al. (HEGRA): The time averaged TeV energy spectrum of Mkn 501 of the extraordinary 1997 outburst as measured with the stereoscopic Cherenkov telescope system of HEGRA. In: *Astron. Astrophys.*, volume 349:pp. 11–28, 1999. `arXiv:astro-ph/9903386`.

[A$^+$01] Aharonian, F.; et al. (HEGRA): The TeV Energy Spectrum of Markarian 501 Measured with the Stereoscopic Telescope System of HEGRA during 1998 and 1999. In: *Astrophys. J.*, volume 546:pp. 898–902, 2001. `arXiv:astro-ph/0008211`.

[A$^+$02] Aharonian, F.; et al. (HEGRA): Variations of the TeV energy spectrum at different flux levels of Mkn 421 observed with the HEGRA system of Cherenkov telescopes. In: *Astron. Astrophys.*, volume 393:pp. 89–99, 2002. `astro-ph/0205499`.

[A$^+$03a] Aharonian, F.; et al. (HEGRA): Detection of TeV gamma-rays from the BL Lac 1ES 1959+650 in its low states and during a major outburst in 2002. In: *Astron. Astrophys.*, volume 406:pp. L9–L13, 2003. `arXiv:astro-ph/0305275`.

[A$^+$03b] Aharonian, F.; et al. (HEGRA): TeV gamma-ray light curve and energy spectrum of Mkn 421 during its 2001 flare as measured with HEGRA CT1. In: *Astron. Astrophys.*, volume 410:pp. 813–821, 2003.

[A$^+$04a] Abbasi, R. U.; et al. (HiRes): Study of Small-Scale Anisotropy of Ultrahigh Energy Cosmic Rays Observed in Stereo by HiRes. In: *Astrophys. J.*, volume 610:p. L73, 2004. `astro-ph/0404137`.

[A$^+$04b] Aharonian, F.; et al. (HEGRA): The Crab Nebula and Pulsar between 500 GeV and 80 TeV: Observations with the HEGRA Stereoscopic Air Cerenkov Telescopes. In: *Astrophys. J.*, volume 614:pp. 897–913, 2004. `astro-ph/0407118`.

[A$^+$04c] Ahrens, J.; et al. (IceCube): Sensitivity of the IceCube detector to astrophysical sources of high energy muon neutrinos. In: *Astropart. Phys.*, volume 20:pp. 507–532, 2004. `astro-ph/0305196`.

[A$^+$05a] Ackerman, M.; et al.: Multiwavelength comparison of selected neutrino point source candidates. In: *Proceedings of the 29th ICRC*, volume 5, pp. 1–4. Pune, India, August 2005.

[A$^+$05b] Aguilar, J. A.; et al. (ANTARES): Transmission of light in deep sea water at the site of the ANTARES neutrino telescope. In: *Astropart. Phys.*, volume 23:pp. 131–155, 2005. `astro-ph/0412126`.

[A$^+$05c] Aharonian, F.; et al. (HESS): Observations of Mkn 421 in 2004 with HESS at large zenith angles. In: *Astron. Astrophys.*, volume 437:pp. 95–99, 2005. `astro-ph/0506319`.

[A$^+$05d] Aharonian, F.; et al. (HESS): Observations of Mkn 421 in 2004 with HESS at large zenith angles. In: *Astron. Astrophys.*, volume 95:p. 437, 2005. `astro-ph/0506319`.

[A$^+$05e] Aharonian, F.; et al. (HESS): Observations of selected AGN with HESS. In: *Astron. Astrophys.*, volume 441:pp. 465–472, 2005. `astro-ph/0507207`.

[A$^+$06a] Ackermann, M.; et al. (IceCube): Optical properties of deep glacial ice at the South Pole. In: *Journal of Geophys. Res. (Atm.)*, volume 111:p. 13203, 2006.

[A$^+$06b] Aguilar, J. A.; et al. (ANTARES): First results of the instrumentation line for the deep-sea ANTARES neutrino telescope. In: *Astropart. Phys.*, volume 26:pp. 314–324, 2006. `astro-ph/0606229`.

[A$^+$06c] Aharonian, F.; et al. (HESS): Observations of the Crab Nebula with HESS. In: *Astron. Astrophys.*, volume 457:pp. 899–915, 2006. `astro-ph/0607333`.

[A$^+$06d] Albert, J.; et al. (MAGIC): Discovery of Very High Energy gamma-rays from Markarian 180 triggered by an optical outburst. In: *Astrophys. J.*, volume 648:pp. 105–109, 2006. `astro-ph/0606630`.

[A$^+$06e] Albert, J.; et al. (MAGIC): Discovery of VHE gamma-ray emission from 1ES 1218+30.4. In: *Astrophys. J.*, volume 642:pp. L119–L122, 2006. `astro-ph/0603529`.

[A$^+$06f] Albert, J.; et al. (MAGIC): Observation of vhe gamma-ray emission from the active galactic nucleus 1es1959+650 using the magic telescope. In: *Astrophys. J.*, volume 639:pp. 761–765, 2006. `astro-ph/0508543`.

[A$^+$06g] Albert, J.; et al. (MAGIC): Variable very high energy gamma-ray emission from the microquasar ls i +61 303. In: *Science*, volume 312:pp. 1771–1773, 2006. `astro-ph/0605549`.

[A$^+$06h] Aliu, E.; et al. (MAGIC): Observation of VHE gamma-ray emission from the active galactic nucleus 1ES1959+650 using the MAGIC telescope. In: *Astrophys. J.*, volume 639:pp. 761–765, 2006. `astro-ph/0508543`.

[A$^+$07a] A., Aguilar J.; et al. (ANTARES): Expected discovery potential and sensitivity of the ANTARES neutrino telescope to neutrino point-like sources. In: *Proceedings of the 30th ICRC*, volume 5, pp. 1373 – 1376. Merida, Mexico, 2007.

[A$^+$07b] Achterberg, A.; et al. (IceCube): Five years of searches for point sources of astrophysical neutrinos with the AMANDA-II neutrino telescope. In: *Phys. Rev.*, volume D75:p. 102001, 2007. `astro-ph/0611063`.

[A$^+$07c] Achterberg, A.; et al. (IceCube): Multi-year search for a diffuse flux of muon neutrinos with AMANDA-II. In: *Phys. Rev.*, volume D76:p. 042008, 2007. `arXiv:0705.1315`.

[A$^+$07d] Ackermann, M.; et al.: Neutrino Triggered Target of Opportunity (NToO) test run with AMANDA and MAGIC. In: *Proceedings of the 30th ICRC*, volume 3, pp. 1257–1260. Merida, Mexico, July 2007.

[A$^+$07e] Aharonian, F.; et al. (HESS): An Exceptional VHE Gamma-Ray Flare of PKS 2155-304. In: *Astrophys. J.*, volume 664:p. L71, 2007.

[A$^+$07f] Albert, J.; et al. (MAGIC): Discovery of very high energy gamma-ray emission from the low-frequency peaked BL Lacertae object BL Lacertae. In: *Astrophys. J. Lett.*, volume 666:p. L17, 2007. `astro-ph/0703084`.

[A$^+$07g] Albert, J.; et al. (MAGIC): Observation of very high energy gamma-rays from the AGN 1ES 2344+514 in a low emission state with the MAGIC telescope. In: *Astrophys. J.*, volume 662:p. 892, 2007. `astro-ph/0612383`.

[A$^+$07h] Albert, J.; et al. (MAGIC): Observations of Mkn421 with the MAGIC Telescope. In: *Astrophys. J.*, volume 663:pp. 125–138, 2007. `astro-ph/0603478`.

[A$^+$07i] Albert, J.; et al. (MAGIC): Unfolding of differential energy spectra in the MAGIC experiment. In: *Nucl. Instrum. Meth.*, volume A583:pp. 494–506, 2007. `0707.2453`.

[A$^+$07j] Albert, J.; et al. (MAGIC): Variable VHE gamma-ray emission from Markarian 501. In: *Astrophys. J.*, volume 669:p. 862, 2007. `astro-ph/0702008`.

[A$^+$07k] Albert, J.; et al. (MAGIC): Very High Energy Gamma-ray Radiation from the Stellar-mass Black Hole Cygnus X-1. In: *Astrophys. J.*, volume 665:p. L51, 2007. `arXiv:0706.1505`.

[A$^+$08a] Abraham, J.; et al. (Pierre Auger): Correlation of the highest-energy cosmic rays with the positions of nearby active galactic nuclei. In: *Astropart. Phys.*, volume 29:pp. 188–204, 2008. `arXiv:0712.2843`.

[A$^+$08b] Abraham, J.; et al. (Pierre Auger): Observation of the suppression of the flux of cosmic rays above 4×10^{19} eV. In: *Phys. Rev. Lett.*, volume 101:p. 061101, 2008. `arXiv:0806.4302`.

[A$^+$08c] Acciari, V. A.; et al. (VERITAS): Observation of gamma-ray emission from the galaxy M87 above 250 GeV with VERITAS. In: *Astrophys. J.*, volume 679:p. 1427, 2008.

[A$^+$08d] Albert, J.; et al. (MAGIC): Implementation of the Random Forest Method for the Imaging Atmospheric Cherenkov Telescope MAGIC. In: *Nucl. Instrum. Meth.*, volume A588:pp. 424–432, 2008. `arXiv:0709.3719`.

[A$^+$08e] Albert, J.; et al. (MAGIC): VHE Gamma-Ray Observation of the Crab Nebula and its Pulsar with the MAGIC telescope. In: *Astrophys. J.*, volume 674:pp. 1037–1055, 2008. `arXive:0705.3244`.

[A$^+$08f] Aliu, E.; et al. (MAGIC): Detection of pulsed gamma-rays above 25 GeV from the Crab pulsar. In: *Science*, volume 322:pp. 1221–1224, 2008. `arXiv:0809.2998`.

[A$^+$09a] Abbasi, R.; et al. (The IceCube): Extending the search for neutrino point sources with IceCube above the horizon. In: *Phys. Rev. Lett.*, volume 103:p. 221102, 2009. `arXiv:0911.2338`.

[A$^+$09b] Abbasi, R.; et al. (IceCube): First Neutrino Point-Source Results From the 22-String IceCube Detector. In: *Astrophys. J.*, volume 701:pp. L47–L51, 2009. `arXiv:0905.2253`.

[A$^+$09c] Abdo, A. A.; et al. (Fermi LAT): Fermi Large Area Telescope Bright Gamma-ray Source List. In: *Astrophys. J. Suppl.*, volume 183:pp. 46–66, 2009. `arXive:0902.1340`.

[A$^+$09d] Acero, F.; et al. (HESS): PKS 2005-489 at VHE: Four Years of Monitoring with HESS and Simultaneous Multi-wavelength Observations. In: *Astronomy and Astrophysics, in press*, 2009. `0911.2709`.

[A+09e] Aliu, E.; et al. (MAGIC): Improving the performance of the single-dish Cherenkov telescope MAGIC through the use of signal timing. In: *Astropart. Phys.*, volume 30:pp. 293–305, 2009. `arXiv:0810.3568`.

[A+09f] Aynutdinov, V.; et al.: Baikal neutrino telescope: an underwater laboratory for astroparticle physics and environmental studies. In: *Nucl. Instrum. Meth.*, volume A598:pp. 282 – 288, 2009.

[Ack06] Ackermann, M.: *Searches for signals from cosmic point-like sources of high energy neutrinos in 5 years of AMANDA-II data.* Ph.D. thesis, Humboldt University, Berlin, Germany, 2006.

[AD03] Atoyan, A. M.; Dermer, C. D.: Neutral beams from blazar jets. In: *Astrophys. J.*, volume 586:pp. 79–96, 2003. `astro-ph/0209231`.

[AD04] Atoyan, A. M.; Dermer, C. D.: Neutrinos and gamma-rays of hadronic origin from AGN jets. In: *New Astron. Rev.*, volume 48:pp. 381–386, 2004. `astro-ph/0402646`.

[Aha00] Aharonian, F.: TeV gamma rays from BL Lac objects due to synchrotron radiation of extremely high energy protons. In: *New Astronomy*, volume 5:pp. 377–395, 2000. `astro-ph/0003159`.

[Aha06] Aharonian, F. A. (HESS): Fast variability of TeV gamma-rays from the radio galaxy M87. In: *Science*, volume 314:p. 1424, 2006. `astro-ph/0612016`.

[B+96] Buckley, J. H.; et al.: Gamma-Ray Variability of the BL Lacertae Object Markarian 421. In: *Astrophys. J. Lett.*, volume 472:p. L9, 1996.

[B+97a] Barrau, A.; et al.: Performances of the CAT imaging telescope and some preliminary results on Mkn 180 and the Crab. In: , 1997. `astro-ph/9710260`.

[B+97b] Bradbury, S. M.; et al. (HEGRA): Detection of gamma-rays above 1.5 TeV from Mkn 501. In: *Astron. Astrophys.*, volume 320:pp. L5–L8, 1997.

[B+98] Barrau, A.; et al.: The CAT imaging telescope for very-high-energy gamma ray astronomy. In: *Nucl. Instrum. Meth.*, volume A416:pp. 278–292, 1998. `astro-ph/9804046`.

[B+99] Biermann, P. L.; et al.: *Numerical data and functional relationships in science and technology. Volume 3: Astronomy and astrophysics. Subvolume c: Interstellar matter, Galaxy, universe.* Springer, 1999. ISBN 3-540-56081-5.

[B+00] Błażejowski, M.; et al.: Comptonization of Infrared Radiation from Hot Dust by Relativistic Jets in Quasars. In: *Astrophys. J.*, volume 545:pp. 107–116, 2000. `astro-ph/0008154`.

[B$^+$02] Bernstein, R. A.; et al.: The First Detections of the Extragalactic Background Light at 3000, 5500, and 8000A (I): Results. In: *Astrophys. J.*, volume 571:pp. 56–84, 2002. `astro-ph/0112153`.

[B$^+$05a] Bottcher, M.; et al. (WEBT-ENIGMA): Multiwavelength Observations of 3C 66A during the WEBT campaign of 2003 - 2004. In: *Astrophys. J.*, volume 631:pp. 169–186, 2005. `astro-ph/0506209`.

[B$^+$05b] Bramall, N. E.; et al. (IceCube): A deep high-resolution optical log of dust, ash, and stratigraphy in South Pole glacial ice. In: *Geophys. Res. Lett.*, volume 32:p. L21815, 2005.

[B$^+$06] Bazzano, A; et al. (INTEGRAL): INTEGRAL/Ibis Census of the Sky Beyond 100 kev. In: *Astrophys. J.*, volume 649:pp. L9–L12, 2006.

[B$^+$07] Braun, J.; et al.: Optimized neutrino point source search strategies for AMANDA and results from 2005. In: *Proceedings of the 30th ICRC*, volume 5, pp. 1437–1440. Merida, Mexico, July 2007.

[B$^+$08] Bretz, T.; et al.: Long-term monitoring of bright blazars with a dedicated Cherenkov telescope. In: *Proceedings of the 4th International Meeting on High Energy Gamma-Ray Astronomy*, volume 1085, pp. 850–853. Heidelberg, Germany, 2008.

[B$^+$09a] Bretz, T.; et al. (MAGIC): The drive system of the Major Atmospheric Gamma-ray Imaging Cherenkov Telescope. In: *Astropart. Phys.*, volume 31:pp. 92–101, 2009. `arXiv:0810.4593`.

[B$^+$09b] Britzger, D.; et al.: Studies of the Influence of Moonlight on Observations with the MAGIC Telescope. In: *Proceedings of the 31st ICRC*. Łódź, Poland, July 2009. `archive:0907.0973`.

[BB99] Beall, J. H.; Bednarek, W.: On the Hadronic Beam Model for Gamma-ray Production in Blazars. In: *Astrophys. J.*, volume 510:p. 188, 1999. `astro-ph/9802001`.

[Bed93] Bednarek, W.: On the gamma-ray emission from 3C 279. In: *Astrophys. J.*, volume 402:p. L 29, 1993.

[Ber89] Bertero, M.: Linear inverse and ill-posed problems. In: *Advances in Electronics and Electron Physics*, volume 75:pp. 1–120, 1989.

[Ber05] Bernardini, E.: Multi-Messenger Studies with AMANDA/IceCube: Observations and Strategies. In: *Proceedings of 7th Workshop Towards a Network of Atmospheric Cherenkov Detectors*. Palaiseau, France, April 2005. `arXiv:astro-ph/0509396`.

[Boe04] Boettcher, M.: Coordinated Multiwavelength Observations and Spectral Variability Modeling of Gamma-Ray Blazars. In: *5th INTEGRAL Workshop on the INTEGRAL Universe*, volume 552, p. 543. October 2004.

[BR90] Blandford R.D., Woltjer L., Netzer H.: *Active Galactic Nuclei. Saas-Fee Advanced Course 20. Lecture Notes 1990. Swiss Society for Astrophysics and Astronomy.* Springer Verlag, 1990. ISBN 978-3-540-53285-9.

[Bri09] Britzger, D.: *Studies of the Influence of Moonlight on Observations with the MAGIC Telescope.* Master's thesis, Ludwig-Maximilians-Universit a, M unchen, 2009.

[Ce05] Chadwick, P. M.; et al.: Simultaneous X-ray and VHE gamma-ray observations of microquasars. In: *Proceedings of the 29th ICRC*, volume 4, p. 263. Pune, India, August 2005.

[Cel08] Celik, O.: *Observations of the Crab Nebula and Pulsar with VERITAS.* Ph.D. thesis, University of California, Los Angeles, 2008.

[CH08] Cuoco, A.; Hannestad, S.: Ultra-high energy Neutrinos from Centaurus A and the Auger hot spot. In: *Phys. Rev.*, volume D78:p. 023007, 2008. `arXive:0712.1830`.

[Che34] Cherenkov, P.A.: Visible emission of clean liquids by action of gamma radiation. In: *Doklady Akad. Nauk SSSR*, volume 2:p. 451, 1934.

[Che08] Cherenkova, E. P.: The discovery of the Cherenkov radiation. In: *Nucl. Instrum. Meth.*, volume 595:pp. 8 – 11, 2008.

[D$^+$99] Djannati-Atai , A.; et al. (CAT): Very High Energy Gamma-ray spectral properties of MKN 501 from CAT Čerenkov telescope observations in 1997. In: *Astron. Astrophys.*, volume 350:pp. 17–24, 1999. `arXiv:astro-ph/9906060`.

[D$^+$08a] DeYoung, Tyce; et al. (IceCube): Results from Seven Years of AMANDA-II. In: *J. Phys. Conf. Ser.*, volume 136:p. 022046, 2008. `arXiv:0810.4513`.

[D$^+$08b] Doro, M.; et al.: The reflective surface of the MAGIC telescope. In: *Nucl. Instrum. Meth.*, volume 595:p. 200, 2008.

[D$^+$09] Donnarumma, I.; et al.: The June 2008 flare of Markarian 421 from optical to TeV energies. In: *Astrophys. J.*, volume 691:pp. L13–L19, 2009. `arXiv:0812.1500`.

[DA98] Dwek, E.; Arendt, R. G.: A Tentative Detection of the Cosmic Infrared Background at 3.5 μm from COBE/DIRBE Observations. In: *Astrophys. J.*, volume 508:pp. L9–L12, 1998. `arXiv:astro-ph/9809239`.

[DL97] Dar, Arnon; Laor, Ari: Hadronic production of TeV gamma-ray flares from blazars. In: *Astrophys. J.*, volume 478:pp. L5–L8, 1997. `astro-ph/9610252`.

[DS93a] Dermer, C. D.; Schlickeiser, R.: Model for the high-energy emission from blazars. In: *Astrophys. J.*, volume 416:p. 458, 1993.

[DS93b] Dermer, C. D.; Schlickeiser, R.: Model for the High-Energy Emission from Blazars. In: *Astrophys. J.*, volume 416:pp. 458–+, 1993.

[dW08] de Wolf, E.: KM3NeT: a next generation neutrino telescope. In: *Proceedings of RICAP07*, volume A588, pp. 86 – 91. Roma, Italy, 2008.

[E$^+$99] Elbaz, D.; et al.: Source counts from the 15 mu m ISOCAM Deep Surveys. In: *Astron. Astrophys.*, volume 351:pp. L37–L40, 1999. `arXiv:astro-ph/9910406`.

[EK88] Edelson, R. A.; Krolik, J. H.: The discrete correlation function - A new method for analyzing unevenly sampled variability data. In: *Astrophys. J.*, volume 333:pp. 646–659, 1988.

[F$^+$94] Fomin, V. P.; et al.: New methods of atmospheric Cherenkov imaging for gamma-ray astronomy. I. The false source method. In: *Astropart. Phys.*, volume 2:pp. 137–150, 1994.

[F$^+$98a] Fixsen, D. J.; et al.: The Spectrum of the Extragalactic Far-Infrared Background from the COBE FIRAS Observations. In: *Astrophys. J.*, volume 508:pp. 123–128, 1998. `arXiv:astro-ph/9803021`.

[F$^+$98b] Fossati, G.; et al.: A Unifying View of the Spectral Energy Distributions of Blazars. In: *Mon. Not. Roy. Astron. Soc.*, volume 299:pp. 433–448, 1998. `astro-ph/9804103`.

[F$^+$00] Finkbeiner, D. P.; et al.: Detection of a Far-Infrared Excess with DIRBE at 60 and 100 Microns. In: *Astrophys. J.*, volume 544:pp. 81–97, November 2000. `arXiv:astro-ph/0004175`.

[F$^+$07] Finley, C.; et al.: One year IceCube point source analysis. In: *Proceedings of the 30th ICRC*, volume 5, pp. 1389–1392. Merida, Mexico, July 2007.

[F$^+$08] Franceschini, A.; et al.: The extragalactic optical-infrared background radiations, their time evolution and the cosmic photon-photon opacity. In: *Astron. Astrophys.*, volume 487:pp. 837–852, 2008. `arXive:0805.1841`.

[FB09] Franke, R.; Bernardini, E. (IceCube): Neutrino triggered high-energy gamma-ray follow-up with icecube. In: *Proceedings of the 31st ICRC*. Łódź, Poland, July 2009.

[Fer49] Fermi, E.: On the Origin of the Cosmic Radiation. In: *Phys. Rev.*, volume 75:pp. 1169–1174, April 1949.

[G^+00] Gorjian, V.; et al.: Tentative Detection of the Cosmic Infrared Background at 2.2 and 3.5 Microns Using Ground-based and Space-based Observations. In: *Astrophys. J.*, volume 536:pp. 550–560, 2000. `arXiv:astro-ph/0103101`.

[G^+06a] Gliozzi, M.; et al.: Long-term X-Ray and TeV variability of Mrk 501. In: *Astrophys. J.*, volume 646:pp. 61–75, 2006. `astro-ph/0603693`.

[G^+06b] Gutierrez, K.; et al. (VERITAS): Multiwavelength Observations of 1ES 1959+650, One Year After the Strong Outburst of 2002. In: *Astrophys. J.*, volume 644:pp. 742–747, 2006. `astro-ph/0603013`.

[G^+07a] Giommi, P.; et al.: ROXA J081009.9+384757.0: a 10^{47} erg/s blazar with hard X-ray synchrotron peak or a new type of radio loud AGN? In: *Astron. Astrophys.*, volume 468:pp. 97–101, 2007.

[G^+07b] Goebel, F.; et al. (MAGIC): Long term monitoring of bright TeV Blazars with the MAGIC telescope. In: *Proceedings of the 30th ICRC*, volume 3, pp. 1025–1028. Merida, Mexico, July 2007. `arXiv:0709.2032`.

[G^+07c] Goebel, F.; et al. (MAGIC): Upgrade of the MAGIC Telescope with a Multiplexed Fiber-Optic 2 GSamples/s FADC Data Acquisition system. In: *Proceedings of the 30th ICRC*, volume 3, pp. 1481–1484. Merida, Mexico, July 2007. `arXiv:0709.2363`.

[G^+08] Galante, N.; et al. (MAGIC): Observation and upper limits of grbs with the magic telescope. In: *Proceedings of the 4th International Meeting on High Energy Gamma-Ray Astronomy*, volume 1085, pp. 411–414. Heidelberg (Germany), 2008.

[Gar06] Garczarczyk, M.: *First Observations of the GRB Prompt and Early Afterglow Emission Phase at ∼100 GeV Energy Regime with the 17 m Diameter MAGIC Imaging Atmospheric Cherenkov Telescope.* Ph.D. thesis, Universität Rostock, 2006.

[Gau06] Gaug, M.: *Calibration of the MAGIC telescope and observation of gamma-ray bursts.* Ph.D. thesis, Universitat Autonoma de Barcelona, Spain, 2006.

[GCC02] Ghisellini, G.; Celotti, A.; Costamante, L.: Low power BL Lacertae objects and the blazar sequence. In: *Astron. Astrophys.*, volume 386(3):pp. 833–842, 2002.

[Gin21] Gini, C.: Measurement of inequality of income. In: *Economic Journal*, volume 31:pp. 22–43, 1921.

[GM96] Ghisellini, G.; Madau, P.: On the origin of the gamma-ray emission in blazars. In: *Mon. Not. Roy. Astron. Soc.*, volume 280:pp. 67–76, 1996.

[Gre66] Greisen, K.: End to the cosmic-ray spectrum? In: *Phys. Rev. Lett.*, volume 16(17):pp. 748–750, 1966.

[Gri95] Grieder, P.K.F.: DUMAND II: String 1 deployment, initial operation, results and system retrieval. In: *Nuclear Physics B - Proceedings Supplements*, volume 43:pp. 145 – 148, 1995.

[Gro06] Gross, A.: *Search for High Energy Neutrinos from Generic AGN classes with AMANDA-II.* Ph.D. thesis, Universität Dortmund, 2006.

[Gru07a] Grube, J. (VERITAS): Observations of the Crab Nebula with the Whipple 10 m Telescope. In: *Proceedings of the 30th ICRC*, volume 2, pp. 691–694. Merida, Mexico, July 2007. `0709.4300`.

[Gru07b] Grube, J.: *X-ray and Gamma-ray Study of TeV Blazars with RXTE, XMM-Newton, and the Whipple 10 m Telescope.* Ph.D. thesis, University of Leeds, UK, 2007.

[H^+98] Hauser, M. G.; et al.: The COBE Diffuse Infrared Background Experiment Search for the Cosmic Infrared Background. I. Limits and Detections. In: *Astrophys. J.*, volume 508:pp. 25–43, 1998. `arXiv:astro-ph/9806167`.

[H^+99a] Hartman, R. C.; et al. (EGRET): The Third EGRET catalog of high-energy gamma-ray sources. In: *Astrophys. J. Suppl.*, volume 123:p. 79, 1999.

[H^+99b] Hess, M.; et al. (HEGRA): The time structure of Cherenkov images generated by TeV gamma-rays and by cosmic rays. In: *Astropart. Phys.*, volume 11:pp. 363–377, 1999. `astro-ph/9812341`.

[H^+03] Holder, J.; et al. (VERITAS): Detection of TeV gamma rays from the BL Lac object 1ES1959+650 with the Whipple 10-m telescope. In: *Astrophys. J.*, volume 583:pp. L9–L12, 2003. `astro-ph/0212170`.

[H^+05] Hao, L.; et al.: Active Galactic Nuclei in the Sloan Digital Sky Survey. I. Sample Selection. In: *Astron. J.*, volume 129:pp. 1783–1794, 2005. `astro-ph/0501059`.

[H^+06] Holder, J.; et al. (VERITAS): The First VERITAS Telescope. In: *Astropart. Phys.*, volume 25:pp. 391–401, 2006. `astro-ph/0604119`.

[H^+09] Holder, J.; et al.: Status of the VERITAS Observatory. In: *AIP Conf. Proc.*, volume 1085:pp. 657–660, 2009. `arXiv:0810.0474`.

[Hes12] Hess, V. F.: Beobachtungen der durchdringenden Strahlung bei sieben Freiballonfahrten. In: *Physikal Zs.*, volume 13:p. 1084, 1912.

[HH05] Halzen, F.; Hooper, D.: High energy neutrinos from the TeV blazar 1ES 1959+650. In: *Astropart. Phys.*, volume 23:pp. 537–542, 2005. `astro-ph/0502449`.

[Hil84] Hillas, A. M.: The origin of ultra-high-energy cosmic rays. In: *Ann. Rev. Astron. Astrophys.*, volume 22:pp. 425–444, 1984.

[Hil85] Hillas, A.M.: Cerenkov light images of EAS produced by primary gamma. In: *Proceedings of 19th ICRC (La Jolla)*, volume 3, p. 445. 1985.

[HT06] Hanson, K.; Tarasova, O.: Design and production of the IceCube digital optical module. In: *Nucl. Instrum. Meth.*, volume A567:pp. 214–217, 2006.

[J$^+$00] Juvela, M.; et al.: Far infrared extragalactic background radiation — I. Source counts with ISOPHOT. In: *Astron. Astrophys.*, volume 360:pp. 813–832, 2000. `arXiv:astro-ph/0005510`.

[J$^+$09] J., Dumm; et al. (IceCube): All-sky point-source search with 40 strings of IceCube. In: *Proceedings of 31st ICRC*. Łódź, Poland, July 2009.

[K$^+$95] Kerrick, A. D.; et al.: Outburst of TeV photons from Markarian 421. In: *Astrophys. J. Lett.*, volume 438:pp. L59–L62, 1995.

[K$^+$01] Krawczynski, H.; et al. (HEGRA): Simultaneous X-ray and TeV gamma-ray observations of the TeV blazar Markarian 421 during February and May 2000. In: *Astrophys. J.*, volume 559:pp. 187–195, 2001. `astro-ph/0105331`.

[K$^+$02] Kneiske, T. M.; et al.: Implications of cosmological gamma-ray absorption. I. Evolution of the metagalactic radiation field. In: *Astron. Astrophys.*, volume 386:pp. 1–11, 2002. `arXiv:astro-ph/0202104`.

[K$^+$04a] Kneiske, T. M.; et al.: Implications of Cosmological Gamma-Ray Absorption II. Modification of gamma-ray spectra. In: *Astron. Astrophys.*, volume 413:pp. 807–815, 2004. `astro-ph/0309141`.

[K$^+$04b] Krawczynski, Henric; et al.: Multiwavelength observations of strong flares from the TeV-blazar 1ES 1959+650. In: *Astrophys. J.*, volume 601:pp. 151–164, 2004. `astro-ph/0310158`.

[K$^+$04c] Kubo, H.; et al.: Status of the CANGAROO-III Project. In: *New Astron. Rev.*, volume 48:pp. 323–329, 2004.

[K$^+$07] Koul, R.; et al.: The TACTIC atmospheric Cherenkov Imaging telescope. In: *Nucl. Instrum. Meth.*, volume A578:pp. 548–564, 2007. `arXiv:0706.2055`.

[K$^+$09] Kranich, D.; et al.: Multi-wavelength observations of Mrk 501 in 2008. In: *Proceedings of the 31st ICRC*. Łódź, Poland, July 2009.

[KC62] Kraushaar, W. L.; Clark, G. W.: Search for primary cosmic gamma rays with the satellite explorer xi. In: *Phys. Rev. Lett.*, volume 8(3):pp. 106–109, 1962.

[Kes01] Kestel, M.: *Ph.D Thesis*. Ph.D. thesis, MPPMU, Muenchen, 2001.

[Khe02] Khelifi, B.: *Recherche de sources gamma par une methode de Maximum de Vraisemblance: Application aux les AGN et aux sources galactiques suivis par le telescope CAT*. Ph.D. thesis, Universite de Caen/Basse-Normandie, 2002.

[KSK01] Katarzynski, K.; Sol, H.; Kus, A.: The multifrequency emission of Mrk 501. In: *Astron. Astrophys.*, volume 367(3):pp. 809–825, 2001.

[KZ66] Kuzmin, V.A.; Zatsepin, G. T.: Upper limit of the spectrum of cosmic rays. In: *JETP Lett.*, volume 4:pp. 78–80, 1966.

[L$^+$99] Lagache, G.; et al.: First detection of the WIM dust emission. Implication for the Cosmic Far-Infrared Background. In: *Astron. Astrophys.*, volume 344:pp. 322–332, 1999. `astro-ph/9901059`.

[L$^+$01] Lessard, R. W.; et al.: A new analysis method for reconstructing the arrival direction of TeV gamma-rays using a single imaging atmospheric Cherenkov telescope. In: *Astropart. Phys.*, volume 15:pp. 1–18, 2001. `astro-ph/0005468`.

[L$^+$09a] L., Bazo-Alba J.; et al. (IceCube): Search for neutrino flares from point sources with IceCube. In: *Proceedings of the 31st ICRC*. Łódź, Poland, July 2009.

[L$^+$09b] Lopez, M.; et al. (MAGIC): Detection of the crab pulsar with MAGIC. In: *Proceedings of the 31st ICRC*. Łódź, Poland, July 2009. `0907.0832`.

[Lan05] Lang, R.: *Search for Point Sources of High-Energy Neutrinos with the AMANDA Detector*. Master's thesis, University of Ulm, 2005.

[Lev06] Levinson, A.: High-energy aspects of astrophysical jets. In: *Int. J. Mod. Phys.*, volume A21:pp. 6015–6054, 2006. `astro-ph/0611521`.

[LM83] Li, T.-P.; Ma, Y.-Q.: Analysis methods for results in gamma-ray astronomy. In: *Astrophys. J.*, volume 272:pp. 317–324, 1983.

[Lon92] Longair, S. M.: *High Energy Astrophysics*. Cambridge University Press, 1992. ISBN 0-521-38374-9.

[LS91] Lipari, P.; Stanev, T.: Propagation of multi-TeV muons. In: *Phys. Rev. D*, volume 44(11):pp. 3543–3554, 1991.

[M$^+$92] Maraschi, L.; et al.: A jet model for the gamma-ray emitting blazar 3C 279. In: *Astrophys. J. Lett.*, volume 397:pp. L5–L9, 1992.

[M$^+$94] Mirzoyan, R.; et al.: The first telescope of the HEGRA air Cherenkov imaging telescope array. In: *Nucl. Instrum. Meth.*, volume A351:pp. 513–526, 1994.

[M$^+$99] Maraschi, L.; et al.: Simultaneous X-Ray and TeV Observations of a Rapid Flare from Markarian 421. In: *Astrophys. J. Lett.*, volume 526:pp. L81–L84, 1999.

[M$^+$03] Muecke, A.; et al.: BL Lac objects in the synchrotron proton blazar model. In: *Astropart. Phys.*, volume 18:pp. 593–613, 2003. `astro-ph/0206164`.

[M$^+$04] Meucci, M.; et al.: The trigger system of the MAGIC telescope: on-line selection strategies for Cherenkov telescopes. In: *Nucl. Instrum. Meth.*, volume A518:pp. 554–556, 2004.

[M$^+$08] Maraschi, L.; et al.: Testing the blazar spectral sequence: X-ray selected blazars. In: *Mon. Not. Roy. Astron. Soc.*, volume 391:pp. 1981–1993, 2008. `arXiv:0810.0145`.

[Man93] Mannheim, K.: The Proton blazar. In: *Astron. Astrophys.*, volume 269:p. 67, 1993. `astro-ph/9302006`.

[Mar60] Markov, M.A.: On high energy neutrinos. In: *Proceedings of Annual Int.Conf on High Energy Physics*, volume 1, p. 578. Rochester, UK, 1960.

[Mig06] Migneco, E.: Status of the NEMO project. In: *Proceedings of NO-VE III International Workshop on Neutrino Oscillations*. February 2006.

[MPR01] Mannheim, K.; Protheroe, R. J.; Rachen, J. P.: On the cosmic ray bound for models of extragalactic neutrino production. In: *Phys. Rev.*, volume D63:p. 023003, 2001. `astro-ph/9812398`.

[MR07] Mazin, D.; Raue, M.: New limits on the density of the extragalactic background light in the optical to the far-infrared from the spectra of all known TeV blazars. In: *Astron. Astrophys.*, volume 471:pp. 439–452, 2007. `astro-ph/0701694`.

[N$^+$99] Nishiyama, T.; et al.: Detection of a new tev gamma-ray source of bl lac object 1es 1959+650. In: *Proceedings of the 26th ICRC*, volume 3, pp. 370–373. Salt Lake City, USA, July 1999.

[Ott07] Otte, M.: *Observation of VHE Gamma-Rays from the Vicinity of magnetized Neutron Stars and Development of new Photon-Detectors for Future Ground based Gamma-Ray Detectors*. Ph.D. thesis, Technische Universität München, October 2007.

[P$^+$98] Pozzetti, L.; et al.: High-redshift galaxies in the Hubble Deep Field - II. Colours and number counts. In: *Mon. Not. Roy. Astron. Soc.*, volume 298:pp. 1133–1144, 1998. `arXiv:astro-ph/9803144`.

[P$^+$01] Piron, F.; et al.: Temporal and spectral gamma-ray properties of Mkn 421 above 250 GeV from CAT observations between 1996 and 2000. In: *Astron. Astrophys.*, volume 374:pp. 895–906, 2001. `astro-ph/0106196`.

[P$^+$03] Puhlhofer, G.; et al. (HEGRA): The Technical Performance of the HEGRA System of Imaging Air Cherenkov Telescopes. In: *Astropart. Phys.*, volume 20:pp. 267–291, 2003. `astro-ph/0306123`.

[Pad07] Padovani, Paolo: The Blazar Sequence: Validity and Predictions. In: *Astrophys. Space Sci.*, volume 309:pp. 63–71, 2007. `astro-ph/0610545`.

[Pir00] Piron, F.: *Etude des proprietes spectrales et de la variabilite de l'emission gamma superieure a 250 GeV des noyaux actifs de galaxies de type blazar observes dans le cadre de l'experience CAT.* Ph.D. thesis, University of Orsay-Paris XI, 2000.

[PS00] Pohl, M.; Schlickeiser, R.: On the conversion of blast wave energy into radiation in Active Galactic Nuclei and Gamma-Ray Bursts. In: *Astron. Astrophys.*, volume 354:pp. 395–410, 2000. `astro-ph/9911452`.

[Q$^+$96] Quinn, J.; et al.: Detection of gamma-rays with E $>$ 300 GeV from Markarian 501. In: *Astrophys. J.*, volume 456:pp. L83–L86, 1996.

[R$^+$05] Rolke, W. A.; et al.: Confidence Intervals with Frequentist Treatment of Statistical and Systematic Uncertainties. In: *Nucl. Instrum. Meth.*, volume A551:pp. 493–503, 2005. `physics/0403059`.

[R$^+$06] Rebillot, P. F.; et al.: Multiwavelength Observations of the Blazar Markarian 421 in 2002 December and 2003 January. In: *Astrophys. J.*, volume 641:pp. 740–751, April 2006. `arXiv:astro-ph/0512628`.

[R$^+$08] Rissi, M.; et al.: A new sum trigger to provide a lower energy threshold for the magic telescope. In: *IEEE Transactions on Nuclear Science*, volume 56:pp. 3840–3843, 2008.

[RM97] R. Mirzoyan, E .Lorenz: On the calibration accuracy of light sensors in atmospheric cherenkov, fluorescence and neutrino experiments. In: *Proceedings of the 25th ICRC*, volume VII, pp. 265–268. Durban, 1997.

[S$^+$87] Soifer, B. T.; et al.: The IRAS bright galaxy sample. II - The sample and luminosity function. In: *Astrophys. J.*, volume 320:pp. 238–257, 1987.

[S$^+$94] Sikora, M.; et al.: Comptonization of diffuse ambient radiation by a relativistic jet: The source of gamma rays from blazars? In: *Astrophys. J.*, volume 421:p. 153, 1994.

[S$^+$96] Schubnell, M. S.; et al.: Very High Energy Gamma-Ray Emission from the Blazar Markarian 421. In: *Astrophys. J.*, volume 460:p. 644, 1996. `astro-ph/9602068`.

[S$^+$02] Schweizer, T.; et al.: The optical calibration of the MAGIC telescope camera. In: *IEEE Transactions on Nuclear Science*, volume 49:pp. 2497–2503, 2002.

[S$^+$07] Satalecka, K.; et al. (IceCube): Cluster search for neutrino flares from predefined directions. In: *Proceedings of the 30th ICRC*, volume 5, pp. 1353–1356. Merida, Mexico, 2007. `arXiv:0711.0353`.

[Sch02] Schmidt, T.: *Aufbau und Funktionsnachweis eines Optischen Moduls mit optisch-analoger Pulsübertragung für den AMANDA-II- und IceCube-Detektor.* Ph.D. thesis, Humboldt Universität Berlin, 2002.

[Sch08] Schultz, O.: The IceCube DeepCore. In: *4th International Meeting on High Energy Gamma-Ray Astronomy*, volume 1085 of *AIP Conf. Ser.*, pp. 783–786. Heidleberg, Germany, July 2008.

[SPS02] Schuster, C.; Pohl, M.; Schlickeiser, R.: Neutrinos from active galactic nuclei as a diagnostic tool. In: *Astron. Astrophys.*, volume 382:pp. 829–837, 2002. `astro-ph/0111545`.

[SS96] Stecker, F. W.; Salamon, M. H.: High energy neutrinos from quasars. In: *Space Sci. Rev.*, volume 75:pp. 341–355, 1996. `astro-ph/9501064`.

[Ste05] Stecker, Floyd W.: A note on high energy neutrinos from AGN cores. In: *Phys. Rev.*, volume D72:p. 107301, 2005. `astro-ph/0510537`.

[T$^+$98a] Tanimori, T.; et al.: Detection of Gamma Rays of up tp 50 TeV from the Crab Nebula. In: *Astrophys. J. Lett.*, volume 492:pp. L33–36, 1998.

[T$^+$98b] Tavecchio, F.; et al.: Constraints on the physical parameters of TeV blazars. In: *Astrophys. J.*, volume 509:pp. 608–619, 1998. `astro-ph/9809051`.

[T$^+$07a] Tescaro, D.; et al.: Study of the performance and capability of the new ultrafast 2 GSample/s FADC data acquisition system of the MAGIC telescope. In: *Proceedings of the 30th ICRC*, volume 3, pp. 1393–1396. Merida, Mexico, July 2007. `arXiv:0709.1410`.

[T$^+$07b] Tluczykont, M.; et al.: Long-term gamma-ray lightcurves and high state probabilities of Active Galactic Nuclei. In: *J. Phys.: Conf. Ser.*, volume 60:pp. 318–320, 2007. `astro-ph/0506319`.

[T$^+$08a] Tagliaferri, G.; et al.: Simultaneous multiwavelength observations of the blazar 1ES1959+650 at a low TeV flux. In: *Astrophys. J.*, volume 679:pp. 1029–1039, 2008. `arXiv:0801.4029`.

[T$^+$08b] Tavani, M.; et al.: The AGILE space mission. In: *Nucl. Instrum. Meth.*, volume A588:pp. 52–62, 2008.

[TA79] Tikhonov, A. N.; Arsenin, V. Ya.: Methods for the solution of ill-posed problems [in russian]. In: *Nauka*, 1979.

[Tes07] Tescaro, D.: *Timing Analysis of the MAGIC Telescope Data after the Installation of the Ultra-fast 2 GSamples/s FADC Readout*. Master's thesis, IFAE Barcelona, 2007.

[Tza03] Tzamarias, S. E. (NESTOR): NESTOR: A deep-sea neutrino telescope. In: *Nucl. Instrum. Meth.*, volume A502:pp. 150–154, 2003.

[V$^+$03] Vaughan, S.; et al.: On characterising the variability properties of X-ray light curves from active galaxies. In: *Mon. Not. Roy. Astron. Soc.*, volume 345:p. 1271, 2003. `astro-ph/0307420`.

[V$^+$04] Villata, M.; et al. (WEBT): The WEBT BL Lacertae Campaign 2001 and its extension. In: *Astron. Astrophys.*, volume 421:pp. 103–114, 2004. `astro-ph/0404155`.

[VR99] Villata, M.; Raiteri, C. M.: Helical jets in blazars. I. The case of Mkn 501. In: *Astron. Astrophys.*, volume 347:pp. 30–36, 1999.

[W$^+$89] Weekes, T. C.; et al.: Observation of TeV gamma rays from the Crab nebula using the atmospheric Cerenkov imaging technique. In: *Astrophys. J.*, volume 342:pp. 379–395, 1989.

[Wag06] Wagner, R. M.: *Temporal and spectral characteristics of the VHE gamma-ray emission of four blazars as observed with the MAGIC telescope and a comparative study of the properties of VHE gamma-ray emitting blazars*. Ph.D. thesis, Technical University, Munich, 2006.

[WB97] Waxman, E.; Bahcall, J. N.: High energy neutrinos from cosmological gamma-ray burst fireballs. In: *Phys. Rev. Lett.*, volume 78:pp. 2292–2295, 1997. `astro-ph/9701231`.

[WB00] Waxman, E.; Bahcall, J. N.: Neutrino afterglow from gamma ray bursts: approx. 10^{18} eV. In: *Astrophys. J.*, volume 541:pp. 707–711, 2000. `hep-ph/9909286`.

[WSBM98] Wiebel-Sooth, B.; Biermann, P. L.; Meyer, H.: Cosmic Rays VII. Individual element spectra: prediction and data. In: *Astron. Astrophys.*, volume 330:pp. 389–398, 1998. `astro-ph/9709253`.

[Y+95] Yoshida, S.; et al.: The cosmic ray energy spectrum above 3×10^{18} eV measured by the Akeno Giant Air Shower Array. In: *Astropart. Phys.*, volume 3:pp. 105–123, 1995.

[ZB02] Zier, Ch.; Biermann, P. L.: Binary black holes and tori in AGN II. Can stellar winds constitute a dusty torus? In: *Astron. Astrophys.*, volume 396:pp. 91–108, 2002. `astro-ph/0203359`.

List of Figures

List of Tables

Acknowlegements

I would like to thank in the first place Dr. Elisa Bernardini, the supervisor of this thesis, for making it all possible to happen. She is in a major part responsible for the, so far, most challenging and exciting three years of my life. I will be always very grateful for her help, guidance and friendship.

I also would like to express my gratitude to Prof. dr hab. Włodzimierz Bednarek and Dr. Fabrizio Tavecchio for interesting discussions on the blazar emission models. In particular to Fabrizio, who allowed me to use his model for the SED of the Mkn 501 presented in this work.

Dr. Pratik Majumdar and Dr. Martin Tluczykont rank high on my personal heroes list - without them my first steps in the field of VHE γ-ray wouldn't be so easy... Pratik gains an extra point as a proof-reader of this thesis ;)

I am very grateful to all of the members from the the Astroparticle Group in Zeuthen for interesting discussions and useful advice on any topic from physics, trough the nuances of German language, to life in general. I appreciated very much the friendly atmosphere during and after the working hours, especially the baikal-fun activities :)

Many thanks to my collegues from the IceCube and MAGIC Collaborations, I learned a lot from you! Special thanks to Nijil for making my first shift at LaPalma such an extraordinary (culinary) experience.

No words can express my gratitude to Jürgen, who was always there for me. His infinite patience to all my follies, delicious chicken soup and warm embrace rescued me in the most difficult moments.

Lew, I thank you from all of my heart for being less of a little monster than I expected...

And finally my parents, all of my family and my best friend Maria – even though you are so far away I always feel your love and support. Thank you!

Selbständigkeitserklärung

Ich erkläre, dass ich die vorliegende Arbeit selbständig und nur unter Verwendung der angegebenen Literatur und Hilfsmittel angefertigt habe.

Berlin, den 28.01.2008 Konstancja Satalecka